

# A THEORETICAL STUDY OF FLUID DYNAMIC ENERGY SEPARATION

by

Philip A. Graham

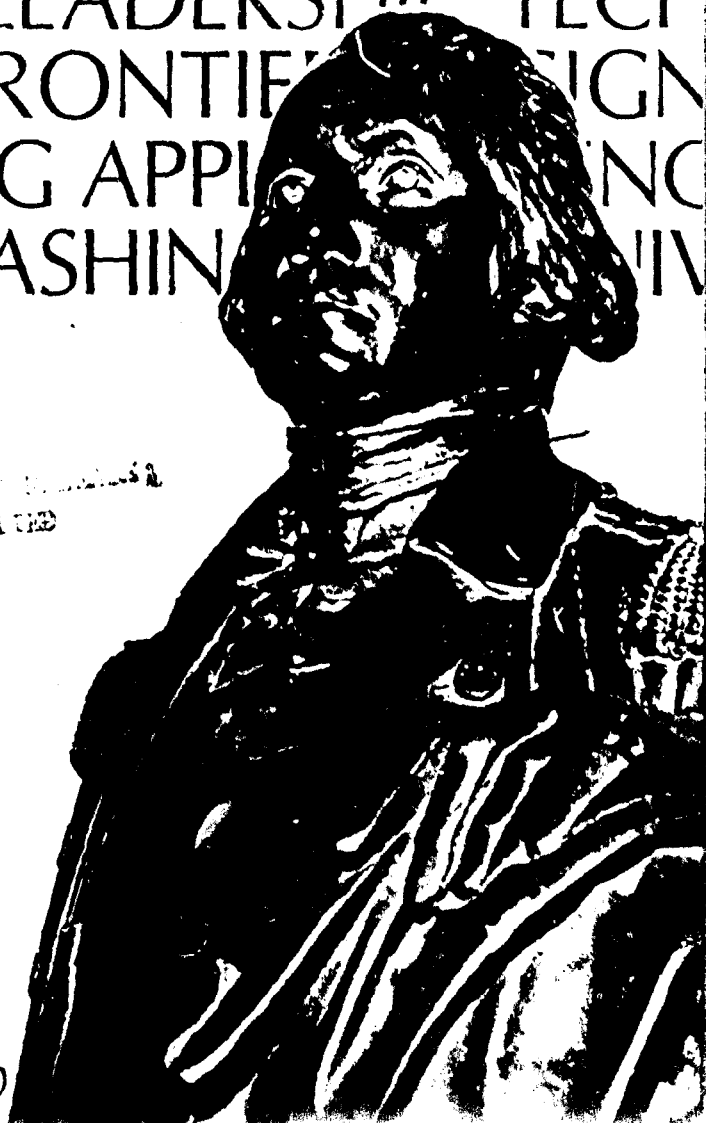
THE  
GEORGE  
WASHINGTON  
UNIVERSITY

STUDENTS FACULTY STUDY R  
ESEARCH DEVELOPMENT FUT  
URE CAREER CREATIVITY CO  
MMUNITY LEADERSHIP TECH  
NOLOGY FRONTIER DESIGN  
ENGINEERING APPLIED INNOV  
GEORGE WASHINGTON UNIV

DISSEMINATION UNLIMITED

**NATIONAL TECHNICAL  
INFORMATION SERVICE**  
U.S. Department of Commerce  
NIST (NBS) 2215

SCHOOL OF ENGINEERING  
AND APPLIED SCIENCE



A THEORETICAL STUDY  
OF FLUID DYNAMIC  
ENERGY SEPARATION

by

Philip A. Graham

Report No. TR-ES-721  
June 1972

APPROVED FOR PUBLIC RELEASE:  
DISTRIBUTION UNLIMITED

1  
School of Engineering and Applied Science  
The George Washington University  
Washington, D.C. 20006

ii

<b>BIBLIOGRAPHIC DATA SHEET</b>		1. Report No. TR-ES-721	2.	3. Recipient's Accession No.
4. Title and Subtitle A Theoretical Study of Fluid Dynamic Energy Separation			5. Report Date June 1, 1972	6.
7. Author(s) Philip A. Graham			8. Performing Organization Rept. No. TR-ES-721	
9. Performing Organization Name and Address George Washington University School of Engineering and Applied Science Washington, D. C. 20006			10. Project/Task/Work Unit No.	
			11. Contract/Grant No. N00019-72-C-0122	
12. Sponsoring Organization Name and Address Naval Air Systems Command Mechanical Equipment Branch Navy Department Washington, D. C. 20360			13. Type of Report & Period Covered N/A	
			14.	
15. Supplementary Notes				
16. Abstracts Three classes of energy separation techniques are analyzed and compared; steady flow, employed by the Ranque-Hilsch vortex tube (RHT); nonsteady flow, utilized by the dynamic pressure exchanger "divider" (DPE); and cryptosteady flow, used in the Foa energy separator (FES). The RHT is analyzed first to establish "upper bound" performance curves which are then compared with the best known experimental data; these exhibit performance generally in the range of one-half to two-thirds of theoretical. The discussion of the DPE is based on experimental data presented in the literature. The data reveal excellent low pressure ratio performance. However, cold fraction for maximum temperature drop decreases rapidly with increasing pressure ratio. The FES is analyzed to provide equations defining the dependence of performance on salient design and operational parameters. Additionally, several output flow collection effects are identified and analyzed. Comparison of the three devices indicates that the FES substantially outperforms the RHT at all pressure ratios and the DPE at all but the lowest pressure ratios.				
17. Key Words and Document Analysis. 17a. Descriptors  Fluid Dynamics Air Conditioning Cryogenics				
17b. Identifiers/Open-Ended Terms				
17c. COSATI Field/Group 2004 Fluid Mechanics, 1301 Air Conditioning, Heating				
18. Availability Statement  Limited Number Available Release Unlimited		19. Security Class (This Report) UNCLASSIFIED	21. No. of Pages 383	
		20. Security Class (This Page) UNCLASSIFIED	22. Price \$6.00	

# CONTENTS

	Page
ABSTRACT . . . . .	viii
I. INTRODUCTION . . . . .	1
A. Description of Existing Energy Separation Devices . . .	1
B. Scope of the Present Study . . . . .	9
II. THE RANQUE-HILSCH TUBE . . . . .	12
A. Historical Review . . . . .	12
1. General . . . . .	12
2. Review of Salient Literature . . . . .	13
3. A Comment on Qualitative Agreement of Performance Theory and Experiment . . . . .	34
B. Theoretical Performance Analysis . . . . .	38
1. Objectives and Approach . . . . .	38
Central purpose of the analysis . . . . .	38
Analytical model: uniflow configuration . . . . .	39
Outline of the analysis . . . . .	42
2. Entry-Plane Flow Conditions . . . . .	47
Flux equations . . . . .	47
Free vortex . . . . .	50
Model A: a priori upper bound . . . . .	52
Model B: estimated lower bound . . . . .	54
Model C: weak backflow . . . . .	55
Model D: strong backflow . . . . .	58
3. Terminal-Plane Flow Conditions . . . . .	61
Flow parameter distributions . . . . .	61
Flux equations . . . . .	65
4. Application of Conservation Equations--Plane I to Plane II . . . . .	79
Dependence of terminal vortex on injection conditions . . . . .	79
Thermodynamic upper bound on $Q_2/\phi_2$ . . . . .	85



	Page
5. Output Flows and Losses . . . . .	93
Tangential flow extraction . . . . .	93
Output flow parameters at plane II . . . . .	94
Exit losses . . . . .	103
Comparison of internal and exit losses . . . . .	111
6. Theoretical "Upper Bound" RHT Performance . . . . .	112
"Nominal split" case . . . . .	112
Standard-format performance plot . . . . .	121
C. Comparison of "Upper Bound" Theory with Experiment . . .	122
Nominal split . . . . .	122
Overall performance . . . . .	126
A new interpretation of the meaning of theoretical RHT performance curves . . . . .	128
III. THE FOA ENERGY SEPARATOR . . . . .	132
A. Historical Review . . . . .	132
B. Core Performance Equations . . . . .	133
1. External-Separation Configuration . . . . .	133
Analytical model . . . . .	133
Analysis . . . . .	136
Effect of pressure differential $\delta p$ in impingement region . . . . .	146
Baseline performance . . . . .	154
Effect of prerotation . . . . .	161
Effect of nozzle efficiency . . . . .	161
Effect of rotor torque . . . . .	163
Effect of offset angle . . . . .	166
Effect of unequal discharge pressures . . . . .	166
2. Internal-Separation Configuration . . . . .	174
Analytical model . . . . .	174
Analysis . . . . .	176
Effect of prerotation . . . . .	192
Effect of nozzle efficiencies . . . . .	194
Effect of unequal nozzle inclinations . . . . .	197
Effect of unequal discharge pressures . . . . .	199
Effect of rotor torque . . . . .	201

	Page
C. Collection Effects . . . . .	203
1. Selection of Effects to be Examined . . . . .	203
2. Viscous Reattachment Effects on External- Separation FES Performance . . . . .	204
Introduction . . . . .	204
Analysis . . . . .	204
3. Nonsteady Collection Effects on External- Separation FES Performance . . . . .	221
Introduction . . . . .	221
Nature and scope of the nonsteady collection analysis . . . . .	227
"Source" boundary condition on duct flow . . . . .	231
Analysis of supercritical flow in source region . . . . .	234
Initial shock conditions . . . . .	243
Perturbation relief transient: supercritical phase . . . . .	249
Perturbation relief transient: subcritical phase . . . . .	256
Description of the nonsteady collection process . . . . .	257
Performance analysis . . . . .	275
Additional performance-perturbing effects . . . . .	295
Results of performance calculations . . . . .	297
Cold-side pressure depression and rotor velocity perturbation . . . . .	303
Anticipated effects of exit plenums . . . . .	309
Anticipated effects of exit port area changes . . . . .	315
Influence of effects neglected in basic analysis . . . . .	319
Summary of principal nonsteady collection effects on performance . . . . .	323
IV. DISCUSSION AND CONCLUSIONS . . . . .	329
A. Review of Principal Findings . . . . .	329
1. The Ranque-Hilsch Tube . . . . .	329
2. The Dynamic Pressure Exchanger "Divider" . . . . .	333
3. The Foa Energy Separator . . . . .	334
B. Some Comparative Observations . . . . .	339
1. Foa Energy Separator and Ranque-Hilsch Tube . . . . .	339
2. Foa Energy Separator and Dynamic Pressure Exchanger . . . . .	341
3. The Generalized Energy Separation Performance Plot and Its Special Cases . . . . .	342

	Page
V. LITERATURE CITED . . . . .	346
APPENDIX A: OBSERVATIONS ON THE DPE DIVIDER . . . . .	A-1
APPENDIX B: NONSTEADY COLLECTION WAVE DIAGRAMS . . . . .	B-1
APPENDIX C: NOMENCLATURE . . . . .	C-1

## ACKNOWLEDGMENT

This research was supported by the Mechanical Equipment Branch of the U.S. Naval Air Systems Command, under Contract No. N00019-72-C-0122.

This report is taken from a thesis submitted in partial fulfillment of the requirements for the degree of Doctor of Philosophy (major subject: Aeronautical Engineering) at Rensselaer Polytechnic Institute.

## ABSTRACT

Techniques for energy separation fall into three distinct fluid mechanical classes. One is steady flow, employed by the Ranque-Hilsch vortex tube (RHT). Another is nonsteady flow, utilized in the dynamic pressure exchanger "divider" (DPE). The third is cryptosteady flow, wherein the flow is nonsteady relative to the reference frame in which it is used but is steady as viewed in a unique moving reference frame; the Foa energy separator (FES) uses this type of flow. A theoretical study of energy separation is presented whose focus is the FES but which also gives contextual attention to the RHT and DPE.

The RHT, historically the first energy separation device, is analyzed first to establish "upper bound" performance characteristics for comparison with the FES. The uniflow rather than the usual counterflow configuration is addressed, after their equivalence is discussed. The primary assumption needed for the present analysis concerns the terminal flow within the tube before output flow extraction; internal flow details need not be described for the "upper bound" analysis. It is well established that viscosity converts the flow within the tube into basically a forced, turbulent, compressible vortex, and that this transformation is responsible for the energy separation that occurs; the terminal vortex flow is therefore assumed to have undergone this conversion process completely. Terminal vortex and nozzle inlet conditions are related through conservation of mass, energy, angular momentum, and axial momentum; output flow conditions are obtained from the terminal vortex with inclusion of exit losses. The axial momentum equation and exit losses have both been neglected in

previous analyses, yet both are important: the momentum equation is required to properly relate performance to pressure ratio, and exit losses prove to be even more important than internal losses. "Upper bound" performance curves are compared with the best known experimental data; these exhibit performance generally in the range of one-half to two-thirds of theoretical, and in no case violate the bounds.

A similarly definitive analysis of the complex DPE would lie beyond the scope of its present contextual consideration. The discussion of the DPE is therefore limited, and is based on experimental data presented in the literature. The data reveal excellent low pressure ratio performance. However, cold fraction for maximum temperature drop decreases rapidly with increasing pressure ratio; if this behavior is an inherent characteristic of the DPE, performance at higher pressure ratios would become relatively unattractive.

The FES is analyzed to provide more comprehensive information on its performance capabilities and limitations than has been available before. "Core performance" equations are developed for both the internal- and external-separation versions of the device, defining the dependence of performance on salient design and operational parameters with full inclusion of the nonlinear interactions among these parameters. Additionally, two important output flow collection effects are identified and analyzed which are of general significance to the external-separation configuration, where collection effects are most relevant. Nonsteadiness in the collection process is found to be detrimental, while viscous reattachment of the deflected jets can be beneficial.

Brief comparison of the three devices indicates that the FES substantially outperforms the RHT, being competitive with the DPE at low pressure ratios where the latter achieves best performance, but without exhibiting similar deterioration in efficiency with increasing pressure ratio.

## PART 1

### INTRODUCTION

#### A. Description of Existing Energy Separation Devices

Energy separation may be defined as any fluid mechanical process in which an initially uniform flow is made to separate into two or more flows having different energy levels, without benefit of external heat transfer or shaft work. This remarkable phenomenon sometimes elicits cries of "Maxwell's demon" from the uninitiated--and, in jest, from the initiated as well<sup>1</sup>--but it is in fact a type of process having a wide range of potential applications. Fields as disparate as auto air conditioning, cryogenics, and environmental control for high-speed aircraft are all possible candidates to derive benefits from efficient energy separation processes.

There are three distinct classes of energy separation processes, and three corresponding types of energy separation apparatus have been devised. They are as follows:

(1) Steady flow (Ranque-Hilsch tube). The oldest type of energy separation device is the Ranque-Hilsch tube, which employs steady flow and has the distinction of using no moving parts. Invented about forty years ago by Ranque,<sup>2</sup> it has been the subject of a large amount of research over the past twenty-five years since publication of a paper by Hilsch.<sup>3</sup> The Ranque-Hilsch tube consists of a constant-area tube of high length-to-diameter ratio with a tangential injection nozzle and two exit ports, the latter being disposed so that flow near the tube axis leaves through one and the remainder of the flow through the other. As

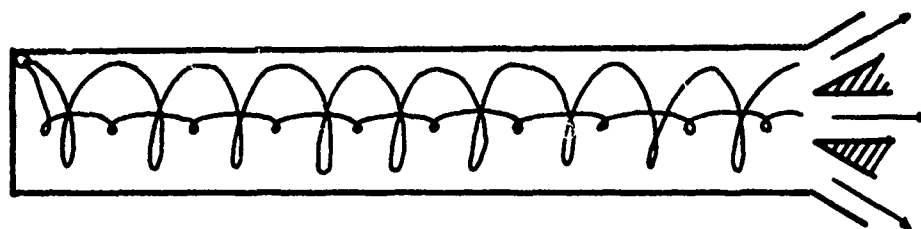


illustrated in Figure 1, there are two basic Ranque-Hilsch tube geometries: (a) "uniflow," in which the input nozzle is located at one end of the tube and both exit ports at the other end, and (b) "counterflow," in which the central portion of the flow must double back and exit through a port located at the injection plane.

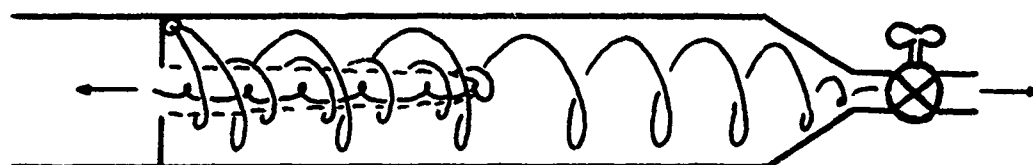
The tangentially injected fluid expands inward to fill the tube, tending to form a potential vortex near the injection plane. As the fluid travels on down the tube, viscous shear causes the velocity distribution to change over toward that of a forced vortex, the outer layers of the flow gaining energy at the expense of the inner layers. Therefore, when the inner and outer regions of the terminal flow are extracted separately through the respective ports, it is found that the average total temperature of the core is lower than that of the input flow, while that of the outer annulus is higher.

(2) Nonsteady flow (dynamic pressure exchanger). The next energy separation device to appear on the scene was the dynamic pressure exchanger "divider," which employs nonsteady wave processes. As has been reviewed by Azoury,<sup>4</sup> the dynamic pressure exchanger has been studied in various forms for several decades; however, the birthdate of the "divider" version apparently is marked approximately by the appearance in 1958 of patents by Spalding<sup>5</sup> and Jendrassik.<sup>6</sup>

As illustrated schematically in Figure 2, the basic elements of the divider are a cylindrical rotor with a large number of slender axial tubes or "cells" on its surface and a pair of end plates with cut-outs for porting purposes. Within each individual cell, a cyclic process takes place which begins with introduction of compressed gas at the



(a) Uniflow



(b) Counterflow

Figure 1  
Basic Ranque-Hiltsch Tube Configurations

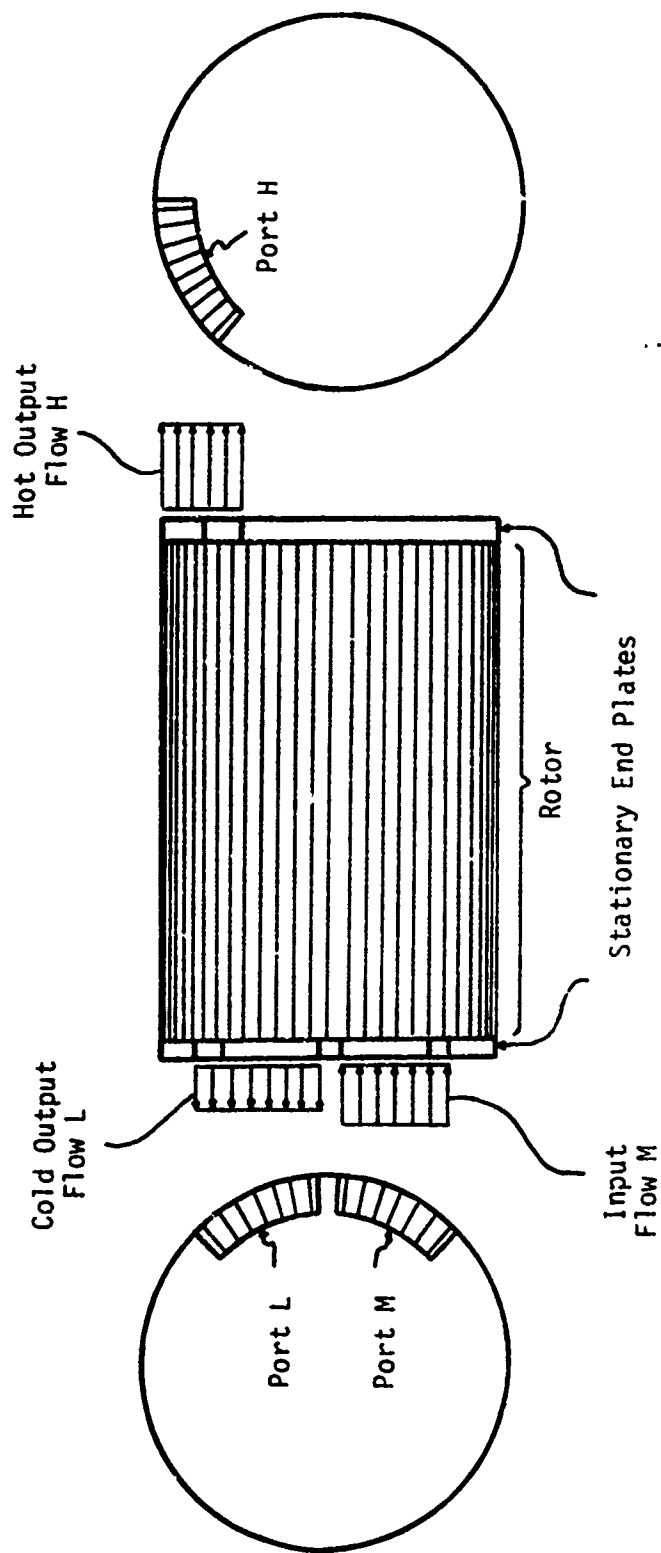


Figure 2  
Schematic Arrangement of Dynamic Pressure Exchanger "Divider"

left end and terminates after gas has been expelled from both ends at altered energy levels. Nonsteady one-dimensional wave processes occur during the cycle which cause the flow leaving at right to be energized while the flow leaving at left is de-energized. Events within the cell are controlled by opening and closing the ends according to a carefully determined schedule and regulating the pressures to which the open ends are exposed; for the left end, which opens twice each cycle, two different pressure levels are experienced.

The periodic opening and closing of the ends of the cell is effected by the end plates and cutouts therein as the cell rotates relative to them. The needed scheduling and timing is provided by adjusting the angular width and relative angular positioning of the ports. Input gas enters through port M (for "medium" energy-level flow), while the high- and low-temperature outputs leave via ports H and L, which are respectively maintained at higher and lower pressure levels than the input flow.

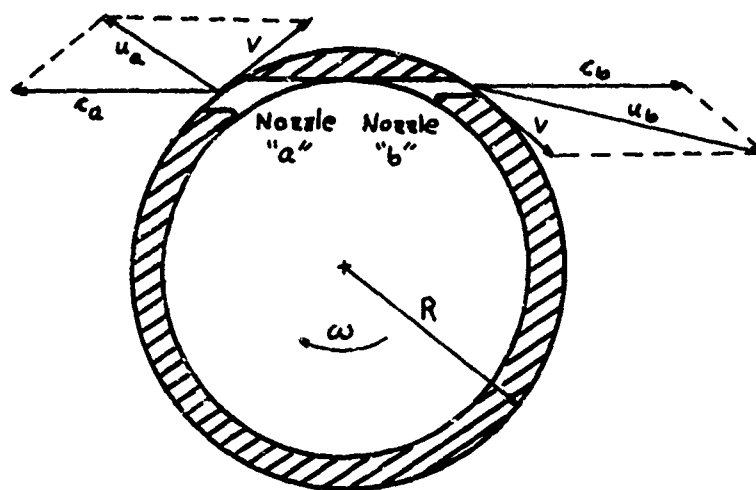
(3) Cryptosteady flow (Foa energy separator). The most recent innovation in the field of energy separation is the Foa energy separator, which first appeared in 1964.<sup>7</sup> This device makes use of cryptosteady flow, which itself is a new realm of fluid mechanics, having been first recognized and described by Foa in 1955.<sup>8</sup>

A cryptosteady flow is nonsteady in the reference frame wherein the flow is utilized, and also in all others except a unique frame  $F_S$ , in which it appears to be steady. The advantage to be gained from flow nonsteadiness, as has been pointed out by Dean,<sup>9</sup> is that it is possible for energy exchange to occur isentropically, whereas this cannot occur

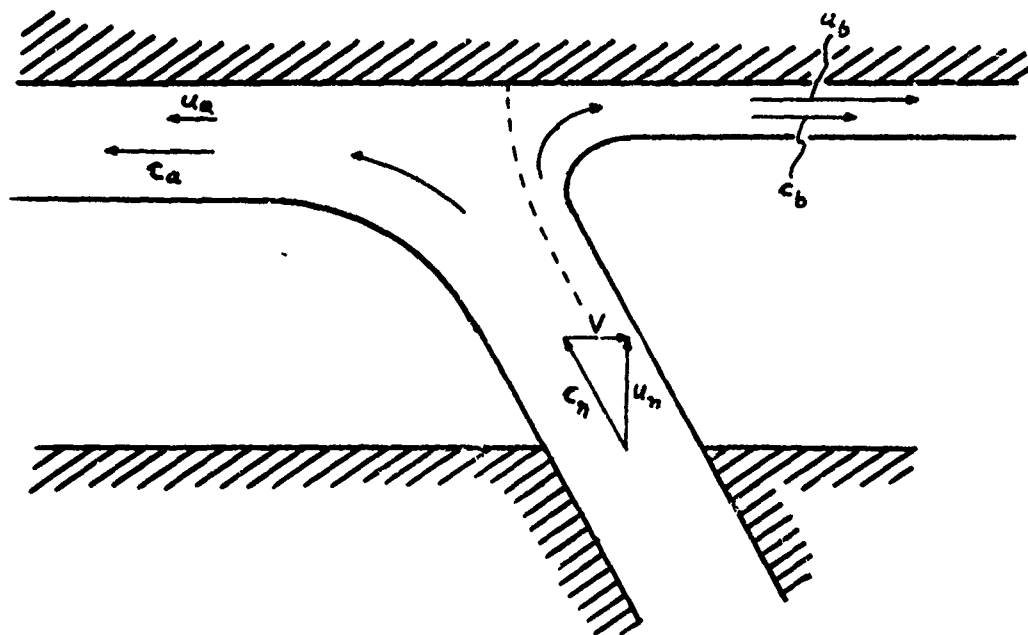
in steady flow. Since the nonsteadiness in cryptosteady flow is the result of a change of reference frame, and since a change of reference frame is reversible, it follows that the basic cryptosteady energy-exchange mode is in fact isentropic. However, use of the special reference frame  $F_S$  allows the flow pattern to be analyzed as if it were steady. Thus, cryptosteady flow confers both the efficiency advantages of non-steady flow and the analytical advantages of steady flow.

Unlike the Ranque-Hilsch tube and the dynamic pressure exchanger "divider," many different mechanical arrangements of the Foa energy separator are possible, examples of which have been presented by Foa in a 1968 patent.<sup>10</sup> This flexibility of arrangement is of considerable practical significance, since it opens the door to design optimization according to the particular performance criteria and constraints applying in any given application. However, the principle of operation is the same in all cases, and will be introduced here with the aid of Figure 3. The present description is intended only to impart a physical grasp of this principle; a more detailed examination of the Foa energy separator is presented later in the paper.

Consider a rotor such as that depicted in Figure 3(a), fitted with two nozzles oriented in opposite senses relative to the radial direction and mounted on frictionless bearings. Suppose, for further concreteness of the example, that the nozzle inclinations are equal and opposite, but that nozzle A is larger than nozzle B. Then if fluid is introduced into the rotor under pressure so that it must exit via the nozzles, the rotor will obviously begin rotating toward nozzle B as shown. The rotor speed established at steady state is such that the total angular momentum



(a) Internal Separation



(b) External Separation

Figure 3  
Basic Foa Energy Separator Schemes

contained in the two flows leaving the rotor is equal to that of the input flow.

At steady state, an observer sitting on the rotor sees a steady flow, whereas the laboratory observer sees a flow pattern which sweeps past a given point in space cyclically, and is therefore unsteady. Accordingly, the rotor-fixed reference frame will be denoted  $F_S$ , the laboratory frame  $F_U$ .

Viewed in  $F_S$ , the flow is steady with nozzle discharge velocities  $c_a$  and  $c_b$ . If the nozzles are equally efficient and discharge to equal static pressures, then  $c_a = c_b$  since the nozzles discharge from a common source. However, the magnitude  $u$  of the discharge velocity as seen in  $F_U$  differs from  $c$ , the value seen in  $F_S$ , by vector addition of the rotor rim speed  $V$ , i.e.  $\vec{u} = \vec{c} + \vec{V}$ . Since the nozzle inclinations are in opposite senses, this leads to  $u_a < c_a$  and  $u_b > c_b$ , as can be seen from Figure 3(a). But, as is easily concluded by considering the flow in  $F_S$ , the thermodynamic states of flows "a" and "b" are the same, and these states are the same in any reference frame. Therefore, it follows that the energy level of flow "b" as measured in  $F_U$  exceeds that of flow "a". Furthermore, since the rotor neither adds nor absorbs energy, the energy levels of flows "a" and "b" must be, respectively, lower and higher than that of the input flow. In other words, energy separation is accomplished.

Figure 3(b) illustrates a different means of achieving the same end as that served by the arrangement of Figure 3(a). Here, there is but a single nozzle, the flow from which is made to impinge on a wall as shown. The flow departs from the impingement region in both directions,

the direction of the larger "a" flow being in the same sense as the tangential component of  $c_n$ , the nozzle-exit velocity in  $F_S$ . For  $p_a = p_b$ , one has  $c_a = c_b = c_n$ , assuming the deflection process to be loss-free. If the flow plane of Figure 3(b) lies in the plane of rotation, then  $u_a = c_n - V$  and  $u_b = c_n + V$ , and one may readily verify that energy separation is once again obtained.

It will be noted that in the arrangement of Figure 3(a), the separation of the initially homogeneous flow into two flows at different energy levels is completed within the confines of the rotor. In the device pictured in Figure 3(b), by contrast, this separation process occurs entirely within the impingement-deflection region after the flow has left the rotor. Therefore, the arrangement of Figure 3(a) will be referred to as "internal separation" and that of Figure 3(b) as "external separation."

#### B. Scope of the Present Study

The present study has been devoted principally to the Foa energy separator, which will hereafter be abbreviated FES. This device appears to have great potential, and has not as yet been subjected to extensive study: indeed, the entire body of published technical literature on the subject is encompassed by the original paper<sup>7</sup> and patent<sup>10</sup> by Foa and a report by Hashem.<sup>11</sup> Accordingly, a theoretical investigation has been carried out to develop a more comprehensive understanding of the performance characteristics and potentials of the FES than has heretofore been available. The analyses performed fall into two distinct categories, which will be referred to as "core performance equations" and "collection



effects." The former embody all the most essential ingredients of the cryptosteady energy separation mechanism, and can in most cases be applied directly. In some cases, however, the manner in which the output flows are collected can alter the performance in ways which are not apparent from the core performance equations, and such effects require separate analyses.

Core performance equations are developed separately for the cases of internal and external separation, Figure 3. However, as different as these two may appear at first glance, it is important to note that they are in fact equivalent. For example, under the restrictions applied to the earlier discussion, an internal-separation FES like that of Figure 3(a) with perfectly tangential nozzles (if this could be built!) would give performance identical to that of a particular external-separation device; the nozzle inclination of the equivalent external-separation model would be that for which the splashing pattern, Figure 3(a), would give a massflow ratio equal to that produced by unequal nozzle areas in the internal-separation design. But from a practical standpoint, it is desirable to have separate performance equations for the two families of configurations, since such equivalency relationships would be very unwieldy in the general case, which could for example involve unequal nozzle inclinations, nozzle efficiencies, and discharge pressures for an internal-separation device.

Output flow collection effects can be expected to have relevance for both families of FES configurations, but they are of more intrinsic concern for external separation than for internal separation. This is because, in external separation, the collection process cannot be

decoupled from the output-flow generation process, since both originate within the impingement-deflection region depicted in Figure 3(b). This contrasts with internal separation, Figure 3(a), wherein separation of the flow into two distinct outputs is completed within the confines of the rotor, after which these output flows enter their respective collection spaces. With these considerations in mind, then, several external-separation collection effects were identified which appeared to be particularly salient, and these have been analyzed.

The treatment of the FES is supplemented herein with some attention to its predecessors in the field of energy separation, the Ranque-Hilsch tube (hereafter abbreviated RHT) and the dynamic pressure exchanger "divider" (hereafter abbreviated DPE), so as to place the FES in proper context. In the case of the RHT, this includes an analysis to establish theoretical upper bounds on performance, since such do not appear to have been developed previously and are clearly of practical interest. Where the DPE is concerned, however, a performance analysis of similar scope would be too formidable to undertake simply for its contextual interest, since extensive method-of-characteristics analyses would be required. Therefore, the material concerning the DPE is limited to an Appendix which briefly discusses divider energy separation characteristics based on published data, this data first being transformed from the format used in the DPE literature to that used in describing RHT and FES performance. For more detailed information, the reader is referred to Azoury<sup>4</sup> and to Kentfield.<sup>12, 13</sup>

## PART II

### THE RANQUE-HILSCH TUBE

#### A. Historical Review

##### 1. General

The field of energy separation was born when a French metallurgist, Georges Joseph Ranque, invented what is known today as the Ranque-Hilsch tube (RHT). As reviewed in an interesting account by Fulton,<sup>14</sup> Ranque was unsuccessful in developing the device himself, although he obtained patents in France and the United States<sup>15</sup> and apparently formed a small company. When he described his invention to the Société Française de Physique in 1933,<sup>2</sup> he was rebuffed as--in essence--not knowing what he was talking about. And the company itself probably went out of existence when the inefficiency of the vortex tube relative to conventional refrigerating machines was realized.

Ranque's tube thus faded into oblivion until it attracted the attention of Rudolph Hilsch, a German physicist, a decade later. He carried out an extensive experimental study and published the results in a paper whose English translation<sup>3</sup> immediately aroused great interest. The ensuing research activity was so intense that by 1954 a survey of research on the RHT published by Westley<sup>16</sup> listed over one hundred references on the subject. The pace of activity has slowed since then, but the RHT remains a subject of active research. A great deal has been learned about the energy separation mechanism involved in the RHT, but this seemingly simple device has stubbornly defied attempts to arrive at anything approaching a "complete" understanding of its behavior and prediction of its performance.

## 2. Review of Salient Literature

The focus of the present study was the Foa energy separator (FES), but it was felt that the results of this study could be best judged as to their significance if presented in context with other energy separation techniques. The RHT especially, as the pioneer in the field and by far the most thoroughly researched and widely known energy separation device, demanded such a hearing.

Accordingly, the RHT literature was searched for an adequate basis for a fair and definitive comparison. Since the FES study was theoretical, theoretical RHT performance predictions were desired for this purpose, rather than experimental data which could in principle lie well below theoretical RHT potential. Rather surprisingly, no RHT analysis was found which was deemed definitive enough for the present purpose, and a new analysis was therefore carried out. However, much was naturally learned which was useful either in constructing the analysis or, especially, in weighing its results. The literature discussion which follows highlights important aspects of some of the more important RHT literature, while presenting that literature chronologically to give the reader a "feel" for the manner in which RHT research has progressed.

One broad observation will be made at the outset, with the aid of Figure 1. Ranque's patent describes both the uniflow and counterflow configurations, but Hilsch investigated only the latter in the study reported in his celebrated paper of 1947. It is interesting to note that Ranque, according to his patent, believed the uniflow configuration to be the better one from a performance standpoint, but it is the counterflow device that has occupied center stage ever since the paper by Hilsch.

Even when the "uniflow configuration" is examined analytically or experimentally, one often finds on close examination that this really means "counterflow configuration with zero cold flow"--not at all what Ranque had in mind. It has never, to the writer's knowledge, been shown that counterflow performance is inherently superior to--or even as good as--uniflow performance, so this narrowing of attention is difficult to justify rationally, except perhaps on grounds of convenience of flow extraction. Fulton<sup>14</sup> pointed out this preoccupation as early as 1950, but apparently to little avail: to date, Lay<sup>17</sup> and Hashem<sup>11</sup> are rather lonely exceptions to what the writer would term the "counterflow syndrome."

Turning to the chronological scan of the literature, we begin of course with Hilsch.<sup>3</sup> As already mentioned, he studied only the counterflow tube, carrying out a very thorough experimental program to explore performance characteristics and ascertain the effect of geometric variables. As sketched in Figure 1, the cold flow in Hilsch's models exited through an orifice and was led away by an extension of the basic tube. He found, through preliminary testing, that the best performance was obtained when the diaphragm was located as close to the inlet plane as possible; however, he gives no hint that he ever considered any cold-port configuration other than an orifice, nor (as perhaps later investigators may have inferred) that he ever tried the uniflow configuration.

Hilsch did all of his testing on models of very small scale, due to compressor limitations. His most complete set of reported data was obtained with his smallest tube (Tube 1), having a diameter of 4.6 mm, with which he tested a range of orifice sizes (diameters of 1.4, 1.8, 2.2, and 2.6 mm). Figure 4 is a replot of the data obtained with the 2.2 mm

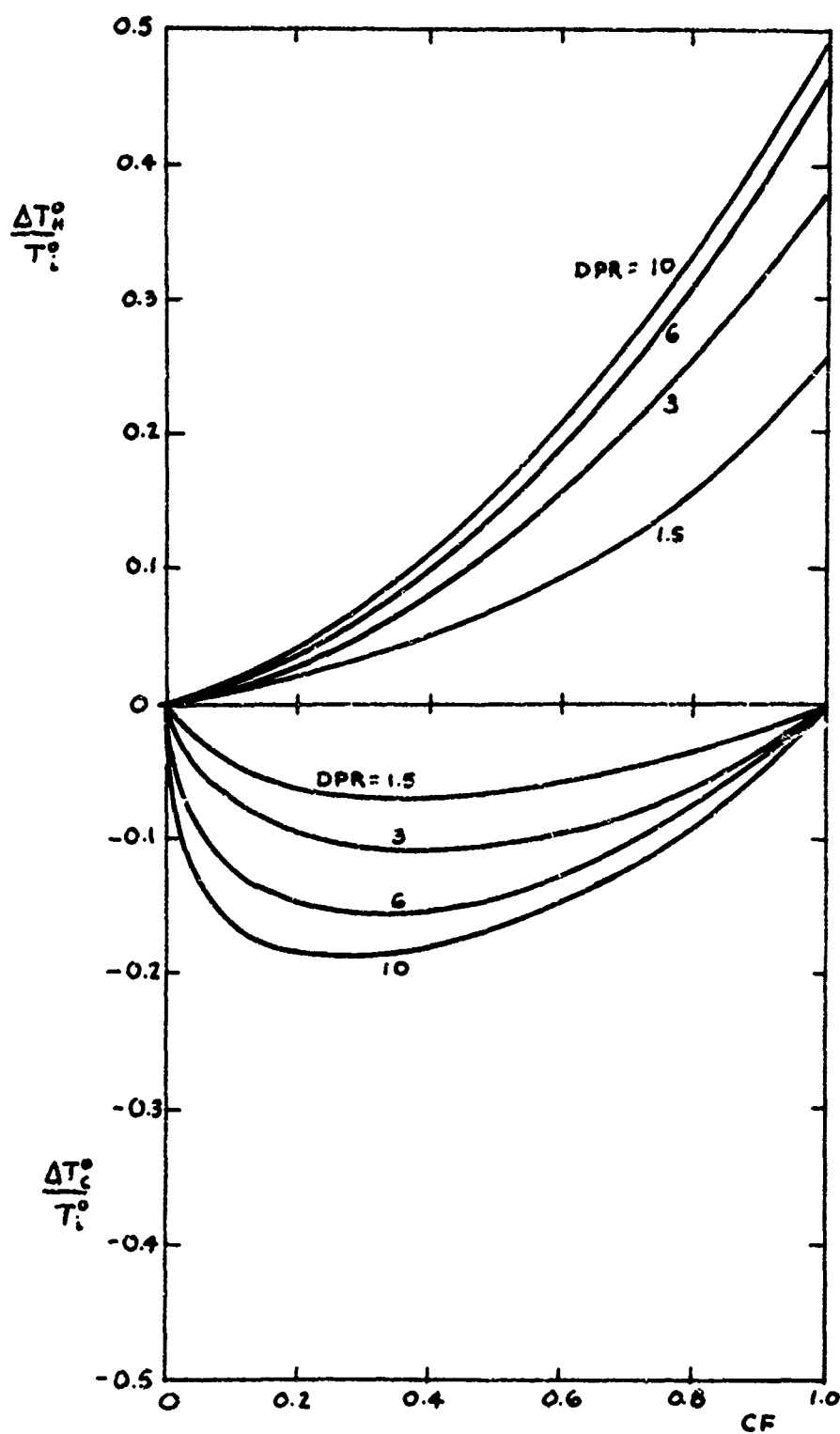
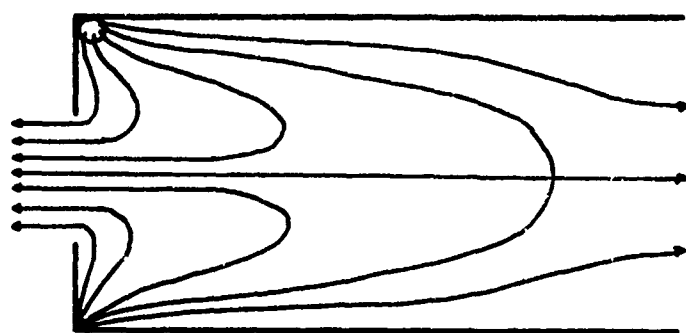


Figure 4  
Experimental Data of Hilsch<sup>3</sup>

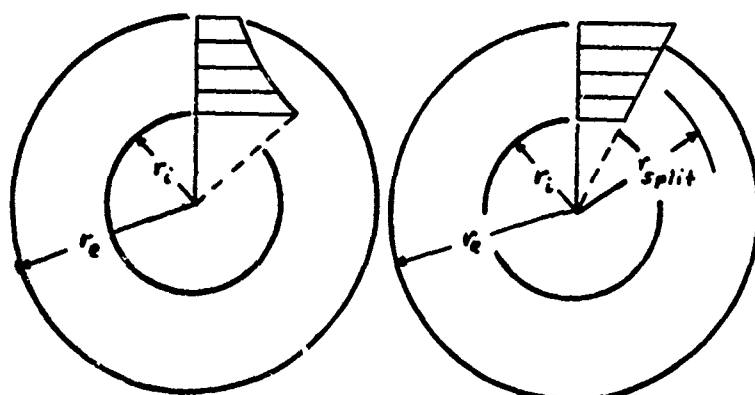
orifice; the others are qualitatively similar, but the position of the minimum in the cold-output curve tends to shift to the left with decreasing orifice size. It should be noted that the Hilsch data were presented in dimensional form, with the inlet total temperature  $T_i^0 = 68^\circ\text{F} = 528^\circ\text{R}$ , but the presentation of Figure 4 has been made dimensionless. Hilsch augmented his basic performance data from Tube 1 with somewhat more limited testing of two larger tubes (diameters of 9.6 and 17.7 mm, respectively) in order to assess the importance of scale. He discovered that an increase in scale was favorable to performance; he presents a plot of maximum temperature drop as a function of pressure ratio for all three tubes from which one may find that the gain in performance with the largest tube is in the neighborhood of 10 to 15% at all pressure ratios represented in Figure 4.

In 1948 Kassner and Knoernschild<sup>18</sup> published the first full-fledged analysis of RHT performance, in which they contributed a great deal to the understanding of the vortex tube. Their analytical model, which was tailored specifically to the counterflow configuration, was based upon the conversion of an initially free vortex into a forced vortex through viscous shear, resulting in a radial redistribution of energy. The manner in which they envision the internal flow in the vortex tube is indicated in Figure 5(a), while Figure 5(b) illustrates the region considered in their vortex conversion model.

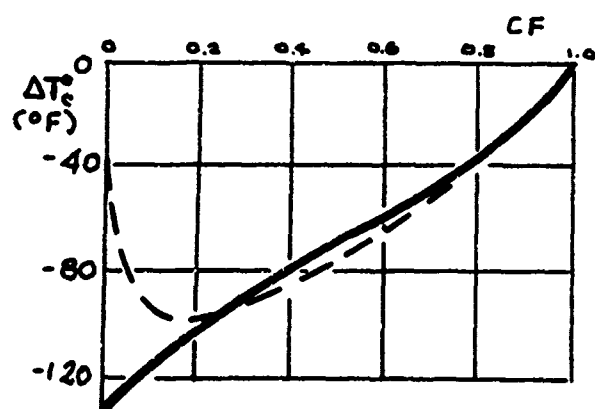
In the neighborhood of the inlet plane, an annular portion of a free vortex is assumed to form, within which there is a core which presumably corresponds essentially to the counterflow region. Wall friction is ignored, so that angular momentum is conserved as the vortex changes



(a) Presumed Internal Flow Pattern



(b) Vortex Conversion Model



(c) Comparison of Theory with Hilsch Data

Figure 5  
Theoretical Model and Results of Kassner and Kncernschild<sup>18</sup>



over to a forced vortex having the same annular extent as the initial vortex. It is pointed out that the forced vortex can be expected to be quite turbulent, with the result that the properties in the vortex should obey the "adiabatic law," just as in a turbulent atmosphere. It is shown that, for the incompressible case they consider, the kinetic energy of the forced vortex is less than that of the free vortex, the difference necessarily appearing as frictional heat; this calculation is one element in arriving at the total temperature distribution of the forced vortex, but it also exposes the dissipative nature of the RHT energy separation mechanism.

Referring to Figure 5(a), Kassner and Knoernschild in effect visualize the forced vortex as being peeled off layer by layer from within, each successive layer ultimately leaving through the cold orifice. They then reason that the remainder of the vortex expands inward to take the extracted layer's place; this would involve some tendency to shift back toward the free-vortex velocity profile, which would initiate some further shearing action and outward energy flux. To take this postulated effect into account, they make the simplifying assumption that the inner layers of the vortex add more to the cold air temperature than the outer layers. Thus, while the cold flow is calculated as the mass of the forced vortex contained between  $r_i$  and  $r_{split}$ , Figure 5(b), the cold-flow temperature is not calculated as the mass-average but rather by simply averaging temperature along the radius from  $r_i$  to  $r_{split}$ .

Kassner and Knoernschild compare theory with experiment for one of Hilsch's curves, as shown in Figure 5(c). It is seen that the agreement is remarkably good, which suggests that their analytical approach

has some validity. However, it should be noted that the theoretical curve was arrived at after carrying out a numerical search for the value of the core radius,  $r_i$ , giving a maximum possible temperature drop at zero cold flow; it is never made clear exactly what the significance of the core in their model is, nor why this optimization process should necessarily have physical meaning. Thus, the excellence of agreement between their theory and the single Hilsch curve against which it was compared must be regarded as possibly somewhat fortuitous.

Kassner and Knoernschild unfortunately do not present a set of more generally applicable performance curves, and their analytical procedures are rather awkward. More importantly, their analysis as structured cannot be applied directly to the uniflow RHT: this would require that the forced vortex extend all the way to the center, which according to their core-radius optimization scheme would result in the disappearance of any energy separation. This embarrassing result also casts real doubt on the physical meaning of the optimization scheme.

Fulton published a paper<sup>14</sup> in 1950 which is well known chiefly for its evaluation of RHT efficiency. The "basic" criterion he uses for evaluation of efficiency is that of "a reversible producer of cold gas, such as a reversible isothermal compressor followed by a reversible adiabatic expander." According to this criterion, he finds from the data of Hilsch that the RHT reaches an efficiency of only about 1%; noting the favorable effect of increasing scale found by Hilsch, he suggests that "larger tubes under ideal conditions" might reach 2%.

Fulton's point in using this efficiency, which pertains to the entire system rather than the RHT portion of it, was to point out a fact

that was not widely realized at that time--i.e., that the RHT demanded very large power expenditures. However, there is also something to be said for considering the efficiency of the RHT (or any other energy separation device) by itself, without burdening it with assumptions about the manner in which the input flow is obtained. Fulton does this with what he terms a "turbine criterion," which amounts to the product of cold-side turbine efficiency (temperature drop divided by the isentropic temperature drop corresponding to the given pressure ratio) and cold fraction (fraction of the total flow which exits as cold air). By this criterion, Fulton finds that the efficiency of the RHT is rather insensitive to pressure ratio, being about 13% and 15% at pressure ratios of 2.5 and 11, respectively. The cold fractions at which these maximum efficiencies occur are about 0.7 and 0.6, respectively.

Fulton also reported an experimental observation which provided the first hint that the RHT really produces its maximum temperature drop at or near zero cold fraction: this is as predicted by the theory of Kassner and Knoernschild and every major theory since, and in contradiction of the experimental results of Hilsch (Figure 4). Fulton brought a small tube up to the mouth of the orifice, splitting the cold flow up into an inner and an outer portion. With a nozzle-inlet total pressure of 105 psia, inlet total temperature of 70°F, and a cold fraction of 0.33, he discovered that the outer 25% of the cold flow had a mean temperature of +30°F while the remaining core averaged -50°F. Subscribing to a belief that the internal flow pattern was similar to that postulated by Kassner and Knoernschild, Figure 5(a), he explained this on the basis that the

streamlines near the orifice were primarily radial, with the result that they had little opportunity to reject energy before emerging.

Less than a year later, Scheper<sup>19</sup> published the first experimental data on the internal flow in the counterflow tube, and in so doing decisively contradicted the neat flow pattern description of Figure 5(a), as Fulton himself pointed out.<sup>20</sup> Scheper found radial outflow to be occurring in the outer regions of the core in a way suggesting a flow pattern qualitatively like that in Figure 6 (inferred by the present writer from Scheper's flow visualization sketches). There is apparently an annular recirculation region of appreciable axial extent which separates the outer annulus and the inner core which is flowing toward the cold orifice.

Based on this flow pattern, Scheper drew an analogy between the vortex tube and a counterflow heat exchanger. He noted that the static temperatures in the core were slightly higher than those in the inner part of the annular vortex surrounding the core, and on this basis constructed a theory of RHT operation that was solely predicated on heat transfer. This theory led to reasonable correlations with the Hilsch data, but this was achieved by employing an empirical correlation factor  $N$ , which he termed the "cooling effectiveness," which was itself chosen on the basis of the data being fitted; Scheper then examined the values of  $N$  needed for this purpose to determine whether they "could be reasonably attributed solely to a heat transfer process." He found that this could not be done on the basis of conventional heat transfer calculations, but nevertheless considered the results to be within a close enough range to be encouraging. However, it must be noted that Scheper's analysis

Recirculating Boundary Region

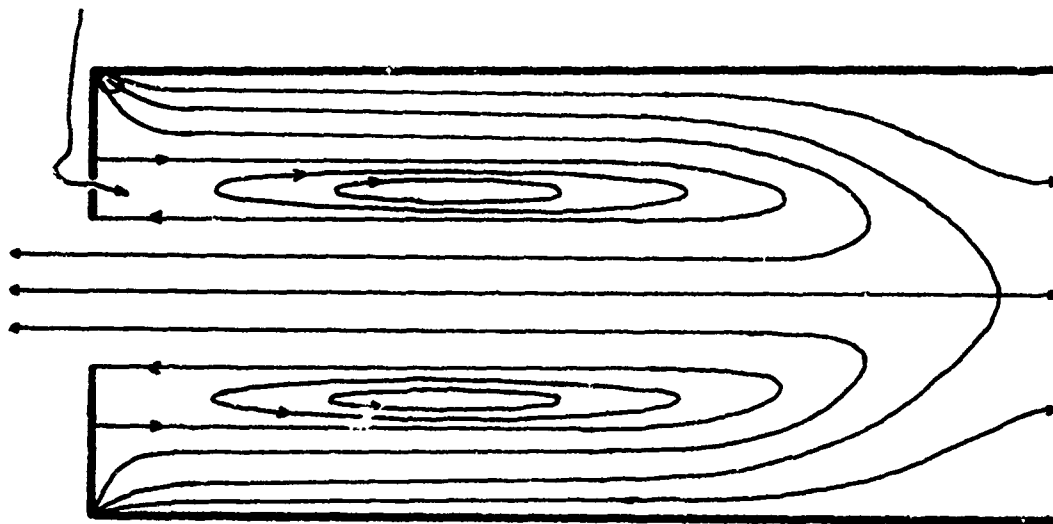


Figure 6  
Counterflow Pattern Inferred from Scheper<sup>19</sup>

neglected radial mixing, for simplification and also because it was felt to be of minor importance, despite his own observation that smoke tests proved useless even at very low pressure ratios because of turbulence. He also believed heat transfer to be the explanation for the energy separation achieved by the RHT "since no mechanical work is involved"--a statement which is not correct in light of the very definite shear work going on between layers. Thus, Scheper's heat transfer theory itself, while interesting, is not convincing. His experimental work, however, constituted a valuable contribution to the RHT literature.

RHT research continued, and as mentioned earlier, Westley published a survey<sup>16</sup> in 1954 which reviewed what was by then a very large body of literature. The next paper that will be discussed here, however, is that of Lay,<sup>17</sup> who in 1959 published a two-part paper reporting an experimental and analytical study of the RHT.

In Part I of his study, Lay presents traverse data and flow visualization obtained with lucite vortex tubes two inches in diameter. This scale was larger than had been used in most previous experimental studies, and enabled Lay to obtain relatively detailed traverse data at a number of axial stations. He did not, unfortunately, employ any wall static-pressure taps or temperature probes, but relied solely on data obtained with a traversing probe. As this probe caused significant flow perturbations near the wall, it is therefore difficult to extrapolate his data to obtain accurate estimates for conditions adjacent to the wall, which would be of interest.

Lay is to be commended for his attention to the uniflow tube as well as the counterflow device, since such attention was not and still

is not common. Unfortunately, he did not present overall performance data for comparison with his internal flow data, so that no assessment of the relative performance merits of the two configurations was made. His traverse data, which apparently was taken entirely on the uniflow device, appears to show primarily the decay of the vortex pattern toward a uniform state as it moves away from the injection plane; apparently, most of the vortex conversion process occurred between the inlet plane and first traverse station. This was perhaps what Lay intended to obtain, following Hilsch's admonition to use a long tube to allow swirl to dissipate; however, Hilsch's comment was made specifically in the counterflow context, so it may be that even Lay was thinking basically in counterflow terms.

Some of Lay's most interesting experimental results have to do with his flow visualization, particularly in the inlet plane. Using water to visualize the flow adjacent to the inlet-plane end wall, he discovered a "limit circle" for both the uniflow and counterflow configurations. This circle, which marks the boundary between the entering, inward-spiraling flow and the core region, has a diameter considerably larger than that of the cold orifice in the counterflow configuration, but is small enough that the flow must spiral inward a considerable distance to reach it; this inward spiral pattern is also visualized in a separate photograph. This limit circle phenomenon tends to corroborate the pattern seen in Figure 6, based on the observations of Scheper; furthermore, its occurrence for both the uniflow and counterflow tubes should be noted well, as it will be referred to as an important link between the uniflow

and counterflow configurations in the analysis presented below by the present writer.

In Part II of his paper, Lay pursued an analysis of the RHT. The bulk of the analysis is compressible, and employs superposition of simple flows in an attempt to describe analytically the internal flow in the RHT. However, insofar as performance prediction is concerned, he drops back to an incompressible analysis. He shows that the forced vortex existing after the action of viscosity has less kinetic energy than the free vortex existing just after entry, paralleling Kassner and Knoernschild; he also shows that, if the vortex spans the entire tube radius, the tangential velocity at the wall in the forced vortex is twice that in the free vortex, again reproducing a result of Kassner and Knoernschild. However, he also points out a scheme by which the "optimum" size for the cold orifice may be obtained: basically, this corresponds to splitting the final vortex at the radius for which the total temperature equals the inlet total temperature. However, he misinterprets its significance as giving the maximum temperature separation; in fact, it corresponds to maximum refrigeration capacity for the nominal case wherein any drop in temperature below the inlet total temperature can be considered as useful. This "nominal split" will also be examined in the present writer's analysis.

In 1960 an analytical work was published by Deissler and Perlmutter<sup>21</sup> which has relevance to the present work. Like some previous analysts,<sup>22,23,24</sup> these authors treat a vortex which is two-dimensional in that it is considered to be the same at all axial positions. Their analysis is turbulent and allows for the presence of both axial and radial



velocity components; indeed, the effect of the radial velocity, as expressed by a turbulent Reynolds number  $Re_0$ , proves to be a governing factor in the energy separation process. However, they attempt to apply this model directly to prediction of RHT performance; thus, the rate of energy separation occurring in a given plane is in effect confused with the integral of that rate--i.e., the overall energy separation occurring between an initial and final plane. In attempting to fit the data of Hilsch, they succeed only by adjusting  $Re_0$  so as to obtain a curve of energy separation performance versus cold fraction that is qualitatively correct; upon doing this, they obtain a very good fit. (Actually, the published fit is better than the real fit, since a scale-factor error can be shown to exist in the Hilsch data as transformed by Deissler and Perlmutter.) The theory is not fully predictive, since there is no good way in their theory to judge the proper value for  $Re_0$  a priori, and they are forced to assume a value for the tangential Mach number at the tip of the vortex.

The most significant thing about the Deissler and Perlmutter paper for the present work is that  $Re_0 = 2$ , which yielded good agreement between theory and the data of Hilsch, also yields a vortex velocity profile which is very close to solid-body rotation. A basic assumption in the present writer's uniflow analysis to follow is that a free-to-forced vortex conversion (à la Kassner and Knoernschild) occurs which terminates in a turbulent vortex with essentially solid-body rotation, and the work of Deissler and Perlmutter shows that this is a realistic assumption. It is also worth noting that the temperature and pressure profiles (static

and total) given by Deissler and Perlmutter for  $Re_0 = 2$  are very similar to those obtained herein for the forced vortex at similar conditions.

1962 saw the publication of a paper by Sibulkin<sup>25</sup> wherein it was asserted that the axial variation of vortex conditions, which is neglected in analyses such as that of Deissler and Perlmutter, is an essential ingredient of the RHT energy separation process; note that this is also implied in the vortex conversion concept of Kassner and Knoernschild.<sup>18</sup> Pointing out the difficulty of fully analyzing the complete, three-dimensional steady flow within the tube, Sibulkin treats the problem instead as a nonsteady two-dimensional problem by riding on a slab of fluid as it travels down the tube from the inlet plane to its destination a very large axial distance downstream. He includes wall friction in his analysis, and the final state of the fluid slab is taken to be free of rotation and uniform in temperature; he notes, in introducing this analytical model, the suggestion by Hilsch that a long tube be used to allow swirl in the hot flow to dissipate fully before extraction. He further notes the absence of this condition as an ingredient in previous analyses, which he considers to have been totally unsuccessful in generating internal pressure and temperature profiles that agree with experiment.

The analysis of Sibulkin is something of a hybrid between uniflow and counterflow, the latter being the actual focus of the analysis. First, the development of the vortex slab as it travels downstream is analyzed for the case of zero cold flow, which as far as internal flow is concerned is the same thing as uniflow; these profiles are then compared with experimental uniflow profiles obtained by Lay.<sup>17</sup> Qualitative agreement is obtained, theory and experiment both revealing the expected

decay of the basic vortex motion as axial distances from the inlet plane become large. Then, to see whether these profiles still have relevance with nonzero cold fraction in the counterflow configuration, Sibulkin refers to data contained in the thesis which formed the basis for the earlier referenced paper by Scheper.\* Finding that the profiles remain qualitatively similar to those at zero cold flow, Sibulkin proceeds with his analysis.

His next step is to take note of the internal flow pattern indicated by Scheper's experiments (Figure 6), and to observe in conjunction with this that the analysis indicates the presence of a positive pressure gradient at the axis with increasing axial distance. He then assumes that all of the cold flow actually originates in the constant-temperature, constant-pressure region far from the inlet plane, and that every element of this cold flow makes its way down the center of the core to the cold orifice. Its temperature decreases en route as a function of both heat conduction and pressure decrease; viscous shear plays no role here, since all elements of the cold flow are assumed to travel down the exact center of the core.

Sibulkin thus arrives at energy separation performance curves which are normalized by  $V^2/2c_p$ ,  $V$  being the maximum velocity in the entry vortex. These are qualitatively similar to the curves obtained in other

-----

\*As of 1962, when Sibulkin did his work, Scheper was still the only investigator to have published experimental internal flow data for the counterflow device with nonzero cold flow. More data of this sort is now available, however, reported by Vennos<sup>26</sup> in 1968. Vennos carried out an elaborate experimental program which included measurement of all three components of velocity as a function of position in the tube.

theoretical treatments, predicting maximum temperature drop at zero cold flow but otherwise appearing much like the experimental data of Hilsch (Figure 4). However, he predicts a very strong, favorable dependence of performance on inlet nozzle height, which is not duplicated in other analyses, and he substantiates this with experimental data.

This inlet-height effect, in the opinion of the present writer, is a misconception which creeps in because Sibulkin's treatment--both analytical and experimental--is confined to extremely low pressure ratios. The analysis assumes that the Mach number is small compared to unity throughout the flow field, and experimental data is taken at the low pressure ratio of 1.2 to satisfy this condition. As a result, a basic assumption in Sibulkin's model--that the radial extent of the annular entry vortex is equal to the nozzle height--proves to be satisfied in his experiments, as flow visualization shows. But this is not a general result: Lay<sup>17</sup> showed both analytically and experimentally that the inlet flow spirals inward very substantially from the inlet nozzle at higher pressure ratios. Furthermore, to the extent that the model developed herein by the present writer approximates physical reality, a large quiescent core like that which Sibulkin's model would give with small nozzle height is forbidden thermodynamically at elevated pressure ratios.

As to the remainder of Sibulkin's theoretical results, one is tempted to seize upon his qualitatively correct RHT performance characteristics as an indication that his theory is basically valid, but this conclusion is quite unwarranted. As Sibulkin himself points out in criticizing the work of his predecessors, and as will be commented upon further in concluding the present review, widely divergent theories have all

accomplished this much. And the Sibulkin theory is not useful quantitatively, since even at the low pressure ratio of 1.5 it predicts performance which is only a small fraction of that obtained experimentally by Hilsch. Thus, the significance of Sibulkin's theory, which differs radically from others, must be probed more carefully.

In this regard, while his unique approach to the analysis of RHT internal flow structure evidently contains some validity, it is the conclusion of the present writer that the performance analysis based thereon does not. The reason is simply that Sibulkin has confused static with stagnation quantities, as Ranque was wrongly accused of doing long ago. This results from applying an energy equation to the particle travelling down the tube axis to the cold orifice that neglects "changes in the kinetic energy of axial motion," in context with the assumption that the pressure difference between the orifice and hot end is proportional to the dynamic pressure of the exiting cold stream. The error of this approach is most readily appreciated at  $CF = 0$ , where the temperature change is brought about solely by pressure change, the heat conduction contribution going to zero there. Physically, this says the particle travels from a region at negligible velocity and high pressure (the hot end) to a region of low static pressure where it possesses appreciable velocity (the cold orifice), without friction, heat transfer, or doing work. This is equivalent to a nozzle flow, which has no effect on total temperature, yet gives maximum temperature drop according to Sibulkin.

Before leaving Sibulkin, however, a significant experimental finding he reported should be noted. Whereas most investigators measure cold-flow temperature just outside the cold orifice, Sibulkin uses a

station just inside the orifice. Thus measured, the lowest temperature is produced by the RHT as the cold fraction drops to zero, just as predicted by his theory as well as those of other analysts. In this context, it is interesting to note the work of Blatt and Trusch,<sup>27</sup> which was also published in 1962. They describe an experimental study of a device which amounts to a zero-cold-flow RHT, which is used to provide a low-temperature environment for a small object which is placed inside the tube, affixed to the center of the inlet-plane end plate--i.e., where the orifice of a counterflow RHT would normally be. Provided the heat load associated with the cooled device is extremely small, this "vortex cooler" can maintain the device at a temperature lower than that associated, in terms of an isentropic temperature drop, with the pressure ratio across the cooler.

In 1965, Hashem<sup>11</sup> carried out an analysis which, so far as the writer has been able to determine, is the only RHT performance analysis in the literature which pertains specifically to the uniflow configuration. His analysis is a conceptual descendent of that of Kassner and Knoernschild,<sup>18</sup> in that he treats the conversion of a free vortex into a forced vortex while conserving total angular momentum and total enthalpy in each slab of fluid as it travels down the tube. However, he abandons the assumption of incompressibility used by Kassner and Knoernschild, and also structures the analysis in a less cumbersome manner. The treatment of the uniflow RHT by the present writer is a close relative of Hashem's analysis; however, Hashem introduced certain artifices and assumptions which are relaxed in the present analysis. Further comments concerning

these will be introduced in context with the new analysis, where they will be more readily appreciated.

Finally, two 1971 references will be cited to round out the picture of the status of RHT performance prediction. The first is a theoretical paper by Linderstrom-Lang,<sup>28</sup> the second a review of vortex literature by Lewellen.<sup>29</sup> These seem to confirm that the counterflow syndrome is still alive and well, and also that the literature still does not contain truly definitive theoretical predictions of RHT performance.

Linderstrom-Lang carries out a very involved, incompressible analysis of the counterflow RHT which is predicated on the supposed equivalence of this device to "counter-current systems with transverse diffusion such as distillation columns and heat exchangers." This analysis is thus on the same family tree as that of Scheper,<sup>19</sup> though Linderstrom-Lang considers the flow to be turbulent and follows an entirely different theoretical approach. He first analyzes the internal flow to arrive at a description of the tangential velocity distributions; he then goes through a separate analysis in order to go from the velocity distributions to distributions of total temperature. As for overall performance, the theory is not capable of quantitative prediction without introduction of some parameters obtained from experiment, and resembles the Scheper theory in this respect. However, it is interesting to note that Linderstrom-Lang succeeds in simulating qualitatively, in a rough way, the decreasing temperature drop as cold fraction approaches zero, specifically by permitting backflow to occur into the orifice at very low cold fractions.

The review by Lewellen concerns the whole field of confined vortex flows, of which the RHT is but one example. His attention to the RHT is therefore relatively brief, but seems rather pointedly in agreement with the present writer's estimate of the status of RHT performance prediction: after observing that previous efforts "although each contributing to the understanding of the tube, have not met with complete success," he carries out a very brief analysis himself in an effort to estimate a bound on the possible energy separation obtainable from an RHT. The bound Lewellen seeks would tell one nothing about the dependence of RHT performance upon the controlling variables of principal interest--cold fraction and pressure ratio--but would nevertheless be of great significance, establishing an absolute maximum in total temperature drop (normalized by inlet total temperature) which could not be exceeded regardless of pressure ratio.

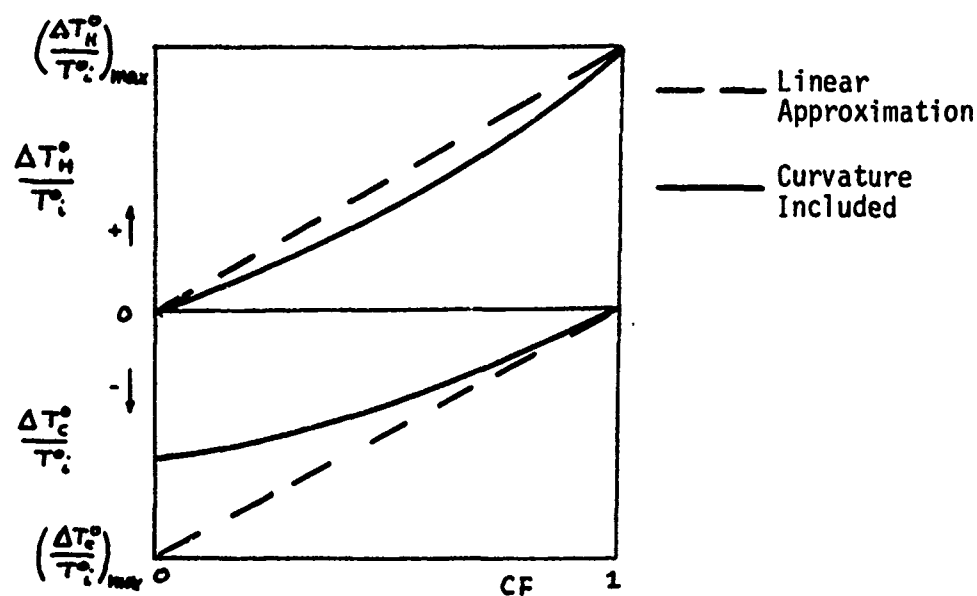
The analysis Lewellen presents is not too convincing to the present writer, principally because he bases it upon a laminar vortex analysis presented elsewhere in the review paper and makes the assumption "that turbulent transport can be related to laminar simply by using a turbulent Prandtl number." And, to be sure, Lewellen himself mentions that such an assumption has yet to be justified. However, proceeding on such a basis, he calculates a normalized temperature-drop bound of 0.185; comparing this with experiment, he finds that this bound is violated somewhat, but not by so much as to indicate that the basic concept of an absolute performance bound is necessarily incorrect. Lewellen has raised a very interesting and potentially significant question which seems not to have arisen anywhere in the RHT literature previously.



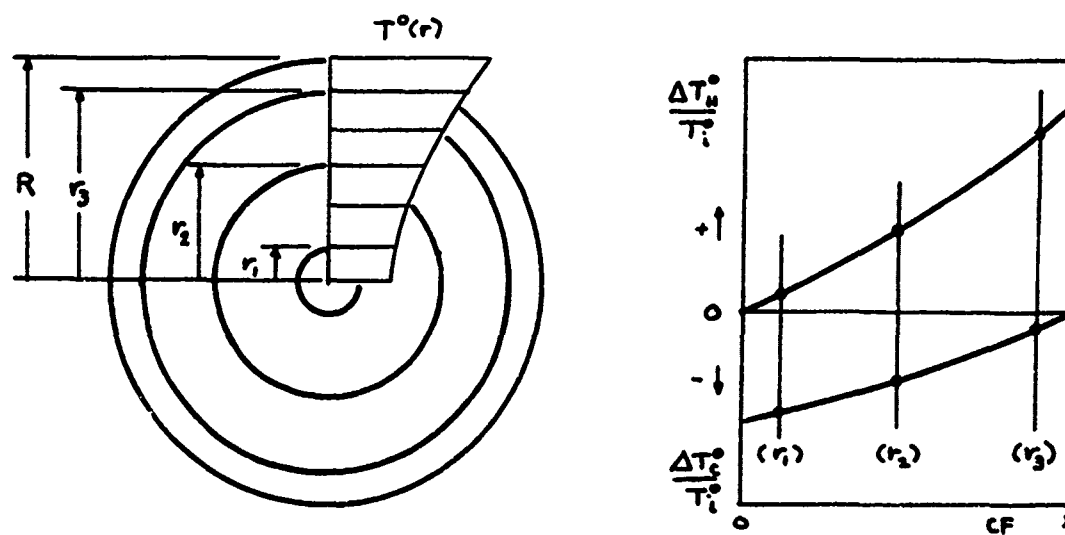
### 3. A Comment on Qualitative Agreement of Performance Theory and Experiment

The RHT is a perverse little device, in that it obligingly permits the analyst to obtain correct qualitative predictions of its behavior with just about any plausible-looking theory. As witness to this, consider the theories of Kassner and Knoernschild,<sup>18</sup> Scheper,<sup>19</sup> Deissler and Perlmutter,<sup>21</sup> and Sibulkin.<sup>25</sup> these are very different from one another in their basic concepts--not merely in analytical detail--and yet one can hardly tell their qualitative predictions apart. Thus, while qualitatively incorrect predictions serve to invalidate a theory, qualitatively correct predictions do not conversely validate it. The hapless theoretician, forced to dig deeper, is at least entitled to ask: "Why should this be so?"

First, some observations are possible which are completely divorced from any understanding of the processes within the RHT, which will be made with the aid of Figure 7(a). Consider the hot output, which contains whatever energy has been lost by the cold flow. As the cold fraction CF (ratio of cold output to total input massflow) goes to zero, the amount of energy extracted from the cold flow goes to zero, regardless of the magnitude of the temperature drop; therefore, the dimensionless temperature increase  $\frac{\Delta T_N^o}{T_i^o} = \frac{T_N^o - T_i^o}{T_i^o}$  of the hot flow must be zero at CF = 0. As CF increases, however, more and more energy is being extracted from the cold flow and deposited in a decreasing amount of hot flow; therefore,  $\frac{\Delta T_N^o}{T_i^o}$  rises with CF. Glancing at Hilsch's data (Figure 4), one notes that the hot-output temperature curves terminate in a finite temperature increment at CF = 1; they are also concave upward,



(a) Performance Characteristics



(b) Physical Explanation

Figure 7  
Qualitative Behavior of the Ranque-Hilsch Tube

but not radically so. As a first approximation, then, suppose one were to assume a linear variation of hot-output temperature increment with CF to see what it implies for the cold output, i.e.:

$$\frac{\Delta T_H^\circ}{T_i^\circ} = CF \cdot \left( \frac{\Delta T_H^\circ}{T_i^\circ} \right)_{\max}$$

The cold-output temperature increment  $\frac{\Delta T_C^\circ}{T_i^\circ} = \frac{T_C^\circ - T_i^\circ}{T_i^\circ}$  is found from the energy balance

$$\frac{\Delta T_C^\circ}{T_i^\circ} = -\mu \frac{\Delta T_H^\circ}{T_i^\circ}$$

where  $\mu$ , the ratio of hot to cold output flow, is related to CF by

$$CF = \frac{1}{1 + \mu}, \quad \mu = \frac{1 - CF}{CF}$$

Substituting the assumed linear variation of hot-output temperature into the energy balance, one has

$$\frac{\Delta T_C^\circ}{T_i^\circ} = -(1 - CF) \left( \frac{\Delta T_H^\circ}{T_i^\circ} \right)_{\max}$$

which gives a cold-output curve parallel to the hot-output curve, as shown in broken lines in Figure 7(a). Thus, we see already that there should be a nonzero temperature drop at CF = 0 and that the temperature drop goes to zero at CF = 1.

If note is taken of the curvature of the experimental hot temperature curves, Figure 4, the picture is modified to that shown in solid lines in Figure 7(a). Temperature drop is still a maximum at CF = 0 for hot-output curve shapes like those of Hilsch, but is smaller than would hold for the linear case: indeed, the magnitude of the temperature drop

at  $CF = 0$  is proportional to the slope of the hot curve there, and since this slope is always nonzero, a nonzero cold performance is to be expected.

The solid curves in Figure 7(a) present the entire qualitative essence of theoretical RHT performance. It is almost difficult not to construct a theory which gives hot-output curves of this nature, and once this element of the analysis is present, the rest inevitably follows.

Figure 7(b) presents a physical explanation as to why RHT behavior should indeed be as indicated in the solid curves of Figure 7(a). On the left is pictured a forced vortex, as generated within the tube. To obtain a hot and a cold output flow, this vortex is split at some radius " $r$ " into inner and outer portions. A total temperature distribution something like that sketched exists, where the minimum occurs at the center and the maximum at the outer edge. When the two flows are extracted separately and their respective temperatures each measured, say, in a settling chamber, it is of course found that the temperature of the inner flow is a mass-average value between  $T^0(r=0)$  and  $T^0(r)$ , while that of the outer flow lies between  $T^0(r)$  and  $T^0(r=R)$ . Thus, the cold flow comes from the central region, the hot flow from the surrounding annulus.

If the flow is split at a small radius  $r_1$ , the inner flow is very cold but very little cold flow is extracted--i.e.,  $CF$  is small. The average total temperature of the annulus, however, is little different from the value one would obtain by averaging over the entire tube radius, which is the inlet total temperature  $T_i^0$ . Thus, two points would be plotted corresponding to  $r_1$  as shown at right in Figure 7(b).

If at the opposite extreme the flow is split at a radius  $r_3$  only a little less than the tube radius, clearly the hot flow comes only

from the hottest outer layers of the vortex, but the hot mass flow is small: CF is near unity. As for the inner flow, the average is now taken over almost the entire tube; the total energy contained in the few outer layers is small, and therefore the average total temperature of the inner flow is only slightly below  $T_i^0$ .

Selection of an intermediate split radius  $r_2$  will, of course, give intermediate results as indicated. Furthermore, the split radius may be made as small or as large as desired, within the range  $0 \leq r \leq R$ , without affecting the existence of the vortex. Thus, a performance plot covering the total range  $0 \leq CF \leq 1$  is generated without difficulty, and its behavior like Figure 7(a) follows quite naturally from physical reasoning. Since there is ample evidence in the literature that conversion of the input flow into a vortex of this sort is the key to RHT performance, this explanation--which is much akin to that of Kassner and Knoernschild<sup>18</sup>--would appear not only to be plausible, but well founded objectively.

## B. Theoretical Performance Analysis

### 1. Objectives and Approach

Central purpose of the analysis. The present theoretical treatment of the RHT was motivated by the simple desire for a clearcut theoretical prediction of RHT performance that would enable fair, conclusive comparisons to be made with the theoretical performance characteristics of the FES. A number of analyses are available in the literature, each contributing worthwhile insights, but none appear to be adequate for the present application. A new analysis has therefore been carried out which yields, as its most important product, theoretical "upper bound" RHT energy

separation performance characteristics as a function of the controlling experimental variables, cold fraction and pressure ratio. While this is not a "least" upper bound--i.e., it embodies assumptions which are known to be generous--it does establish the range within which RHT performance must fall at any selected operating condition up to a pressure ratio of about 10. So far as is known, such performance bounds have not been established previously.

Analytical model: uniflow configuration. Previous RHT performance analysts have, with the exception of Hashem,<sup>11</sup> tended to focus attention on the counterflow configuration. This necessarily entails accounting for the counterflow internal flow pattern, Figure 6, in one way or another. However, a complete analytical description of this flow pattern would doubtless be too complex for full incorporation into a performance analysis, even if it were available; therefore, counterflow performance analyses are relatively heavily dependent upon simplifying assumptions and approximations regarding the details of the internal flow.

However, much of the ambiguity of RHT performance analysis evaporates if it is noted that the counterflow and uniflow devices are basically equivalent, since uniflow analysis is much more tractable than counterflow. It seems clear that, in either device, energy separation takes place basically because of conversion of a free vortex into a forced vortex--or, to reduce grounds for controversy even further, because the uniform flow injected at the inlet plane is somehow transformed within the tube into a forced vortex. It is also abundantly clear, both from experiment and from analysis (particularly Deissler and Perlmutter<sup>21</sup>) that this forced vortex is turbulent. And as for the reverse-flow core in the

counterflow device, which at first blush might seem to constitute a salient difference between the two configurations, the observations of Scheper,<sup>19</sup> Lay,<sup>17</sup> and Sibulkin<sup>25</sup> all are relevant. Scheper, whose flow visualization experiments provided the basis for Figure 6, indicates in his sketches that the core is if anything more pronounced at zero than at nonzero cold flow (cold fraction in his strictly counterflow rig being controlled by hot-end valve setting). Even more to the point, Lay discovered experimentally that there is a "limit circle" at the inlet plane which marks the boundary between the inward-spiraling entry flow and a central core, and that this limit circle occurs in qualitatively the same manner for both unflow and counterflow. And Sibulkin, although his performance analysis is specifically oriented toward the counterflow configuration, begins with an internal flow analysis which pertains only to the unflow condition; he notes the presence of a positive axial pressure gradient at the axis which would bring about reverse flow. He makes use of this only for nonzero cold flow calculations, but the fact remains that his analytical prediction of backflow arises specifically in a unflow context. Furthermore, he compares predicted internal profiles with experiment for both unflow and counterflow and finds no qualitative change. Thus, there would seem to be every reason to believe that there is a counterflow core with qualitatively similar properties in both devices, and that the energy separation process is not different in any basic way.

The only real difference between unflow and counterflow then, would appear to be that in unflow the central, cold portion of the forced vortex is allowed to travel down the tube in company with the hot outer portion to a common extraction plane, whereas in counterflow this central

portion of the vortex is required to double back and leave in a direction opposite to that of the main flow. The present writer is of the opinion that, to the extent that this difference induces secondary influences on performance, the advantage probably lies with the uniflow device. Here, the vortex can in principle achieve a minimum of axial shear between layers before extraction; in the counterflow configuration, by contrast, the existence of a strong net counter current will presumably give rise to increased axial shear in the boundary region between the two flows. Axial shear, unlike tangential shear, contributes nothing to energy separation, but it does produce losses. Thus, analysis of the uniflow configuration appears to be in keeping with the desired derivation of "upper bound" RHT performance characteristics.

The analysis below disregards wall friction; this is clearly an optimistic assumption, but perhaps not too gross in terms of the ultimate potential of a properly designed RHT. This is the case because there is evidence to suggest that vortex conversion--the source of RHT energy separation--is actually accomplished within a rather short distance of the inlet plane. It is true that very large length-to-diameter ratios are normally associated with vortex tubes (Hilsch suggests 50 tube diameters from inlet plane to hot valve), but it must be noted carefully that this arises in the context of counterflow tubes, and has to do with swirl attenuation rather than with establishment of the basic forced vortex. One may readily discern, in the experimental traverse data of Lay,<sup>17</sup> the fact that the successive stations record the gradual decay of a vortex pattern established quite near the inlet plane (i.e. within a diameter or so). Additionally, Savino and Ragsdale<sup>30</sup> noted, in an experimental



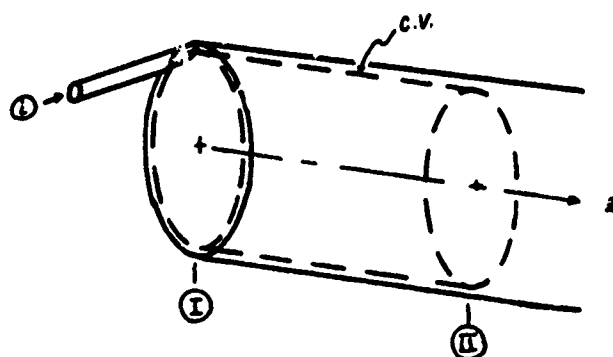
study of a vortex arrangement with small axial length, that flow profiles were produced exhibiting considerable energy separation. Thus, if one were to use a uniflow tube, it would appear that flow extraction would be possible within a relatively short distance of the inlet plane, so that wall friction would not be able to exert a major influence. It must be emphasized that this is contrary to standard RHT practice, but there is no theoretical reason against it.

Outline of the analysis. The analysis carried out below is simple in concept, but becomes rather lengthy in execution. Consequently, the analytical scheme is summarized in broad terms here. It is hoped that this brief glimpse of the forest will prove a useful prelude to the walk through the trees.

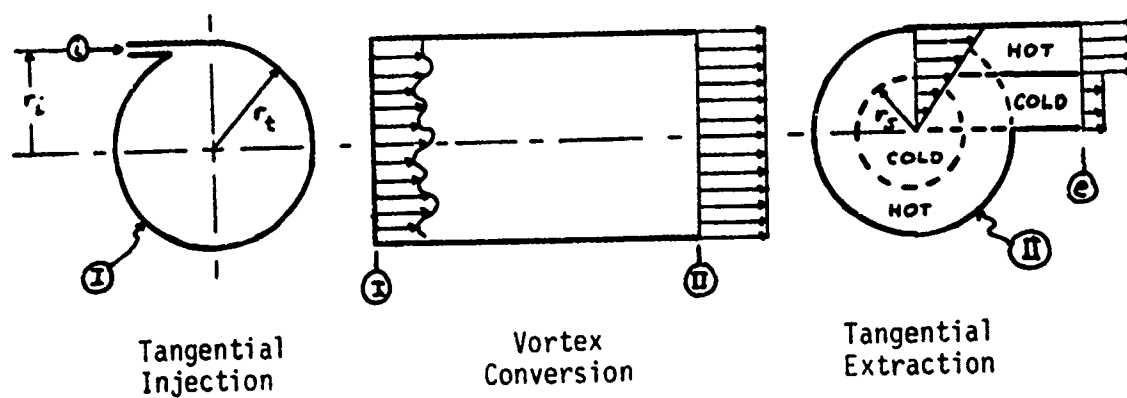
There are essentially three phases to the analysis:

- 1) Considering a control volume which corresponds to the vortex conversion region within the tube (Figure 8), apply the relevant conservation equations to relate conditions in the forced vortex at the "terminal plane" to nozzle inlet conditions.

The conservation equations which are required are those for mass, energy, axial momentum, and angular momentum. An appropriate description is of course needed for the terminal vortex in order to apply these equations, and this is done under the assumption that the vortex is turbulent and in solid-body rotation; as noted earlier, this assumption appears on the basis of the work of Deissler and Perlmutter<sup>21</sup> to be an entirely reasonable approximation. As for the flow in the inlet plane, no assumptions whatever are required for the "upper bound" performance calculation; however, several flow models are explored as one means of judging the possible looseness of the performance bounds.



(a) Vortex Tube Control Volume



(b) Overall Flow History

Figure 8  
Overall Analytical Model for RHT

- 2) Derive output flows from the terminal-plane vortex, as a function of vortex tip Mach number (tangential) and flow split radius, and with consideration of exit losses.

The output flows are taken to be extracted tangentially through constant-area frictionless ducts. This, too, departs from normal RHT practice, and should give results better than standard practice.

- 3) Link nozzle-inlet to output conditions, and exchange roles between the independent analytical variables (injection Mach number, split radius) and normal independent experimental variables (pressure ratio, cold fraction) to present RHT performance in standard form.

As depicted in Figure 8, flow enters the tube through the injection nozzle "i" with no axial component of velocity, but is forced to acquire an axial velocity component within the tube to satisfy continuity requirements. As the flow spirals down the tube, it must eventually succeed in filling the tube, which, if the flow were inviscid, would imply formation of a free vortex to conserve angular momentum. However, viscosity succeeds in eliminating the shear between layers that this would produce, and the flow eventually reaches a condition of solid-body rotation and uniform axial velocity, at which point adjacent layers are no longer shearing past one another. The flow in this final state is assumed to be turbulent, so all velocities are of course mean velocities.

It is recognized that turbulence and perfect solid-body rotation cannot, strictly speaking, coexist: the tendency is for the vortex to shift over to a laminar state as true solid-body rotation is established. However, as found by Deissler and Perlmutter,<sup>21</sup> a vortex can have a tangential velocity profile very close to solid-body rotation while still turbulent, and furthermore this sort of vortex is apparently needed in order to explain RHT performance characteristics.

The final turbulent, forced vortex is then divided at a "terminal plane" into an inner and an outer portion and extracted, respectively, as the "cold" and "hot" flows. As indicated in Figure 8(b), each flow is extracted tangentially through constant-area, frictionless, adiabatic ducts wherein uniformization is accomplished prior to the exit port "e". (Note that one or both of these ducts may discharge to other than ambient conditions: for example, the cold duct might discharge to a subsonic diffuser, and the hot duct to a throttle valve to reduce the pressure to atmospheric.)

The present treatment was inspired by that of Hashem,<sup>11</sup> which in turn is a conceptual descendent of the pioneering work of Kassner and Knoernschild.<sup>18</sup> The latter analyzed counterflow RHT performance by considering the flow to be incompressible and treating the conversion of an initially free, annular vortex into a turbulent forced vortex having the same annular dimensions; inside this annulus lay the reverse-flow core containing fluid moving toward the cold orifice. Hashem applied a similar concept to the uniflow configuration, but treated the flow as compressible; he also calculated output temperatures strictly as mass-average temperatures (as in Figure 7) instead of applying a contrived weighting scheme like that of Kassner and Knoernschild to magnify the importance of the cold inner layers.

The physical description of the postulated forced vortex at plane II as used below is the same as that of Hashem: solid-body rotation, uniform axial velocity, and uniform entropy brought about by turbulence. Certain simplifying assumptions utilized by Hashem, however, will be abandoned here. The most striking one is that he assumes the inlet

flow to form a free vortex which spirals in to the radius at which the static pressure would theoretically drop to zero, and then replaces the vacuum core with a solid core which extends the length of the tube with constant radius. As this does not correspond to normal RHT geometry, it will be dispensed with here. It is worth noting that one could build an RHT with such a central core, but its performance would presumably be degraded because the innermost layers of the vortex would lie at a finite radius and therefore, in solid-body rotation, retain some kinetic energy that would be absent at zero radius.

Hashem also assumes the static pressure at the wall to be the same at stations I and II, basing this on the experimental traverse data of Lay.<sup>17</sup> This would at best be a rough approximation, since Lay obtained no wall static tap data, necessitating extrapolation of his profiles toward the wall, near which his data are clearly affected strongly by probe interference. A more serious objection, though, is the fact that Lay's data is taken too far downstream to give information on the vortex conversion region, showing instead the gradual decay of the forced vortex. Thus, in the present analysis, the axial momentum equation is used instead of any assumptions about wall static pressure variation.

An additional, perhaps subtler facet of Hashem's analysis is that he follows a vortex slab "of unit length" from plane I to plane II. Examination of his treatment reveals that he thereby, though perhaps unintentionally, constrains the total volume (or equivalently, the mean density) of the vortex to be the same at I and II. Since the pressure and temperature distributions are very different at I and II, and since there

is in addition an entropy rise, the tacit assumption of equal mean densities is not a valid one unless by happenstance.

## 2. Entry-Plane Flow Conditions

Flux equations. Conditions in the "terminal vortex" at plane II will be related to nozzle inlet conditions through application of the conservation equations to the control volume of Figure 8(a). For this purpose, the "flux" of each quantity to be conserved--massflow, angular momentum flow, total enthalpy flow, stream force--will be expressed separately for planes I and II in terms of appropriate variables. Then, application of the conservation equations will consist of requiring that the flux of each quantity be the same at both planes.

Consider conditions in plane I, where the flow enters the vortex tube through nozzle "i". As sketched in Figure 8(b), flow enters at the mass-average radius  $r_i \leq r_t$  where  $r_t$  is the tube radius and the equality holds only in the limit of vanishing nozzle height. All fluxes at plane I are determined by nozzle injection conditions except for stream force, which depends upon the entry-plane flow pattern. That is, we have:

$$\dot{m}_I = \dot{m}_i \quad \text{Mass} \quad (1)$$

$$\dot{L}_I = \dot{L}_i \quad \text{Angular Momentum} \quad (2)$$

$$\dot{H}_I = \dot{H}_i \quad \text{Energy} \quad (3)$$

while the stream force at plane I, where there is no axial velocity, is just the integrated pressure force:

$$\begin{aligned}
 \Phi_I &= \int_I p \, d\alpha \\
 &= p_i \alpha_t \int_I \left( \frac{p}{p_i} \right)_t \frac{d\alpha}{\alpha_t} \\
 &= p_i \alpha_t \int_{\tilde{r}=0}^{\tilde{r}=1} \frac{p_z(\tilde{r})}{p_i} 2\tilde{r} \, d\tilde{r} \quad \frac{\text{Axial Stream}}{\text{Force}} \quad (4)
 \end{aligned}$$

where  $p$  denotes pressure,  $\alpha$  flow area, and  $\tilde{r} = \frac{r}{r_t}$  normalized radius.

The analysis will be carried out assuming that the nozzle height is small enough to assume, to an acceptable degree of approximation, that the flow exiting the nozzle is one-dimensional. Then, with the aid of Foa,<sup>31</sup> p. 42, we may write immediately

$$\dot{m}_t = \sqrt{\frac{\gamma}{R}} \frac{p_i^0 D_i}{\sqrt{T_i^0}} \left( \frac{\alpha_i}{\alpha_t} \right) \alpha_t \quad (1')$$

where the notation  $( )^0$  denotes stagnation quantities,  $R$  is in ft-lbf/slug °R if English units are used, and  $D_i$  is in accordance with Foa's definition of  $D$  :

$$D_i \equiv \frac{M_i}{\left( 1 + \frac{\gamma-1}{2} M_i^2 \right)^{\frac{\gamma+1}{2(\gamma-1)}}}$$

Then, since

$$\dot{L}_i = \dot{m}_i u_i r_i$$

and  $u_i$  may be written as

$$u_i = \frac{M_i \sqrt{\gamma R T_i^0}}{\sqrt{1 + \frac{\gamma-1}{2} M_i^2}} = \frac{M_i \sqrt{\gamma R T_i^0}}{\sqrt{f_T(M_i)}}$$

where the notation  $f_T(M) = 1 + \frac{\gamma-1}{2} M^2$  is introduced, there follows

$$\dot{Q}_1 = \frac{\gamma p_i^0 M_i^2}{f_T(M_i)} \left( \frac{\alpha_i}{\alpha_t} \right) r_i \alpha_t \quad (2')$$

in which the similar notation  $f_p(M) = \left(1 + \frac{\gamma-1}{2} M^2\right)^{\frac{\gamma}{\gamma-1}}$  is introduced. Similarly,

$$\dot{H}_i^0 = \dot{m}_i c_p T_i^0$$

which gives

$$\dot{H}_i^0 = \frac{\gamma}{\gamma-1} p_i^0 \sqrt{c_p T_i^0} D_i \left( \frac{\alpha_i}{\alpha_t} \right) \alpha_t \quad (3')$$

As for the calculation of the inlet-plane stream force  $\Phi$ , note that the information needed from the inlet flow pattern is  $\frac{\Phi_i}{p_i \alpha_t} = \frac{\Phi_t}{p_t}$ , i.e. the ratio of the area-average inlet plane pressure to the nozzle pressure. As will be shown later in the analysis, "upper bound" RHT performance characteristics of the type sought can be arrived at without any attention to the specifics of the entry flow pattern; however, it is instructive to consider several simple models for the entry flow for the physical insight they provide. This is accordingly done next.

Each of the models considered below is comprised of an annular region wherein the inward-spiraling flow is considered to form a free vortex, and a core region with different properties; according to the experimental findings of Lay,<sup>17</sup> this model is well justified physically. Imposition of different physical assumptions about the nature of the core leads to varying results as to the size of the core and the pressure distribution



within it, and consequent alterations in the value of  $\phi$ . For each model, however, the injection Mach number  $M_i$  is the controlling variable.

Free vortex. The postulated free vortex will first be analyzed, since a part or all of it is a component of each model. Consideration of the radial equilibrium wherein outward-directed inertial (centrifugal) force on a fluid element must be balanced by inward-directed pressure force leads to

$$dp = \rho v^2 \frac{dr'}{r'}$$

where  $r'$  is the radius of curvature of the particle path. If the height of the spiraling stream tube is negligible, the path at each point is essentially circular with radius equal to the distance from the tube axis, and one may write

$$dp = \rho v^2 \frac{dr}{r} \quad (5)$$

Also, due to conservation of angular momentum, the velocity distribution must be given by

$$vr = v_i r_i \quad (6)$$

One may combine equations (5) and (6) with the perfect gas equation of state and the stipulation of constant total enthalpy per unit mass to arrive at the variation of Mach number, and hence pressure and temperature, as a function of radius; this has been done by Hashem. Alternatively, one may note that under the conditions for which (5) is valid--negligible stream thickness--properties within a given stream tube vary insignificantly between the inner and outer boundaries of the tube.

Therefore, one-dimensional flow relations may be applied as follows to reproduce Hashem's free vortex description.

Define a dimensionless velocity

$$M^* \equiv \frac{U}{a^*}$$

where  $a^*$  is the speed of sound corresponding to expansion from the given nozzle stagnation conditions isentropically to Mach 1. With this definition, equation (6) may be rewritten

$$M^*(r) = \frac{M_i^*}{r} \quad (6')$$

The item of concern is the static pressure distribution, for which in one-dimensional isentropic flow one may write

$$\frac{p(r)}{p_i} = \left(1 + \frac{\gamma-1}{2} M(r)^2\right)^{-\frac{\gamma}{\gamma-1}}$$

From Shapiro,<sup>32</sup> p. 81, one has the inverse relationships

$$M^2 = \frac{\frac{2}{\gamma+1} M^{*2}}{1 - \frac{\gamma-1}{\gamma+1} M^{*2}}, \quad M^{*2} = \frac{\frac{\gamma+1}{2} M^2}{1 + \frac{\gamma-1}{2} M^2}$$

whence one readily obtains

$$\frac{p(r)}{p_i} = \left(1 - \frac{\gamma-1}{\gamma+1} M^{*2}\right)^{\frac{\gamma}{\gamma-1}}$$

Thus, the static pressure distribution is given by

$$\frac{p(r)}{p_i} = \left[ \frac{1 - \frac{\gamma-1}{\gamma+1} M^{*2}(r)}{1 - \frac{\gamma-1}{\gamma+1} M_i^{*2}} \right]^{\frac{\gamma}{\gamma-1}}$$

or, applying equation (6') and the second of the inverse relationships

above, the final expression for the free vortex pressure distribution becomes:

$$\frac{p(\tilde{r})}{p_i} \bigg|_{\substack{\text{free} \\ \text{vortex}}} = \left[ 1 - \frac{\gamma-1}{2} M_i^2 \left( \frac{1-\tilde{r}^2}{\tilde{r}^2} \right) \right]^{\frac{\gamma}{\gamma-1}} \quad (7)$$

Equation (7) describes, for a given injection Mach number  $M_i$ , the static pressure distribution acting on plane I over the annular region wherein free vortex flow applies (i.e., outside the core region). The smallest radius to which this free vortex flow can penetrate is that at which the pressure drops to zero. Ideally, it may be shown from equation (7) that this radius is

$$\tilde{r}_{\text{vac}} = \left[ \frac{\frac{\gamma-1}{2} M_i^2}{1 + \frac{\gamma-1}{2} M_i^2} \right]^{\frac{1}{2}} \quad (8)$$

where the "vac" subscript indicates that the region within this radius would be a vacuum.

Figure 9 presents static pressure distributions from equation (7) for a range of injection Mach numbers from 0 to  $\sqrt{5}$ . The significance of this upper value of  $M_i$  will become apparent presently. The pressure distributions are plotted against  $\tilde{r}^2$  (proportional to area) rather than  $\tilde{r}$ , so that the significance of low pressures in contributing to the integrated pressure force is seen directly.

Model A: a priori upper bound. An immediate, if overly generous, upper bound for  $\frac{p_i}{p_i}$  is obtained by assuming that the entry flow from the infinitesimal-height nozzle makes only one revolution (adjacent to the tube wall) before moving off downstream, rather than forming an inward spiral. In this situation, the core region would extend all the way from

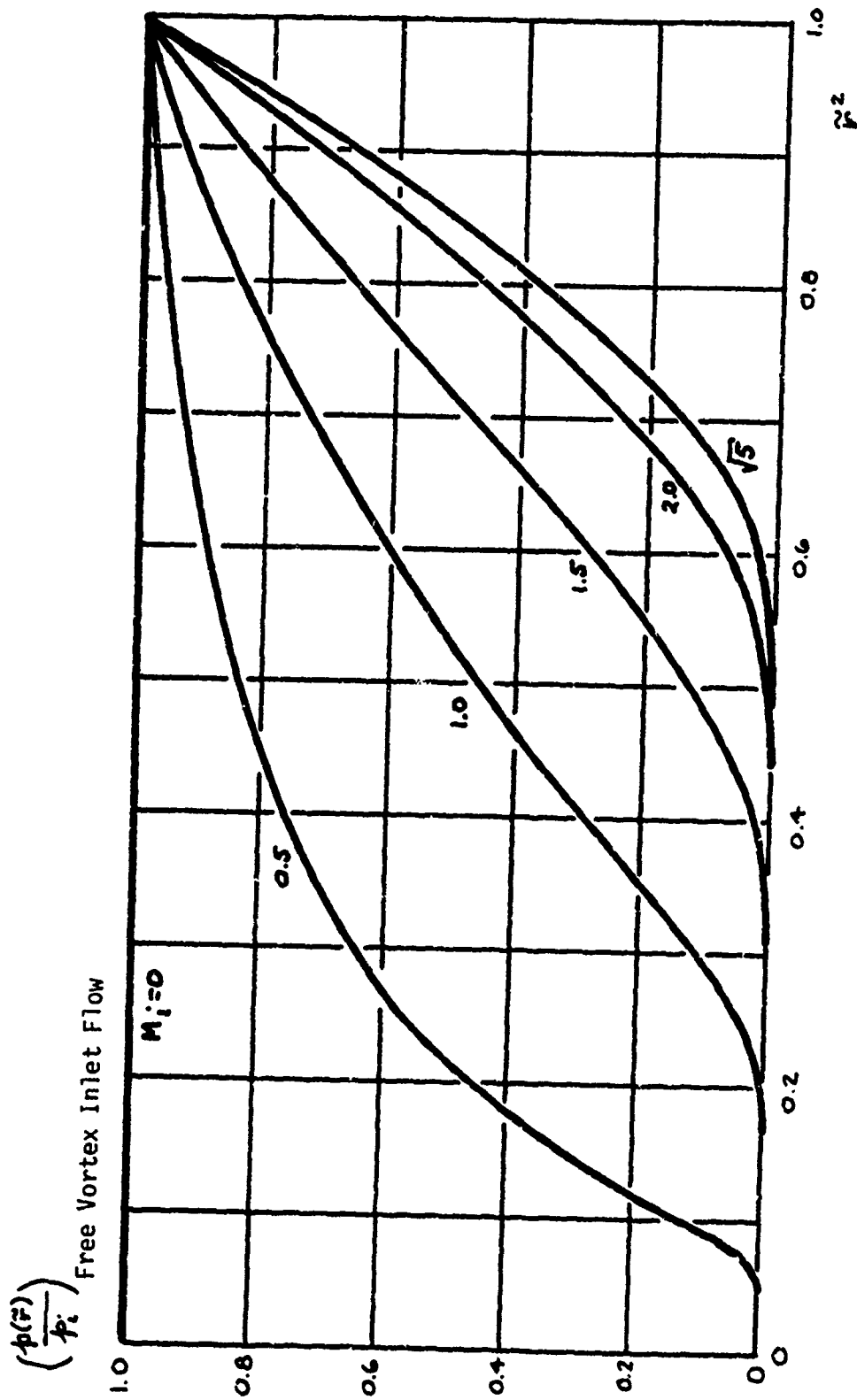


Figure 9  
Free Vortex Pressure Distributions

the center to within a vanishingly small distance  $dr$  of the tube wall,  $dr$  being the height of the entering flow filament. Therefore, the pressure at the core boundary differs only infinitesimally from the injection-nozzle static pressure  $p_i$  (measured at the tube wall), and if the core is assumed in addition to be quiescent ( $p = \text{const}$ ), there follows:

$$\left(\frac{\phi_z}{p_i}\right)_A = 1 \quad (4A')$$

regardless of  $M_i$ . Note that this is precisely the model that one would postulate for a vanishingly small nozzle height on the basis of Sibulkin,<sup>25</sup> if one were to assume his treatment to retain validity beyond the range of his specific analysis and experimentation, which is limited to the case of very small Mach number.

Model B: estimated lower bound. The opposite extreme from Model A, wherein the influence of the free vortex region on  $\frac{\phi_z}{p_i}$  is negligible compared with that of the core, is the model wherein the free vortex flow completely determines  $\frac{\phi_z}{p_i}$ . In this case, the flow spirals all the way in to the vacuum radius, equation (8), and the integrated pressure force reflects not only the low pressure of inner layers of the vortex, but indeed a central region or core at zero pressure. It is difficult to think of a plausible physical model for the inlet flow that would give a lower value for  $\frac{\phi_z}{p_i}$  than this one. Note that this is the model used by Hashem as his inlet flow model, except for his replacement of the vacuum core by a solid rod of the same dimensions.

Substituting the pressure distribution from equation (7) into equation (4) and noting that the region  $0 \leq \tilde{r} \leq \tilde{r}_{vac}$  contributes no pressure force, model B gives:

$$\left(\frac{\phi_r}{r}\right)_B = \int_{\tilde{r}_{vac}}^{\tilde{r}=1} \left[1 - \frac{\gamma-1}{2} M_i^2 \left(\frac{1-\tilde{r}^2}{\tilde{r}^2}\right)\right]^{\frac{\gamma}{\gamma-1}} 2 \tilde{r} d\tilde{r} \quad (4B')$$

where  $\tilde{r}_{vac}$  is given by equation (8), and the integral will be evaluated graphically.

Model C: weak backflow. It would not seem plausible that the vacuum core at plane I could sustain itself, given the fact that the terminal vortex spans the tube with nonzero pressure; therefore, one would expect from the present model that some backflow should occur to fill up the core, and in so doing establish a modified core. That this indeed happens seems well supported by the experimental findings of Scheper<sup>19</sup> and Lay.<sup>17</sup> The strength of this backflow is, however, in question, and one model each will be used to simulate weak and strong backflow.

As a minimal effect of backflow, suppose that the core at plane I is a forced vortex with a centerline pressure of zero. This reflects the tendency of the free vortex to generate zero pressure in the center, while not permitting a finite area at zero pressure to exist.

The overall inlet-plane flow pattern for model C is obtained by matching the inner boundary of the free vortex to the outer boundary of a forced vortex. This must be done in such a way that the pressure, temperature, and velocity is the same for either vortex at the boundary and so that the centerline pressure is zero. Assuming the forced vortex to be turbulent, thanks to its presumed origin downstream where turbulence indeed exists, the generalized description for a forced vortex developed for the terminal plane may be used. It will be shown that the pressure distribution in such a vortex is given by

$$\left. \frac{p(\tilde{r})}{p_t} \right|_{\text{forced vortex}} = \left[ 1 - \frac{\gamma-1}{2} M_{\theta t}^2 (1 - \tilde{r}^2) \right]^{\frac{\gamma}{\gamma-1}}$$

where  $p_t$  is the pressure at the tube wall and  $M_{\theta t}$  is the tangential Mach number at the tube wall.

At plane I, the forced vortex is contained not by the tube wall but by the core boundary. Adapting the above equation to account for this gives, with "cb" denoting "core boundary":

$$\left. \frac{p(\tilde{r})}{p_{cb}} \right|_{\text{core, c}} = \left[ 1 - \frac{\gamma-1}{2} (M_{\theta})_{cb}^2 \left( 1 - \frac{\tilde{r}^2}{\tilde{r}_{cb}^2} \right) \right]^{\frac{\gamma}{\gamma-1}} \quad (9)$$

Requiring  $p = 0$  at  $\tilde{r} = 0$  then gives

$$(M_{\theta})_{cb} = \sqrt{\frac{2}{\gamma-1}} \quad (10)$$

Equation (10) shows that the core-boundary tangential Mach number is always  $\sqrt{\frac{2}{\gamma-1}}$ , or  $\sqrt{5}$  for  $\gamma = 1.4$ . Thus, when  $M_i$  reaches  $\sqrt{5}$ , the core will according to this model fill the tube; this is the reason for choosing  $\sqrt{5}$  as the largest injection Mach number considered in Figure 9, since larger values of  $M_i$  will no longer give a nonzero area of zero pressure at the tube center.

The normalized core radius  $\tilde{r}_{cb}$  may now be calculated as a function of injection Mach number  $M_i$ :

$$\begin{aligned}
 \tilde{r}_{cb} &= \frac{U_i}{U_{cb}} \\
 &= \left[ \frac{2 c_p (T_i^e - T_i)}{2 c_p (T_i^e - T_{cb})} \right]^{\frac{1}{2}} \\
 &= \left[ \frac{1 - \frac{1}{1 + \frac{\gamma-1}{2} M_i^2}}{1 - \frac{1}{1 + \frac{\gamma-1}{2} (M_\infty)_{cb}^2}} \right]^{\frac{1}{2}}
 \end{aligned}$$

which with equation (10) gives

$$\tilde{r}_{cb} = \left[ 2 \cdot \frac{\frac{\gamma-1}{2} M_i^2}{1 + \frac{\gamma-1}{2} M_i^2} \right]^{\frac{1}{2}} \quad (11)$$

or, noting equation (8),

$$\tilde{r}_{cb} = \tilde{r}_{vac} \cdot \sqrt{2} \quad (11')$$

It is desired now to determine  $\frac{\phi_s}{p_i}$  for model C, i.e.,

$$\left( \frac{\phi_s}{p_i} \right)_C = \int_{\tilde{r}=0}^{\tilde{r}_{cb}} \frac{p_{cb}}{p_i} \left( \frac{p(\tilde{r})}{p_{cb}} \right)_{core,C} 2 \tilde{r} d\tilde{r} + \int_{\tilde{r}_{cb}}^{\tilde{r}=1} \left( \frac{p(\tilde{r})}{p_i} \right)_{free \text{ vortex}} 2 \tilde{r} d\tilde{r}$$

where the pressure distributions are given respectively by equations (9) and (7). The second integral will be evaluated graphically; for the first, however, it is convenient to define  $\hat{r} \equiv \frac{\tilde{r}}{\tilde{r}_{cb}}$  and rewrite the core integral as

$$\int_{\tilde{r}=0}^{\tilde{r}_{cb}} \frac{p_{cb}}{p_i} \left( \frac{p(\tilde{r})}{p_{cb}} \right)_{core,C} 2 \tilde{r} d\tilde{r} = \frac{p_{cb}}{p_i} \tilde{r}_{cb}^2 \int_{\hat{r}=0}^{\hat{r}=1} \frac{p(\hat{r})}{p_{cb}} 2 \hat{r} d\hat{r}$$



where, in terms of the new variable, equation (9) may be rewritten

$$\frac{p(\hat{r})}{p_{cb}} = \left[ 1 - \frac{\gamma-1}{2} (M_\theta)_{cb}^2 (1 - \hat{r}^2) \right]^{\frac{\gamma}{\gamma-1}}$$

This pressure integral is evaluated in closed form in the section below pertaining to the forced vortex at plane II; for  $(M_\theta)_{cb} = \sqrt{\frac{2}{\gamma-1}}$ , this gives

$$\int_{\hat{r}=0}^{\hat{r}=1} \frac{p(\hat{r})}{p_{cb}} 2\hat{r} d\hat{r} = \frac{\gamma-1}{2\gamma-1}$$

Using equation (11) for  $\tilde{r}_{cb}^2$  and equation (7) with  $\tilde{r} = \tilde{r}_{cb}$  for  $\frac{p_{cb}}{p_i}$ , one may thus evaluate the core integral in closed form so that  $\frac{Q_2}{P_i}$  becomes, for model C:

$$\left(\frac{Q_2}{P_i}\right)_C = \frac{(\gamma-1)^2}{2\gamma-1} \left(\frac{1}{2}\right)^{\frac{\gamma}{\gamma-1}} M_i^2 \left(1 + \frac{\gamma-1}{2} M_i^2\right)^{\frac{1}{\gamma-1}} + \int_{\tilde{r}_{cb}}^{\tilde{r}=1} \left[ 1 - \frac{\gamma-1}{2} M_i^2 \left(\frac{1-\tilde{r}^2}{\tilde{r}^2}\right) \right]^{\frac{\gamma}{\gamma-1}} 2\tilde{r} d\tilde{r} \quad (4C')$$

where, of course, the lower limit for the graphical integration over the free vortex region is given by equation (11).

Model D: strong backflow. Qualitatively, one might presume that the effect of stronger backflow--with an attendant stagnation point at the centerline and outward radial flow within the core region of plane I--would be superimposed on what is still basically a forced-vortex core. The result would be to raise the pressures in this region relative to model C.

To obtain a very rough grasp of the possible influence of this stronger backflow, it will be assumed for model D that the core region

is the same size at any given injection Mach number  $M_i$  as the core in model C, but that the core has a constant pressure equal to that at the core boundary. Thus:

$$\int_{\hat{r}=0}^{\hat{r}=1} \frac{p(\hat{r})}{p_{cb}} 2\hat{r} d\hat{r} = 1$$

and for model D there follows:

$$\left(\frac{Q_2}{P_i}\right)_D = 6\pi \left(\frac{1}{2}\right)^{\frac{\gamma}{\gamma-1}} M_i^2 \left(1 + \frac{\gamma-1}{2} M_i^2\right)^{\frac{1}{\gamma-1}} + \int_{\hat{r}_{cb}}^{\hat{r}=1} \left[1 - \frac{\gamma-1}{2} M_i^2 \left(\frac{1-\hat{r}^2}{\hat{r}^2}\right)\right]^{\frac{\gamma}{\gamma-1}} 2\hat{r} d\hat{r} \quad (4D')$$

where the integral over the annular free vortex region is identical to that for model C.

Figure 10 presents  $\frac{Q_2}{P_i}$  as a function of  $M_i$  for all four entry-plane flow models, and in addition includes an upper bound on  $\frac{Q_2}{P_i}$  which, as will be shown subsequently, is imposed by the second law of thermodynamics. It will be noted that model A (quiescent core spanning essentially all of plane I) violates this thermodynamic bound except in the limit as  $M_i$  goes to zero. Model B (vacuum core) lies a comfortable distance below this bound, but follows its behavior qualitatively. Model C, which allows for weak backflow, is hardly distinguishable from model B below an injection Mach number of about 1.0, but the strong backflow posited in model D has a pronounced effect, leading indeed to violation of the thermodynamic bound at  $M_i \approx 1.35$ . It is interesting, however, to note the qualitative similarity between the shapes of the bound and model D at high inlet Mach numbers: physically, the thermodynamic bound apparently

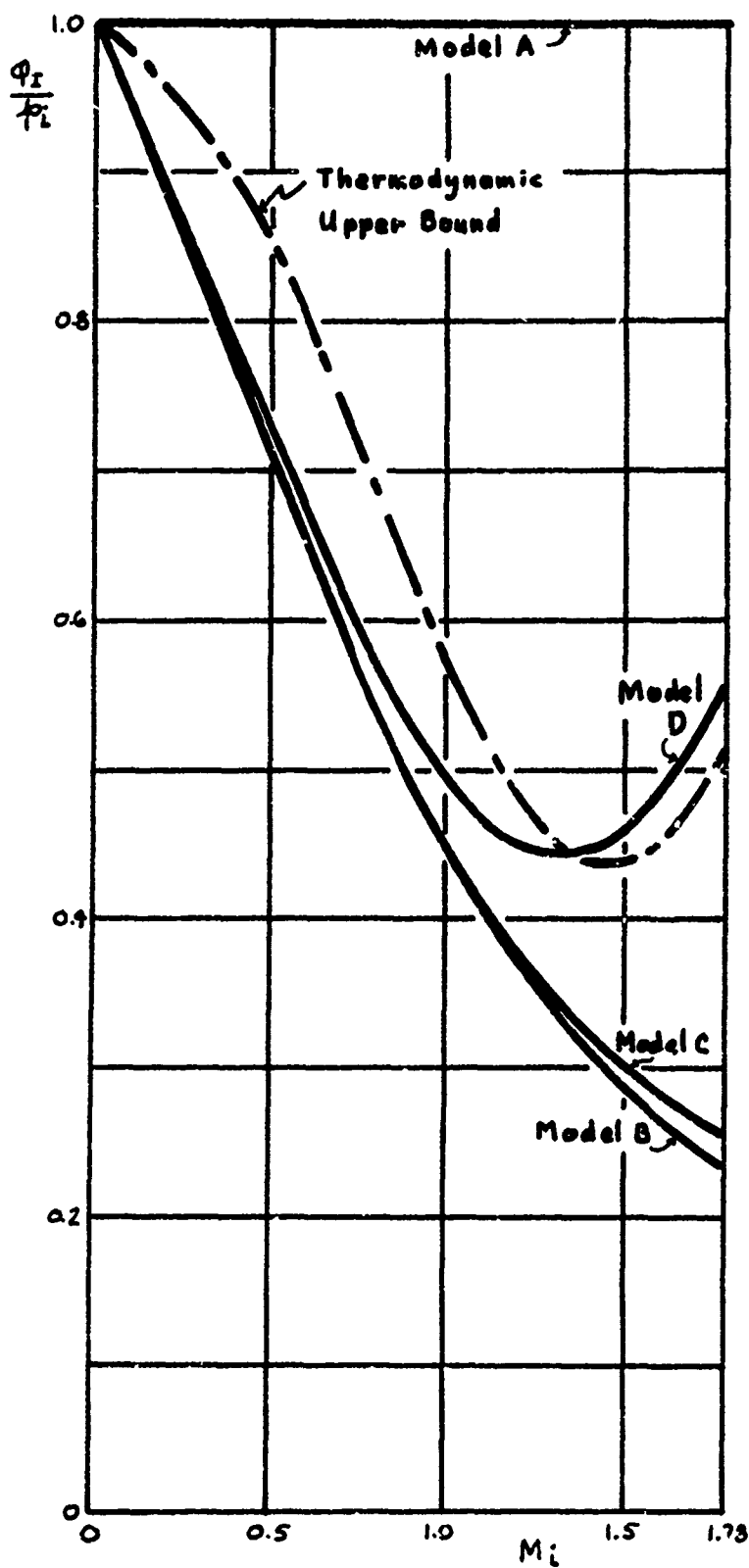


Figure 10  
Variation of Inlet-Plane  
Average Pressure with  
Injection Mach Number

corresponds to rather vigorous backflow, though with its strength depending on Mach number in a different manner from any of the simple flow models considered.

### 3. Terminal-Plane Flow Conditions

Flow parameter distributions. It is assumed that at plane II the flow is in pure solid-body rotation, with uniform entropy and axial velocity. Denoting the tangential component of velocity  $v_\theta$ , equation (5) gives

$$dp = \rho v_\theta^2 \frac{dr}{r} \quad (5')$$

and for solid-body rotation,

$$v_\theta = \omega r \quad (12)$$

where  $\omega$  is independent of  $r$ . Combining equations (5') and (12),

$$dp = \rho \omega^2 r dr \quad (13)$$

From the assumption that  $s_{II}(\bar{r}) = \text{constant}$ , where  $s_{II}$  denotes the entropy per unit mass in the terminal vortex, one has:

$$p(\bar{r}) = k_1 T(\bar{r})^{\frac{\gamma}{\gamma-1}}$$

$$\rho(\bar{r}) = k_2 T(\bar{r})^{\frac{1}{\gamma-1}}$$

where  $k_1$  and  $k_2$  are constants. Equation (13) then becomes

$$dT = \frac{k_2}{k_1} \frac{\gamma-1}{\gamma} \omega^2 r dr$$

But

$$\frac{h_2}{h_1} = \frac{\rho T^{-\frac{1}{\gamma-1}}}{\rho T^{-\frac{1}{\gamma-1}}} = \frac{1}{R}$$

One therefore obtains, in terms of the normalized radius  $\tilde{r}$ ,

$$dT = \frac{\gamma-1}{\gamma} \frac{\omega^2 r_t^2}{R} \tilde{r} d\tilde{r} \quad (14)$$

Integrating inward from the tube wall:

$$\int_1^{\tilde{r}} dT(\tilde{r}) = \int_1^{\tilde{r}} \frac{\gamma-1}{\gamma} \frac{\omega^2 r_t^2}{R} \tilde{r} d\tilde{r}$$

$$T(\tilde{r}) - T_t = \frac{\gamma-1}{2} \frac{\omega^2 r_t^2}{\gamma R} (\tilde{r}^2 - 1)$$

$$\frac{T(\tilde{r})}{T_t} = 1 - \frac{\gamma-1}{2} \frac{\omega^2 r_t^2}{\gamma R T_t} (1 - \tilde{r}^2)$$

Defining the tangential Mach number

$$M_\theta \equiv \frac{v_\theta}{a} = \frac{\omega r}{\sqrt{\gamma R T}}$$

the static temperature distribution is thus:

$$\left( \frac{T(\tilde{r})}{T_t} \right)_\Pi = 1 - \frac{\gamma-1}{2} M_{\theta t}^2 (1 - \tilde{r}^2) \quad (15)$$

and because of the uniform entropy, there immediately follow also the static pressure and density distributions:

$$\left(\frac{p}{p_t}\right)_{II} = \left[1 - \frac{\gamma-1}{2} M_{\theta t}^2 (1 - \tilde{r}^2)\right]^{\frac{\gamma}{\gamma-1}} \quad (16)$$

$$\left(\frac{\rho}{\rho_t}\right)_{II} = \left[1 - \frac{\gamma-1}{2} M_{\theta t}^2 (1 - \tilde{r}^2)\right]^{\frac{1}{\gamma-1}} \quad (17)$$

The total temperature at a radial location  $\tilde{r}$  is given by

$$\begin{aligned} T^o(\tilde{r}) &= T(\tilde{r}) + \frac{\vec{v}(\tilde{r}) \cdot \vec{v}(\tilde{r})}{2 c_p} \\ &= T(\tilde{r}) + \frac{\omega^2 r_t^2 \tilde{r}^2 + v_z^2}{2 c_p} \end{aligned}$$

where  $v_z$  is the axial velocity. With the axial Mach number  $M_a \equiv \frac{v_z}{a}$ , the total temperature distribution nondimensionalized by wall static temperature is found, with the aid of equation (15), to be given by:

$$\left(\frac{T^o(\tilde{r})}{T_t}\right)_{II} = 1 + \frac{\gamma-1}{2} \left[ M_{\theta t}^2 (2\tilde{r}^2 - 1) + M_{zt}^2 \right] \quad (18)$$

Introducing the ratio of static to total pressure at the tube wall, the normalized total temperature distribution follows:

$$\left(\frac{T^o(\tilde{r})}{T_t}\right)_{II} = \frac{1 + \frac{\gamma-1}{2} \left[ M_{\theta t}^2 (2\tilde{r}^2 - 1) + M_{zt}^2 \right]}{1 + \frac{\gamma-1}{2} (M_{\theta t}^2 + M_{zt}^2)} \quad (19)$$

and because of the uniformity of the entropy, the normalized total pressure distribution is:

$$\left(\frac{p^0(\tilde{r})}{p_t^0}\right)_{II} = \left\{ \frac{1 + \frac{\gamma-1}{2} [M_{\theta t}^2 (2\tilde{r}^2 - 1) + M_{zt}^2]}{1 + \frac{\gamma-1}{2} (M_{\theta t}^2 + M_{zt}^2)} \right\}^{\frac{\gamma}{\gamma-1}} \quad (20)$$

Finally, from the definition of tangential Mach number and equations (12) and (15), the tangential Mach number distribution is readily found to be:

$$\frac{M_{\theta}(\tilde{r})}{M_{\theta t}} = \frac{\tilde{r}}{\sqrt{1 - \frac{\gamma-1}{2} M_{\theta t}^2 (1 - \tilde{r}^2)}} \quad (21)$$

For the "upper bound" performance analysis, the case of small  $M_{zt}$  (compared to both unity and  $M_{\theta t}$ ) will be of interest, since kinetic energy of axial translation raises the total temperature of the core, which one wishes to be as cold as possible. For this case, indicated by the notation  $( )^{(0)}$ , equations (18) through (20) reduce to:

$$\left(\frac{T^0(\tilde{r})}{T_t^0}\right)_{II}^{(0)} = 1 + \frac{\gamma-1}{2} M_{\theta t}^2 (2\tilde{r}^2 - 1) \quad (18')$$

$$\left(\frac{T^0(\tilde{r})}{T_t^0}\right)_{II}^{(0)} = \frac{1 + \frac{\gamma-1}{2} M_{\theta t}^2 (2\tilde{r}^2 - 1)}{1 + \frac{\gamma-1}{2} M_{\theta t}^2} \quad (19')$$

$$\left(\frac{p^0(\tilde{r})}{p_t^0}\right)_{II}^{(0)} = \left[ \frac{1 + \frac{\gamma-1}{2} M_{\theta t}^2 (2\tilde{r}^2 - 1)}{1 + \frac{\gamma-1}{2} M_{\theta t}^2} \right]^{\frac{\gamma}{\gamma-1}} \quad (20')$$

The distributions of equations (15) through (17) and (21) are unchanged.

Figures 11a-11e present plots of the radial distributions of flow parameters at plane II versus normalized radius  $\tilde{r}$  for several values of  $M_{\theta t}$ , the tangential Mach number at the outer edge of the vortex (the tube wall), ranging from 0 to  $\sqrt{5}$ , the latter being the value which results in a centerline static pressure of zero. Figures 11a and 11b present static temperature and pressure distributions; the density distribution lies between these two and looks qualitatively like the pressure distribution. The radial distribution of tangential Mach number appears in Figure 11c. These three Figures are valid regardless of the magnitude of the axial velocity; Figures 11d and 11e, however, which present total temperature and pressure distributions, apply to the case of  $M_{\theta t}$  small and are obtained from equations (19') and (20') respectively.

Flux equations. Next, the information on flow-parameter distributions is used to develop the terminal-plane flux equations. Consider an annular element of flow area of height  $dr$  at radius  $r$ : the massflow through it is

$$d\dot{m}_I(r) = \rho(r) v_z 2\pi r dr$$

$$d\dot{m}_I(\tilde{r}) = \rho_t v_z \alpha_t \left( \frac{\rho(\tilde{r})}{\rho_t} \right)_I 2\tilde{r} d\tilde{r}$$

The total massflow through plane II is then

$$\dot{m}_I = \rho_t v_z \alpha_t \int_{\tilde{r}=0}^{\tilde{r}=1} \left( \frac{\rho(\tilde{r})}{\rho_t} \right)_I 2\tilde{r} d\tilde{r}$$



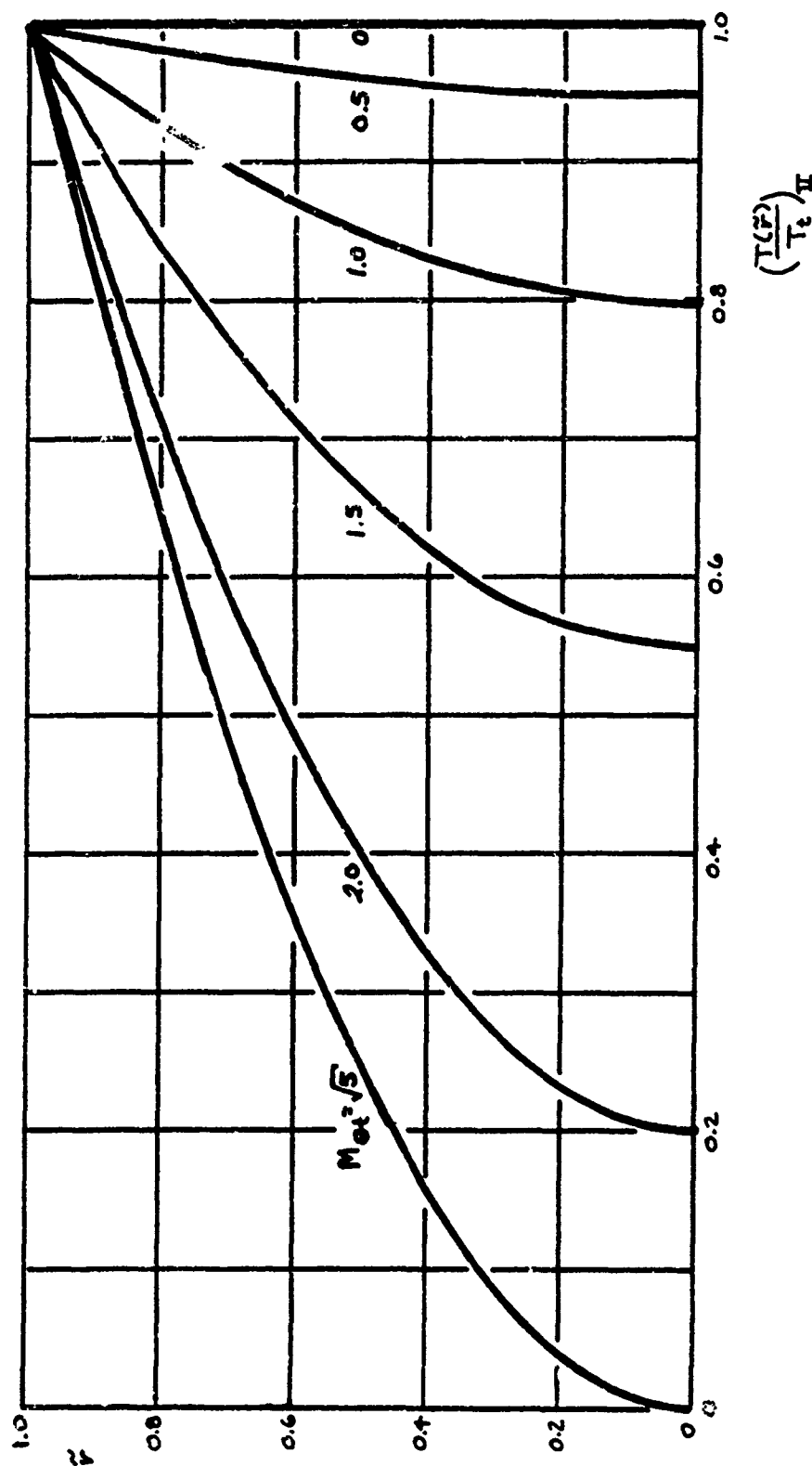


Figure 11(a)  
Terminal Vortex Static Temperature Distributions

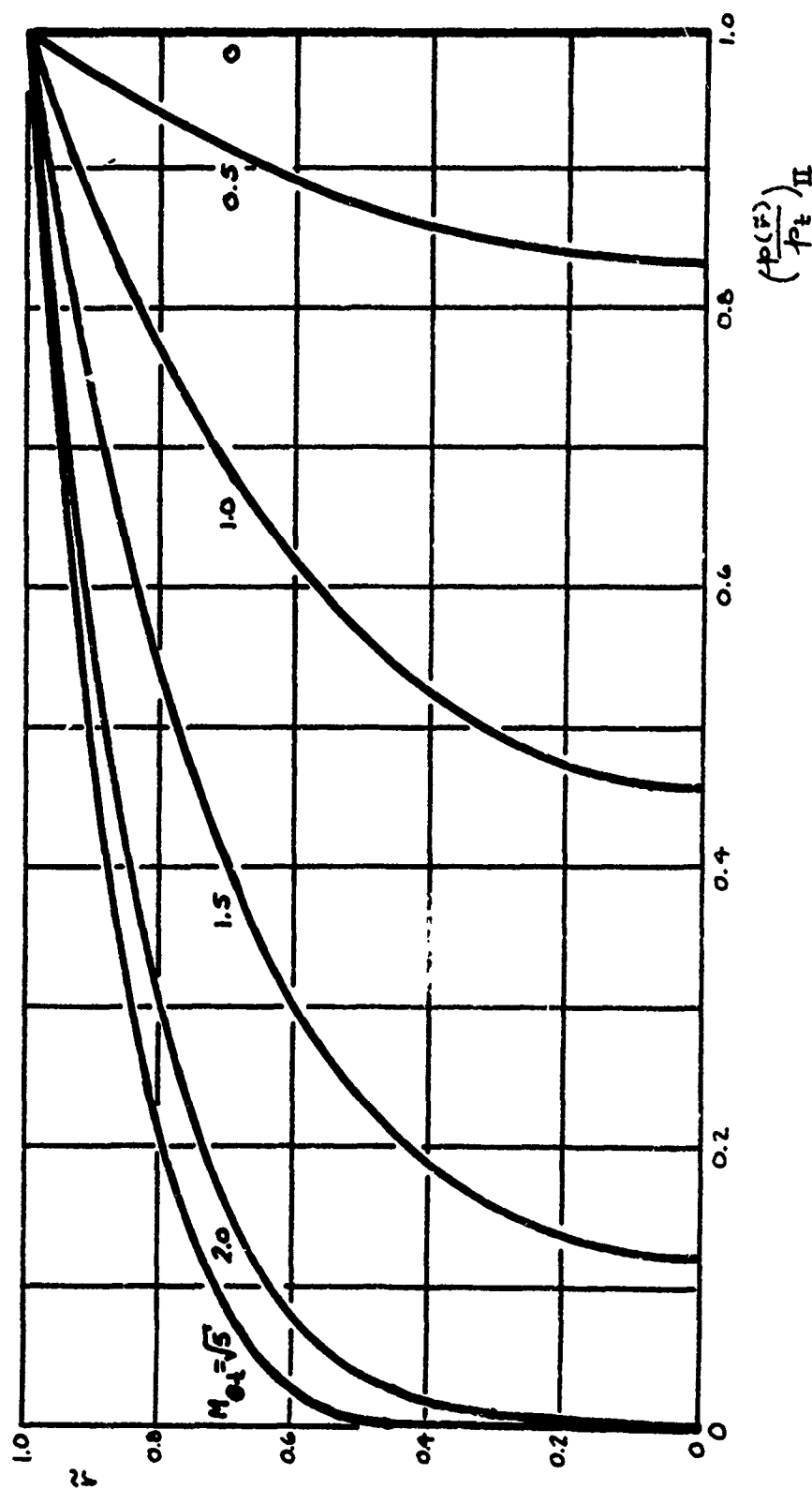


Figure 11(b)  
Terminal Vortex Static Pressure Distributions

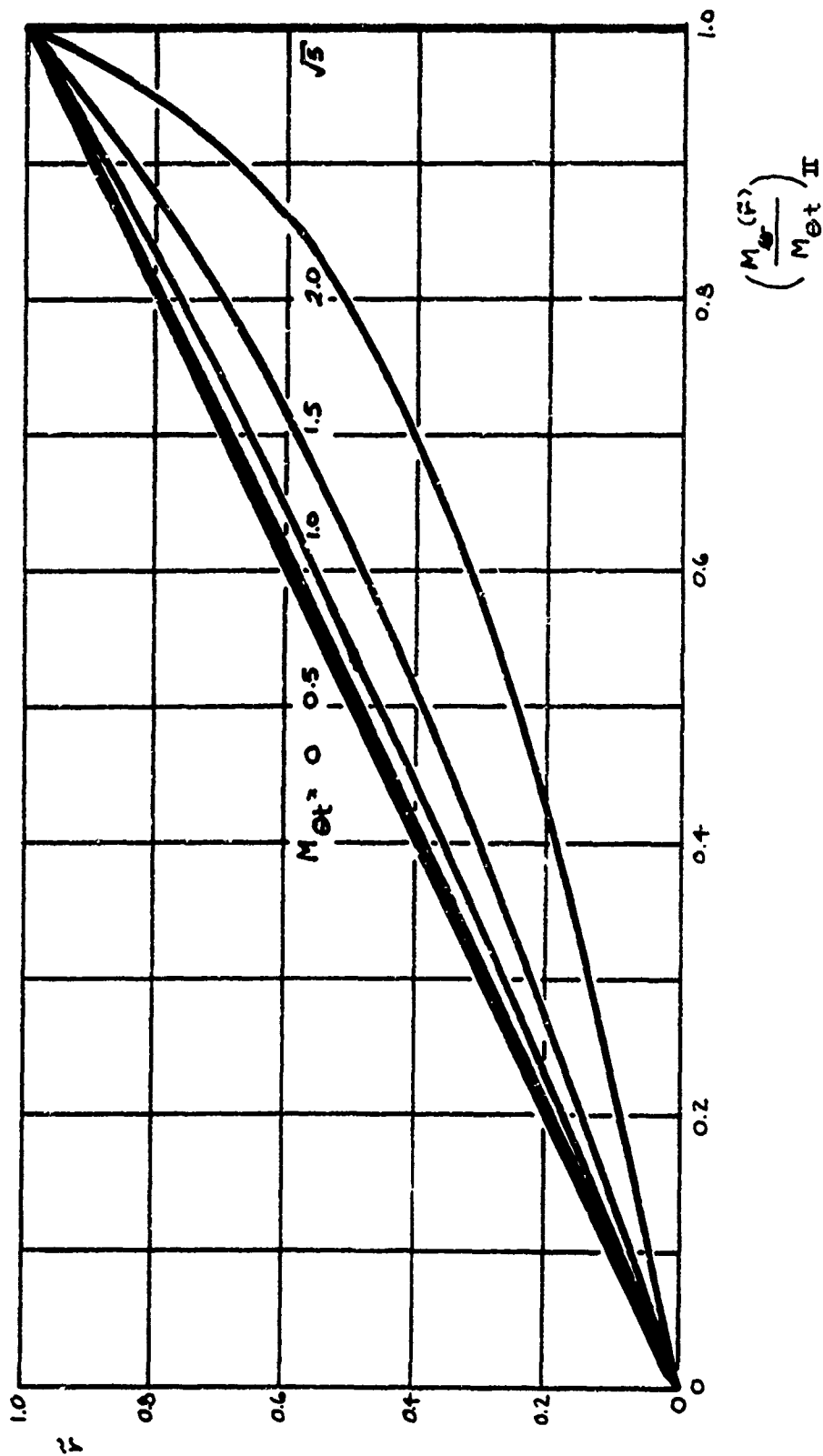


Figure 11(c)  
Terminal Vortex Tangential Mach Number Distributions

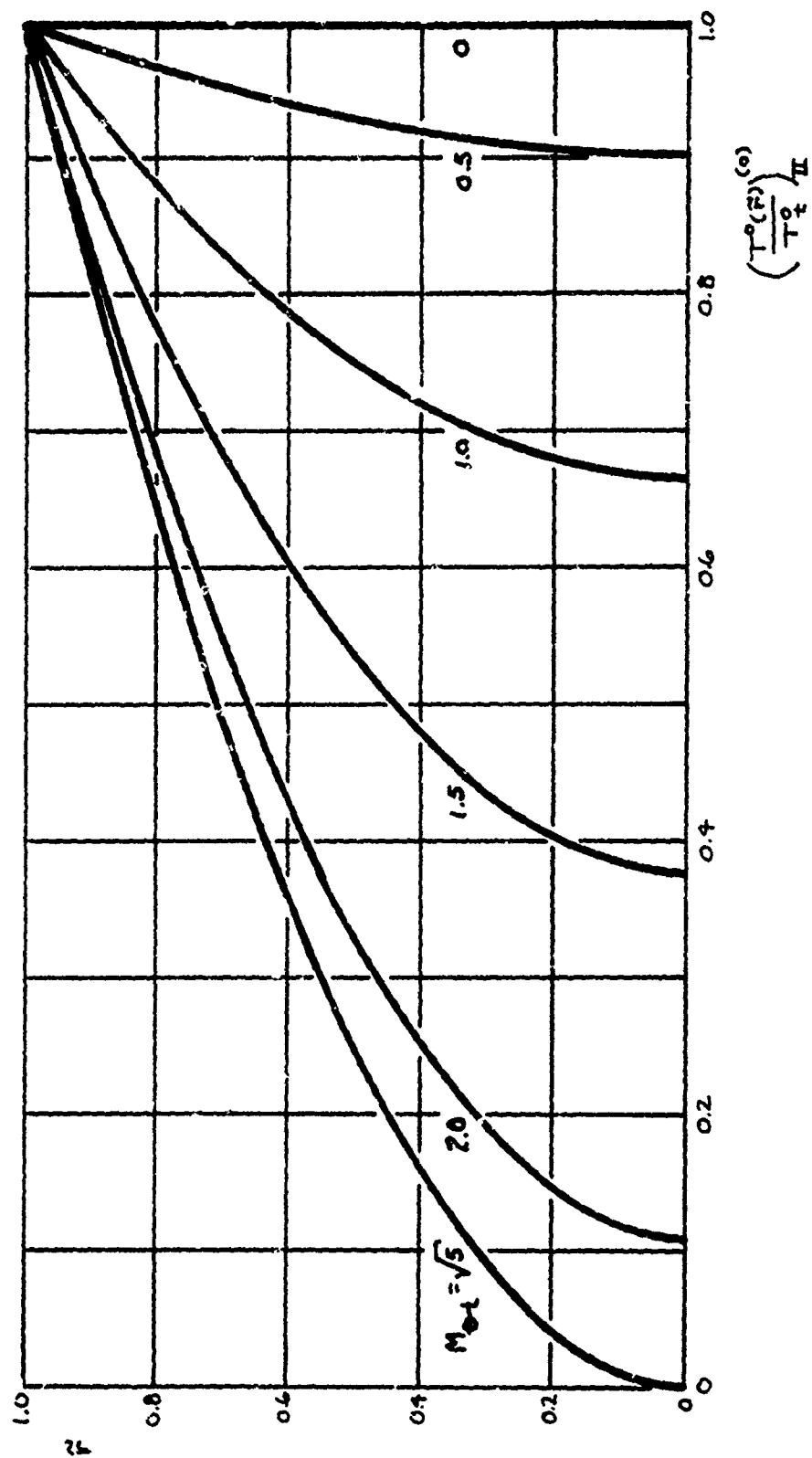


Figure 11(d)  
Terminal Vortex Total Temperature Distributions

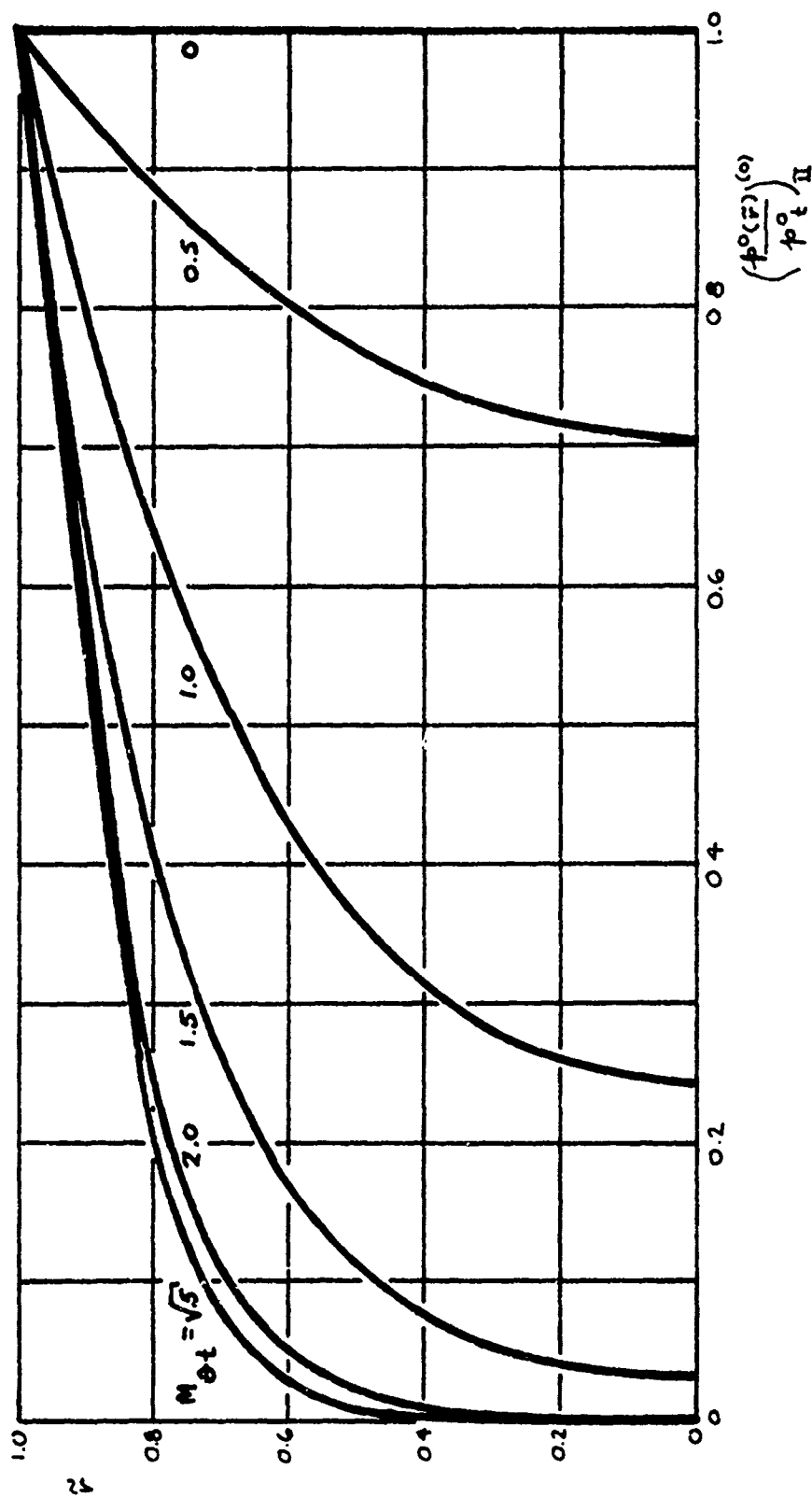


Figure 11(e)  
Terminal Vortex Total Pressure Distributions

Defining

$$Q_m \equiv \int_{\tilde{r}=0}^{\tilde{r}=1} \left( \frac{\rho(\tilde{r})}{\rho_t} \right)_{II} 2\tilde{r} d\tilde{r}$$

and noting that

$$v_z = M_{zt} \sqrt{\gamma R T_t}$$

$$p_t = \frac{p_t}{R T_t}$$

the equation for total massflow through plane II may be written:

$$\dot{m}_x = \sqrt{\frac{\gamma}{R}} \frac{p_t}{\sqrt{T_t}} M_{zt} \alpha_t Q_m \quad \text{Mass} \quad (22)$$

Similarly, the angular momentum per unit mass is

$$l_{II}(r) = v_\theta r$$

and the flow of angular momentum through the annular area element is therefore

$$d\dot{L}_{II}(r) = l_{II}(r) \cdot d\dot{m}_{II}(r)$$

$$d\dot{L}_{II}(\tilde{r}) = \omega r_t \cdot p_t v_z \alpha_t r_t \left( \frac{\rho(\tilde{r})}{\rho_t} \right)_{II} 2\tilde{r}^3 d\tilde{r}$$

Noting from the definition of tangential Mach number that

$$\omega r_t = M_{\theta t} \sqrt{\gamma R T_t}$$

there follows

$$d\dot{J}_H(\tilde{r}) = \gamma M_{ot} M_{at} \rho_t \alpha_t r_t \left( \frac{\rho(\tilde{r})}{\rho_t} \right)_H 2\tilde{r}^3 d\tilde{r}$$

Defining

$$Q_J \equiv \int_{\tilde{r}=0}^{\tilde{r}=1} \left( \frac{\rho(\tilde{r})}{\rho_t} \right)_H 2\tilde{r}^3 d\tilde{r}$$

the total flow of angular momentum through plane II may be written:

$$\dot{J}_H = \gamma \rho_t \alpha_t r_t (M_{ot} M_{at} Q_J) \quad \text{Angular Momentum} \quad (23)$$

In like manner, the flow of total enthalpy through the area element is

$$d\dot{H}_H^o(r) = h_H^o(r) \cdot d\dot{m}_H(r)$$

where  $h_H^o(r) = c_p T_H^o(r)$  is the total enthalpy per unit mass locally.

One readily obtains

$$d\dot{H}_H^o(\tilde{r}) = c_p T_t \sqrt{\frac{\gamma}{R}} \frac{\rho_t}{\sqrt{T_t}} M_{at} \alpha_t \left( \frac{T(\tilde{r})}{T_t} \right)_H \left( \frac{\rho(\tilde{r})}{\rho_t} \right)_H 2\tilde{r} d\tilde{r}$$

Defining

$$Q_H \equiv \int_{\tilde{r}=0}^{\tilde{r}=1} \left( \frac{T(\tilde{r})}{T_t} \right)_H \left( \frac{\rho(\tilde{r})}{\rho_t} \right)_H 2\tilde{r} d\tilde{r}$$

the total flow of stagnation enthalpy through plane II is given by:

$$\dot{H}_H^o = \frac{\gamma}{\sqrt{\gamma-1}} \rho_t \sqrt{c_p T_t} M_{at} \alpha_t Q_H$$

or

$$\dot{M}_{II}^{\circ} = \dot{M}_{II} c_p T_t \frac{Q_H}{Q_m} \quad \text{Energy} \quad (24)$$

Finally, for the axial stream force one may write

$$d\Phi_{II}(r) = p(r) d\alpha(r) + v_z d\dot{M}_{II}(r)$$

from which

$$d\Phi_{II}(\tilde{r}) = p_t \alpha_t \left[ \left( \frac{p(\tilde{r})}{p_t} \right)_{II} 2\tilde{r} d\tilde{r} + \gamma M_{\infty t}^2 \left( \frac{p(\tilde{r})}{p_t} \right)_{II} 2\tilde{r} d\tilde{r} \right]$$

Defining

$$Q_p \equiv \int_{\tilde{r}=0}^{\tilde{r}=1} \left( \frac{p(\tilde{r})}{p_t} \right)_{II} 2\tilde{r} d\tilde{r}$$

and noting the mass flux integral  $Q_m$ , the total axial stream force at plane II may be expressed as:

$$\Phi_{II} = p_t \alpha_t (Q_p + \gamma M_{\infty t}^2 Q_m) \quad \text{Axial Stream Force} \quad (25)$$

The flux integrals  $Q_m$ ,  $Q_x$ ,  $Q_H$ , and  $Q_p$  are evaluated with the aid of the distributions given by equations (16), (17), and (18). Defining

$$Y \equiv 1 - \frac{\gamma-1}{2} M_{\infty t}^2$$



the flux integrals become:

$$Q_M = \frac{2}{\gamma M_{ot}^2} \left(1 - \gamma^{\frac{\gamma}{\gamma-1}}\right) \quad (26a)$$

$$Q_L = \frac{2}{\gamma M_{ot}^2} \left[1 - \frac{2}{(2\gamma-1)M_{ot}^2} \left(1 - \gamma^{\frac{2\gamma-1}{\gamma-1}}\right)\right] \quad (26b)$$

$$Q_H = \left[ \frac{4}{(2\gamma-1)M_{ot}^2} \left(1 - \gamma^{\frac{2\gamma-1}{\gamma-1}}\right) - \frac{2\gamma}{\gamma M_{ot}^2} \left(1 - \gamma^{\frac{\gamma}{\gamma-1}}\right) \right] + \left[ \frac{\gamma-1}{\gamma} \left(\frac{M_{zt}}{M_{ot}}\right)^2 \left(1 - \gamma^{\frac{\gamma}{\gamma-1}}\right) \right] \quad (26c)$$

$$Q_P = \frac{2}{(2\gamma-1)M_{ot}^2} \left(1 - \gamma^{\frac{2\gamma-1}{\gamma-1}}\right) \quad (26d)$$

Examining equations (26a-d), it is seen that all but the energy flux integral  $Q_H$  are strictly functions of  $M_{ot}$ , and that  $Q_H$  consists of a part dependent only on  $M_{ot}$  (first bracket) and an additional part which depends upon both  $M_{ot}$  and  $M_{zt}$ . Clearly, the dependence on  $M_{zt}$  is negligible if  $M_{zt}$  is sufficiently small, and in this case the second bracket of equation (26c) may be neglected. Numerical analysis reveals that the error in  $Q_H$  which results from this approximation is always less than 2% so long as  $M_{zt}$  satisfies both of the following criteria:

- i)  $M_{zt} \leq M_{ot}$
- ii)  $M_{zt} \leq 0.3$

Furthermore, the accuracy of the approximation improves with increasing  $M_{ot}$  for a given value of  $M_{zt}$ . From here on, the small- $M_{zt}$  approximation will be used.

It is now useful to examine the flux equations (22) through (25) in anticipation of application of the conservation equations between planes I and II. The values of  $\dot{m}_I$ ,  $\dot{z}_I$ ,  $\dot{h}_I^\circ$ , and  $\Phi_I$  may be regarded as known, since they are to be obtained via the conservation equations. The geometric parameters  $\alpha_t$  and  $r_t$  merely reflect the tube size, which may be chosen arbitrarily, and  $\gamma$  and  $R$  are gas properties. Therefore, the flux equations are four equations in the four variables  $p_t$ ,  $T_t$ ,  $M_{ot}$ , and  $M_{at}$ . Before solving for these variables, it is convenient to eliminate the tube size dependence, thus:

$$\dot{m}_I \equiv \frac{\dot{m}_I}{\alpha_t} = \sqrt{\frac{\gamma}{R}} \frac{p_t}{\sqrt{T_t}} M_{at} Q_m \quad (22')$$

$$\underline{\dot{z}}_I \equiv \frac{\dot{z}_I}{\alpha_t r_t} = \gamma p_t M_{ot} M_{at} Q_z \quad (23')$$

$$\dot{h}_I^\circ \equiv \frac{\dot{h}_I^\circ}{\alpha_t} = \dot{m}_I c_p T_t \frac{Q_h}{Q_m} \quad (24')$$

$$\Phi_I \equiv \frac{\Phi_I}{\alpha_t} = p_t (Q_p + \gamma M_{ot}^2 Q_m) \quad (25')$$

where the underline in  $\underline{\dot{z}}_I$  is to emphasize that it is divided by the product of tube area and radius, rather than tube area alone.

From equation (24') one may write

$$T_t = \frac{\dot{h}_I^\circ}{\dot{m}_I c_p} \frac{Q_m}{Q_h} \quad (27)$$

From (23'),

$$p_t = \frac{j_{II}}{\gamma M_{ot} M_{at} Q_d} \quad (28)$$

Alternatively,  $p_t$  may be obtained from (22') and (27) as

$$p_t = \frac{\sqrt{\gamma-1}}{\gamma} \frac{m_{II} h_{II}^0}{M_{at} \sqrt{Q_m Q_n}}$$

Equating the right side with that of equation (28) leads to

$$\frac{M_{ot} Q_d}{\sqrt{Q_m Q_n}} = \frac{j_{II}}{\sqrt{(\gamma-1) m_{II} h_{II}^0}} \quad (29)$$

the left side of which is a function of  $M_{ot}$  only (under the small- $M_{at}$  approximation). From (25'),

$$M_{at}^2 = \frac{1}{\gamma Q_m} \left( \frac{\phi_{II}}{p_t} - Q_p \right)$$

Substitution for  $p_t$  from (28) leads to

$$M_{at}^2 + \left[ -\frac{\phi_{II}}{j_{II}} \frac{M_{ot} Q_d}{Q_m} \right] M_{at} + \frac{Q_p}{\gamma Q_m} = 0$$

the solution to which is

$$M_{at} = \frac{1}{2} \left\{ \frac{\phi_{II}}{j_{II}} \frac{M_{ot} Q_d}{Q_m} \pm \sqrt{\left[ \frac{\phi_{II}}{j_{II}} \frac{M_{ot} Q_d}{Q_m} \right]^2 - \frac{4}{\gamma} \frac{Q_p}{Q_m}} \right\} \quad (30)$$

Equations (27) through (30) are the solutions of the flux equations for the desired reference flow parameters evaluated at the wall,  $p_t$ ,  $T_t$ ,  $M_{a,t}$ , and  $M_{o,t}$  (the solution being implicit rather than direct in the case of  $M_{o,t}$ ) in terms of the flux parameters  $\dot{m}_I$ ,  $i_I$ ,  $h_I^o$ , and  $\phi_I$ , which are conserved from plane I to plane II. From (29) is obtained  $M_{o,t}$ , which then enables calculation of  $T_t$  from (27) and  $M_{a,t}$  from (30); having  $M_{o,t}$  and  $M_{a,t}$ ,  $p_t$  may be found using (28).

Examination of equations (27) through (30) reveals that the following functions of  $M_{o,t}$  are relevant to the numerical analysis which will ultimately be required:

$$\gamma_1 \equiv \frac{M_{o,t} Q_2}{\sqrt{Q_m Q_H}}$$

$$\gamma_2 \equiv \frac{M_{o,t} Q_2}{Q_m}$$

$$\gamma_3 \equiv \frac{Q_P}{Q_m}$$

$$\gamma_4 \equiv \frac{Q_m}{Q_H}$$

These functions are plotted in Figure 12, together with  $Q_2$  which appears in the equation for  $p_t$ . With the definitions above, equations (27) through (30) become:

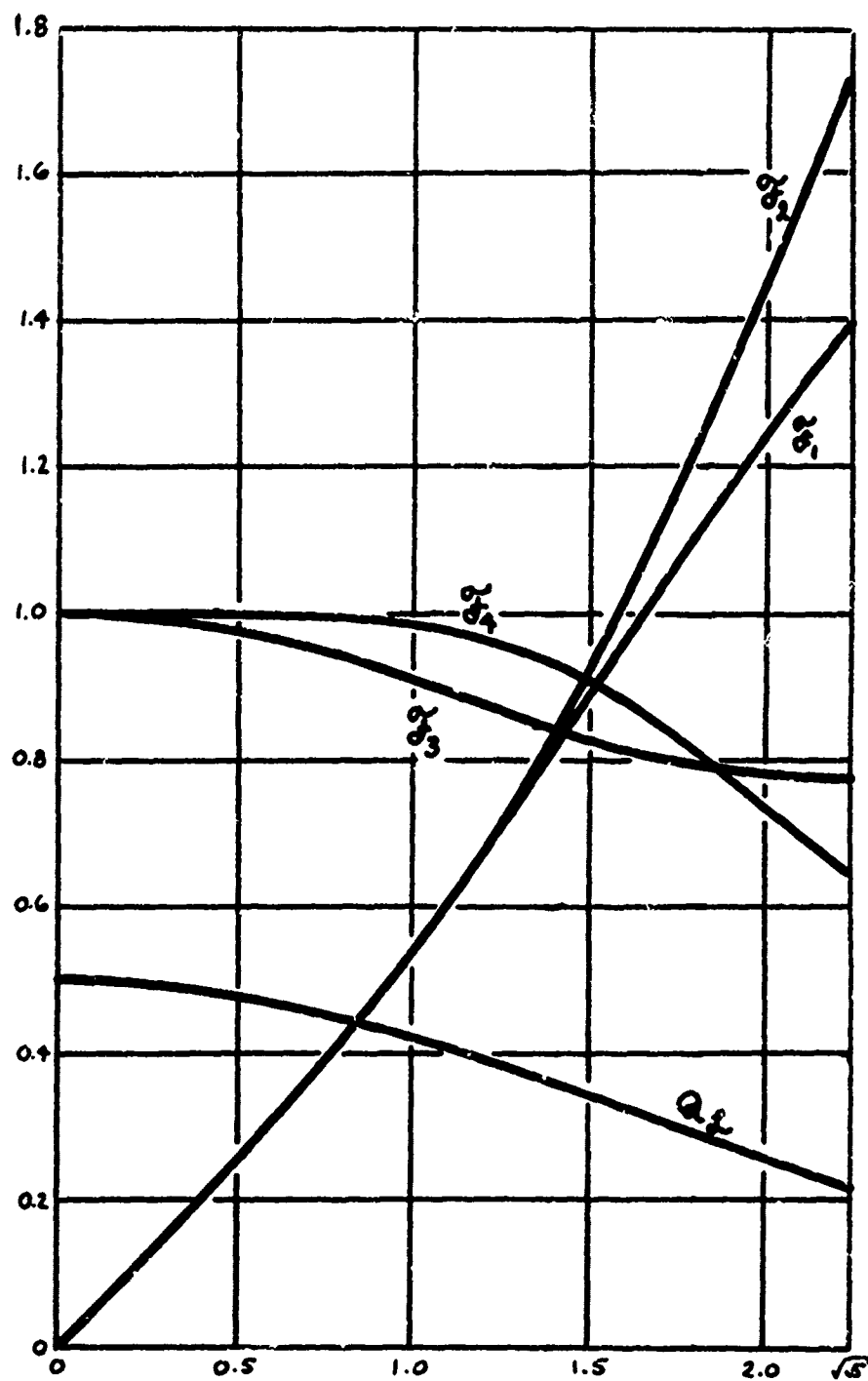


Figure 12  
Analytical Functions of  $M_{0t}$

$$T_t = \frac{\dot{h}_H^o}{\dot{m}_H c_p} T_2 \quad (27')$$

$$p_t = \frac{\dot{h}_H}{\gamma M_{0t} M_{2t} Q_2} \quad (28)$$

$$\sigma_2 = \frac{\dot{h}_H}{\sqrt{(\gamma-1)} \dot{m}_H \dot{h}_H^o} \quad (29')$$

$$M_{2t} = \frac{1}{2} \left\{ \frac{\phi_H}{\dot{h}_H} \sigma_2 \pm \sqrt{\left( \frac{\phi_H}{\dot{h}_H} \sigma_2 \right)^2 - \frac{4}{\gamma} \sigma_2} \right\} \quad (30')$$

where (28) remains unchanged but is repeated for ease of reference.

#### 4. Application of Conservation Equations--Plane I to Plane II

Dependence of terminal vortex on injection conditions. Consider now the transition from plane I to plane II of the control volume defined in Figure 8. Mass is neither added nor subtracted between planes I and II of the constant-area, adiabatic, frictionless tube, nor is there any shaft work. The conservation equations are therefore simply:

$$\dot{m}_H = \dot{m}_I \quad \text{Continuity} \quad (31)$$

$$\dot{h}_H = \dot{h}_I \quad \text{Angular Momentum} \quad (32)$$

$$\dot{h}_H^o = \dot{h}_I^o \quad \text{Energy} \quad (33)$$

$$\dot{\phi}_H = \dot{\phi}_I \quad \text{Axial Momentum} \quad (34)$$

or, if the dependence on tube size is eliminated as done for equations (22') through (25'), one has equivalently:

$$\dot{m}_2 = \dot{m}_1 \quad (31')$$

$$\dot{h}_2 = \dot{h}_1 \quad (32')$$

$$\dot{h}_2^0 = \dot{h}_1^0 \quad (33')$$

$$\phi_2 = \phi_1 \quad (34')$$

where the corresponding fluxes for plane I are given by:

$$\dot{m}_1 = \sqrt{\frac{\gamma}{R}} \frac{p_i^0 D_i}{\sqrt{T_i^0}} \left( \frac{\alpha_i}{\alpha_t} \right) \quad (1'')$$

$$\dot{h}_1 = \gamma p_i^0 \frac{M_i^2}{f_p(M_i)} \left( \frac{\alpha_i}{\alpha_t} \right) \frac{r_i}{r_t} \quad (2'')$$

$$\dot{h}_1^0 = \frac{\gamma}{\sqrt{\gamma-1}} p_i^0 \sqrt{c_p T_i^0} D_i \left( \frac{\alpha_i}{\alpha_t} \right) \quad (3'')$$

$$\phi_1 = \left( \frac{\phi_1}{p_i^0} \right) p_i^0 \quad (4'')$$

Note in equation (2'') that  $\frac{r_i}{r_t}$  is the normalized mass-average radius at which the injected flow enters the tube; this will be taken equal to unity in the remainder of the analysis, since this leads to maximum performance. As for (4''), the value of  $\frac{\phi_1}{p_i^0}$  is a function of  $M_i$  and the inlet flow model used, and is obtainable for a given  $M_i$  from Figure 10.

The flux equations at plane II, (22') through (25'), could now be used with those at plane I, (1'') through (4''), together with the conservation equations (31') through (34'), to relate conditions in the terminal vortex to injection conditions. However, the writer has chosen instead an

equivalent approach making use of equations (27') through (30'), in which it is noted that the flux groupings therein are the same at planes I and II by virtue of the conservation equations. The groupings required, which are evaluated with the aid of equations (1'') through (4'') are the following:

$$\frac{h''_2}{m_2 c_p} = T''_1$$

$$\frac{s''_2}{\gamma} = f''_1 \frac{M_1^2}{f_p(M_1)} \left( \frac{\alpha_1}{\alpha_2} \right)$$

$$\frac{\dot{L}_2}{\sqrt{(\gamma-1) m_2 h''_2}} = \frac{M_1}{\sqrt{f_T(M_1)}}$$

$$\frac{\phi_2}{\dot{L}_2} = \frac{(\phi_2/p_1)}{\gamma M_1^2 (\alpha_1/\alpha_2)}$$

Substitution of these into equations (27') through (30') gives:

$$\sigma_1(M_{02}) = \frac{M_1}{\sqrt{f_T(M_1)}} \quad (35)$$

$$M_{02} = \frac{1}{2} \frac{(\phi_2/p_1)}{\gamma M_1^2 (\alpha_1/\alpha_2)} \sigma_2 \left\{ 1 \pm \sqrt{1 - \frac{4}{\gamma} \frac{\sigma_2^2}{[(\phi_2/p_1) \sigma_2 / \gamma M_1^2 (\alpha_1/\alpha_2)]^2}} \right\} \quad (36)$$

$$\frac{T_2}{T''_1} = \sigma_T \quad (37)$$

$$\frac{h_2}{f''_1} = \frac{M_1^2}{f_p(M_1)} \cdot \frac{(\alpha_1/\alpha_2)}{M_{02} M_{02} Q_2} \quad (38)$$



A simpler expression for  $M_{2t}$  is clearly desirable, since equation (36) is unwieldy. This may be obtained with the aid of the binomial expansion, provided  $\frac{\alpha_i}{\alpha_t}$  is sufficiently small that

$$\frac{4}{\gamma} \frac{\sigma_3}{[(\phi_2/p_i) \sigma_2 / \gamma M_i^2 (\alpha_i/\alpha_t)]^2} \ll 1$$

holds. In this case, one obtains

$$M_{2t} \doteq \frac{1}{2} \frac{(\phi_1/p_i) \sigma_2}{\gamma M_i^2 (\alpha_i/\alpha_t)} \left\{ 1 \pm \left( 1 - \frac{2}{\gamma} \frac{\sigma_3}{[(\phi_2/p_i) \sigma_2 / \gamma M_i^2 (\alpha_i/\alpha_t)]^2} \right) \right\}$$

or

$$M_{2t} \doteq \begin{cases} \frac{(\phi_1/p_i) \sigma_2}{\gamma M_i^2 (\alpha_i/\alpha_t)} - \frac{\sigma_3 / \gamma}{[(\phi_2/p_i) \sigma_2 / \gamma M_i^2 (\alpha_i/\alpha_t)]} \\ \frac{\sigma_3 / \gamma}{[(\phi_2/p_i) \sigma_2 / \gamma M_i^2 (\alpha_i/\alpha_t)]} \end{cases}$$

Inspection of the behavior of the two solutions indicates that they are conjugate in nature, the first being supersonic and the second subsonic. Only the latter will be considered further, the other being inconsistent with the small- $M_{2t}$  approximation embodied in the rest of the analysis.

The approximate, subsonic solution for  $M_{2t}$  above may be expressed equivalently as:

$$\frac{M_{2t}/M_i}{(\alpha_i/\alpha_t)} = \frac{M_i}{(\phi_1/p_i)} \frac{\sigma_3}{\sigma_2} \quad (36')$$

This approximate expression tends to underestimate  $M_{at}$  by an amount which depends, for a given injection Mach number, upon  $\frac{\alpha_i}{\alpha_t}$ . By considering the criterion used in applying the binomial expansion, it may be shown that the error in  $M_{at}$  is not larger than 2.5% relative to the exact solution provided  $\frac{\alpha_i}{\alpha_t}$  does not exceed the value calculated as follows:\*

$$\left(\frac{\alpha_i}{\alpha_t}\right)_{2.5\%} = \frac{\phi_I/p_i}{\gamma M_i^2} \sqrt{\frac{0.18}{1 + \gamma_3}} \gamma_2 \quad (39)$$

Also, with the aid of (36'), (38) becomes:

$$\frac{p_t}{p_i} = \frac{\gamma_2}{f_p(M_i) M_{at} a_2 \gamma_3} \left(\frac{\phi_I}{p_i}\right) \quad (38')$$

Noting from (35) that  $M_{at}$  is a function of  $M_i$  only, all factors in (38') except  $\frac{\phi_I}{p_i}$  are strictly determined by  $M_i$ , independent of the inlet flow model. Thus, for any given  $M_i$ ,  $\frac{p_t}{p_i}$  is directly proportional to  $\frac{\phi_I}{p_i}$ .

The terminal-vortex tip tangential Mach number  $M_{at}$  is determined as a function of  $M_i$  by means of (35), thereby establishing also the values of  $\gamma_2$ ,  $\gamma_3$ ,  $\gamma_4$ , and  $a_2$ . The latter enable  $M_{at}$ ,  $\frac{T_t}{T_i}$ , and  $\frac{p_t}{p_i}$  to be found using equations (36'), (37) and (38'). The

---

\*It will be shown in Figure 15, after the thermodynamic limit on  $\phi_I/p_i$  has been defined, that the error in  $M_{at}$  as calculated by (36') is quite small for values of  $\alpha_i/\alpha_t$  likely to be of practical interest. Furthermore, such error as does exist is in the direction which will produce overestimation of RHT performance, and therefore introduces no inconsistency into the "upper bound" RHT performance analysis.

state of the vortex at plane II is now fully determined as a function of inlet-plane conditions; other particular relationships between injection and terminal flow parameters may be constructed as needed, with the aid of the equations developed above and the equations for the flow property distributions within the terminal vortex.

Of most direct concern for performance prediction are the changes in stagnation temperature and pressure from the point of injection to points within the terminal vortex, since this information is needed to calculate energy separation as a function of pressure ratio and cold fraction. With respect to stagnation temperatures, one may write:

$$\frac{T_{II}^o(\bar{r})}{T_i^o} = \frac{T_{II}^o(\bar{r})}{T_e^o} \cdot \frac{T_e^o}{T_t^o} \cdot \frac{T_t^o}{T_i^o} \quad (40)$$

where the first factor is found from distribution equation (19'), the second is a function of  $M_{ot}$  which is found from (35), and the third is obtained from (37). Similarly for stagnation pressures:

$$\frac{p_{II}^o(\bar{r})}{p_i^o} = \frac{p_{II}^o(\bar{r})}{p_e^o} \cdot \frac{p_e^o}{p_t^o} \cdot \frac{p_t^o}{p_i^o} \quad (41)$$

where the factors are evaluated with the aid of (20'), (35), and (38'), respectively. Another item of interest is the change in wall static pressure; using (38') and noting that  $f_p(M) = \frac{p_i^o}{p_i}$ , one finds:

$$\frac{p_t}{p_i} = \frac{(\phi_z/p_i) \sigma_z^2}{M_{ot} Q_z \sigma_z^2} \quad (42)$$

Figure 13 indicates the manner in which  $M_{et}$  varies as a function of  $M_i$  on the basis of equation (35). The Figure gives  $M_{et}$  directly, so that Figure 12 may be entered for solution of equations (36'), (37), and (38'); in addition, the ratio  $\frac{M_{et}}{M_i}$  is shown. The latter shows that as the injection Mach number tends toward zero, the tangential velocity at the rim of the forced vortex tends to twice the injection velocity (since at low Mach numbers the Mach number is essentially proportional to velocity). This recalls analogous results obtained under the assumption of incompressible flow by Kassner and Knoernschild<sup>18</sup> and Lay.<sup>17</sup> As the injection Mach number  $M_i$  increases, however, this ratio drops off significantly: the decrease in velocity ratio is a shade less than that in Mach number ratio due to increased static temperature at the rim of the forced vortex (about 3% at  $M_i = 1.0$ ), but the trend is similar.

Thermodynamic upper bound on  $\phi_z/p_i$ . Equations (36') and (38'), and of course any subsequent relations built around them, involve a dependence on  $\frac{\phi_z}{p_i}$ , the value of which depends upon the nature of the flow pattern in entry plane I. Figure 10 presents the results of  $\frac{\phi_z}{p_i}$  calculations based on several simple entry-plane flow models, but selection of any one of these models would introduce ambiguity which is not acceptable for the intended purpose of deriving "upper bound" RHT performance characteristics.

However, one unambiguous stipulation is available which has not yet been applied: namely, that the flow from plane I to plane II not violate the second law of thermodynamics. Noting the uniformity of the entropy at plane II, this may be expressed as

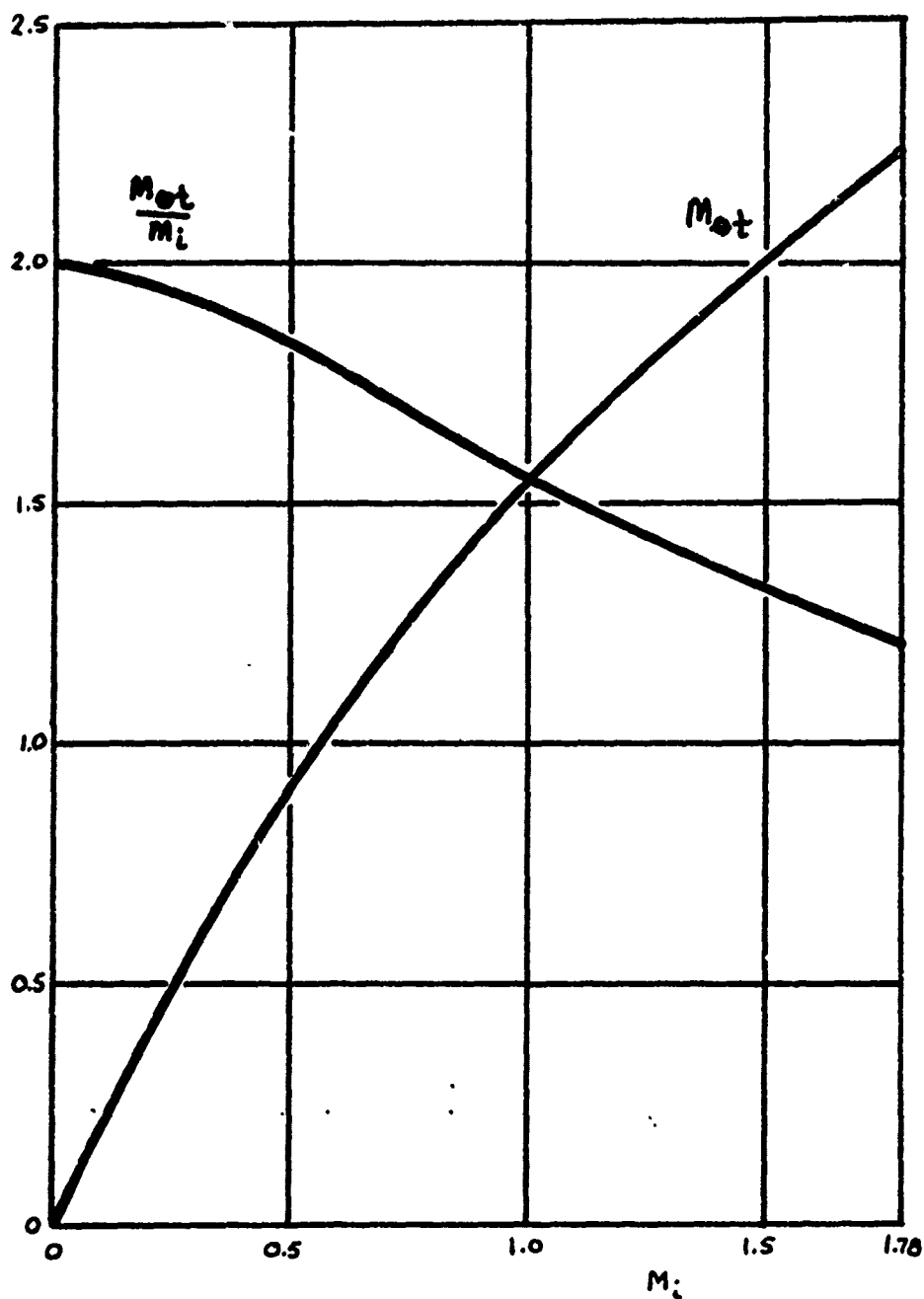


**Figure 13**  
Dependence of Terminal Vortex Wall Tangential  
Mach Number on Injection Mach Number

$$s_{II}(\tilde{r}) - s_i \geq 0 \quad (43)$$

where  $\tilde{r}$  may be chosen arbitrarily between 0 and 1. The entropy change may be written in terms of stagnation quantities as

$$s_{II}(\tilde{r}) - s_i = c_p \ln \frac{T_{II}^o(\tilde{r})}{T_i^o} - R \ln \frac{p_{II}^o(\tilde{r})}{p_i^o} \quad (44)$$

A particularly convenient value of  $\tilde{r}$  for the present purpose, and one having further significance as well, is what will be termed the "nominal" radius  $\tilde{r}_0$ , defined by:

$$T_{II}^o(\tilde{r}_0) \equiv T_i^o \quad (45)$$

The total temperature in the terminal plane is everywhere less than  $T_i^o$  for  $\tilde{r} < \tilde{r}_0$  and greater than  $T_i^o$  for  $\tilde{r} > \tilde{r}_0$ . With the choice of  $\tilde{r} = \tilde{r}_0$ , the first term in (44) vanishes, and the entropy increment is a function of the total pressure ratio  $\frac{p_{II}^o(\tilde{r}_0)}{p_i^o}$  only.

The most favorable assumption, of course, is that the internal flow between planes I and II is isentropic, i.e.,

$$s_{II}(\tilde{r}) - s_i = 0 \quad (43')$$

This gives

$$s_{II}(\tilde{r}_0) - s_i = 0 = -R \ln \frac{p_{II}^o(\tilde{r}_0)}{p_i^o}$$

or, as the thermodynamic limit condition:

$$\left( \frac{p_{\infty}^{\circ}(\tilde{r}_o)}{p_i^{\circ}} \right)_{\tau_L} = 1 \quad \begin{array}{l} \text{Thermodynamic} \\ \text{Limit} \\ \text{Condition} \end{array} \quad (46)$$

An alternative form of this condition is expressed in terms of the vortex stagnation pressure at the wall,

$$\left( \frac{p_t^{\circ}}{p_i^{\circ}} \right)_{\tau_L} = \frac{1}{(p_{\infty}^{\circ}(\tilde{r}_o)/p_t^{\circ})} \quad (46')$$

Since  $\tilde{r}_o$  is a function of  $M_{ot}$  only [or equivalently, of  $M_i$  by virtue of equation (35)], and since the total pressure distribution is also [equation (20')], it follows that  $\frac{p_{\infty}^{\circ}(\tilde{r}_o)}{p_t^{\circ}}$  and hence  $\left( \frac{p_t^{\circ}}{p_i^{\circ}} \right)_{\tau_L}$  is a function only of  $M_i$ . The expression for  $\tilde{r}_o$  is found by writing

$$\begin{aligned} \frac{T_{\infty}^{\circ}(\tilde{r}_o)}{T_i^{\circ}} &= 1 = \frac{T_{\infty}^{\circ}(\tilde{r}_o)}{T_t} \cdot \frac{T_t}{T_i^{\circ}} \\ &= \left[ 1 + \frac{\gamma-1}{2} M_{ot}^2 (2\tilde{r}_o^2 - 1) \right] \mathcal{F}_4 \end{aligned}$$

where use has been made of equations (18') and (37). Solving for  $\tilde{r}_o$  gives:

$$\tilde{r}_o = \sqrt{\frac{1}{2} \left[ 1 + \frac{2}{(\gamma-1) M_{ot}^2} \left( \frac{1}{\mathcal{F}_4 - 1} \right) \right]} \quad \begin{array}{l} \text{Nominal} \\ \text{Radius} \end{array} \quad (47)$$

Figure 14 provides a plot of  $\tilde{r}_o$  and  $\frac{p_{\infty}^{\circ}(\tilde{r}_o)}{p_t^{\circ}}$  as a function of  $M_i$ .

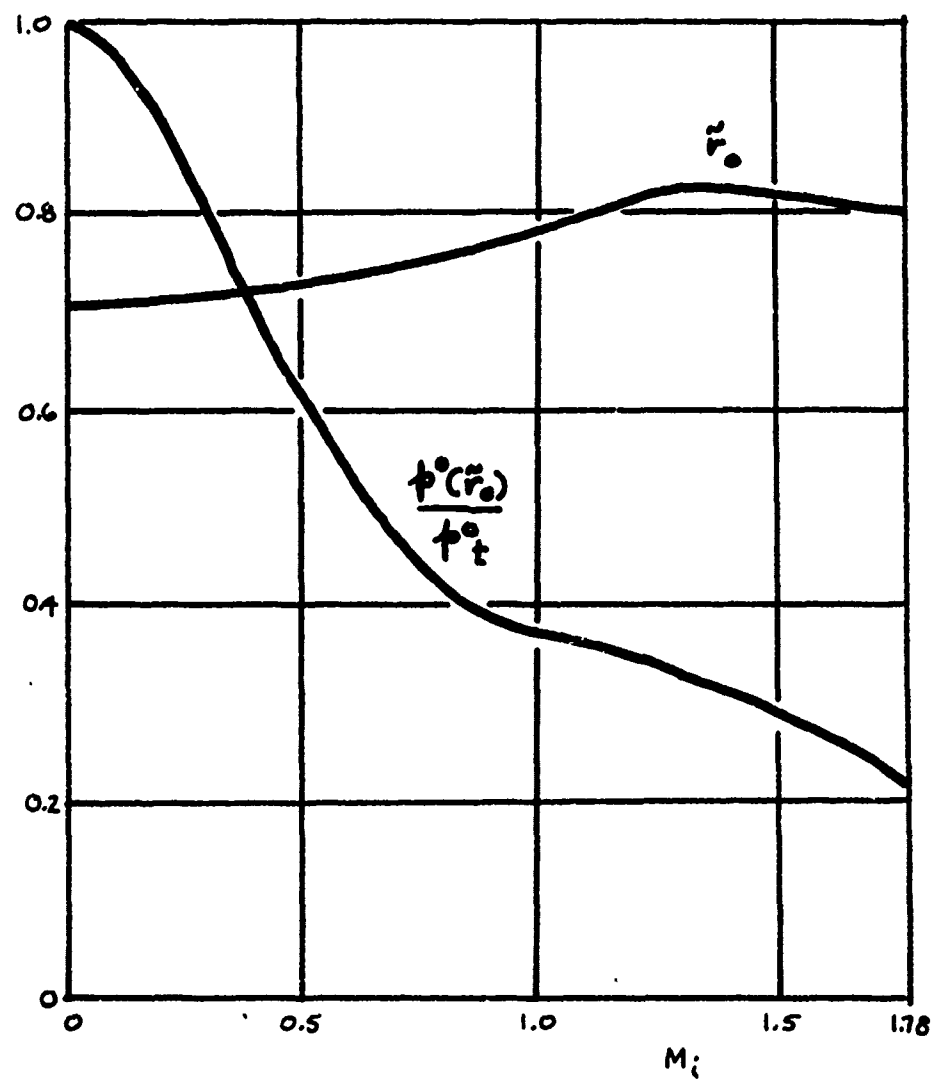


Figure 14  
Conditions at Nominal Radius



The thermodynamic upper bound on  $\frac{\phi_I}{p_i}$  may now be found as follows. From equation (41), one may write

$$\frac{p_{II}^o(\bar{r}_0)}{p_i^o} = \frac{p_{II}^o(\bar{r}_0)}{p_t^o} \cdot \frac{p_t^o}{p_t} \cdot \frac{p_t}{p_i^o}$$

The first two factors are functions only of  $M_{ot}$ , the first being obtained from (20'), and for the thermodynamic limiting case the left hand side is unity by equation (46). Denoting the product of the first two factors on the right by  $P(M_{ot})$ , then, one has

$$\left(\frac{p_t}{p_i^o}\right)_{TL} = \frac{1}{P(M_{ot})} \quad (48)$$

But from (38'),

$$\left(\frac{p_t}{p_i^o}\right)_{TL} = \frac{\sigma_2}{f_p(M_i) M_{ot} Q_2 \sigma_3} \left(\frac{\phi_I}{p_i}\right)_{TL}$$

which with (48) gives:

$$\left(\frac{\phi_I}{p_i}\right)_{TL} = \frac{f_p(M_i) M_{ot} Q_2 \sigma_3}{P(M_{ot}) \sigma_2} \quad (49)$$

This limiting value of  $\frac{\phi_I}{p_i}$  has been plotted as a function of  $M_i$  in Figure 10.

Figures 15 and 16 are presented to indicate the importance of the gap between the thermodynamic limit, equation (49), and model B, equation (48'); within the limitations of the present analytical model for the

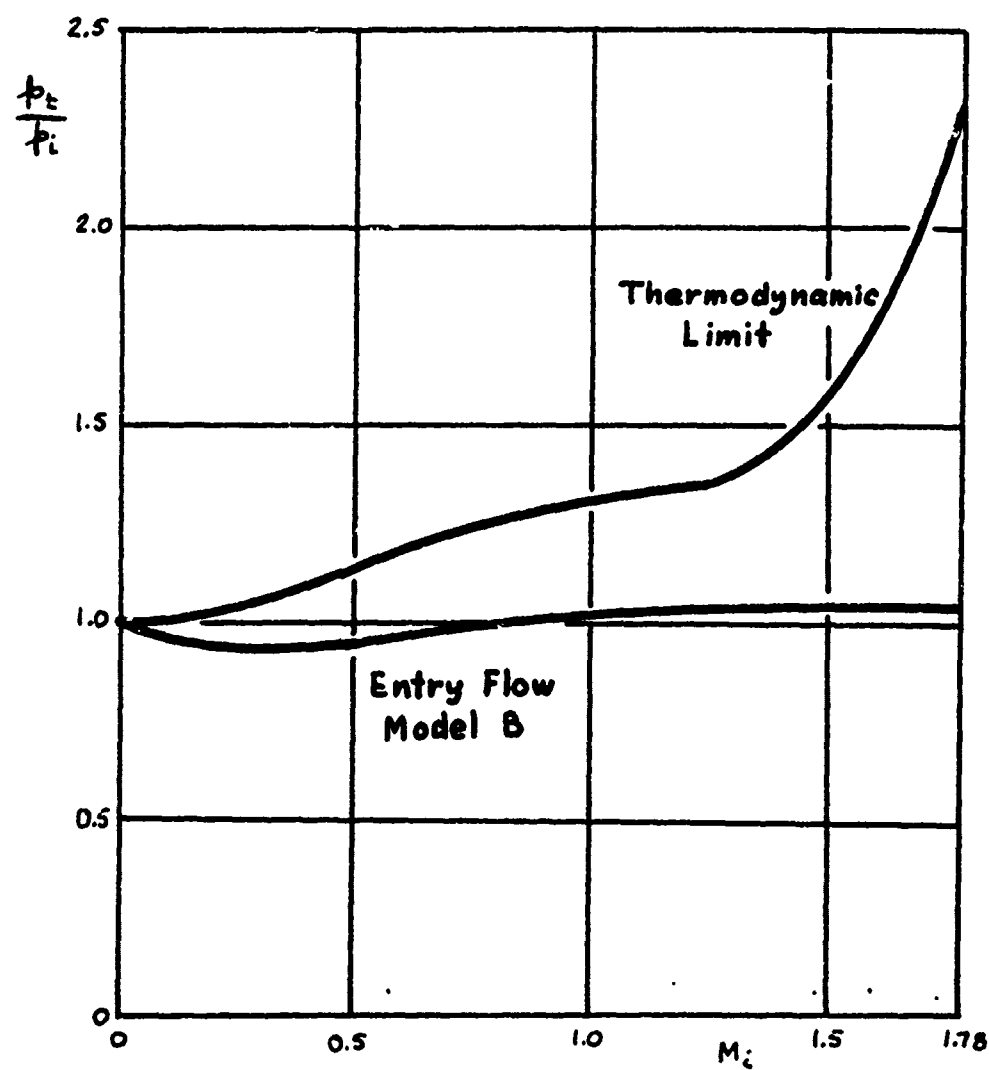


Figure 15  
Wall Static Pressure at Terminal Plane

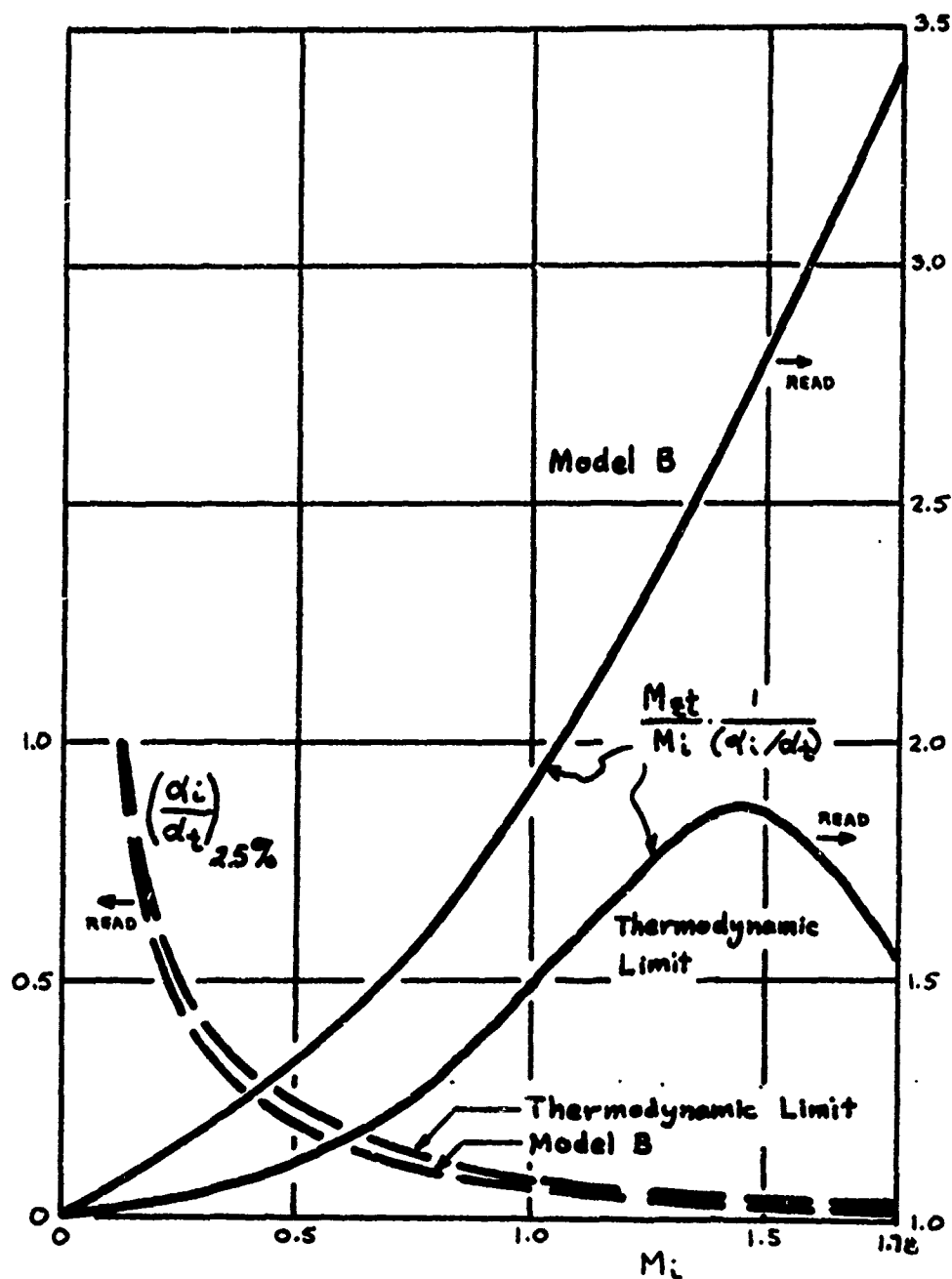


Figure 16  
Dependence of Terminal Axial Mach Number  
on Injection Mach Number

RHT, the actual solution should fall somewhere in this range. Figure 15 illustrates the effect on the wall static pressure: interestingly, if the inlet flow approximates model B (or model C, there being little effective difference on  $\frac{p_s}{p_i}$  as seen in Figure 10), the assumption by Hashem<sup>11</sup> of equal wall pressures at planes I and II is surprisingly good. However, if the centerline backflow is more vigorous, there is a significant rise in static pressure from I to II. Figure 16 shows the effect on the axial Mach number at the wall  $M_{at}$  based on equation (36'), and also indicates the ratio of nozzle to tube area for which the plotted values would underestimate  $M_{at}$  by 2.5%. It is seen that the difference between model B and the thermodynamic limit is considerable as regards the kinetic energy of axial motion at plane II, this kinetic energy acting to degrade RHT performance.

## 5. Output Flows and Losses

Tangential flow extraction. As depicted in the right-hand portion of Figure 8(b), the output flows are assumed to be obtained by dividing the terminal vortex into two concentric regions and extracting them tangentially through frictionless, constant-area ducts. The inner portion produces the "cold" flow and the outer annulus the "hot" flow, the boundary between them defining what will be termed the "split radius" and denoted nondimensionally as  $\tilde{r}_s$ . Referring to the discussion of Figure 7(b), it is clear that for a given  $M_i$  (hence  $M_{ot}$ ) both the energy separation and the cold fraction are determined by  $\tilde{r}_s$ .

The analysis of the RHT output flows will proceed in two steps. First, the "hot" and "cold" portions of the flow in plane II will be

characterized in terms of the controlling variables  $M_{ot}$  and  $\tilde{r}_s$ . Then, losses associated with removing and uniformizing the outputs will be calculated for the given flow extraction scheme. It is important to note, although it appears to have been largely ignored in the literature heretofore, that substantial exit losses are an inherent feature of RHT operation and can be expected to significantly influence overall performance. They are inherent because they spring from the nonuniformity of the flow generated within the vortex tube; and they influence performance by increasing the pressure ratio required at a given cold fraction to produce a terminal vortex having a specified value of  $M_{ot}$ .

In harmony with the "upper bound" orientation of the present study, the flow extraction scheme has been chosen to reflect what would probably be the practical ultimate in flow extraction techniques. Some other process, such as constant-pressure mixing, might theoretically be capable of somewhat better results, but could not be implemented without enormously greater understanding of the details of the uniformization process. Indeed, even the constant-area duct configuration as applied in the analysis below implies variable geometry, since the duct areas are always chosen to suit the amount of flow they are to pass. The contrast between this degree of flow process optimization and the normal (counterflow) practice of exhausting the swirling cold flow through an axially-directed orifice is considerable.

Output flow parameters at plane II. Appropriate mean values for the total temperature and total pressure are needed as functions of  $M_{ot}$  and  $\tilde{r}_s$  in order to characterize the "hot" and "cold" portions of the flow in plane II. Let "C" refer to the cold flow, "H" to the hot

flow, and "j" to a generalized flow which lies between any two normalized radii  $\tilde{r}_{1j}$  and  $\tilde{r}_{2j}$ ; it will be convenient to develop many of the equations which follow for the generalized flow "j" and then specialize them to "C" and "H".

Considering total temperatures first, one may write the mass-average total temperature

$$\bar{T}_j^{\circ} = \frac{\dot{M}_j^{\circ}}{c_p \dot{m}_j} = \frac{(\dot{M}_j^{\circ} / \dot{M}_{II}^{\circ})}{(\dot{m}_j / \dot{m}_{II})} \frac{\dot{M}_{II}^{\circ}}{\dot{m}_{II} c_p}$$

where capital script symbols refer to the total flux of the given quantity through the subscripted area--"II" referring to the entire tube cross-sectional area at II, "j" to that portion of it pertaining to the output flow in question. Noting that

$$\frac{\dot{M}_{II}^{\circ}}{\dot{m}_{II} c_p} = T_i^{\circ}$$

one has

$$\frac{\bar{T}_j^{\circ}}{T_i^{\circ}} = \frac{\dot{M}_j^{\circ} / \dot{M}_{II}^{\circ}}{\dot{m}_j / \dot{m}_{II}}$$

For the cold flow ( $j = C$ ), noting that  $\dot{m}_C / \dot{m}_{II} = CF$ , this gives

$$\frac{\bar{T}_C^{\circ}}{T_i^{\circ}} = \frac{\dot{M}_C^{\circ} / \dot{M}_{II}^{\circ}}{CF} \quad (50C)$$

while for the hot flow ( $j = H$ ), one has

$$\frac{\bar{T}_H^o}{T_i^o} = \frac{1 - (\dot{M}_c^o / \dot{M}_H^o)}{1 - CF} \quad (50H)$$

Noting that  $\mathfrak{A}_{II}(\bar{r}) = \text{constant}$  by assumption, the overall total pressure level of each flow may conveniently be characterized by an "isentropic average" defined thus:

$$\left( \frac{\bar{p}_j^o}{p_t^o} \right)_{II} = \left( \frac{\bar{T}_j^o}{T_t^o} \right)^{\frac{\gamma}{\gamma-1}} \quad (51)$$

Physically, this is the total pressure the given flow would have if brought isentropically to a uniform state from its nonuniform condition in plane II. Rewriting,

$$\left( \frac{\bar{p}_j^o}{p_t^o} \right)_{II} = \left( \frac{\bar{T}_j^o / T_i^o}{T_t^o / T_i^o} \right)^{\frac{\gamma}{\gamma-1}}$$

Using (37) with (40) and setting  $\bar{r} = 1$  gives

$$\frac{T_t^o}{T_i^o} = \left( 1 + \frac{\gamma-1}{2} M_{ot}^2 \right) \gamma_+ \quad (52)$$

One therefore has for the cold and hot flows respectively

$$\left( \frac{\bar{p}_c^o}{p_t^o} \right)_{II} = \left( \frac{\bar{T}_c^o / T_i^o}{T_t^o / T_i^o} \right)^{\frac{\gamma}{\gamma-1}} \quad (51C)$$

$$\left( \frac{\bar{p}_H^o}{p_t^o} \right)_{II} = \left( \frac{\bar{T}_H^o / T_i^o}{T_t^o / T_i^o} \right)^{\frac{\gamma}{\gamma-1}} \quad (51H)$$

where the needed total temperature ratios are given by (50C), (50H), and (52).

Examining the above equations, it may be seen that CF and  $(\mathcal{H}_c^\circ/\mathcal{H}_t^\circ)$  are needed as functions of  $M_{0t}$  and  $\tilde{r}_3$  to enable the output flows at plane II to be fully characterized. Returning to the development of equation (22), which gives the total massflow through plane II, it is easily seen that a parallel development for the "cold" portion of this massflow yields

$$\dot{m}_c = \sqrt{\frac{\gamma}{R}} \frac{p_t}{\sqrt{T_t}} M_{0t} \alpha_t g_m(\tilde{r}_3) \quad (53)$$

where  $g_m(\tilde{r}_3)$  is the cold mass-flux integral, defined as

$$g_m(\tilde{r}_3) \equiv \int_0^{\tilde{r}_3} \left( \frac{\rho(\tilde{r})}{\rho_t} \right)_{II} 2\tilde{r} d\tilde{r}$$

Similarly, the "cold" total enthalpy flow is obtained in parallel with (24) as

$$\dot{\mathcal{H}}_c^\circ = \dot{m}_{II} c_p T_t g_H(\tilde{r}_3) \quad (54)$$

where  $g_H(\tilde{r}_3)$  is the cold energy-flux integral, defined as

$$g_H(\tilde{r}_3) \equiv \int_0^{\tilde{r}_3} \left( \frac{T^\circ(\tilde{r})}{T_t} \right)_{II} \left( \frac{\rho(\tilde{r})}{\rho_t} \right)_{II} 2\tilde{r} d\tilde{r}$$

Using (53) and (22),



$$CF = \frac{\dot{m}_c}{\dot{m}_H} = \frac{g_m(\tilde{r}_3)}{Q_m} \quad (55)$$

while with (54) and (24),

$$\frac{\dot{M}_c^0}{\dot{M}_H^0} = \frac{g_M(\tilde{r}_3)}{Q_M} \quad (56)$$

All of the flux integrals in (55) and (56) are of course functions of  $M_{ot}$ , but only the additional dependence of the cold flux integrals on  $\tilde{r}_3$  is emphasized in the notation.

The cold flux integrals may be evaluated with the aid of distribution equations (17) and either (18) or (18'), (18') being appropriate for the present small-  $M_{ot}$  treatment. Defining

$$Y \equiv 1 - \frac{\gamma-1}{2} M_{ot}^2$$

as before and

$$y \equiv \frac{\gamma-1}{2} M_{ot}^2 (1 - \tilde{r}_3^2)$$

equations (55) and (56) then become

$$CF = \frac{(1-y)^{\frac{\gamma}{\gamma-1}} - Y^{\frac{\gamma}{\gamma-1}}}{1 - Y^{\frac{\gamma}{\gamma-1}}} \quad (55')$$

and

$$\frac{\dot{N}_c^o}{\dot{N}_\Pi^o} = \frac{\frac{2\gamma}{2\gamma-1} \left[ (1-\gamma)^{\frac{2\gamma-1}{\gamma-1}} - \gamma^{\frac{2\gamma-1}{\gamma-1}} \right] - \gamma \left[ (1-\gamma)^{\frac{\gamma}{\gamma-1}} - \gamma^{\frac{\gamma}{\gamma-1}} \right]}{\frac{2\gamma}{2\gamma-1} \left[ 1 - \gamma^{\frac{2\gamma-1}{\gamma-1}} \right] - \gamma \left[ 1 - \gamma^{\frac{\gamma}{\gamma-1}} \right]} \quad (56')$$

CF and  $\dot{N}_c^o/\dot{N}_\Pi^o$  are plotted against  $\tilde{r}_s^2$  (normalized cold flow area at plane II) for various values of  $M_{ot}$  in Figures 17 and 18 respectively. As  $M_{ot}$  tends to zero, both curves become linear because the density and total temperature become uniform; as  $M_{ot}$  increases, both curves bow out in the direction of increasing radius. In Figure 17, this is strictly an effect of compressibility, centrifugal force causing density to increase with radius. In Figure 18, the curves reflect both this tendency of mass to concentrate in the outer regions of the vortex and the radial migration of energy which has occurred from inner to outer layers of mass.

Noting the qualitative similarity of the curves in Figure 17 and 18, it is reasonable to question whether perhaps the compressibility effect largely washes out when the area variable  $\tilde{r}_s^2$  is eliminated in favor of CF, the variable of experimental interest. This question would seem particularly pertinent in light of the fact that it is not uncommon to carry out RHT analyses on an incompressible basis (see, e.g., Kassner and Knoernschild,<sup>18</sup> Lay<sup>17</sup> as regards performance-related items, Sibulkin,<sup>25</sup> and Linderstrom-Lang<sup>28</sup>). As one means of assessing this, the characteristics of an incompressible forced vortex were considered for comparison with those of the compressible vortex considered in the overall analysis. The incompressible analysis will not be repeated here, as it parallels

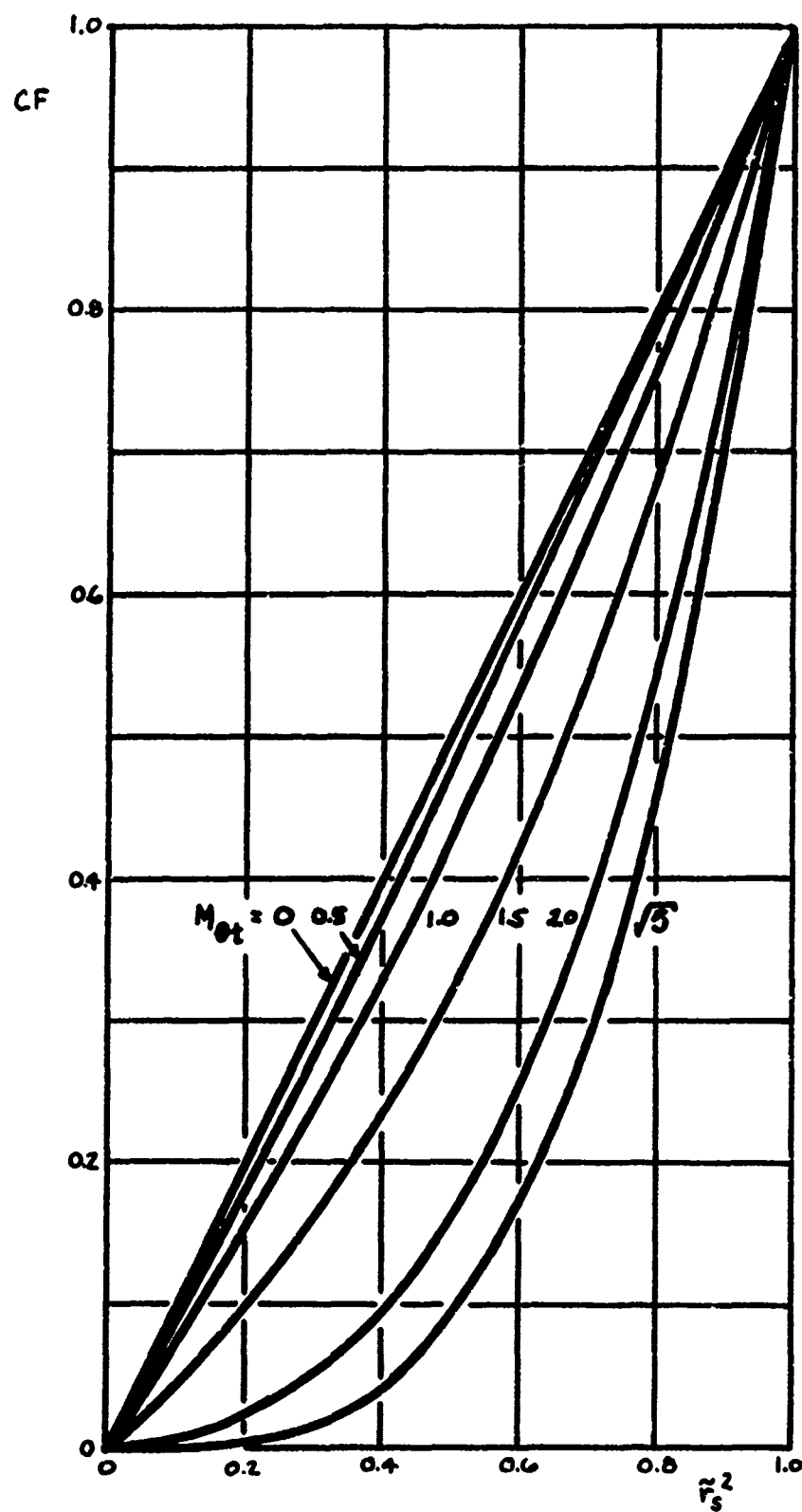


Figure 17  
Cold Fraction versus Terminal-Plane Cold Flow Area

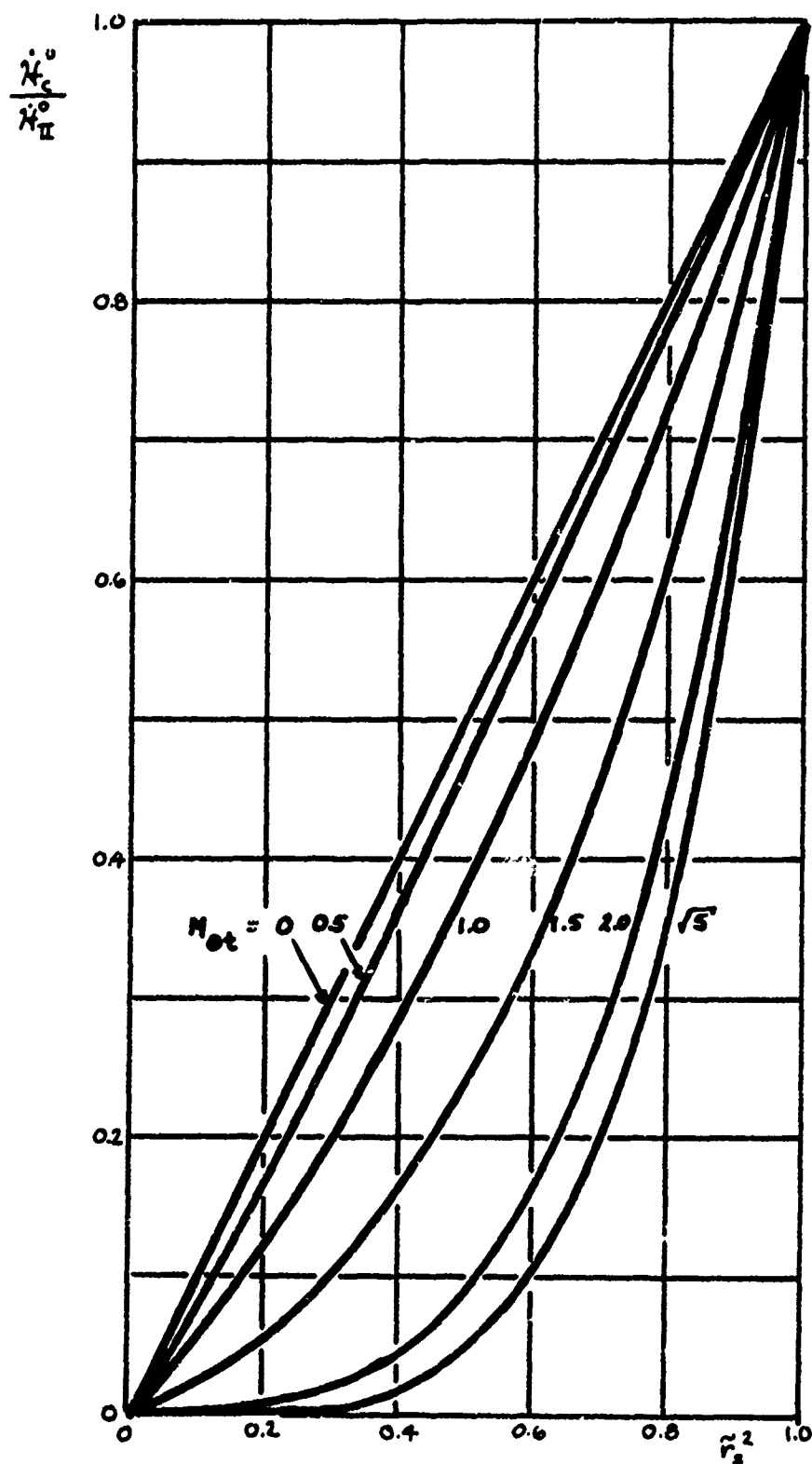


Figure 18  
Terminal-Plane Cold-Flow Energy Content versus Flow Area

the compressible analysis conceptually. However, some observations it afforded will be mentioned here; the overall comment to be made is that while incompressible treatment of the RHT can indeed yield insights into its operation, it can also lead the analyst into significant errors.

i) One cannot simultaneously specify uniform density and uniform entropy in the forced vortex: the first gives  $T(r) \sim p(r)$ , the second  $T(r) \sim p(r)^{\frac{\gamma-1}{\gamma}}$ . The former is simply an approximation, and is imposed for analytical convenience; the latter, however, is an analytical means of reflecting an important and well established feature of vortex tube flow--i.e., its turbulence.

ii) The quantitative errors in performance estimation induced by the constant-density assumption for the forced vortex grow rapidly with pressure ratio. For example, the centerline pressure of the forced vortex goes to zero when  $M_{0t} \approx 1.2$ ; the value from the compressible analysis is  $\sqrt{5}$ . Furthermore, the radial gradient of entropy in the incompressible vortex is positive, so that the entropy of the cold flow is underestimated relative to the compressible case. It should be noted in this regard that  $s_{\text{max}}(r) = \text{constant}$  is no doubt generous itself, in that the innermost core is probably laminar and suffers more from inward heat conduction than is assumed; the constant density assumption thus pushes the analysis further away from physical reality.

Continuing now with the compressible analysis, equations (55') and (56') enable the output total temperature and total pressure parameters at plane II to be calculated by means of equations (50C,H) and (51C,H). In particular, a cross-plot of energy separation performance-- $\bar{T}_c^0/T_i$  and  $\bar{T}_H^0/T_i$ --versus CF may be generated for each value of  $M_{0t}$

represented in Figures 17 and 18, and this is done in Figure 19. A gross similarity between Figure 19 and typical RHT performance plots may be noted, as well as substantial differences; however, it must be kept in mind that the curves of Figure 19 are for constant  $M_{ot}$  rather than for constant pressure ratio.

Exit losses. Consider the extraction of the generalized flow "j" defined earlier. Neglecting the influence of axial velocity, which has been assumed small, only the velocity component in the plane normal to the tube axis will be accounted for in calculating losses incurred by the tangential extraction scheme of Figure 8(b). The equations developed in Foa,<sup>31</sup> Chapter 7, for flow uniformization in a constant-area frictionless duct will be used for this purpose. Adapting the notation therein as needed for the present purpose, define:

$p_{ej}$  = static pressure at exit of duct "j"

$M_{ej}$  = Mach number of uniform flow at exit of duct "j"

$\alpha_j$  = cross-sectional area of duct "j"

$\Phi_{\theta j}$  = stream force of output flow "j" in direction of exit duct axis

$\dot{m}_j$  = total massflow through duct "j"

$\epsilon_j$  = mean total enthalpy per unit mass of flow "j"

and

$$\xi_j \equiv \sqrt{1 - 2 \frac{\gamma^2 - 1}{\gamma^2} \frac{\dot{m}_j^2 \epsilon_j}{\Phi_{\theta j}^2}} \quad (57)$$

The losses incurred by flow "j" due to uniformizing are reflected in the total pressure recovery factor  $\frac{p_{\theta j}^0}{p_{\pi j}^0}$ :

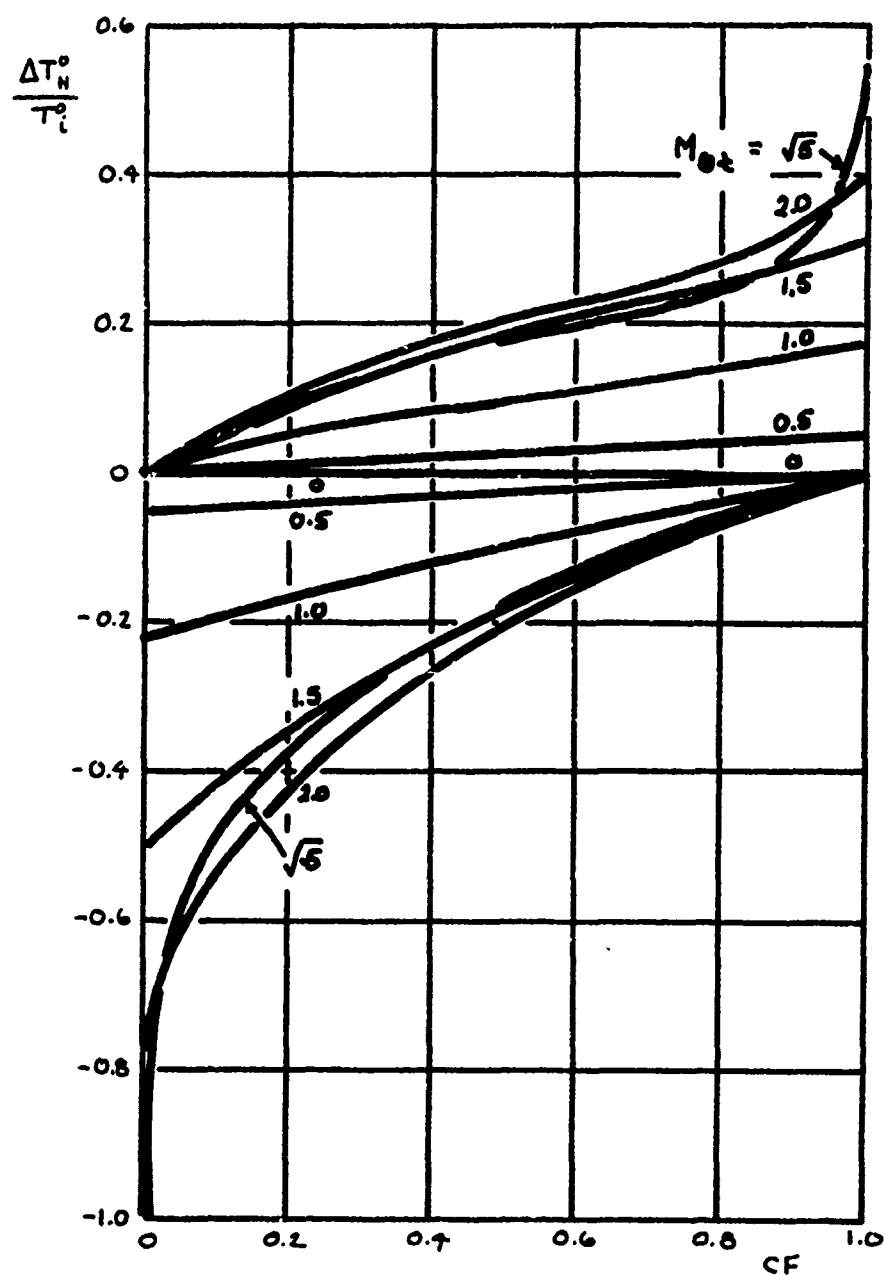


Figure 19  
Constant- $M_{\theta t}$  Energy Separation Curves

$$\frac{p_{ej}^0}{P_{\pi j}^0} = \frac{p_{ej}^0}{p_t} \cdot \frac{p_t}{p_t^0} \cdot \frac{p_t^0}{P_{\pi j}^0} \quad (58)$$

where the first factor reflects the uniformization process, the second is just a function of  $M_{ot}$ , and the third is obtained in inverted form from equation (51C) or (51H). The first factor may be written as

$$\begin{aligned} \frac{p_{ej}^0}{p_t} &= \left( \frac{p^0}{p} \right)_{ej} \frac{p_{ej}}{p_t} \\ &= \left( 1 + \frac{\gamma-1}{2} M_{ej}^2 \right)^{\frac{\gamma}{\gamma-1}} \frac{p_{ej}}{p_t} \end{aligned}$$

From Foa, one has

$$p_{ej} = \frac{\Phi_{ej}}{(\gamma+1)\alpha_j} (1 + \gamma \beta_j)$$

$$M_{ej}^2 = \frac{1 \pm \beta_j}{1 + \gamma \beta_j}$$

with which one obtains

$$\frac{p_{ej}^0}{p_t} = \frac{\Phi_{ej}}{p_t \alpha_j} \frac{1 + \gamma \beta_j}{\gamma + 1} \left[ 1 + \frac{\gamma-1}{2} \frac{1 \pm \beta_j}{1 + \gamma \beta_j} \right]^{\frac{\gamma}{\gamma-1}} \quad (59)$$

As may be seen by inspection of (57) and (59), and as would be expected physically, the magnitude of the exit loss incurred for a terminal vortex of given  $M_{ot}$  depends on whether the flow is extracted



from inner or outer layers of the vortex and on the fraction of the total vortex massflow being extracted. To find  $\alpha_j$ , consider an annular element of the vortex at radius  $r$  and of height  $dr$ , which must leave via an exit-duct area element of height  $dr$  and width  $w_j(r)$ . The flow through the annular area element is

$$d\dot{m}_{\Pi}(r) = \rho_{\Pi}(r) v_z 2\pi r dr$$

while that through the duct area element is

$$d\dot{m}_j(r) = \rho_{\Pi}(r) v_{\theta}(r) w_j(r) dr$$

Equating the two elemental massflows gives for the duct width

$$w_j(r) = \frac{v_z}{v_{\theta}(r)} 2\pi r$$

But, by virtue of the solid-body rotation of the forced vortex,

$$v_{\theta}(r) = \frac{r}{r_t} v_{\theta t}$$

which leads, with the aid of the definitions of  $M_{\theta t}$  and  $M_{zt}$ , to

$$w_j(r) = \frac{M_{zt}}{M_{\theta t}} 2\pi r_t$$

or, normalizing:

$$\tilde{w}_j \equiv \frac{w_j}{r_t} = 2\pi \frac{M_{zt}}{M_{\theta t}} \quad (60)$$

and the duct area for flow "j" is

$$\alpha_j = \tilde{w}_j (\tilde{r}_{2j} - \tilde{r}_{1j}) r_t^2 \quad (61)$$

Equation (60) shows that the exit duct width is independent of radius--that is, that it should be rectangular in shape--for the present model wherein the axial velocity is uniform. One may also note that a given duct width is only correct at one value of  $M_{\theta t}$  (or equivalently,  $M_i$ ). Thus, a given choice of exit port sizes defined by  $\tilde{r}_j$  and  $\tilde{\omega}_j$  corresponds to a specific CF at a particular pressure ratio. This implies that operation of a given, fixed geometry at any other pressure ratio or CF (e.g., by constricting the hot exit flow with a valve) constitutes "off design" operation.

The stream force  $\Phi_{\theta j}$  is also needed:

$$\Phi_{\theta j} = \int_{r_{ij}}^{r_{2j}} p(r) d\alpha_j(r) [1 + \gamma M_{\theta}^2(r)]$$

or, in terms of the terminal vortex distributions and normalized radii:

$$\frac{\Phi_{\theta j}}{p_t \alpha_j} = \frac{1}{\tilde{r}_{2j} - \tilde{r}_{1j}} \int_{\tilde{r}_{1j}}^{\tilde{r}_{2j}} \left( \frac{p(\tilde{r})}{p_t} \right)_{\Pi} \left[ 1 + \gamma M_{\theta t}^2 \left( \frac{M_{\theta}(\tilde{r})}{M_{\theta t}} \right)_{\Pi}^2 \right] d\tilde{r} \quad (62)$$

where the distributions of equations (16) and (21) are used to evaluate the integral in (62). Specializing "j" to "C" and "H" in (62), plots of  $\frac{\Phi_{\theta C}}{p_t \alpha_C}$  and  $\frac{\Phi_{\theta H}}{p_t \alpha_H}$  respectively are generated and plotted in Figures 20(a) and 20(b). Note that the plots in this case are against  $\tilde{r}_j$  rather than  $\tilde{r}_j^2$ , since exit-duct area is linear with radius.

Finally, the quantity  $\frac{\pi_j^2 \epsilon_j}{\Phi_{\theta j}}$  is needed in order to evaluate  $\mathcal{F}_j$ , given by (57). Writing

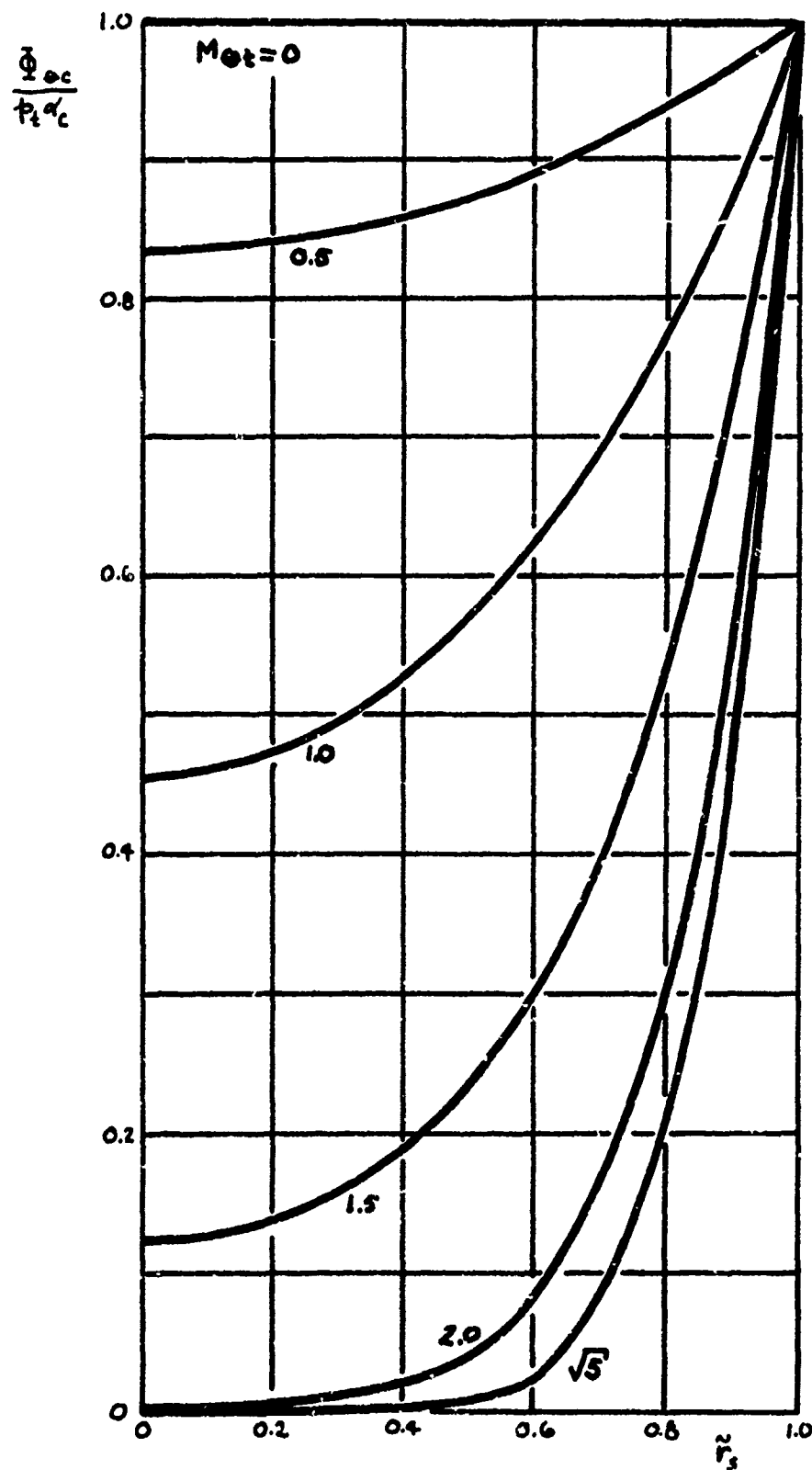


Figure 20(a)  
Cold Flow Tangential Stream Force

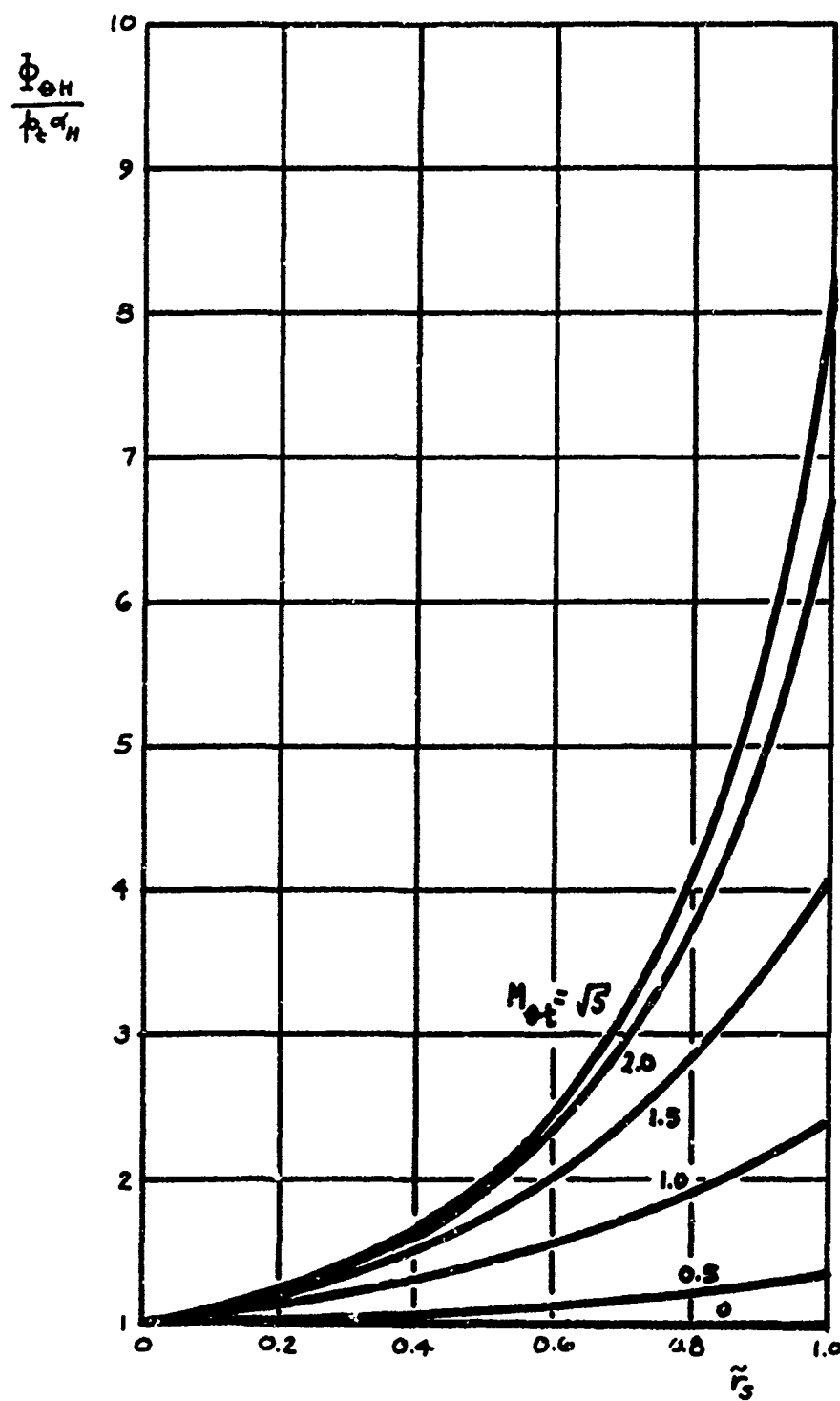


Figure 20(b)  
Hot Flow Tangential Stream Force

$$\begin{aligned} \dot{m}_j^2 &= \left( \frac{\dot{m}_j}{\dot{m}_\Sigma} \right)^2 \dot{m}_\Sigma^2 \\ &= \left( \frac{\dot{m}_j}{\dot{m}_\Sigma} \right)^2 \frac{\gamma}{R} \frac{p_t^2}{T_t} M_{\Sigma t}^2 \alpha_t^2 Q_m^2 \end{aligned}$$

$$\begin{aligned} \epsilon_j &= \frac{\mathcal{H}_j^0}{\dot{m}_j} \\ &= c_p T_i^0 \left( \frac{\bar{T}_j^0}{T_i^0} \right) \end{aligned}$$

$$\Phi_{\Theta j}^2 = p_t^2 \alpha_j^2 \left( \frac{\Phi_{\Theta j}}{p_t \alpha_j} \right)^2$$

one has

$$\frac{\dot{m}_j^2 \epsilon_j}{\Phi_{\Theta j}^2} = \frac{\left( \frac{\dot{m}_j}{\dot{m}_\Sigma} \right)^2 \frac{\gamma}{R} \frac{p_t^2}{T_t} M_{\Sigma t}^2 \alpha_t^2 Q_m^2 c_p T_i^0 \left( \frac{\bar{T}_j^0}{T_i^0} \right)}{p_t^2 \alpha_j^2 \left( \frac{\Phi_{\Theta j}}{p_t \alpha_j} \right)^2} \quad (63)$$

Also, using  $\alpha_t = \pi r_t^2$  together with (60) and (61),

$$\left( \frac{\alpha_t}{\alpha_j} \right)^2 = \frac{M_{\Theta t}^2}{4 M_{\Sigma t}^2 (\tilde{r}_{2j} - \tilde{r}_{1j})^2}$$

which, upon substituting into (63) and simplifying, gives

$$\frac{\dot{m}_j^2 \epsilon_j}{\Phi_{\Theta j}^2} = \frac{\gamma^2}{4(\gamma-1)} \frac{M_{\Theta t}^2 Q_m^2}{(T_t/T_i^0)} \left\{ \frac{(\dot{m}_j/\dot{m}_\Sigma)}{(\tilde{r}_{2j} - \tilde{r}_{1j}) (\Phi_{\Theta j}/p_t \alpha_j)} \right\}^2 \left( \frac{\bar{T}_j^0}{T_i^0} \right) \quad (63')$$

The portion of (63') inside the bracket is a function of both  $M_{ot}$  and  $\tilde{r}_s$ , while the factor multiplying the bracket is a function of  $M_{ot}$  only. If the bracketed quantity is referred to as  $K_j$ , i.e.,

$$K_j = K_j(M_{ot}, \tilde{r}_s) \equiv \left[ \frac{\dot{m}_j / \dot{m}_{II}}{(\tilde{r}_{2j} - \tilde{r}_{1j})(\tilde{\phi}_{oj} / t_{t\alpha_j})} \right]^2 \left( \frac{\tilde{T}_1^o}{T_i^o} \right)$$

use of (63') in (57) yields

$$\xi_j = \sqrt{1 - \frac{\gamma+1}{2} \frac{M_{ot}^2 Q_{ot}^2}{(T_t / T_i^o)} K_j} \quad (64)$$

Use of equations (37), (50C,H), (55'), and (62)--the last two of which are plotted in Figures 17 and 20(a,b) respectively--enables  $\xi_j$  to be found from (64). Use of equation (59) with (62) and (64) then allows determination of the total pressure recovery ratio, equation (58), for either exit flow at any desired  $M_{ot}$  and  $\tilde{r}_s$ .

Comparison of internal and exit losses. The vortex tube takes what is initially a uniform flow and converts it into a nonuniform one--the forced vortex. The tangential exit ducts must undo this, returning each output flow back to a uniform condition. Therefore, it is reasonable to wonder if exit losses, even under the very favorable flow extraction conditions assumed analytically, might be of the same order as the internal losses. The internal losses will, of course, be neglected altogether in the "upper bound" performance calculations, but some estimate of the actual losses is of interest.

Consider the "nominal split" case, where  $\tilde{r}_s = \tilde{r}_o$ ,  $\tilde{r}_o$  being defined by equation (45). Also, consider only the subsonic solution

for exit flow conditions at each port. The total pressure recovery factor for each flow in this case is presented as a function of  $M_i$  in Figure 21, and it will be noted that for the "nominal split" case the exit losses are particularly severe for the cold flow. The contribution to the cold exit loss corresponding to the normal shock which differentiates the subsonic from the supersonic solution is indicated, and it is seen to be minor: most of the loss is solely attributable to the nonuniformity of the flow.

For comparison, the total pressure recovery factor  $\frac{p^0_{\pi}(\tilde{r}_0)}{p^0_i}$  which characterizes the internal flow [compare the thermodynamic limit condition, equation (46)] is presented as calculated on the basis of inlet flow model B, which will be recalled as the one which would give the most severe internal losses. It is seen that the exit flow losses for the cold flow are of the same order as the internal losses, and indeed exceed the internal flow losses at elevated values of  $M_i$  even for this severe inlet flow model. Since centerline backflow presumably reduces the magnitude of the internal losses below that shown in Figure 21, and since exit losses in typical RHT configurations can be expected to be worse than those in the present analytical model, it may be concluded that the dominant losses in the RHT are likely to be those incurred in output flow extraction.

#### 6. Theoretical "Upper Bound" RHT Performance

"Nominal split" case. The "nominal" radius  $\tilde{r}_0$ , as defined by equation (45), is that at which the total temperature in the terminal, forced vortex equals the total temperature of the flow injected at the

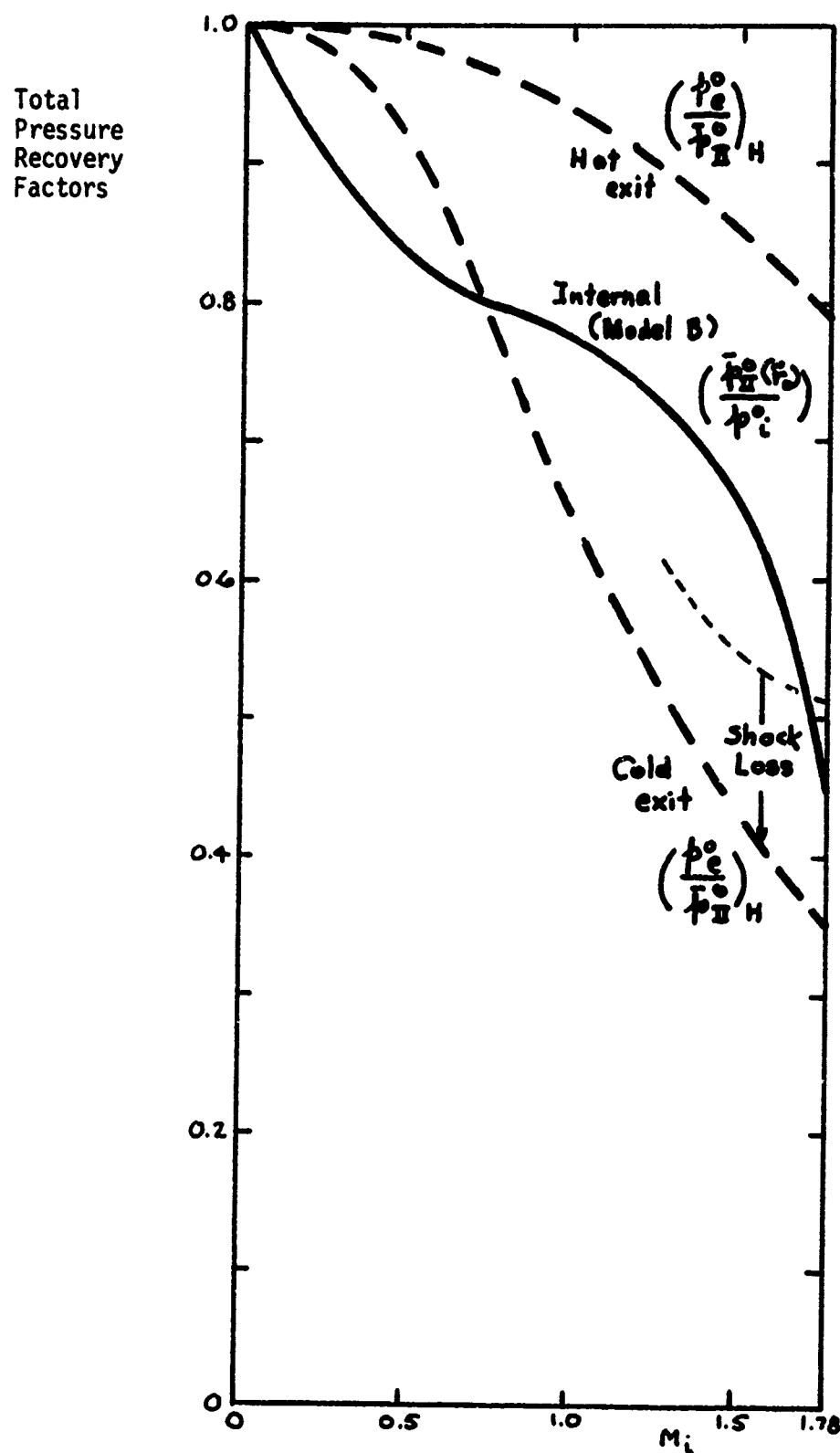


Figure 21  
Comparison of Internal and Exit Losses for "Nominal Split" Case



nozzle in plane 1. If the split radius  $\tilde{r}_s$  is chosen equal to  $\tilde{r}_o$ , the "nominal split" results wherein all portions of the vortex having a total temperature lower than that of the inlet exit via the "cold" port and all having a higher total temperature depart via the "hot" port. For a vortex having a given value of  $M_{ot}$ , this is the split which would give a maximum in refrigeration capacity.

It is instructive to examine the theoretical performance characteristics at nominal split and to compare them with experiment. Define now the "driving pressure ratio"

$$DPR \equiv \frac{p_i^o}{p_{ec}^o}$$

this being the pressure ratio referred to in experimental data such as that of Hilsch<sup>3</sup> (Figure 4). For the "upper bound" performance calculation, no exit losses beyond those incurred in output uniformization will be accounted for; in reality, some additional loss is a certainty even if the tangential flow-extraction ducts discharge into good subsonic diffusers, so here again is a strictly optimistic assumption. Then, for the "upper bound" calculations,

$$DPR_{ub} = \frac{p_i^o}{p_{ec}^o}$$

Now

$$DPR_{ub} = \frac{p_i^o}{p_x^o(r_o)} \cdot \frac{p_x^o(r_o)}{p_{xc}^o} \cdot \frac{p_{xc}^o}{p_{ec}^o} \quad (65)$$

where

$$\frac{p_i^o}{p_{ic}^o(\tilde{r}_o)} = 1$$

since internal losses are neglected in the "upper bound" analysis;

$$\frac{p_{ic}^o(\tilde{r}_o)}{p_{ic}^o} = \left( \frac{T_{ic}^o(\tilde{r}_o)}{T_{ic}^o} \right)^{\frac{\gamma}{\gamma-1}} = \left( \frac{T_i^o}{T_c^o} \right)^{\frac{\gamma}{\gamma-1}}$$

and the inverse of  $\frac{T_i^o}{T_c^o}$  is obtained from (50C); and the inverse of  $\frac{p_{ic}^o}{p_{ec}^o}$  is obtained from (58). Thus,  $DPR_{ub}$  may be found as a function of  $M_i$  for any given split radius  $\tilde{r}_s$ , and this is done for the "nominal split" case in Figure 22, both for the "upper bound" analysis and--for purposes of comparison--with inclusion of internal losses corresponding to inlet flow model B.

From equations (55C,H) with Figures 17 and 18 [obtained from equations (55') and (56')], energy separation performance in terms of hot- and cold-flow temperatures may be calculated as a function of  $M_i$  and  $\tilde{r}_s$ . This has been done for the "nominal split" case and these temperatures plotted against  $M_i$  along with CF in Figure 23.

Having generated Figure 23, it is a simple matter to crossplot energy separation versus cold fraction for the "nominal split" case, thereby generating Figure 24. The position on this "nominal split operating line" is a function of  $M_i$  or, by virtue of Figure 22,  $DPR_{ub}$  as indicated. Points corresponding to  $DPR_{ub} = 1.5, 3.0, 6.0$ , and 10 are noted, these being the pressure ratios in the Hilsch experimental data of Figure 4.

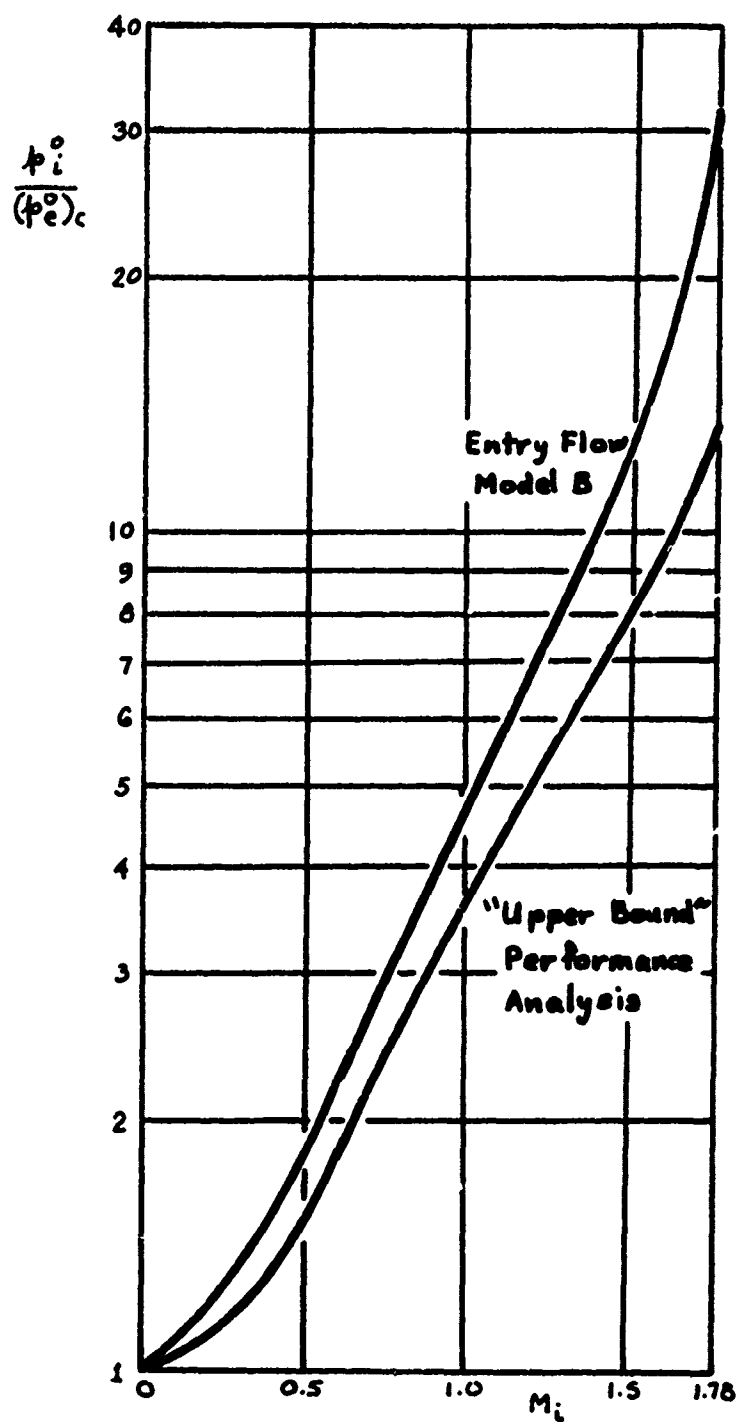


Figure 22  
Driving Pressure Ratio versus Injection Mach Number at "Nominal Split"

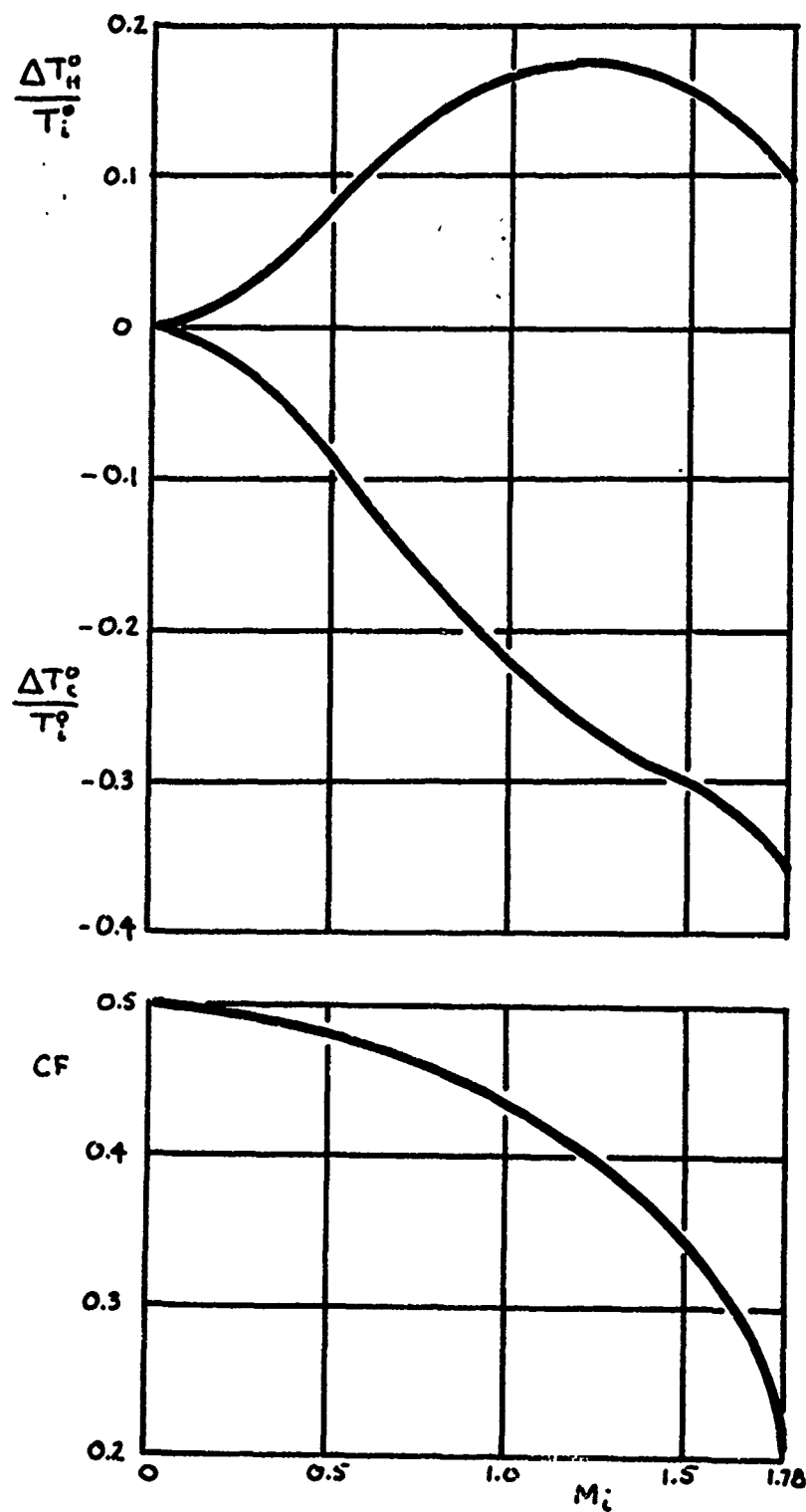


Figure 23  
"Nominal Split" Energy Separation and Cold Fraction Dependence on  $M_i$

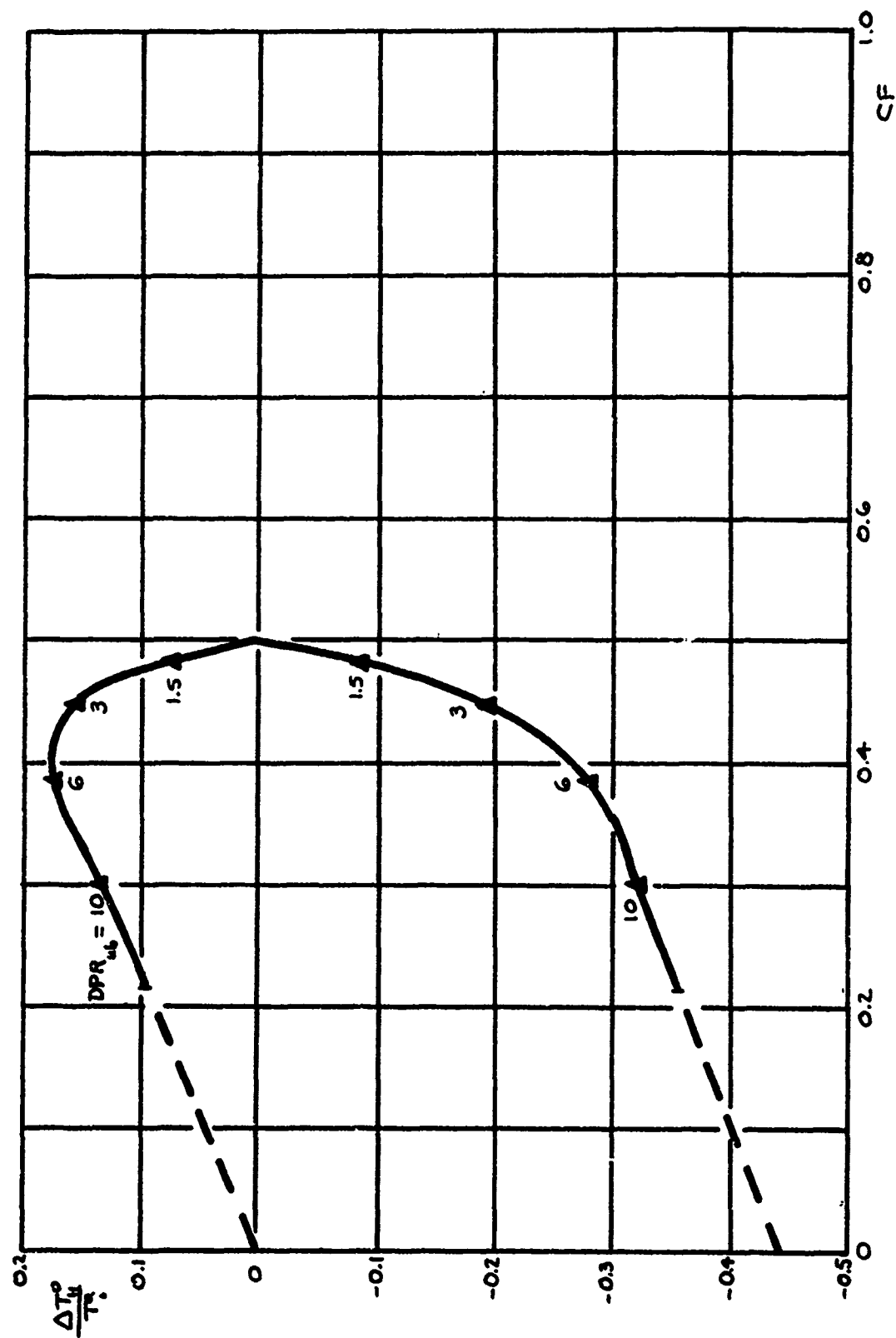


Figure 24  
Theoretical "Upper Bound" Performance at Nominal Split

It is worthy of note on the basis of Figure 24 that, as pressure ratio increases, a smaller and smaller share of the total massflow ends up at plane II with a total temperature below  $T_i^o$ , the inlet value. If one considers the effect of this on maximum refrigeration capacity, which corresponds to the maximum value of the product  $CF \cdot \frac{\Delta T_c^o}{T_i^o}$ , one notes that the "cold" branch of the operating line in Figure 24 is steep (CF dropping only slowly) up to a pressure ratio of around 6; in this region, the rapidly increasing magnitude of  $\frac{\Delta T_c^o}{T_i^o}$  with pressure ratio dominates and refrigeration capacity increases. At higher pressure ratios, however, the curve becomes shallow, the magnitude of  $\frac{\Delta T_c^o}{T_i^o}$  increasing only slowly with  $DPR_{ub}$  while CF drops rapidly. There must, therefore, come a point at which the maximum refrigeration capacity actually decreases with increasing pressure ratio, this despite the fact that the optimum temperature drop is becoming larger with pressure ratio.

Indeed, Figure 24 hints at the existence of an absolute bound on RHT energy separation performance, as was suggested first by Lewellen<sup>29</sup> from a different analytical perspective. Referring to Figure 7(a) and the accompanying discussion of qualitative RHT characteristics, note that after the two branches of the nominal split operating line in Figure 24 "turn the corner," so to speak, they are essentially linear for the remainder of the range of calculations. Furthermore, the upper branch appears to be aimed rather squarely at the origin. If one simply extends the upper branch to the origin as a straight line, then recalling the "linear" case discussed in Figure 7(a), the lower branch is extended parallel to it, and gives a value of  $\frac{\Delta T_c^o}{T_i^o}$  at  $CF = 0$  of about -0.44. This is a great deal larger than Lewellen's bound of -0.185; however, it will be recalled

that his bound was arrived at on the basis of a very abbreviated treatment which was basically rooted in a laminar vortex analysis, and also that his bound is in fact violated experimentally.

The writer must hasten to emphasize that any conclusions drawn from this extrapolation in Figure 24 must be regarded as strictly tentative and suggestive in nature, and that they must be interpreted cautiously. The "bound" found from the lower branch extrapolation is not quite equivalent in meaning to that of Lewellen: it corresponds to the point at which refrigeration capacity goes to zero rather than as a lower envelope below which  $\frac{\Delta T_c}{T_c}$  cannot dip regardless of CF or DPR. Further, the extrapolation in Figure 24 may be challenged on the ground that it extends into an operational regime which the writer has not directly explored analytically. However, the discussion of qualitative RHT performance characteristics is felt at least to lend sufficient plausibility to the matter to suggest, in context with Lewellen's independent conclusion on this score, that the question of an absolute bound on RHT performance deserves further attention.

One further point should be made regarding the meaning of the "nominal split" condition. It was stated earlier that this is the division which, for a forced vortex having a given value of  $M_{ot}$ , gives the maximum refrigeration capacity. However, it must be borne in mind that at a given DPR,  $M_{ot}$  is itself a function of the split radius  $\tilde{r}_s$ ,  $M_{ot}$  tending to increase as  $\tilde{r}_s$  increases. An increase in  $M_{ot}$  increases the overall energy separation existing in the vortex; therefore, although increasing  $\tilde{r}_s$  above the nominal value  $\tilde{r}_0$  will begin admitting some vortex fluid elements at a total temperature above  $T_i^0$ , this may be outweighed within some  $\tilde{r}_s$  range by the increased vigor of the vortex

and the concomitant lower mean temperature of the portion within  $\tilde{r}_0$ . Thus, while the trend in maximum refrigeration capacity should follow qualitatively the nominal split operating line in Figure 24, the actual values of CF involved would be expected to be somewhat larger.

Standard-format performance plot. The equations have been developed herein, together with auxiliary plots of certain key functions, so as to enable calculation of "upper bound" performance at any pressure ratio  $DPR_{ub}$  and any CF, provided the combination of these does not lead to a vortex having a value of  $M_{ot}$  outside the range over which calculations were performed. However, this is only carried out here to the extent of generating approximate curves for  $DPR_{ub} = 1.5, 3.0, 6.0$ , and  $10.0$ , these being the pressure ratios for the classical Hilsch data. The present analytical scheme is rather arduous in application, and therefore the approximate curves have been generated using only three values of CF per value of  $DPR_{ub}$ : the points obtained from the nominal split operating line, Figure 24, and the end points at  $CF = 0$  and  $1$ .

At  $CF = 1$ , the temperature drop is zero, as discussed in connection with Figure 7. As CF approaches zero, the nonuniformity of the cold flow tends to zero; also, since the kinetic energy becomes negligible at the center of the vortex, there is no occasion for shock losses. Therefore, the temperature drop calculated for  $CF = 0$  is that associated with isentropic expansion over the pressure ratio  $DPR_{ub}$ . Note here the optimism built into the analytical neglect of internal losses for "upper bound" purposes, since there is in fact an entropy rise from plane I to plane II and the isentropic temperature drop certainly cannot really be attained. Furthermore, it must be borne in mind that the cold exit port



is assumed always matched to the magnitude of the cold flow, which implies vanishing port size--yet without viscous exit losses--as CF goes to zero.

In sketching the curves, considerable aid is obtained from the fact that the points extracted from Figure 24 for the selected values of  $DPR_{ub}$  occur over a range of values of CF. Fairing the curves, Figure 25 is obtained. It doubtless contains minor deviations from the curves that would be obtained from a point-by-point application of the calculation scheme, but there is no reason to suspect such deviations to be of major significance as regards cold output performance. With regard to the hot output, however, it should be mentioned that for  $DPR_{ub} = 6$  and 10, the "upper bound" analysis leads to such a vigorous vortex that  $M_{ot}$  exceeds  $\sqrt{5}$ , the limit included in the calculations, at  $CF = 1$ . The hot-output curves are therefore sketched in with broken lines as being similar beyond the "nominal split" condition to the curves at lower pressure ratio, but could of course be in substantial error quantitatively.

### C. Comparison of "Upper Bound" Theory with Experiment

Nominal split. Figure 26 presents a comparison between theoretical "upper bound" performance along the nominal-split operating line and corresponding experimental performance according to Hilsch.<sup>3</sup> Points are indicated on the theoretical operating line at which  $DPR_{ub} = 1.5, 3.0, 6.0,$  and  $10.0$ , these being the pressure ratios for which Hilsch reported data as in Figure 4. The experimental points corresponding to a given pair of theoretical points are obtained by reading from the curve in Figure 4 at the given pressure ratio (say, 3.0) and at the value of CF read from the theoretical curve (0.45, for pressure ratio 3.0).

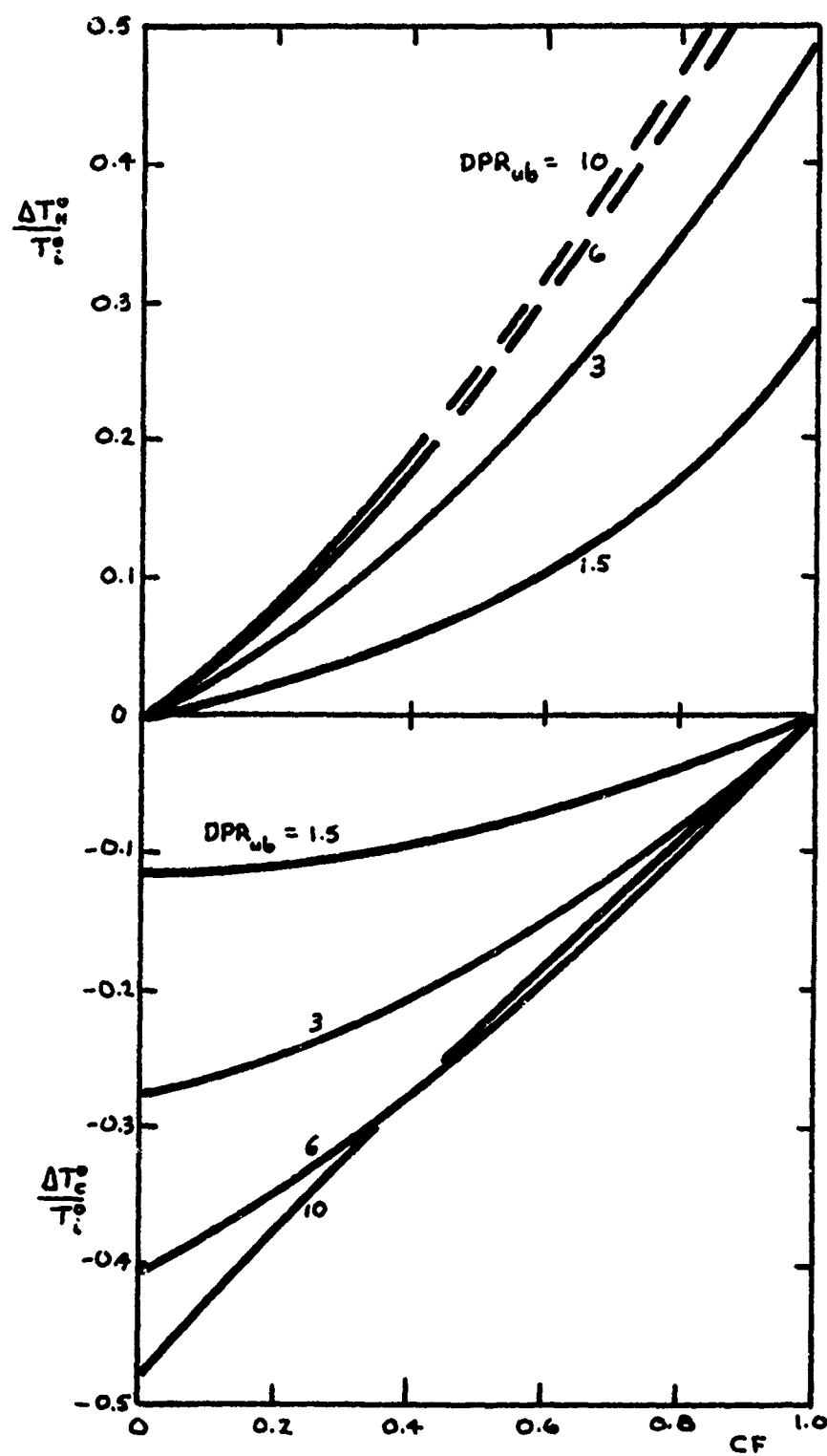


Figure 25  
Theoretical "Upper Bound" Performance

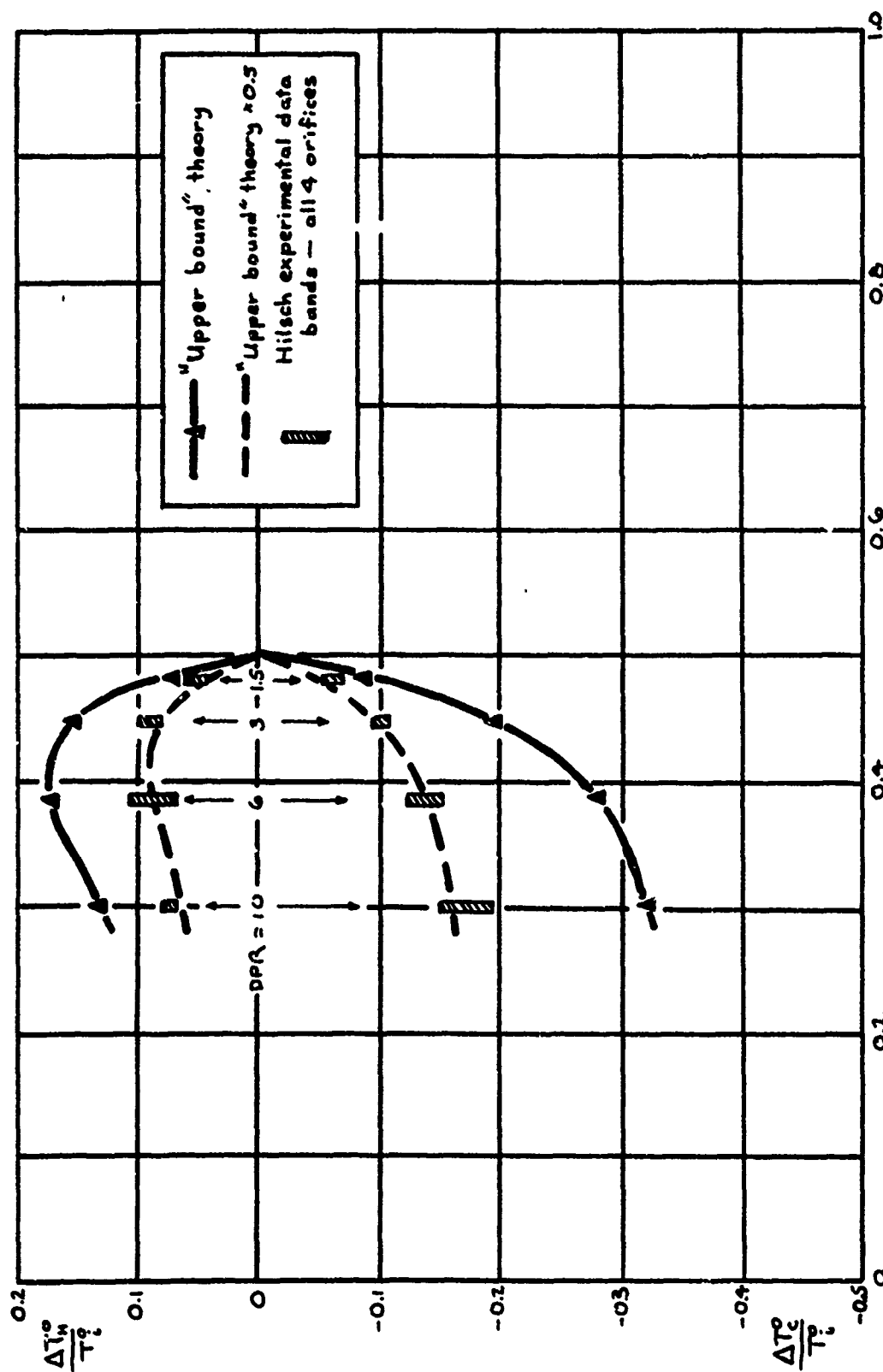


Figure 26  
Comparison of Theory and Experiment at Nominal Split

Figure 4 presents data obtained by Hilsch with what he considered to be the overall optimum orifice size tested, but he also presented similar curves obtained with one larger and two smaller orifices. The present theory contains an implication, mentioned earlier, that off-design performance effects will occur for any fixed geometry RHT, and of course these will depend on orifice size; however, these should be (and are, from a simple look at Hilsch's plots) of a secondary nature, and in any case all should be bracketed by the present theory. Therefore, readings were taken in the manner described above from all four sets of Hilsch data, leading to the data bands shown for each combination of DPR and CF in Figure 26.

It is seen that the "upper bound" nominal-split operating line does easily bracket the experimental data. In addition, experiment seems to support the physical mechanism of RHT operation assumed in the analysis, since the qualitative behavior of the nominal-split operating line is discernible in the experimental data as it should be. First, this is seen in Figure 26: the broken lines were obtained simply by multiplying the theoretical curve by 0.5, and it is seen that these lines constitute a rather good fairing of the Hilsch data. Second, the behavior of the "turbine criterion" efficiency as observed by Fulton<sup>14</sup> is entirely as would be expected theoretically, this efficiency being directly related to maximum refrigeration capacity. Fulton observed maximum turbine-criterion efficiencies based on the Hilsch data of 13% at  $DPR = 2.5$  and  $CF = 0.7$ , and 15% at  $DPR = 11$  and  $CF = 0.6$ . Thus, maximum refrigeration capacity occurs at CF values somewhat larger than the theoretical "nominal split" values, but with these CF values dropping with DPR; that this

should be expected theoretically was pointed out earlier. Also, refrigeration capacity increases with DPR, which is entirely to be expected within this moderate-pressure ratio range.

Overall performance. The analysis of RHT performance carried out herein has been structured so as to arrive at "upper bound" characteristics which would define the range within which RHT performance must fall as a function of the controlling variables, DPR (driving pressure ratio) and CF (cold fraction). No attempt has been made to define least upper bounds, as this would be a very much more formidable task; but at least bounds which are meaningful and not capable of violation have, it is believed, been arrived at.

It is of course extremely important to compare the "upper bound" RHT performance theory with the best known experimental results, so as to obtain an objective check on their success. To this end, Figure 27 presents a comparison of the predictions of the theory with experimental data from three different sources. The theoretical curves of Figure 25 are repeated in solid lines, while broken lines and diamonds pertain to experiment.

First, the Hilsch data of Figure 4 have been augmented by 15% to reflect approximately the gain in performance Hilsch observed with the largest of the tubes he tested, which had nearly four times the diameter of "Tube 1" used for the data of Figure 4. Comparing each experimental curve for a given pressure ratio (DPR) with the corresponding theoretical curve ( $DPR_{ub}$ ), it is seen that the Hilsch data are well within the theoretical bounds.

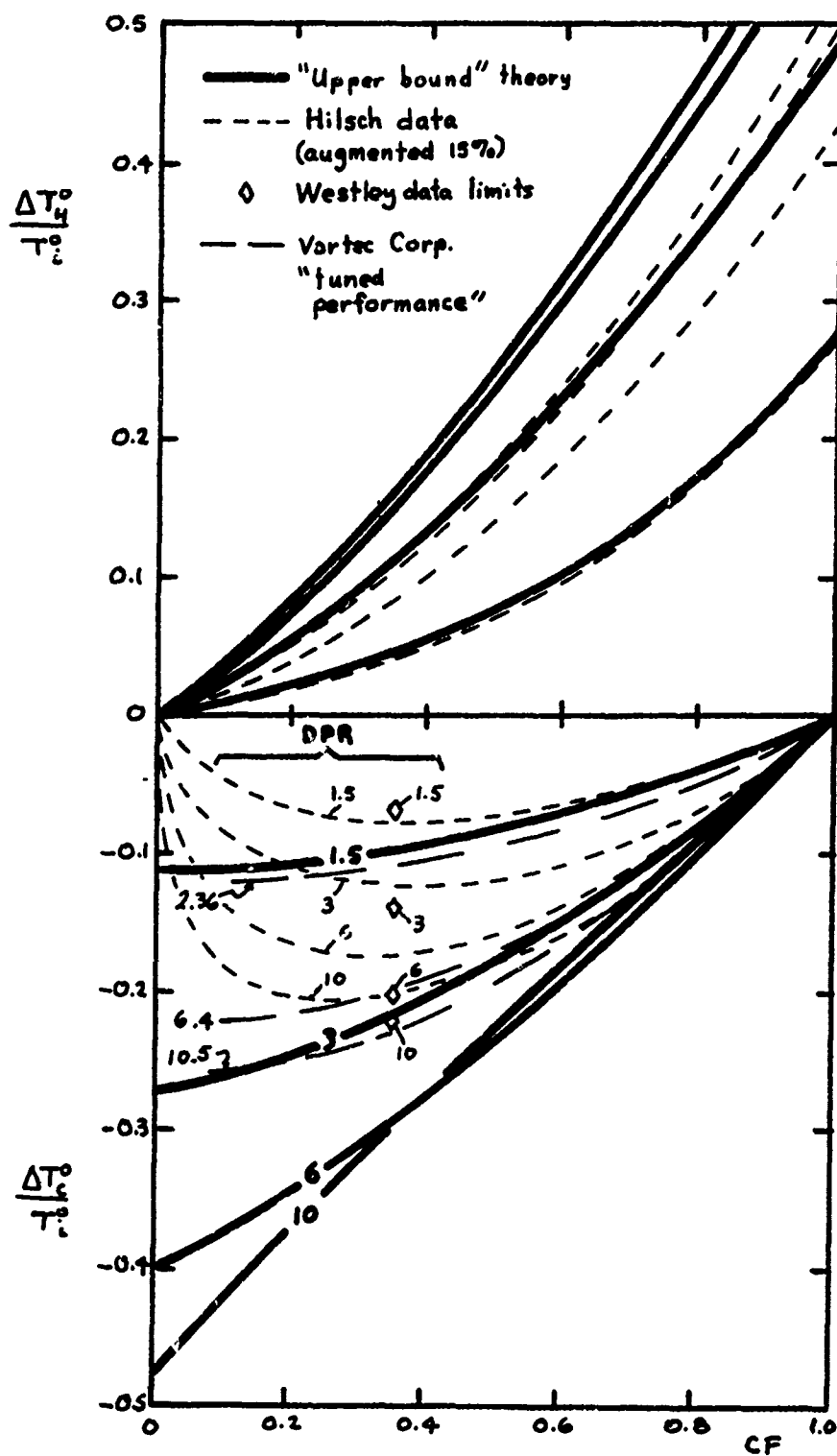


Figure 27  
Comparison of "Upper Bound" Performance with Experiment

Second, the diamonds in Figure 27 have been located on the basis of optimum-performance data from Westley,<sup>33</sup> cited by Lewellen<sup>29</sup> as "(o)ne of the best sources of data for determining optimum performance of the tube." Lewellen reproduces a curve of Westley for maximum temperature drop as a function of pressure ratio, as obtained with experimentally optimized geometry. Maximum temperature drop was obtained in the range  $0.15 \leq CF \leq 0.35$ , but CF corresponding to the optimal point for any given pressure ratio is not cited. Data from the Westley maximum-temperature-drop curve are therefore all plotted at  $CF = 0.35$ , since this provides the theoretical bounding curves with as severe a test as possible. Comparing pressure ratio for pressure ratio as before, it is seen that once again the data lie well inside the bounds.

Finally, recent performance data published in a brochure<sup>34</sup> by the Vortec Corporation are included as most probably being representative of the forefront of the vortex tube art. The vortex tube is the entire focus of activity of this company, which was founded eleven years ago by a well-known researcher in the field, C. D. Fulton. Tabulated "tuned" performance data (that is, with configuration optimized for each data point) presented in dimensional form in the brochure have been nondimensionalized and plotted in Figure 27. It is seen that these data, too, are contained within the theoretical "upper bound" curves.

A new interpretation of the meaning of theoretical RHT performance curves. It is well known that conventional, fixed-geometry Ranque-Hilsch tubes may be depended upon to behave experimentally as reported by Hilsch (Figure 4), exhibiting a maximum temperature drop for any given DPR at an intermediate CF and zero drop at  $CF = 0$  and 1. It is

equally well known that theory persistently predicts nonzero temperature drop--indeed, maximum temperature drop in all the theories examined by the writer--at  $CF = 0$ . There is experimental data, as has been mentioned earlier, which indicates that the theoretical prediction is indeed meaningful--that, for example, if the cold flow temperature is measured just inside the orifice it reaches its coldest as  $CF$  tends to zero, as found by Sibulkin<sup>25</sup>--but this still is not completely satisfying. One could argue that the tiny net outflow occurring through the orifice with  $CF$  just greater than zero accomplishes some cooling whether one properly measures its temperature amidst the local recirculation pattern or not, but this would seem rather academic: if extremely low cold fractions are acceptable, then it is not refrigeration capacity but temperature itself that is at a premium.

To the mind of the writer, the most proper interpretation of the significance of theoretical RHT performance characteristics is that they correspond to an envelope for any given pressure ratio, which (if they were sufficiently exact) would have a point of tangency with the performance curve for any given fixed-geometry RHT at its design point. This concept is readily illustrated with the ever-reappearing data of Hilsch, who presented data taken on his smallest tube with four different cold orifice sizes. He noted that there was a tendency for the position of maximum temperature drop to shift to the left (to lower  $CF$ ) as the cold orifice size was reduced, an effect which is readily interpreted in the light of the present theory as simply shifting the design point by matching the cold port size to the cold massflow, and which also bespeaks an envelope effect. In Figure 28, the cold output portion of Figure 4 is



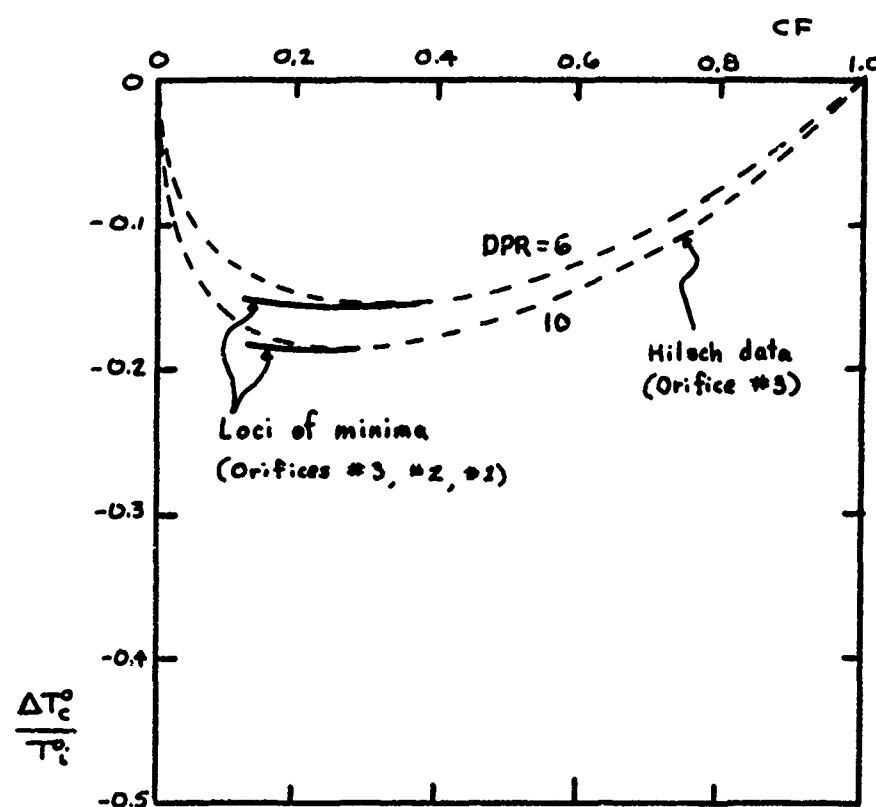


**Figure 28**  
Interpretation of Theory as Performance Envelope

reproduced, and the locus of minima as obtained with the aid of the two data sets involving smaller orifices than that for Figure 4 is indicated for each of the two highest pressure ratios. At lower pressure ratios, the curves are so shallow that these loci become hard to define precisely, but they are clearly present. These loci, which are envelopes locally on the experimental data, appear to be aimed toward decidedly nonzero temperature drop at  $CF = 0$ , just as theory predicts. The Vortec experimental data plotted in Figure 27 should also be noted in this context, since the "tuned" performance data describe envelopes of exactly this sort, and it is seen that the behavior of said experimental envelopes is predicted very well by theory.

### PART III

#### THE FOA ENERGY SEPARATOR

##### A. Historical Review

The historical preface to the analysis of the Foa energy separator (FES) must be a brief one, for a very simple reason: the FES, as the most recent entry into the field of energy separation, is so new that most of its history presumably still lies ahead of it. The Ranque-Hilsch tube, for example, lay dormant for about fifteen years before it kindled major interest; the FES, by contrast, has begun generating increased interest<sup>35</sup> in a fraction of that time, but is as yet in the infancy of its development.

The first technical discussion of the FES was a paper<sup>7</sup> published by Foa in 1964. The basic theory of FES operation is presented, an analysis is performed for the performance of the internal-separation configuration [see Figure 3(a)], and initial experimental data are presented. This paper has remained the principal source of theoretical information on the FES up to the present time, although in 1965 Hashem<sup>11</sup> gave brief attention to the FES in the same paper in which he analyzed the RHT. Finally, a patent<sup>10</sup> was awarded to Foa in 1968 which, while it of course does not delve deeply into the theory, describes the principle of operation together with a wide range of possible embodiments of the device. Several possible applications are also described in the realm of heating and air conditioning.

In the analyses which follow, two aspects of FES performance characteristics are explored. The first and most basic has to do with

"core performance equations," meaning the equations which delineate the fundamental behavior of the FES. The work in this section, which is at root an extension and generalization of that in the original paper by Foa, is patterned after Foa's approach as much as possible. However, the present analysis is broadened to include effects not treated originally--including, in particular, the important effect of prerotation--and has been carried out for both the internal-separation and external-separation configurations. As pointed out in the INTRODUCTION, the two configuration types are equivalent in principle, but from a practical standpoint call for performance equations which are tailored to them separately. In the second section, which deals with "collection effects," the analyses have to do with matters lying outside the scope of previous FES literature.

## B. Core Performance Equations

### 1. External-Separation Configuration

Analytical model. Figure 29 is a schematic representation of the external-separation FES configuration introduced in Figure 3(b), with salient analytical items noted. Flow "i" is that introduced into the rotor, which may in general possess prerotation  $\mu_i$ , defined to be positive in the direction of rotation. The rotor contains a single nozzle (or more generally, a set of identical nozzles arranged so as not to interfere with one another), through which flow exits at an effective radius  $R$  from the center of rotation; a radial-flow arrangement is depicted, but the flow could in principle be axial instead. The angular velocity of the rotor, which may be subject to a resisting torque  $L$ , is  $\omega$  and the tangential velocity of the nozzle exit is therefore  $V = \omega R$ .

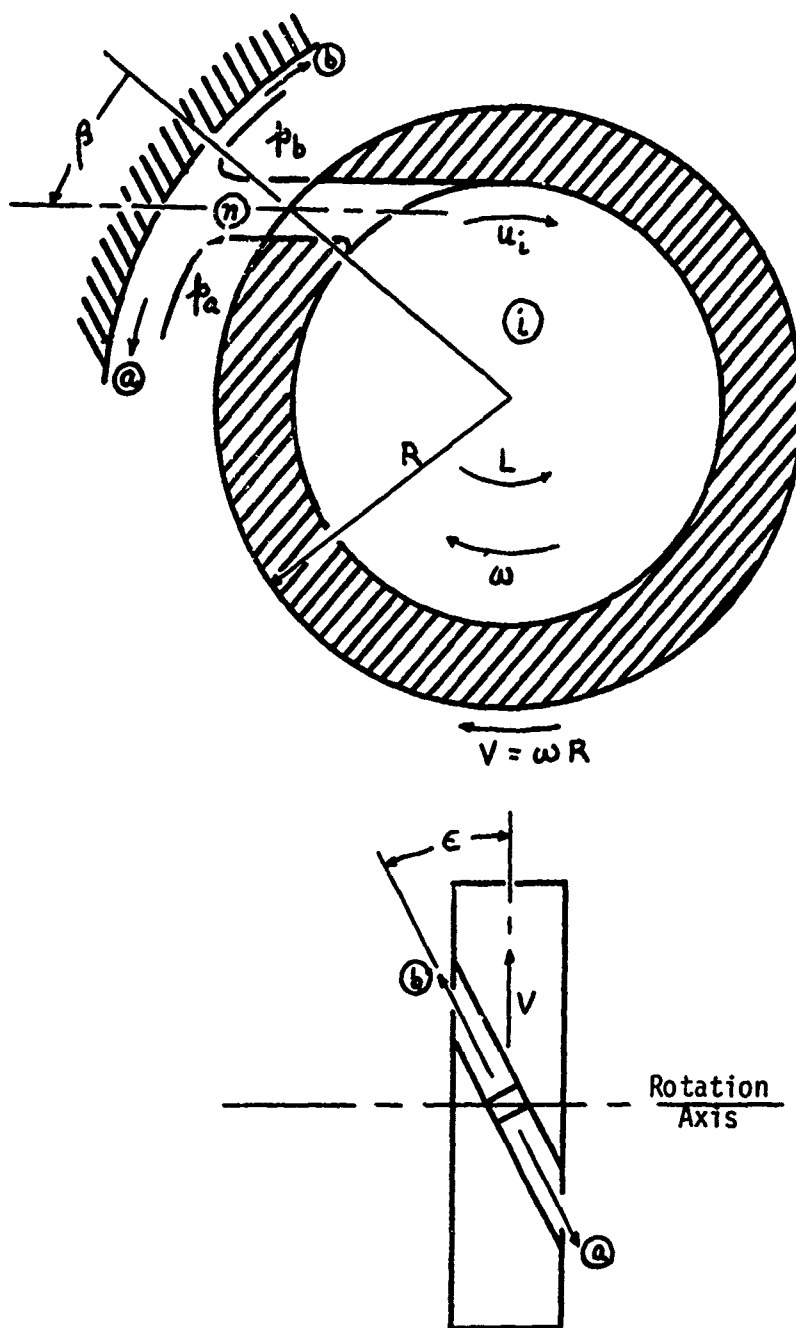


Figure 29  
External-Separation FES Configuration

The nozzle axis is inclined at an angle  $\beta$  relative to the radial direction, and the effective static pressure at the nozzle exit is  $p_n$ .

The static pressures  $p_a$  and  $p_b$  to which the deflected flows discharge may be unequal, so that  $p_n$  and all other flow parameters as measured at the nozzle are appropriately defined mean values. Finally, as illustrated in the lower half of Figure 29, the plane in which the flows discharge may in general be misaligned with the plane of rotation by what will be termed the "offset angle"  $\epsilon$ , which is normally small but of considerable significance nonetheless.

It may be noted from Figure 29 that in some cases of practical interest, the radial height of the annular collection channel may be a non-negligible fraction of the rotor radius  $R$ . As pointed out by Foa,<sup>7</sup> this will cause the flow impingement angle at the wall to differ slightly from the nozzle inclination, the relationship between the value  $\beta_w$  at the wall and  $\beta_n$  at the nozzle exit being given by

$$\tan \beta_w = \frac{r_{wall}}{R} \tan \beta_n$$

The massflow ratio  $\mu = \frac{\dot{m}_b}{\dot{m}_a}$ , a primary parameter in describing FES performance, is determined by  $\beta_w$  rather than  $\beta_n$ ; the difference in total enthalpies of the two deflected flows,  $h_b^0 - h_a^0$ , is also determined through  $\beta_w$  provided  $c_n$  (the nozzle-exit velocity in  $F_5$ ) is known. However,  $c_n$  is dependent upon the nozzle pressure ratio  $\frac{p_0}{p_n}$  and  $\beta_n$ , rather than  $\beta_w$ . It is thus to be expected that the performance equations would be complicated considerably by full inclusion of this effect, and yet it is of less intrinsic concern than the others considered below. Therefore, while it is noted here as a matter which

would require closer examination should designs be considered with very large channel heights, this effect is neglected in the performance equations to follow.

Analysis. The difference in the total enthalpies per unit mass of the two deflected flows is

$$h_b^0 - h_a^0 = (h_b - h_a) + \frac{1}{2}(u_b^2 - u_a^2)$$

Here,  $u$  denotes flow velocity as measured in the unsteady (laboratory) reference frame  $F_U$ ; velocities as measured in the steady frame  $F_S$  will be denoted by  $\kappa$ . The static-enthalpy difference included above arises only if there is a difference in static pressures across the jet; this pressure differential will be denoted by

$$\delta p \equiv p_b - p_a$$

and therefore the static-enthalpy difference will be written as  $\delta h \equiv h_b - h_a$ .

Now,

$$\vec{u} = \vec{\kappa} + \vec{V}$$

where  $\vec{V}$  is the vector velocity of  $F_S$  relative to  $F_U$ . Since  $u^2 = \vec{u} \cdot \vec{u}$ , one obtains

$$\frac{1}{2}(u_b^2 - u_a^2) = \frac{1}{2}(\kappa_b^2 - \kappa_a^2) + (\vec{\kappa}_b - \vec{\kappa}_a) \cdot \vec{V}$$

Noting that

$$\vec{\kappa}_b \cdot \vec{V} = +\kappa_b V \cos \epsilon$$

$$\vec{\kappa}_a \cdot \vec{V} = -\kappa_a V \cos \epsilon$$

the total enthalpy difference is given by

$$h_b^0 - h_a^0 = \delta h + \frac{1}{2} \delta c (c_b + c_a) + (c_b + c_a) V \cos \epsilon \quad (1)$$

where the notation  $\delta c \equiv c_b - c_a$  is used to highlight the fact that the velocity difference is due to  $\delta \beta$ .

If attention is restricted to the case of  $\frac{\delta \beta}{\beta_n}$  small, the effective nozzle exit velocity in  $F_S$  is essentially equal to the average of the two deflected velocities, i.e.,

$$c_n = \frac{c_a + c_b}{2}$$

Therefore, (1) becomes in approximation

$$h_b^0 - h_a^0 \doteq 2 c_n V \cos \epsilon + c_n \delta c + \delta h \quad (1')$$

Referring to Figure 30, the tangential momentum equation may be written as

$$\dot{m}_n (U_{nx} - U_{ix}) + F_x = 0$$

where  $\dot{m}_n$  is the massflow through the nozzle,  $F_x$  is the tangential resisting force, and  $u_{ix}$  and  $u_{nx}$  are the tangential components of velocity entering and leaving the nozzle, respectively. Since

$$U_{ix} = u_i \quad (\text{prerotation})$$

and

$$U_{nx} = -c_n \sin \beta \cos \epsilon + V$$



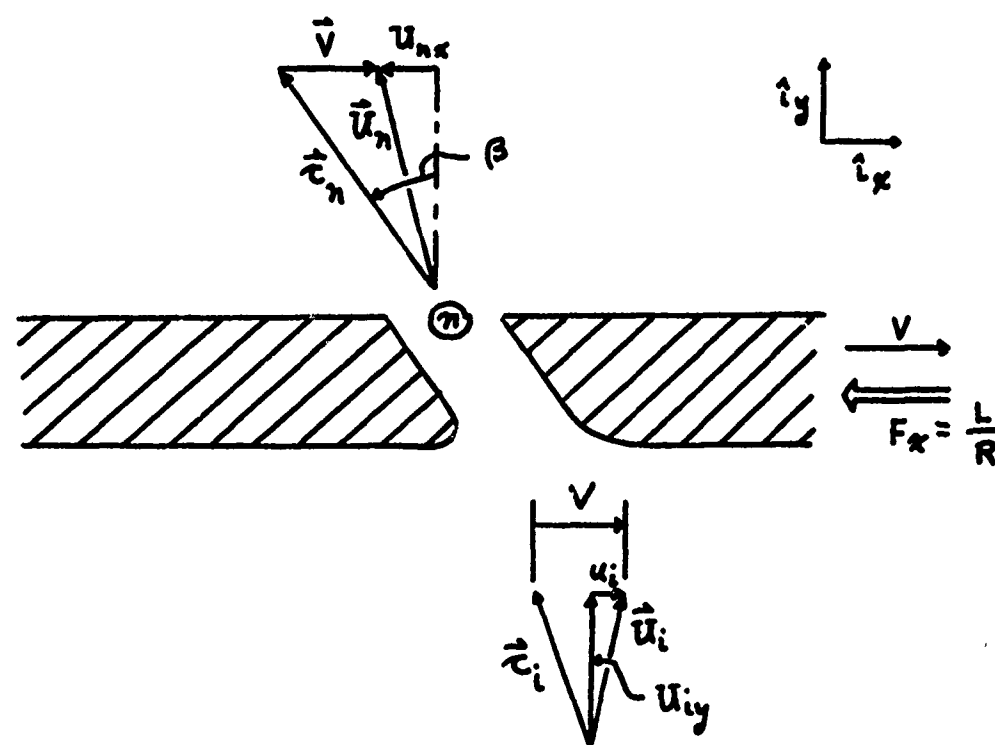


Figure 30  
Inlet and Exit Velocity Triangles at Nozzle

the momentum equation is

$$\dot{m}_n (-c_n \sin \beta \cos \epsilon + V - u_i) = -F_x$$

Multiplying by  $-\frac{V}{\dot{m}_n}$  and noting that  $F_x = \frac{L}{R}$  and  $\omega = \frac{V}{R}$ , one obtains

$$c_n V \sin \beta \cos \epsilon - V^2 + u_i V = \frac{L \omega}{\dot{m}_n} \quad (2)$$

Next, it is necessary to relate the stagnation enthalpy as measured in  $F_S$  to that in  $F_U$ . Stagnation conditions in  $F_U$ , where the flow is ultimately utilized, will be denoted by  $( )^0$ , while those in the moving reference frame  $F_S$  will be signified by  $( )^\bullet$ . Conservation of energy in  $F_S$  during passage through the nozzle may be written as

$$h_n^\bullet = h_n + \frac{c_n^2}{2} = h_i + \frac{c_i^2}{2}$$

where  $\vec{c}_i$  and  $\vec{c}_n$  are as shown in Figure 30. Considering the velocity triangles for the flow entering the nozzle,

$$\begin{aligned} \vec{c}_i &= \vec{u}_i - \vec{V} \\ &= (u_i - V) \hat{i}_x + u_{iy} \hat{i}_y \end{aligned}$$

where  $u_i$  is the prerotation component of  $\vec{u}_i$ . Hence,

$$\begin{aligned} c_i^2 &= \vec{c}_i \cdot \vec{c}_i \\ &= (u_i - V)^2 + u_{iy}^2 \\ \frac{c_i^2}{2} &= \frac{u_i^2}{2} + \frac{u_{iy}^2}{2} + \frac{V^2}{2} - u_i V \\ &= \frac{u_i^2}{2} + \frac{V^2}{2} - u_i V \end{aligned}$$

Since

$$h_i^0 = h_i + \frac{u_i^2}{2}$$

there follows finally

$$h_n^0 = h_n + \frac{c_n^2}{2} = h_i^0 + \frac{v^2}{2} - u_i V \quad (3)$$

Now,

$$h_a^0 = h_a + \frac{u_a^2}{2}$$

$$\vec{u}_a = \vec{c}_a + \vec{V}$$

$$= (-c_a \cos \epsilon + V) \hat{i}_x + (c_a \sin \epsilon) \hat{i}_z$$

where  $\hat{i}_z$  is normal to the plane of rotation. Then taking  $u_a^2 = \vec{u}_a \cdot \vec{u}_a$  one obtains

$$h_a^0 = h_a + \frac{1}{2} (c_a^2 - 2 c_a V \cos \epsilon + V^2)$$

and similarly for the "b" flow,

$$h_b^0 = h_b + \frac{1}{2} (c_b^2 - 2 c_b V \cos \epsilon + V^2)$$

Adding,

$$h_b^0 + h_a^0 = (h_b + h_a) + \frac{1}{2} (c_b^2 + c_a^2) + (c_b - c_a) V \cos \epsilon + V^2 \quad (4)$$

If attention is once again limited to  $\frac{\delta p}{p_n}$  sufficiently small to enable the effective value of any given flow parameter at the nozzle exit to be approximated as the mean of the values in flows "a" and "b", one may write

$$h_n \doteq \frac{h_a + h_b}{2}, \quad c_n \doteq \frac{c_a + c_b}{2}$$

$$h_a = h_n - \frac{1}{2} \delta h, \quad h_b = h_n + \frac{1}{2} \delta h$$

$$c_a = c_n - \frac{1}{2} \delta c, \quad c_b = c_n + \frac{1}{2} \delta c$$

Introducing these approximations into (4) produces

$$h_b^0 + h_a^0 \doteq 2 h_n + c_n^2 + V \delta c \cos \epsilon + V^2$$

which with the aid of equation (3) gives finally

$$h_b^0 + h_a^0 \doteq 2 (h_i^0 + V^2) - 2 u_i V + V \delta c \cos \epsilon \quad (4')$$

Now define:

$$\frac{1}{2} u_{oa}^2 \equiv h_i^0 \left[ 1 - \left( \frac{p_a}{p_i^0} \right)^{\frac{\gamma-1}{\gamma}} \right] \quad (5a)$$

$$\frac{1}{2} u_{on}^2 \equiv h_i^0 \left[ 1 - \left( \frac{p_n}{p_i^0} \right)^{\frac{\gamma-1}{\gamma}} \right] \quad (5b)$$

$$\eta \equiv \frac{h_i^0 - h_n}{\frac{1}{2} u_{on}^2} \quad (5c)$$

$$\lambda \equiv \frac{L\omega / \dot{m}_m}{h_i^0 - h_n} \quad (5d)$$

The velocities  $u_{oa}$  and  $u_{on}$  in (5a) and (5b) are, respectively, the discharge velocities which would be produced with a locked rotor discharging isentropically from the stagnation conditions within the rotor to the cold-output static pressure  $p_a$  and to the nozzle-exit static pressure

$p_n$ . The former defines the driving pressure ratio  $DPR = \frac{p_i^0}{p_a}$ ,

which is of thermodynamic significance; the latter, however, defines the nozzle pressure ratio  $\text{NPR} = \frac{p_0}{p_n}$ , which governs the rotor speed. Equation (5c) is the nozzle efficiency, while (5d) expresses the removal of energy from the rotor by shaft torque, e.g. due to friction.

Equation (2) may be divided by  $u_{on}^2$  to give a dimensionless equation:

$$\frac{c_n V}{u_{on}^2} \sin \beta \cos \epsilon - \left( \frac{V}{u_{on}} \right)^2 + \frac{u_i V}{u_{on}^2} = \frac{L\omega/\dot{m}_n}{u_{on}^2}$$

which, with the aid of  $\eta$  and  $\lambda$  defined above, becomes:

$$\frac{c_n V}{u_{on}^2} \sin \beta \cos \epsilon - \left( \frac{V}{u_{on}} \right)^2 + \frac{u_i V}{u_{on}^2} = \frac{1}{2} \eta \lambda \quad (2')$$

A dimensionless version of (3) is also needed. Rearranging,

$$\frac{c_n^2}{2} = h_i^0 - h_n + \frac{V^2}{2} - u_i V$$

Dividing by  $\frac{1}{2} u_{on}^2$  and using the definition of  $\eta$  yields:

$$\left( \frac{c_n}{u_{on}} \right)^2 = \eta + \left( \frac{V}{u_{on}} \right)^2 - 2 \frac{u_i V}{u_{on}^2} \quad (3')$$

Equations (2') and (3') are to be solved for  $\frac{V}{u_{on}}$  and  $\frac{c_n}{u_{on}}$ .

Defining

$$B_e \equiv \sin \beta \cos \epsilon$$

equation (2') becomes

$$\left(\frac{v}{u_{on}}\right)^2 + \frac{1}{2} \gamma \lambda = B_e \frac{c_n}{u_{on}} \frac{v}{u_{on}} + \frac{u_i}{u_{on}} \frac{v}{u_{on}}$$

Squaring, substituting for  $\frac{c_n}{u_{on}}$  in the resulting equation by means of (3'), and collecting terms, one obtains

$$\left(\frac{v}{u_{on}}\right)^4 (1 - B_e^2 + D_e) + \left(\frac{v}{u_{on}}\right)^2 [\gamma(\lambda - B_e^2) - C_e] + \frac{1}{4} \gamma^2 \lambda^2 = 0 \quad (5)$$

where

$$C_e \equiv \left(\frac{u_i}{u_{on}}\right)^2 + 2 B_e \frac{u_i}{u_{on}} \sqrt{\gamma + \left(\frac{v}{u_{on}}\right)^2} - 2 \frac{u_i v}{u_{on}^2}$$

$$D_e \equiv 2 B_e^2 \frac{(u_i / u_{on})}{(v / u_{on})}$$

Equation (5) is a quadratic in  $\left(\frac{v}{u_{on}}\right)^2$  whose coefficients, alas, are themselves functions of  $\frac{v}{u_{on}}$  if prerotation is present. For zero prerotation, the solution for  $\left(\frac{v}{u_{on}}\right)^2$  will be in closed form; otherwise, the solution becomes iterative.

Defining

$$\bar{M}_e \equiv \frac{(B_e^2 - \lambda) + \frac{C_e}{\gamma} + B_e \sqrt{(1 - \lambda) - (1 - B_e^2)} + 2(B_e^2 - \lambda) \frac{C_e}{\gamma} + \left(\frac{C_e}{\gamma}\right)^2 - D_e \lambda^2}{2(1 - B_e^2 + D_e)}$$

the solution for  $\left(\frac{v}{u_{on}}\right)^2$  is found to be

$$\left(\frac{v}{u_{on}}\right)^2 = \gamma \bar{M}_e \quad (6)$$

and that for  $\left(\frac{c_n}{u_{on}}\right)^2$  follows as

$$\left(\frac{c_n}{u_{on}}\right)^2 = \gamma(1 + \bar{M}_e) - 2 \frac{u_i}{u_{on}} \sqrt{\gamma \bar{M}_e} \quad (7)$$

Dividing equation (1') by  $u_{on}^2$  gives

$$\frac{h_b^0 - h_a^0}{u_{on}^2} = 2 \frac{c_n}{u_{on}} \frac{V}{u_{on}} \cos \epsilon + \left( \frac{c_n}{u_{on}} \right)^2 \frac{\delta c}{c_n} + \frac{1}{2} \frac{\delta h}{h_n} \frac{h_n}{\frac{1}{2} u_{on}^2} \quad (1'')$$

and (4') yields similarly

$$\frac{h_b^0 + h_a^0}{u_{on}^2} = \frac{h_i^0}{\frac{1}{2} u_{on}^2} + 2 \left( \frac{V}{u_{on}} \right)^2 - 2 \frac{u_i}{u_{on}} \frac{V}{u_{on}} + \frac{V}{c_n} \left( \frac{c_n}{u_{on}} \right)^2 \frac{\delta c}{c_n} \cos \epsilon \quad (4'')$$

Adding equations (1'') and (4'') and subtracting  $\frac{h_i^0}{\frac{1}{2} u_{on}^2}$ , one obtains

$$\frac{h_b^0 - h_i^0}{\frac{1}{2} u_{on}^2} = 2 \left[ \left( \frac{V}{u_{on}} \right)^2 - \frac{u_i}{u_{on}} \frac{V}{u_{on}} + \frac{c_n}{u_{on}} \frac{V}{u_{on}} \cos \epsilon \right] + \frac{V}{c_n} \left( \frac{c_n}{u_{on}} \right)^2 \frac{\delta c}{c_n} \cos \epsilon + \left( \frac{c_n}{u_{on}} \right)^2 \frac{\delta c}{c_n} + \frac{1}{2} \frac{\delta h}{h_n} \frac{h_n}{\frac{1}{2} u_{on}^2} \quad (8)$$

while subtracting equation (1'') and  $\frac{h_i^0}{\frac{1}{2} u_{on}^2}$  from (4'') gives

$$\frac{h_a^0 - h_i^0}{\frac{1}{2} u_{on}^2} = 2 \left[ \left( \frac{V}{u_{on}} \right)^2 - \frac{u_i}{u_{on}} \frac{V}{u_{on}} - \frac{c_n}{u_{on}} \frac{V}{u_{on}} \cos \epsilon \right] + \frac{V}{c_n} \left( \frac{c_n}{u_{on}} \right)^2 \frac{\delta c}{c_n} \cos \epsilon - \left( \frac{c_n}{u_{on}} \right)^2 \frac{\delta c}{c_n} - \frac{1}{2} \frac{\delta h}{h_n} \frac{h_n}{\frac{1}{2} u_{on}^2} \quad (9)$$

Equations (8) and (9) contain the  $\frac{\delta p}{p_n}$ -dependent quantities  $\frac{\delta c}{c_n}$  and  $\frac{\delta h}{h_n}$ , expressions for which remain to be derived. An analysis is carried out below for the effect of  $\delta p$  on the massflow ratio  $\mu$  wherein it is also shown that, for  $\frac{\delta p}{p_n}$  small,

$$\frac{\delta c}{c_n} \doteq - \frac{1}{\gamma M_n^2} \frac{\delta p}{p_n}$$

and

$$\frac{\delta h}{h_n} \doteq \frac{\gamma-1}{\gamma} \frac{\delta p}{p_n}$$

Noting that

$$M_n^2 = \frac{c_n^2}{\gamma R T_n} = \frac{c_n^2}{(\gamma-1) h_n}$$

one may rewrite  $\frac{\delta c}{c_n}$  as

$$\frac{\delta c}{c_n} = -\frac{\gamma-1}{2\gamma} \frac{(h_n / \frac{1}{2} u_{on}^2)}{(c_n / u_{on}^2)} \frac{\delta p}{p_n}$$

Substituting for  $\frac{\delta c}{c_n}$  and  $\frac{\delta h}{h_n}$  in equations (8) and (9) and noting with the aid of (5b) and (5c) that

$$\frac{h_n}{\frac{1}{2} u_{on}^2} = \left[ 1 - \left( \frac{p_n}{p_{oi}} \right)^{\frac{\gamma-1}{\gamma}} \right]^{-1} - \gamma$$

there follows

$$\frac{h_b^o - h_i^o}{\frac{1}{2} u_{on}^2} = 2 \left[ \left( \frac{V}{u_{on}} \right)^2 - \frac{u_i V}{u_{on}^2} + \frac{c_n V}{u_{on}^2} \cos \epsilon \right] - \frac{\gamma-1}{2\gamma} \left\{ \left[ 1 - \left( \frac{p_n}{p_{oi}} \right)^{\frac{\gamma-1}{\gamma}} \right]^{-1} - \gamma \right\} \frac{V}{c_n} \cos \epsilon \frac{\delta p}{p_n} \quad (8')$$

and

$$\frac{h_a^o - h_i^o}{\frac{1}{2} u_{on}^2} = 2 \left[ \left( \frac{V}{u_{on}} \right)^2 - \frac{u_i V}{u_{on}^2} - \frac{c_n V}{u_{on}^2} \cos \epsilon \right] - \frac{\gamma-1}{2\gamma} \left\{ \left[ 1 - \left( \frac{p_n}{p_{oi}} \right)^{\frac{\gamma-1}{\gamma}} \right]^{-1} - \gamma \right\} \frac{V}{c_n} \cos \epsilon \frac{\delta p}{p_n} \quad (9')$$

Energy separation performance is obtained in the desired form by

$$\frac{h_j^o - h_i^o}{h_i^o} = \frac{h_j^o - h_i^o}{\frac{1}{2} u_{on}^2} \cdot \frac{\frac{1}{2} u_{on}^2}{\frac{1}{2} u_{on}^2} \cdot \frac{\frac{1}{2} u_{on}^2}{h_i^o} \quad (10)$$

where "j" may refer to either flow "a" or flow "b" and the first factor comes from equation (8') or (9'). The second factor reflects the influence



of  $\delta p$ , being equal to unity when  $\delta p = 0$ ; from (5a) and (5b),

$$\frac{\frac{1}{2} u_{on}^2}{\frac{1}{2} u_{oa}^2} = \frac{1 - (p_n/p_o)^{\frac{\gamma-1}{\gamma}}}{1 - (p_a/p_o)^{\frac{\gamma-1}{\gamma}}}$$

where  $\frac{p_n}{p_o} = \frac{p_a}{p_o} \cdot \frac{p_n}{p_a}$  may be written, for  $\frac{\delta p}{p_n}$  small, as

$$\begin{aligned} \frac{p_n}{p_o} &= \frac{p_a}{p_o} \left[ 1 - \frac{1}{2} \frac{\delta p}{p_n} \right]^{-1} \\ &= \frac{p_a}{p_o} \left[ 1 + \frac{1}{2} \frac{\delta p}{p_n} \right] \end{aligned}$$

Thus, the differential-pressure factor becomes for  $\frac{\delta p}{p_n}$  small

$$K_{\delta p} \equiv \frac{\frac{1}{2} u_{on}^2}{\frac{1}{2} u_{oa}^2} = 1 - \frac{\gamma-1}{2\gamma} \frac{(\text{DPR})^{-\frac{\gamma-1}{\gamma}}}{1 - (\text{DPR})^{-\frac{\gamma-1}{\gamma}}} \frac{\delta p}{p_n}$$

The third factor is a scale factor dependent upon the driving pressure ratio, and is seen from (5a) to be

$$K_{\text{DPR}} \equiv \frac{\frac{1}{2} u_{on}^2}{h_o} = 1 - (\text{DPR})^{-\frac{\gamma-1}{\gamma}}$$

Thus, the energy separation is given by

$$\frac{h_i - h_o}{h_o} = K_{\delta p} K_{\text{DPR}} \frac{h_i - h_o}{\frac{1}{2} u_{on}^2} \quad (10')$$

where  $K_{\delta p}$  and  $K_{\text{DPR}}$  are as given above.

Effect of pressure differential  $\delta p$  in impingement region. If there is a pressure differential across the jet issuing from the nozzle, Figure 29, the effect is felt not only in the output temperatures as explored above but also in the massflow ratio  $\mu$ . If, for example,

$p_b > p_a$ . this will cause the jet pattern to shift toward the "a" flow direction.

Figure 31 depicts the analytical model which will be considered in assessing the effect of  $\delta p$  on  $\mu$ . The collection channel curvature is neglected, and the flow is considered to be two-dimensional, inviscid, adiabatic, steady in  $F_S$ , and free of body forces. The deflected flows "a" and "b" are assumed to be uniform as they leave the control volume shown in Figure 31; the flow entering from the nozzle, however, is necessarily nonuniform, the velocity at the left edge being  $c_a$  and that at the right edge being  $c_b$ . It is assumed that wall proximity does not significantly affect the nozzle exit velocity profile; judging from theoretical flow patterns for two-dimensional jet impact presented by Taylor,<sup>36</sup> this assumption would appear to be reasonable for channel heights approximately equal to the nozzle height (as measured in the plane of Figure 31) or larger.

The momentum equation in the tangential ("x") direction for the control volume is

$$(p_b + p_b c_b^2 \frac{\alpha_b}{\alpha_d}) - (p_a + p_a c_a^2 \frac{\alpha_a}{\alpha_d}) = - \frac{J_n}{\alpha_d} \sin \beta \quad (11)$$

where flow area  $\alpha = w W$ ,  $W$  being the dimension normal to the plane of Figure 31, and

$$J_n = \int_0^{w_n} p_n(\kappa_n) c_n^2(\kappa_n) \cdot W d\kappa_n$$

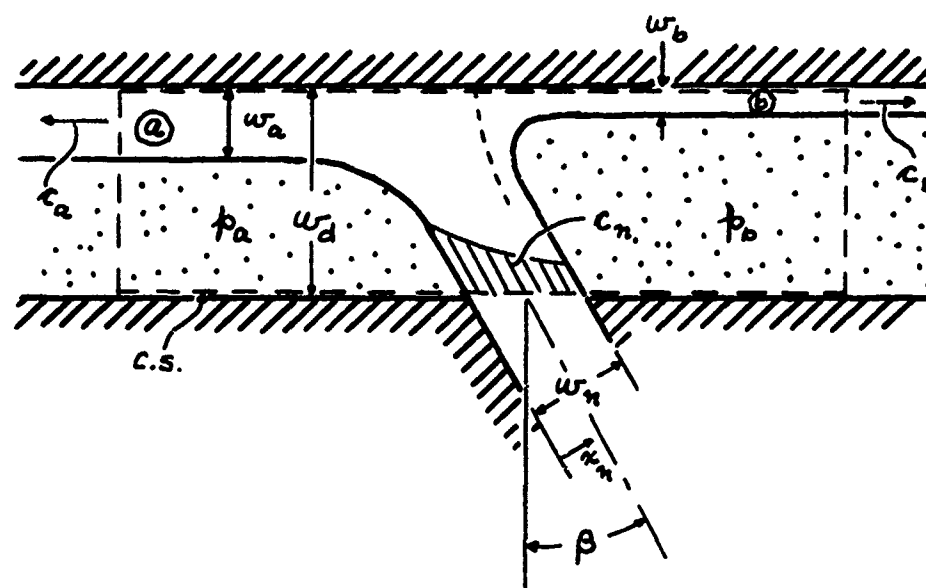


Figure 31  
Analytical Model for Impingement-Deflection Process

is the jet momentum at the nozzle exit. The continuity equation is

$$\rho_a c_a \alpha_a + \rho_b c_b \alpha_b = \dot{m}_n \quad (12)$$

where

$$\dot{m}_n = \int_0^{w_n} \rho_n(x_n) c_n(x_n) \cdot w \, dx_n$$

is the total nozzle massflow.

Attention will be restricted to the case of  $\frac{\delta p}{p_n}$  small, such that it is an acceptable approximation to write

$$X_n \doteq \frac{X_a + X_b}{2}$$

for the mean value of any flow property of interest at the nozzle exit (e.g.,  $p$ ,  $\rho$ , or  $c$ ), this mean value being adequate for both the continuity and momentum equations. Then

$$J_n = \rho_n c_n^2 \alpha_n$$

$$\dot{m}_n = \rho_n c_n \alpha_n$$

and the momentum and continuity equations become

$$(p_b + \rho_b c_b^2 \frac{\alpha_b}{\alpha_d}) - (p_a + \rho_a c_a^2 \frac{\alpha_a}{\alpha_d}) = -\rho_n c_n^2 \frac{\alpha_n}{\alpha_d} \sin \beta \quad (11')$$

$$\rho_a c_a \alpha_a + \rho_b c_b \alpha_b = \rho_n c_n \alpha_n \quad (12')$$

Equations (11') and (12') are to be solved for  $\frac{a_a}{a_m}$  and  $\frac{a_b}{a_m}$  to enable  $\mu$  to be calculated. The momentum and continuity equations may be rearranged as

$$\frac{P_a}{P_m} \left( \frac{c_a}{c_m} \right)^2 \frac{a_a}{a_m} - \frac{P_b}{P_m} \left( \frac{c_b}{c_m} \right)^2 \frac{a_b}{a_m} = \frac{a_d}{a_m} \frac{\delta p}{P_m c_m^2} + \sin \beta \quad (11'')$$

$$\frac{P_a}{P_m} \frac{c_a}{c_m} \frac{a_a}{a_m} + \frac{P_b}{P_m} \frac{c_b}{c_m} \frac{a_b}{a_m} = 1 \quad (12'')$$

The density ratios  $\frac{P_a}{P_m}$  and  $\frac{P_b}{P_m}$  and the velocity ratios  $\frac{c_a}{c_m}$  and  $\frac{c_b}{c_m}$  are needed as functions of  $\frac{\delta p}{P_m}$ . For any flow parameter  $X$ ,

$$\left. \begin{aligned} \delta X &\equiv X_b - X_a \\ \frac{X_a}{X_m} &= 1 - \frac{1}{2} \frac{\delta X}{X_m}, \quad \frac{X_b}{X_m} = 1 + \frac{1}{2} \frac{\delta X}{X_m} \end{aligned} \right\} \quad (13)$$

and  $\frac{\delta X}{X_m}$  is small by virtue of  $\frac{\delta p}{P_m}$  small. Since the flow is homentropic,

$$\frac{dT}{T} = \frac{\gamma-1}{\gamma} \frac{dp}{p}$$

$$\frac{dp}{p} = \frac{1}{\gamma} \frac{dh}{h}$$

hence, in approximation,

$$\frac{\delta T}{T_m} = \frac{\delta h}{h_m} \doteq \frac{\gamma-1}{\gamma} \frac{\delta p}{P_m} \quad (13a)$$

$$\frac{\delta p}{P_m} \doteq \frac{1}{\gamma} \frac{\delta p}{P_m} \quad (13b)$$

The velocity change across the jet is found, neglecting the slight density variation, from the Bernoulli equation:

$$\begin{aligned} p_a + \frac{1}{2} \rho_m c_a^2 &= p_b + \frac{1}{2} \rho_m c_b^2 \\ \delta p &= -\frac{\rho_m}{2} (c_b^2 - c_a^2) \\ &= -\rho_m c_m \delta c \end{aligned}$$

where  $c_m = \frac{c_a + c_b}{2}$  has been used, or

$$\begin{aligned} \frac{\delta c}{c_m} &= -\frac{\rho_m}{\rho_m c_m^2} \frac{\delta p}{\rho_m} \\ \frac{\delta c}{c_m} &= -\frac{1}{\gamma M_m^2} \frac{\delta p}{\rho_m} \end{aligned} \quad (13c)$$

Note that equations (13a) and (13c) were utilized earlier in deriving equations (8') and (9').

Equation (11'') may be rewritten, with the aid of (12''), as

$$\frac{c_a}{c_m} \left[ 1 - \frac{\rho_b}{\rho_m} \frac{c_b}{c_m} \frac{d_b}{d_m} \right] - \frac{\rho_b}{\rho_m} \left( \frac{c_b}{c_m} \right)^2 \frac{d_b}{d_m} = \frac{d_d}{d_m} \frac{\delta p}{\rho_m c_m^2} + \sin \beta$$

or, with (13c),

$$\frac{d_b}{d_m} \frac{\rho_b c_b}{\rho_m c_m} \left( \frac{c_a + c_b}{c_m} \right) = \frac{c_a}{c_m} - \sin \beta - \frac{1}{\gamma M_m^2} \frac{d_d}{d_m} \frac{\delta p}{\rho_m}$$

Noting that  $c_m = \frac{c_a + c_b}{2}$  and rearranging,

$$\frac{\alpha_b}{\alpha_n} = \frac{1}{2} \frac{\rho_n c_n}{\rho_b c_b} \left[ (1 - \sin \beta) - \frac{2 \frac{\alpha_d}{\alpha_n} - 1}{2 \gamma M_n^2} \frac{\delta p}{p_n} \right] \quad (14)$$

or, with the aid of (13), (13b), and (13c),

$$\frac{\alpha_b}{\alpha_n} = \frac{1 - \sin \beta}{2} \left\{ 1 - \frac{1}{2 \gamma M_n^2} \left[ \frac{2 \frac{\alpha_d}{\alpha_n} - 1}{1 - \sin \beta} - (1 - M_n^2) \right] \frac{\delta p}{p_n} \right\} \quad (14')$$

Similarly, one may obtain

$$\frac{\alpha_a}{\alpha_n} = \frac{1}{2} \frac{\rho_n c_n}{\rho_a c_a} \left[ (1 + \sin \beta) + \frac{2 \frac{\alpha_d}{\alpha_n} - 1}{2 \gamma M_n^2} \frac{\delta p}{p_n} \right] \quad (15)$$

or

$$\frac{\alpha_a}{\alpha_n} = \frac{1 + \sin \beta}{2} \left\{ 1 + \frac{1}{2 \gamma M_n^2} \left[ \frac{2 \frac{\alpha_d}{\alpha_n} - 1}{1 + \sin \beta} - (1 - M_n^2) \right] \frac{\delta p}{p_n} \right\} \quad (15')$$

Equations (14') and (15') may be used to calculate the deflected flow areas. To find the expression for  $\mu$ , however, it is convenient to use (14) and (15):

$$\frac{\dot{m}_b}{\dot{m}_n} = \frac{\rho_b c_b \alpha_b}{\rho_n c_n \alpha_n} = \frac{1}{2} \left[ (1 - \sin \beta) - \frac{2 \frac{\alpha_d}{\alpha_n} - 1}{2 \gamma M_n^2} \frac{\delta p}{p_n} \right]$$

$$\frac{\dot{m}_a}{\dot{m}_n} = \frac{\rho_a c_a \alpha_a}{\rho_n c_n \alpha_n} = \frac{1}{2} \left[ (1 + \sin \beta) + \frac{2 \frac{\alpha_d}{\alpha_n} - 1}{2 \gamma M_n^2} \frac{\delta p}{p_n} \right]$$

so that

$$\mu = \frac{\dot{m}_b}{\dot{m}_a} = \frac{\left[ (1 - \sin \beta) - \frac{2 \frac{d_d}{d_n} - 1}{2 \gamma M_n^2} \frac{\delta p}{p_n} \right]}{\left[ (1 + \sin \beta) + \frac{2 \frac{d_d}{d_n} - 1}{2 \gamma M_n^2} \frac{\delta p}{p_n} \right]}$$

or, after some rearrangement:

$$\mu = \frac{1 - \sin \beta}{1 + \sin \beta} \left[ 1 - \frac{1}{\gamma M_n^2} \frac{(2 \frac{d_d}{d_n} - 1)}{(1 - \sin^2 \beta)} \frac{\delta p}{p_n} \right] \quad (16)$$

Note that if  $\delta p = 0$ , the massflow ratio reduces to

$$\mu_0 = \frac{1 - \sin \beta}{1 + \sin \beta} \quad (16')$$

as given by Foa<sup>7</sup> for that case. An alternative version of (16) is

$$\frac{\mu}{\mu_0} = 1 - \frac{1}{\gamma M_n^2} \frac{(2 \frac{d_d}{d_n} - 1)}{(1 - \sin^2 \beta)} \frac{\delta p}{p_n} \quad (16'')$$

Since energy separation performance characteristics will be presented as a function of cold fraction CF, it should be noted here that

$$CF = \frac{\dot{m}_a}{\dot{m}_n} = \frac{1}{1 + \mu} \quad (17)$$

By using equations (6) and (7), (8') and (9'), and (10') together with equations (16) and (17), energy separation performance characteristics may be generated as a function of DPR (driving pressure ratio) and CF, with inclusion of the effects of prerotation, rotor torque, nozzle efficiency, offset angle, and unequal discharge pressures.



Baseline performance. The basic nature of FES energy separation characteristics is revealed most simply by the idealized "baseline" case, wherein:

Prerotation	$u_i = 0$	} (18)
Nozzle efficiency	$\eta = 1$	
Torque	$L = 0$	
Offset angle	$\epsilon = 0$	
Discharge pressure differential	$\delta p = 0$	

For this case, equations (6) and (7) reduce to simply

$$\frac{V}{u_{0a}} = \tan \beta$$

$$\frac{c_n}{u_{0a}} = \sqrt{1 + \tan^2 \beta}$$

and (8') and (9') become

$$\frac{h_b^0 - h_i^0}{\frac{1}{2} u_{0a}^2} = 2 \tan \beta \left[ \sqrt{1 + \tan^2 \beta} + \tan \beta \right]$$

$$\frac{h_a^0 - h_i^0}{\frac{1}{2} u_{0a}^2} = \dots 2 \tan \beta \left[ \sqrt{1 + \tan^2 \beta} - \tan \beta \right]$$

where it is noted that  $u_{0n} = u_{0a}$ . The massflow ratio is  $\mu_0$ , given by (16').

It is seen that baseline performance is a function only of the nozzle inclination  $\beta$  and the driving pressure ratio, the latter determining the magnitude of  $u_{0a}$ . The effect of  $\beta$  is both to determine the cold fraction CF [equation (17)] and to establish the velocity of

reference frame  $F_S$  relative to  $F_U$ , this change-of-reference-frame effect being the whole key to the FES energy separation mechanism.

The performance is modified for better or worse by each of the effects neglected in the baseline case, and these effects will be explored below. The equations as developed permit the cumulative influence of any combination of these effects to be assessed all at once, with inclusion of the nonlinear interactions among the several variables, and this capability could be of practical importance in design optimization studies. For the present, however, each effect will be examined separately as to the manner in which performance is altered from the baseline case, and all parameters except that being studied in a given instance will be taken equal to the baseline values. It may be noted that linear superposition of the perturbations induced by departure of the parameters in equations (18) from their baseline values is an acceptable procedure for estimation of cumulative effects, so long as these perturbations are small.

Figure 32 presents massflow ratio and cold fraction as functions of  $\beta$  for the case of  $\delta p = 0$ , which of course is satisfied in the baseline instance. Figure 33(a) shows baseline energy separation performance as a function of CF, with an additional scale for  $\beta$  along the abscissa, while Figure 33(b) indicates the corresponding variation of rotor velocity. The curves in Figure 33 are independent of pressure ratio; those of Figure 33(a) yield normalized energy separation performance ( $\frac{T_3 - T_1}{T_0}$  and  $\frac{T_3 - T_2}{T_0}$ ) by applying the scale factor  $K_{DPR}$  according to equation (10').  $K_{DPR}$  is plotted for a range of driving pressure ratios in Figure 34.

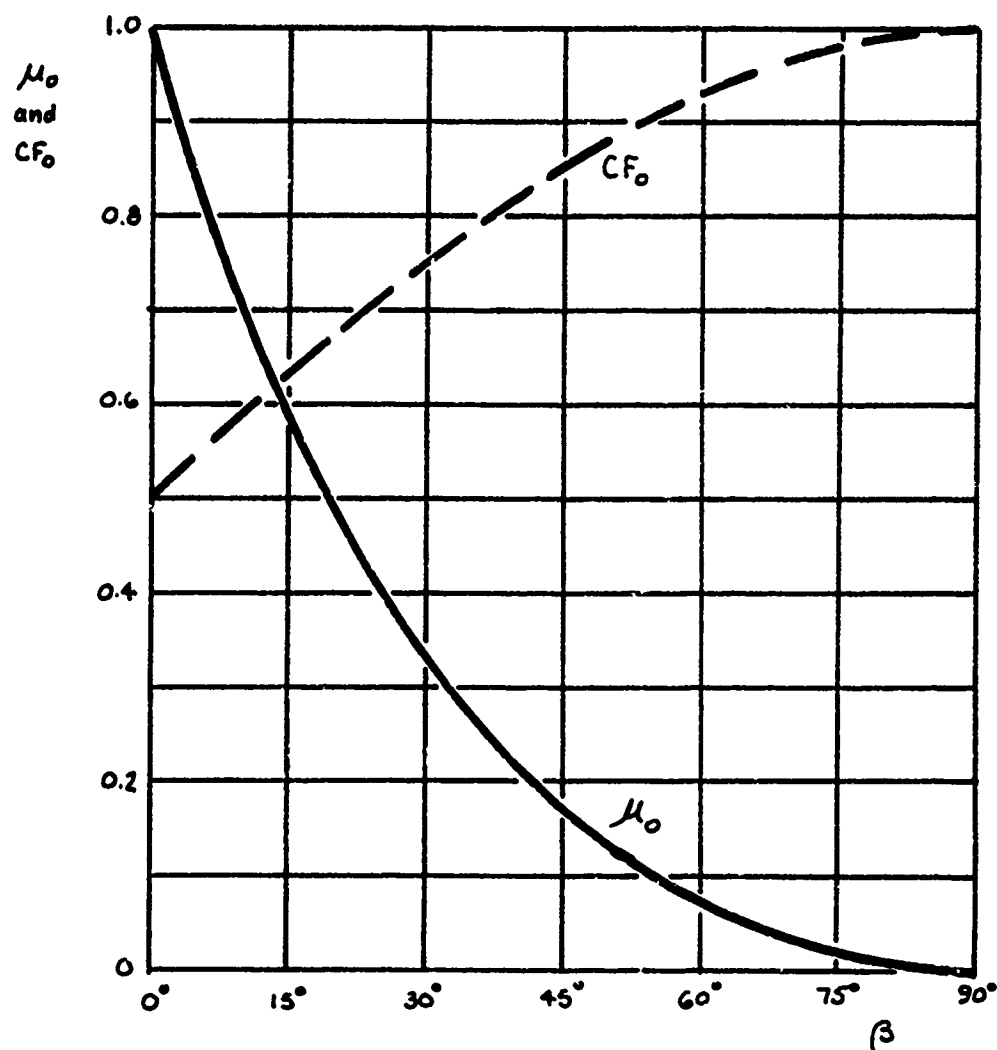


Figure 32  
Dependence of Massflow Ratio and Cold Fraction on  
Nozzle Inclination (Equal Discharge Pressures)

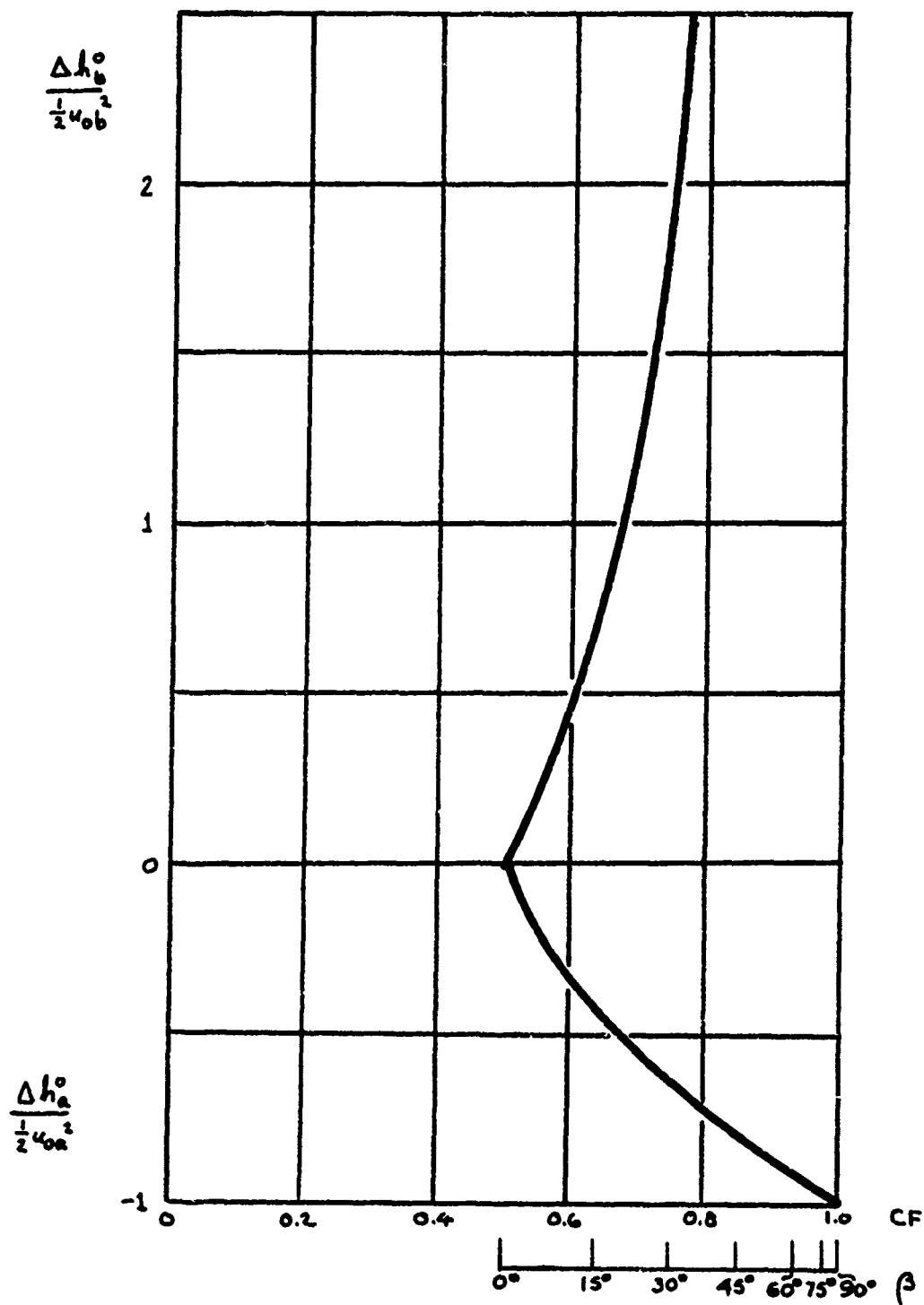


Figure 33(a)  
Baseline Energy Separation for External Separation FES

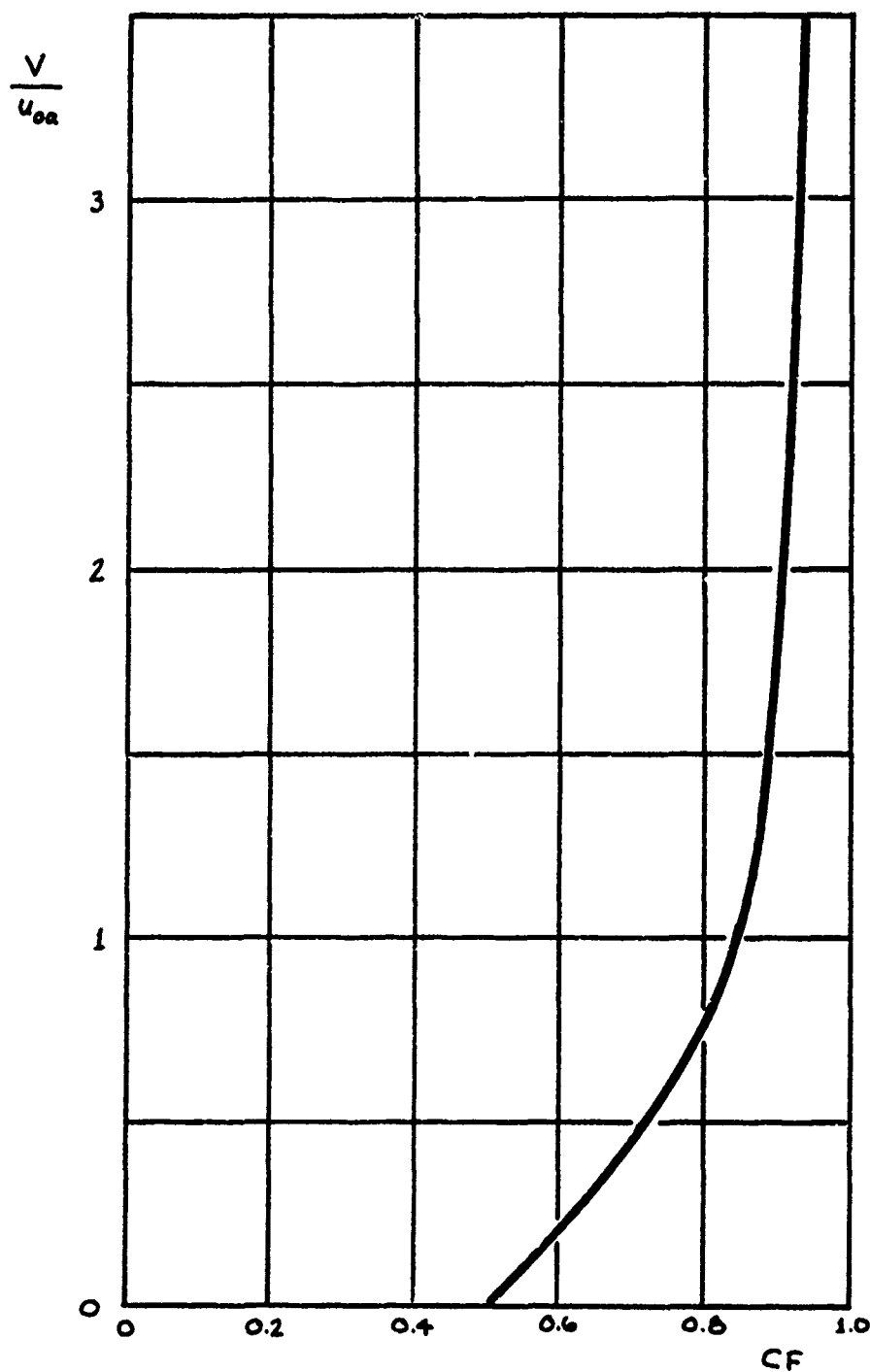


Figure 33(b)  
Baseline Rotor Velocity for External-Separation FES

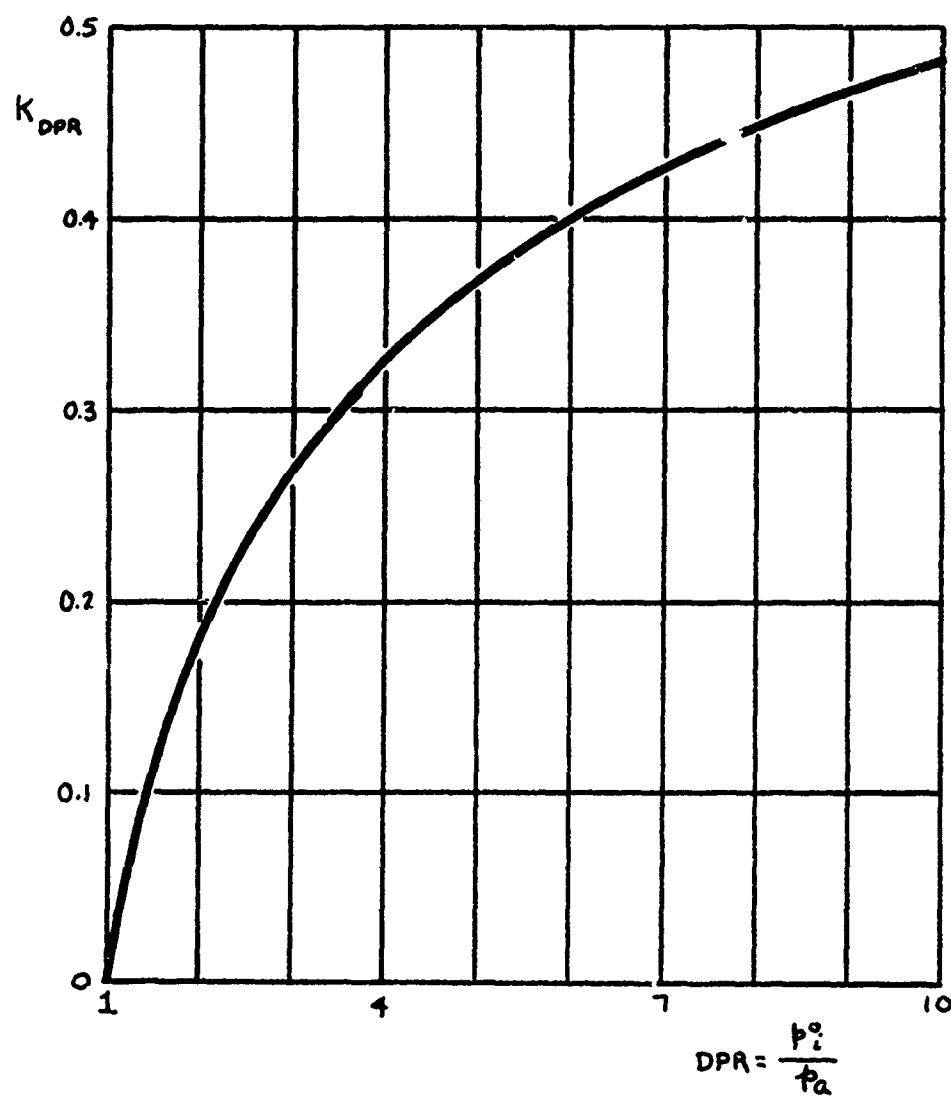


Figure 34  
Pressure Ratio Scale Factor

It is seen from Figure 33(a) that for the baseline case, wherein there is no prerotation, the minimum obtainable CF is 0.5, corresponding to  $\beta = 0$ . No energy separation occurs at this condition, since the rotor velocity is zero. The jet emerging from the nozzle splits isentropically into two jets (Figure 31) of equal size which, since the nozzle is stationary in  $F_U$ , also have stagnation temperatures equal to the inlet value  $T_i^0$ . As  $\beta$  is increased, both CF and energy separation increase rapidly: at the modest nozzle inclination of  $30^\circ$ ,  $CF = 0.75$  and the cold output exhibits a total temperature drop that is already 67% of the maximum that is possible thermodynamically for any given DPR. As  $\beta$  tends toward  $90^\circ$ , CF tends to unity and the total temperature drop tends to the thermodynamic maximum: the residual kinetic energy in flow "a" vanishes,  $T_a^0 = T_a$ , and therefore one has in the theoretical limit at  $90^\circ$

$$\left(\frac{T_a^0}{T_i^0}\right)_{\beta=90^\circ} = \left(\frac{p_a^0}{p_i^0}\right)^{\frac{\gamma-1}{\gamma}} = \left(\frac{1}{DPR}\right)^{\frac{\gamma-1}{\gamma}}$$

This theoretical limit cannot actually be reached, of course, since both the hot output total temperature and rotor velocity tend to infinity as  $\beta \rightarrow 90^\circ$ ; however, it is clear that the optimum value of CF for the FES is necessarily large, and there is every reason to expect the total temperature drop at the optimum condition to be a large fraction of the isentropic value based on DPR calculated above.

When the various effects pertaining to equations (18) are introduced, the principal effects are seen in the cold output; the hot output and rotor velocity are of course also affected somewhat, but this is of less direct concern for the present discussion than the cold output effect.

Therefore, the influences of the various effects explored next will be summarized primarily by means of the cold-output (lower) portion of the energy separation performance diagram.

From here on, the term "temperature drop" will be used for brevity in discussing the cold output, but it is to be understood that this always refers to total temperature.

Effect of prerotation. Figure 35 shows performance as modified by prerotation, together with an auxiliary plot of the effect on rotor velocity. Several values of the dimensionless prerotation  $\frac{u_i}{u_{0a}}$  are indicated, and it is seen that positive prerotation is beneficial, except at very large values of  $\beta$ : an optimum prerotation exists for any given  $\beta$  such that  $u_a = 0$ , hence  $T_a^* = T_a$ . Smaller  $u_i$  leaves  $u_a > 0$  while larger  $u_i$  causes  $u_a < 0$ . Thus, a given magnitude of temperature drop can be achieved at a smaller  $\beta$  with prerotation than is required without it; since there are practical physical limitations on the values of  $\beta$  which can be built into a real device, this in effect means that prerotation can enable greater temperature drops to be attained than would be possible otherwise. It is seen that prerotation also increases the rotor velocity at any given  $\beta$  (hence, CF), but it is worthy of note that a given temperature drop is obtained at a lower rotor speed with prerotation than without. A penalty is, however, paid for this in a reduction of CF, since  $\beta$  is reduced.

Effect of nozzle efficiency. The nozzle efficiency  $\eta$  enters into the performance equations in a variety of rather complicated ways if the other items in equations (18) differ from the baseline values, as one may see by glancing back through the analysis, and it would be well



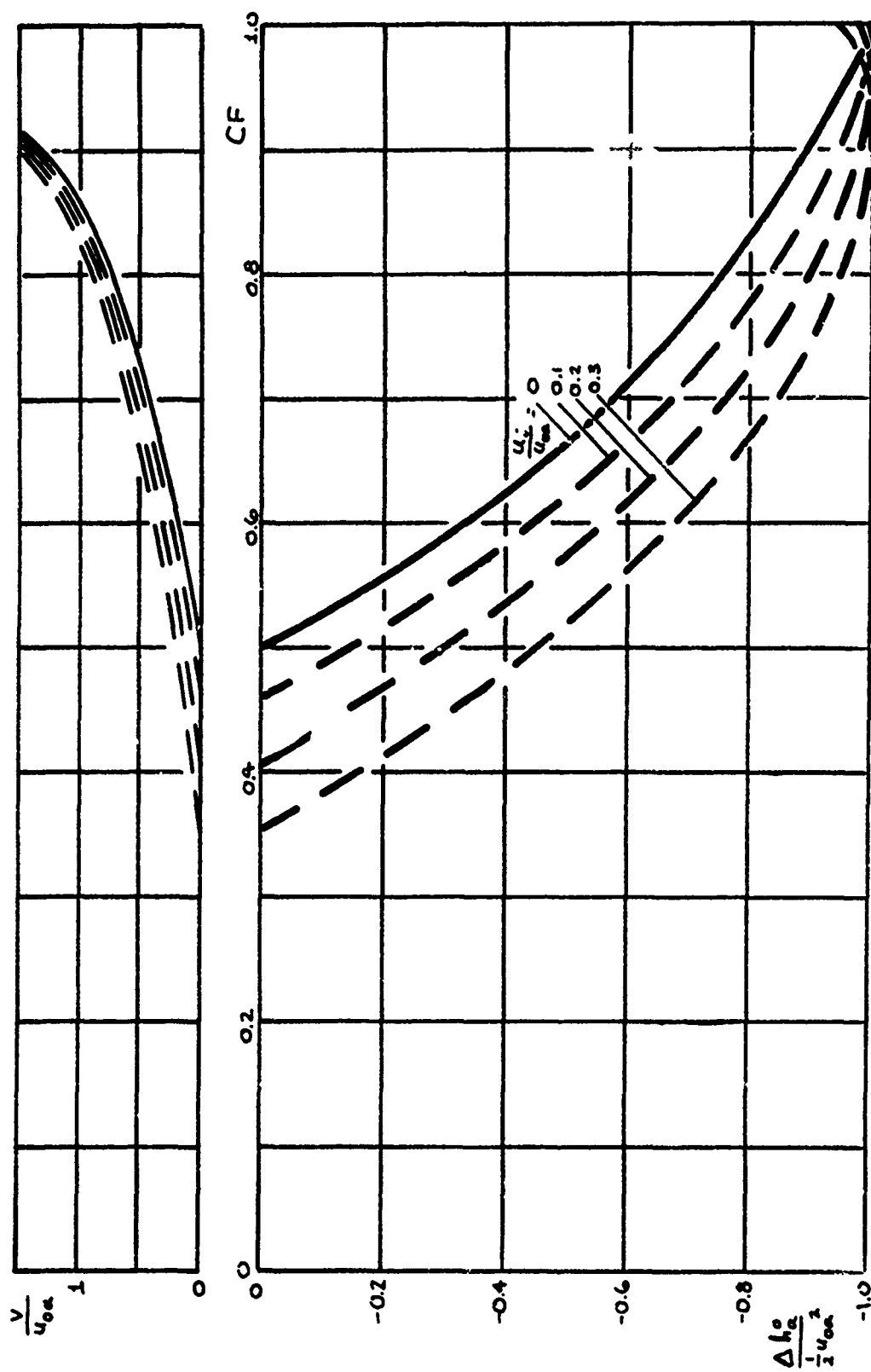


Figure 35  
Effect of Prerotations (External Separation)

to remember this for design optimization. However, when  $\eta$  is considered alone, its effect on the temperature drop could hardly be simpler: temperature drop is directly proportional to  $\eta$ . This can be seen by inspecting equations (6), (7), and (9'), and is depicted in Figure 36.

Effect of rotor torque. Figure 37 presents the effect of rotor torque for several values of the rotor torque parameter  $\lambda$ . The effect is seen to be distinctly nonlinear: for small values of  $\lambda$ , the cold output temperature is degraded but little, but the sensitivity to  $\lambda$  increases as  $\lambda$  does. It is also to be noted that the larger  $\beta$  (hence  $CF$ ) is, the less sensitive the performance is to rotor torque.

It will be noticed that the curves for  $\lambda \neq 0$  terminate in a line of maximum power extraction, rather than at zero temperature drop. This does not mean that the region above this curve is not physically meaningful, since obviously it is. Rather, the explanation may be seen with the aid of the auxiliary sketch of  $\lambda$  versus  $L$ , wherein  $L_{lock}$  is the torque necessary to lock a rotor having a given  $\beta$  and operating at a given DPR. The parameter  $\lambda$  is proportional to the product of  $L$  and  $\omega$ , and hence goes to zero both when the torque is zero and when  $\omega$  is large enough to lock the rotor ( $\omega = 0$ ); in between, there is a maximum, corresponding to maximum shaft power extraction. One may therefore define a maximum power extraction line like that shown. If it were desired to cover the entire torque range  $0 \leq L \leq L_{lock}$ , this could be done by simply considering both branches of the  $\lambda$  curves. However, since rotor torque is considered in the present context as a perturbation presumably caused by bearing friction, only small values of torque are considered

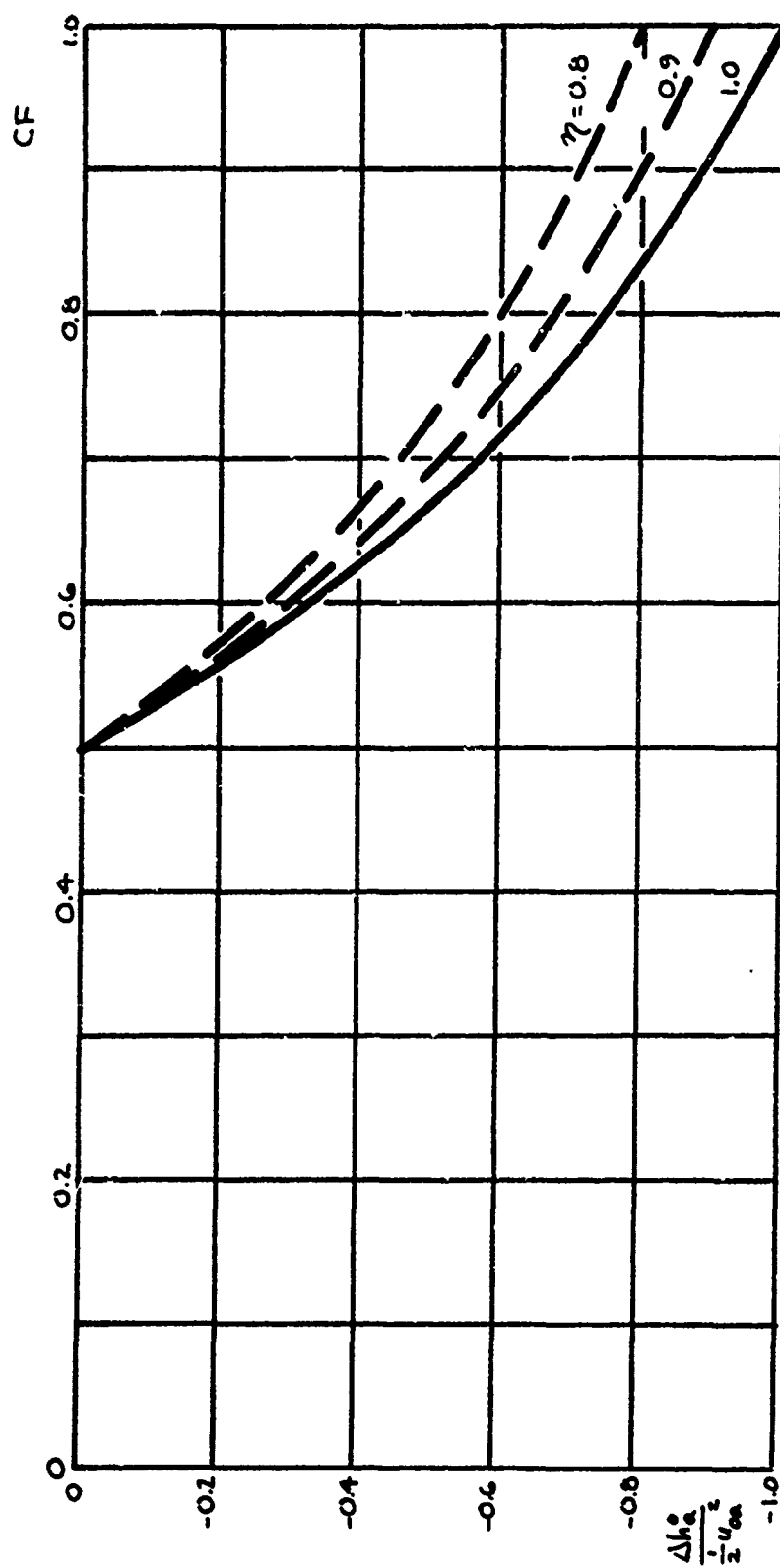


Figure 36  
Effect of Nozzle Efficiency (External Separation)

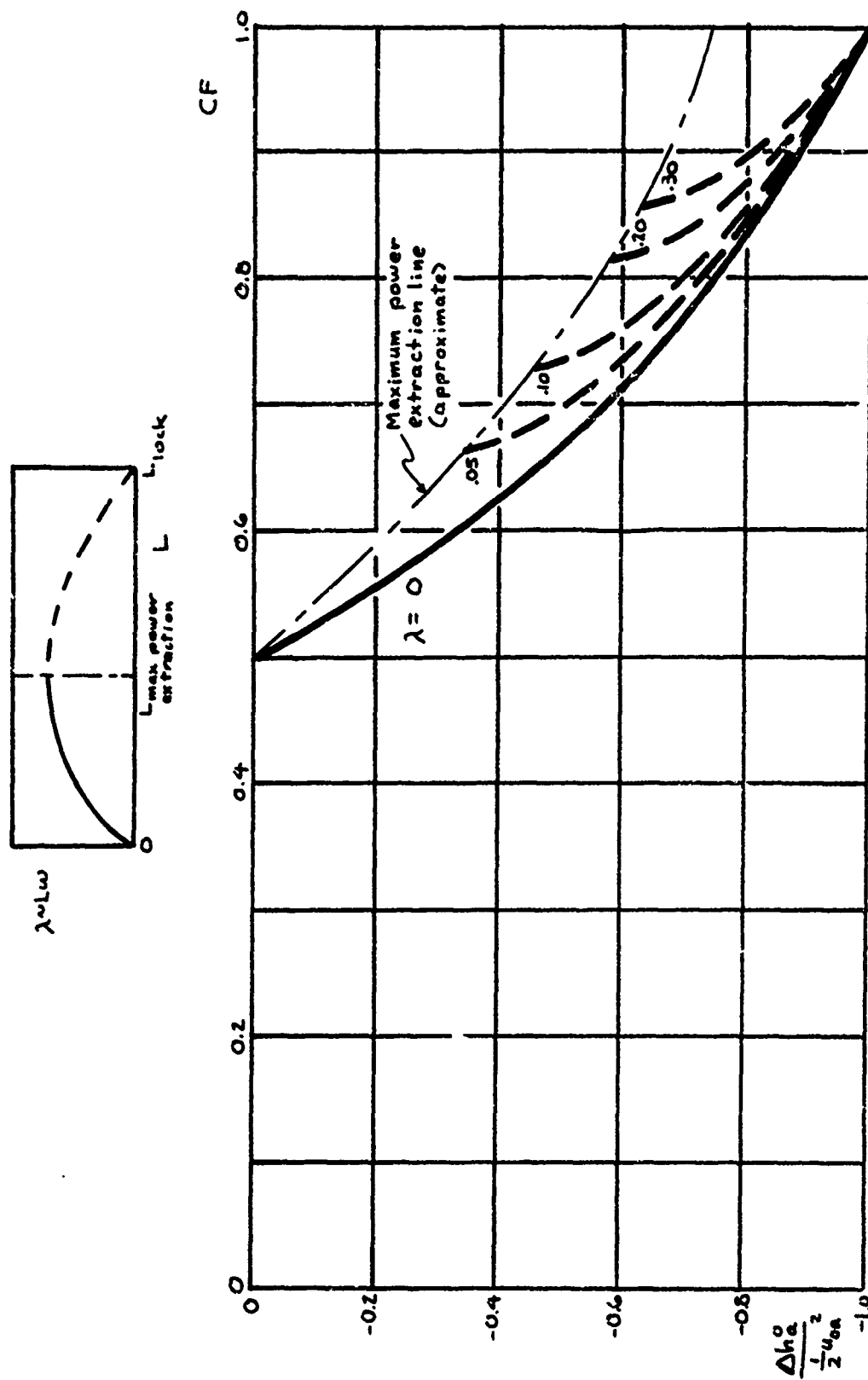


Figure 37  
Effect of Rotor Torque (External Separation)

relevant, and therefore only the low-torque branch of each  $\lambda = \text{constant}$  curve is included.

Effect of offset angle. As will be seen in the portion of the paper dealing with collection effects, a nonzero offset angle  $\epsilon$  is relevant both for the avoidance of nonsteadiness and for minimization of the influence of the boundary layer on the impingement wall, which is moving as viewed by an observer in  $F_S$ . Figure 38 depicts the influence of  $\epsilon$  on performance.

It is seen that a nonzero  $\epsilon$  causes the temperature drop curve to take on a qualitatively different character at large values of  $\beta$  (hence CF). Instead of tending to maximum temperature drop at  $CF = 1$ , the maximum occurs for some CF which is large but less than unity, with the temperature drop decreasing to zero at  $CF = 1$ . If  $\epsilon$  is small, which would presumably be the case, the curve remains very close to the  $\epsilon = 0$  curve up to a CF very close to unity, whereas for larger values of  $\epsilon$  both the magnitude of the maximum temperature drop and the CF at which it occurs are more markedly reduced.

Effect of unequal discharge pressures. The effect of a discharge pressure differential  $\delta p$  enters analytically by three routes: (i) by the last term of equations (8') and (9'); (ii) by the differential-pressure factor  $K_{\delta p}$ , defined with reference to equation (10'); and (iii) through modification of the massflow ratio  $\mu$  according to (16").

Consider again  $K_{\delta p}$ . Since  $\frac{\delta p}{p_m}$  is taken to be small,  $\frac{\delta p}{p_m} \doteq \frac{\delta p}{p_a}$ . Also, note that

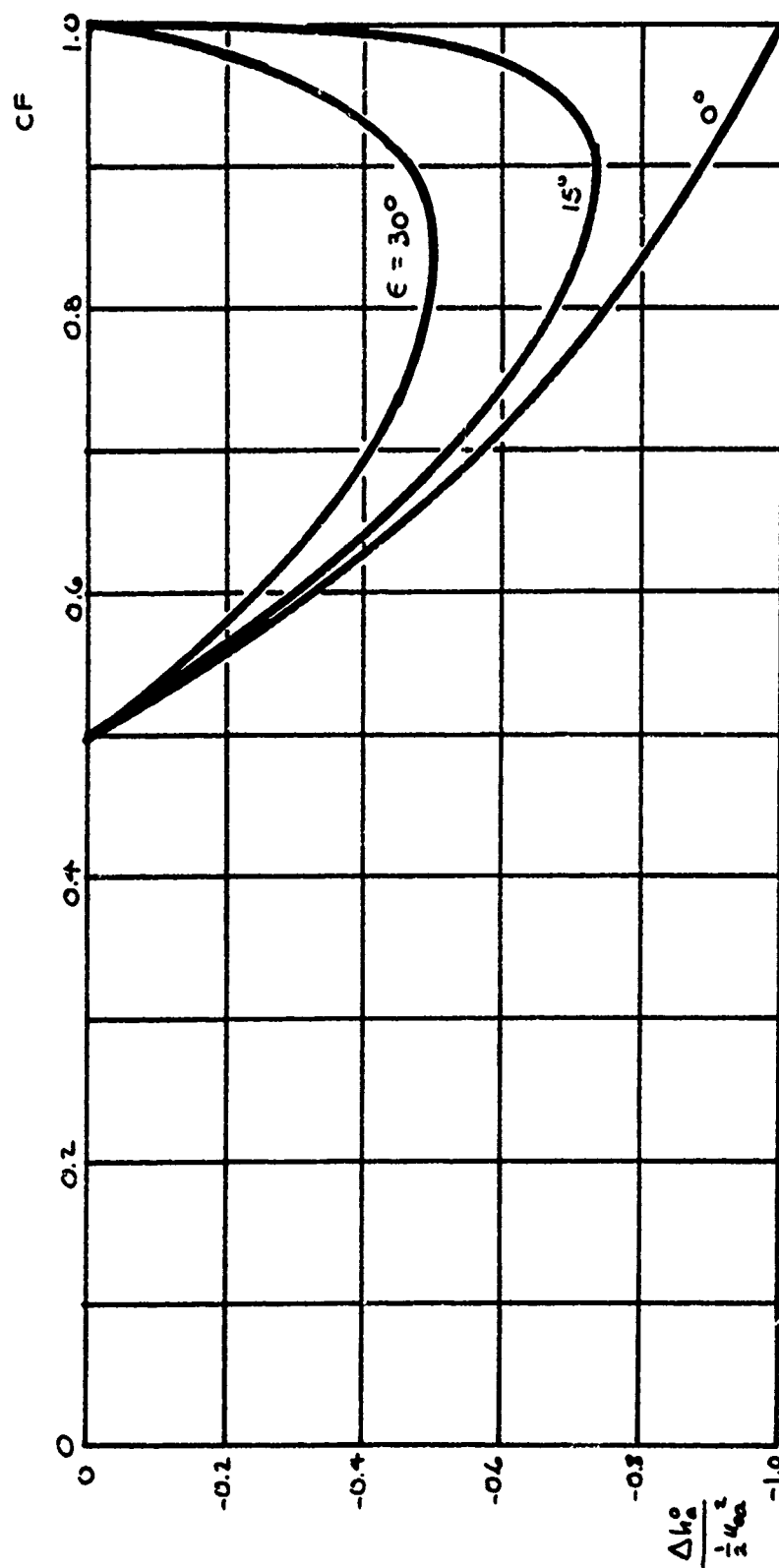


Figure 38  
Effect of Offset Angle

$$\begin{aligned}\frac{u_{ob}}{u_{oa}} &= \frac{u_{ob}}{u_{on}} \cdot \frac{u_{on}}{u_{oa}} \\ &= \left(\frac{u_{on}}{u_{oa}}\right)^2 \\ &= K_{\delta p}\end{aligned}$$

so that

$$\left(\frac{u_{ob}}{u_{oa}}\right)^2 = \left[1 - \frac{\gamma-1}{2\gamma} \frac{(DPR)^{-\frac{\gamma-1}{\gamma}}}{1 - (DPR)^{-\frac{\gamma-1}{\gamma}}} \frac{\delta p}{p_a}\right]^2$$

or

$$\frac{\delta p}{p_a} = \frac{\gamma}{\gamma-1} \left(DPR^{\frac{\gamma-1}{\gamma}} - 1\right) \left[1 - \left(\frac{u_{ob}}{u_{oa}}\right)^2\right] \quad (19)$$

In Figure 39,  $\frac{\delta p}{p_a}$  is plotted as a function of DPR and  $\left(\frac{u_{ob}}{u_{oa}}\right)^2$ . Thus, in assessing the effect of a pressure differential, one may stipulate the ratio  $\left(\frac{u_{ob}}{u_{oa}}\right)^2$  in plots of energy separation performance nondimensionalized by  $\frac{1}{2}u_{oa}^2$  and then, at any given DPR, use Figure 39 to determine the dimensionless pressure differential  $\frac{\delta p}{p_a}$  to which this corresponds.

Noting the definitions of  $K_{DPR}$  and  $K_{\delta p}$ , the bracketed portion of the coefficient of  $\frac{\delta p}{p_m}$  in equations (8') and (9') may be written

$$\left\{ \left[1 - \left(\frac{p_m}{p_o}\right)^{\frac{\gamma-1}{\gamma}}\right]^{-1} - \eta \right\} = \left\{ \frac{1}{K_{\delta p} K_{DPR}} - \eta \right\}$$

Here,  $K_{\delta p}$  follows from the stipulated value of  $\left(\frac{u_{ob}}{u_{oa}}\right)^2$ .  $K_{\delta p}$  is always near unity given the restriction of the analysis to small  $\frac{\delta p}{p_m}$ , and  $\eta = 1.0$

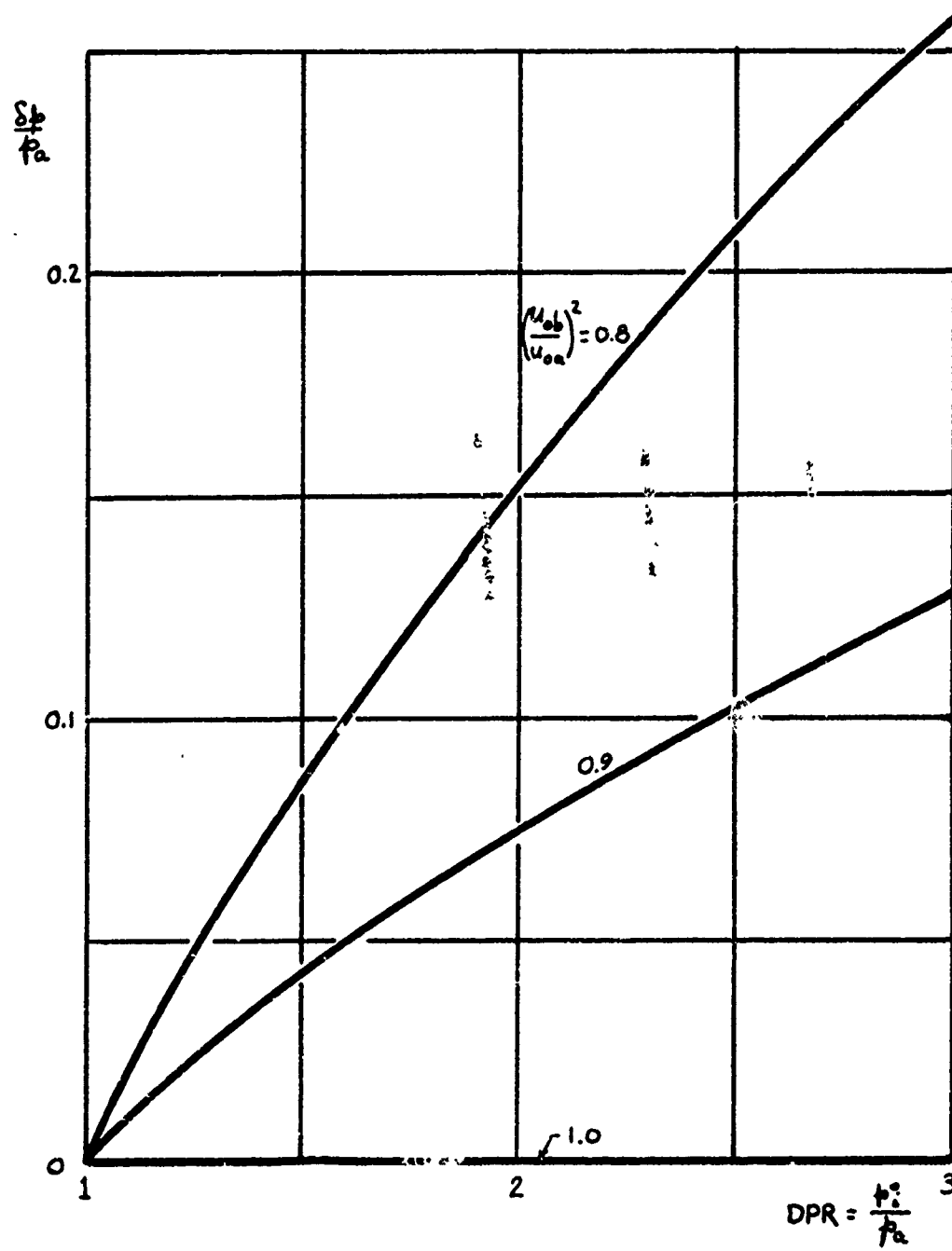


Figure 39  
Required  $\delta p$  to Give Prescribed  $\left(\frac{u_{ob}}{u_{oe}}\right)^2$



for the present case, so the bracket may be written approximately as

$$\left\{ \frac{1}{K_{DPR}} - 1 \right\} = \frac{1}{DPR^{\frac{\gamma-1}{\gamma}} - 1}$$

Therefore, equation (9') reduces for the present case, noting that  $u_i = 0$  and  $\frac{V}{C_n} = \sin \beta$ , to

$$\frac{h_a^0 - h_i^0}{\frac{1}{2} u_{en}^2} = 2 \left[ \left( \frac{V}{u_{en}} \right)^2 - \frac{C_n V}{u_{en}^2} \right] - \left[ 1 - \left( \frac{u_{ob}}{u_{oa}} \right)^2 \right] \frac{\sin \beta}{2}$$

As for the influence of the differential pressure on  $\mu$ , (16") reduces to a very simple form if all items in equations (18) have their baseline values except, of course, for  $\frac{\delta p}{p_n}$ . Since  $\frac{\delta p}{p_n}$  is small, (16") may be written as

$$\frac{\mu}{\mu_0} = 1 - \frac{1}{8 M_0^2} \frac{(2 \frac{d}{d_n} - 1)}{(1 - \sin^2 \beta)} \frac{\delta p}{p_a}$$

where  $M_0$  denotes the nozzle-exit Mach number in  $F_5$  which would be obtained at the given DPR with no pressure differential across the jet. With zero prerotation and a loss-free nozzle,

$$M_0 = \frac{M_{DPR}}{\cos \beta}$$

where

$$M_{DPR} = \sqrt{\frac{2}{\gamma-1} \left[ (DPR)^{\frac{\gamma-1}{\gamma}} - 1 \right]}$$

Substituting for  $M_o$  and noting that  $\cos^2 \beta = 1 - \sin^2 \beta$ ,

$$\frac{\mu}{\mu_o} = 1 - \frac{(2 \frac{d_d}{d_m} - 1)}{\gamma M_{DPR}^2} \frac{\delta p}{p_a} \quad (16'')$$

where  $M_{DPR}$  is as defined above. Equation (16'') applies if all conditions except  $\delta p$  are "baseline," and in this case it is seen that  $\frac{\mu}{\mu_o}$  rather remarkably is independent of  $\beta$ . Figure 40 presents a plot of the baseline differential-pressure sensitivity,

$$K_{\mu} \equiv \frac{(2 \frac{d_d}{d_m} - 1)}{\gamma M_{DPR}^2}$$

as a function of DPR and the channel-height factor  $\frac{d_d}{d_m}$ . It will be noted that the larger the channel height, the greater the sensitivity to a pressure differential, as would be expected physically; and this channel-height effect is a very strong one.

Combining equations (16'') and (19) and using the definition of  $M_{DPR}$ , the DPR dependence in  $\frac{\mu}{\mu_o}$  drops out to leave:

$$\frac{\mu}{\mu_o} = 1 - (2 \frac{d_d}{d_m} - 1) \left[ 1 - \left( \frac{u_{ob}}{u_{oa}} \right)^2 \right] \quad (20)$$

Thus, by treating the differential-pressure effect in terms of  $\left( \frac{u_{ob}}{u_{oa}} \right)^2$ , it proves possible to suppress all dependencies on DPR except that contained in the basic scale factor  $K_{DPR}$ . Generalized performance plots for the effect of unequal discharge pressures may now be drawn.

Figure 41 shows the effect of unequal discharge pressures for two values of  $\left( \frac{u_{ob}}{u_{oa}} \right)^2$  and three values of the channel-height factor  $\frac{d_d}{d_m}$ .

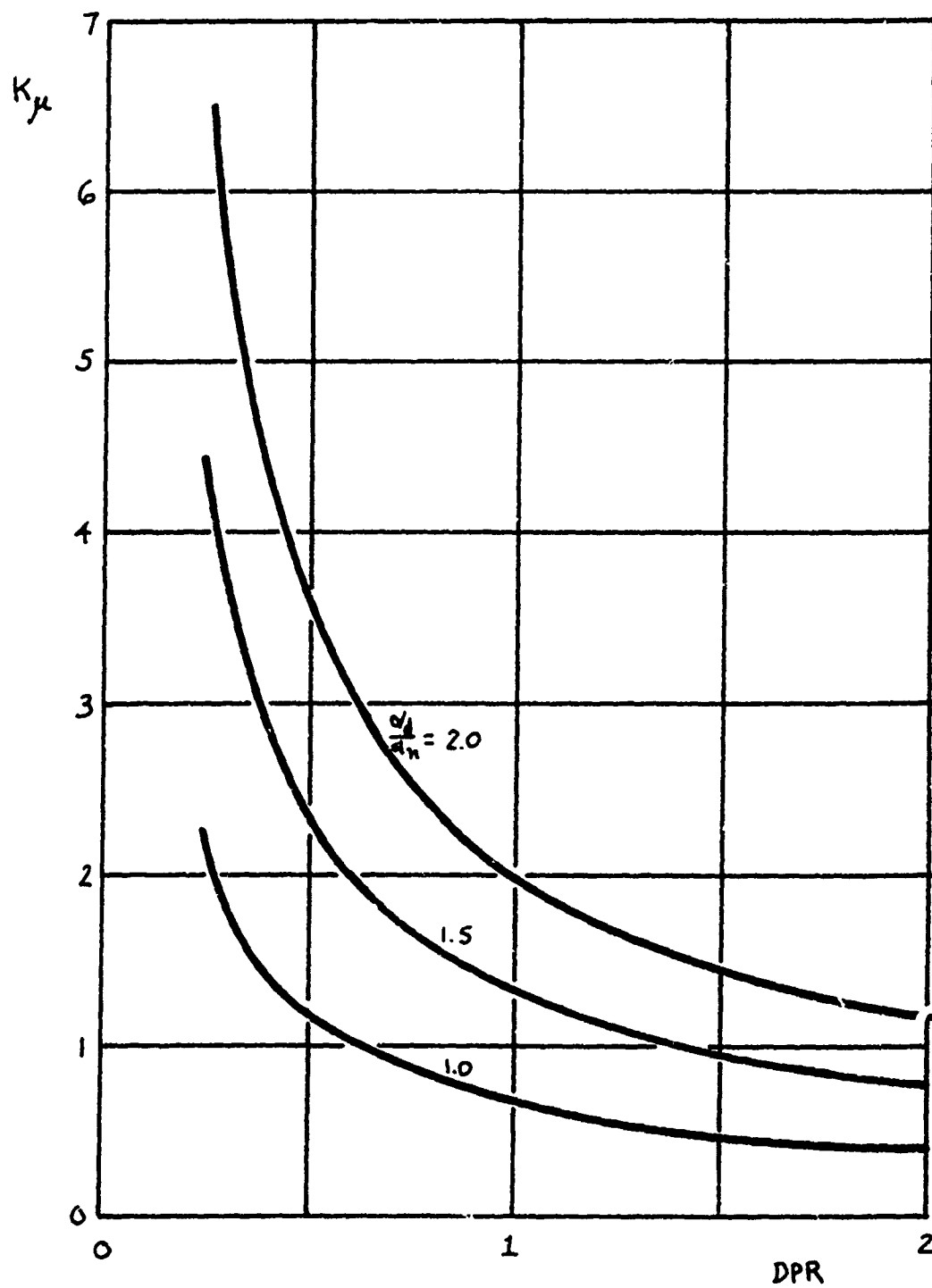


Figure 40  
Baseline Pressure-Differential Sensitivity

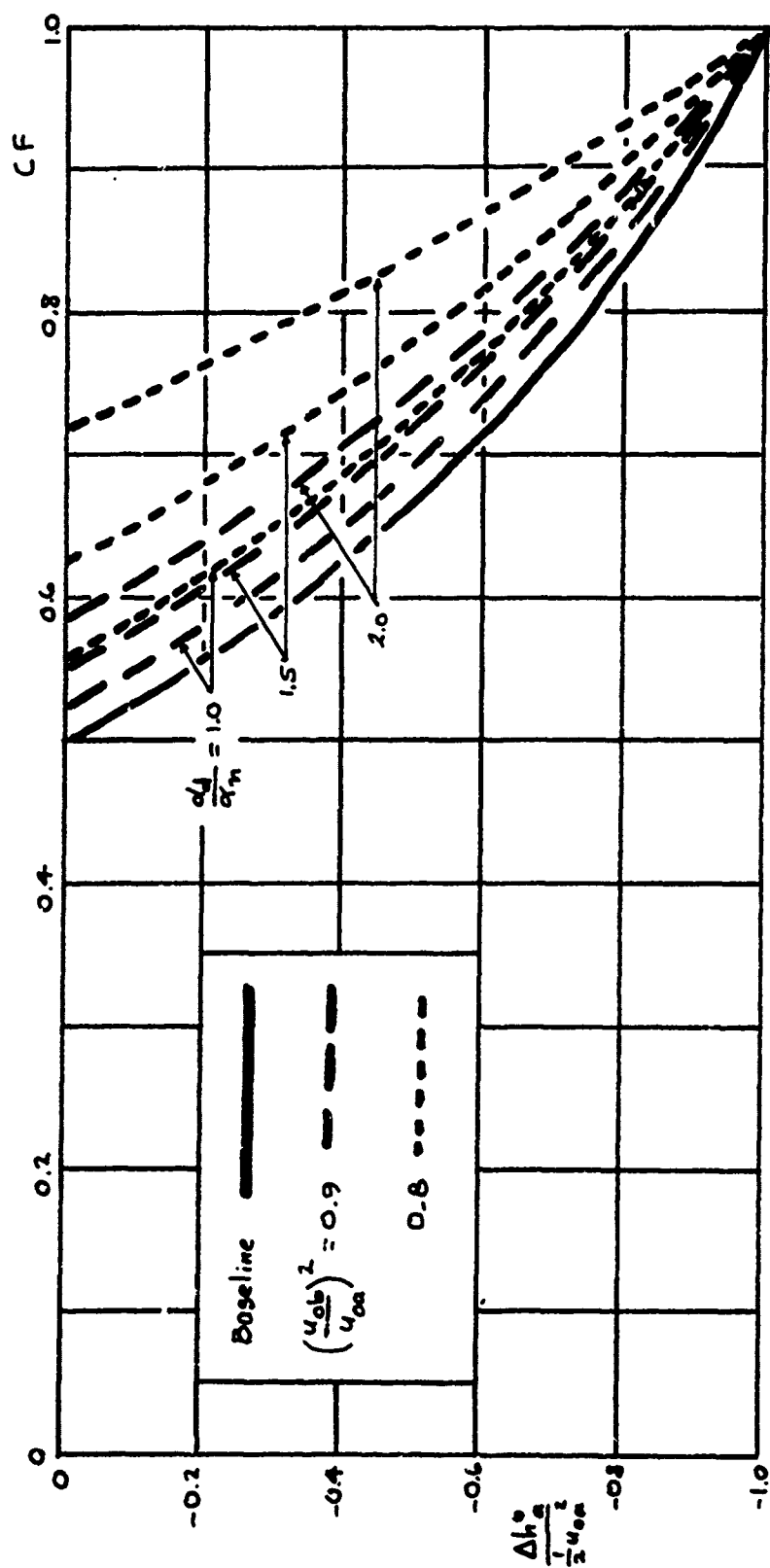


Figure 41  
Effect of Unequal Discharge Pressures (External Separation)

It may be seen that the effect of a positive  $\delta p$  --i.e., flow "b" discharging to a higher pressure than flow "a"--is to shift the performance characteristics to the right. This comes about through the combined effects of a slight reduction in the magnitude of the temperature drop and a pronounced increase in the cold fraction. For a given, fixed-geometry energy separator and a given driving pressure ratio, therefore, use of an elevated back pressure for the "b" flow would result in increased refrigeration capacity with only a minor penalty in the magnitude of the temperature drop.

## 2. Internal-Separation Configuration

Analytical model. Figure 42 depicts schematically the internal-separation FES configuration, compare Figure 3(a), with important analytical parameters indicated. As in the external-separation design, Figure 29, flow "i" is introduced into the rotor with, in general, some prerotation  $\omega_i$  which is positive if in the direction indicated. There is a pair of nozzles (or more generally, a set or such nozzle pairs) which discharge in opposite senses relative to rotation, flow "b" being the one discharged in a positive sense. For the sake of diagrammatic simplicity, the two nozzles are drawn as if they discharged in the same plane; in reality, they would be arranged so as to discharge into separate collectors, which is readily accomplished by placing the two nozzles in different planes. Both nozzles are assumed to discharge at the same effective distance  $R$  from the center of rotation, so that the tangential velocity at each nozzle exit is  $V = \omega R$ . As with the external-separation design, a radial-flow arrangement is sketched, but the flow may be axial instead; indeed,

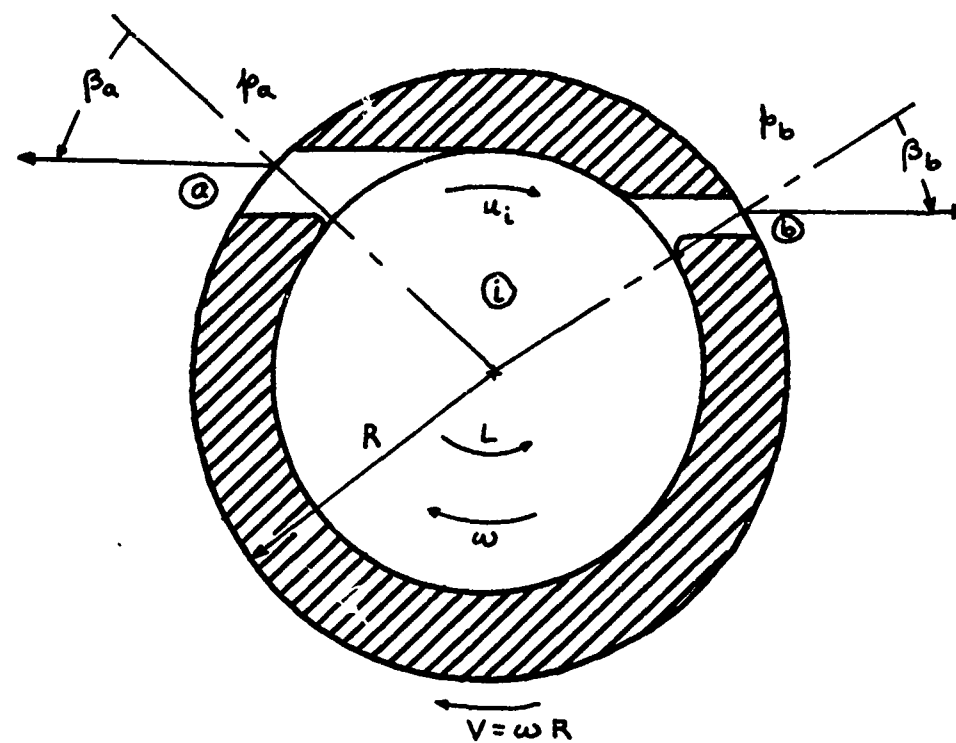


Figure 42  
Internal-Separation FES Configuration

internal-separation devices have been built in both radial and axial forms. As in the external-separation analysis, allowance is made for the presence of a resisting torque  $L$  and for inequality of the discharge pressures  $p_a$  and  $p_b$ .

In the external-separation device, it will be recalled that the nozzle inclination  $\beta$  was of prime importance, governing (with modifications due to the other effects considered) both  $\mu$  and the rotor velocity, hence energy separation. In the internal-separation device, an equivalent role is played by the ratio of nozzle areas. The analog of the offset angle  $\epsilon$  which appears in the external-separation device is seen in the internal-separation configuration for the case of  $\beta_a = \beta_b \equiv 90^\circ - \epsilon$ ; consideration of unequal nozzle inclinations  $\beta_a$  and  $\beta_b$  which will be included is equivalent to considering  $\epsilon$  to be different for the "a" than for the "b" discharge in the external-separation case. The effect of the overall level of nozzle efficiency is also included, as was done in the external-separation analysis; however, it is additionally relevant to consider here the possibility that  $\eta_a \neq \eta_b$ , since for example turning losses may be more serious for the "b" nozzle than for the "a" nozzle.

Analysis. In the external-separation analysis, it was necessary to take explicit account of the impingement-deflection process whereby the single flow emerging from the nozzle is divided into two flows "a" and "b". It was natural in that case to develop the basic energy separation equations (8') and (9') and the massflow ratio equation (16) with reference to mean conditions at the nozzle exit, and then to apply the adjustment factor  $K_{sp}$  in arriving at energy separation performance in the desired form, equation (10'). Further, it proved useful to restrict

the analysis to the case of small differences between the discharge pressures in order to simplify the analysis.

Where the internal-separation configuration is concerned, however, flows "a" and "b" are of course not the products of an impingement-deflection process. Therefore, the mean between the "a" and "b" discharge conditions no longer retains the same physical significance, and one might as well take the reference discharge condition to be that of flow "a". Also, the difference in discharge velocities  $\kappa_a$  and  $\kappa_b$  (which in the internal-separation case reflects differences in both discharge pressures and nozzle efficiencies) need not be restricted to small values, and this requirement is therefore dispensed with for the internal-separation analysis.

The equation for the total enthalpy difference is

$$h_b^0 - h_a^0 = (h_b - h_a) + \frac{1}{2}(\kappa_b^2 - \kappa_a^2) + (\bar{\kappa}_b - \bar{\kappa}_a) \cdot \bar{V}$$

where

$$\bar{\kappa}_b \cdot \bar{V} = \kappa_b V \sin \beta_b$$

$$\bar{\kappa}_a \cdot \bar{V} = -\kappa_a V \sin \beta_a$$

Thus, one may readily arrive at:

$$h_b^0 - h_a^0 = \left(1 + \frac{\kappa_b}{\kappa_a} \frac{\sin \beta_b}{\sin \beta_a}\right) \kappa_a V \sin \beta_a + \frac{1}{2}(\kappa_b^2 - \kappa_a^2) + (h_b - h_a)$$

Noting that

$$h_a + \frac{1}{2} \kappa_a^2 = h_a^0 \quad , \quad h_b + \frac{1}{2} \kappa_b^2 = h_b^0$$

$$h_a^0 = h_b^0 = h_n^0$$



the last two terms cancel leaving

$$h_b^o - h_a^o = \left(1 + \frac{c_b}{c_a} \frac{\sin \beta_b}{\sin \beta_a}\right) c_a V \sin \beta_a \quad (21)$$

The tangential momentum equation may be obtained by noting the equivalence of the internal-separation rotor to two dissimilar external-separation rotors, mechanically connected in such a way that one (corresponding to the "a" nozzle) drives the other backwards. This equivalence may be traced with the aid of Figure 43. Part (a) of the Figure illustrates the conceptual division of the rotor into two single-nozzle components, each of which is subjected to a torque such that the resultant rotor velocity is the one that occurs in the real rotor. This reflects the fact that the two halves of the internal-separation rotor exert equal and opposite torques on one another at steady state, except as modified by bearing friction. Figure 43(b) points out the fact that rotor "b" as it emerges from Figure 43(a) is physically equivalent to its mirror image, which may then be compared with the definitions made in Figure 29.

It is also worth noting parenthetically here a further implication of this equivalence: namely, that an impingement-deflection pattern like that of Figure 29 can well occur for each flow, "a" and "b", after it leaves the nozzle. For example, a design which is attractive for its simplicity uses a radial-flow rotor with perhaps two "a" nozzles in one axial plane and two "b" nozzles in another. The flow from each nozzle strikes the outer wall of the annular collector and splits up in a manner similar to that in Figure 29. Of course, this has no effect on the net total temperature of the flow as it is removed from the collector, since the subflows come back together to depart via the common port; but losses

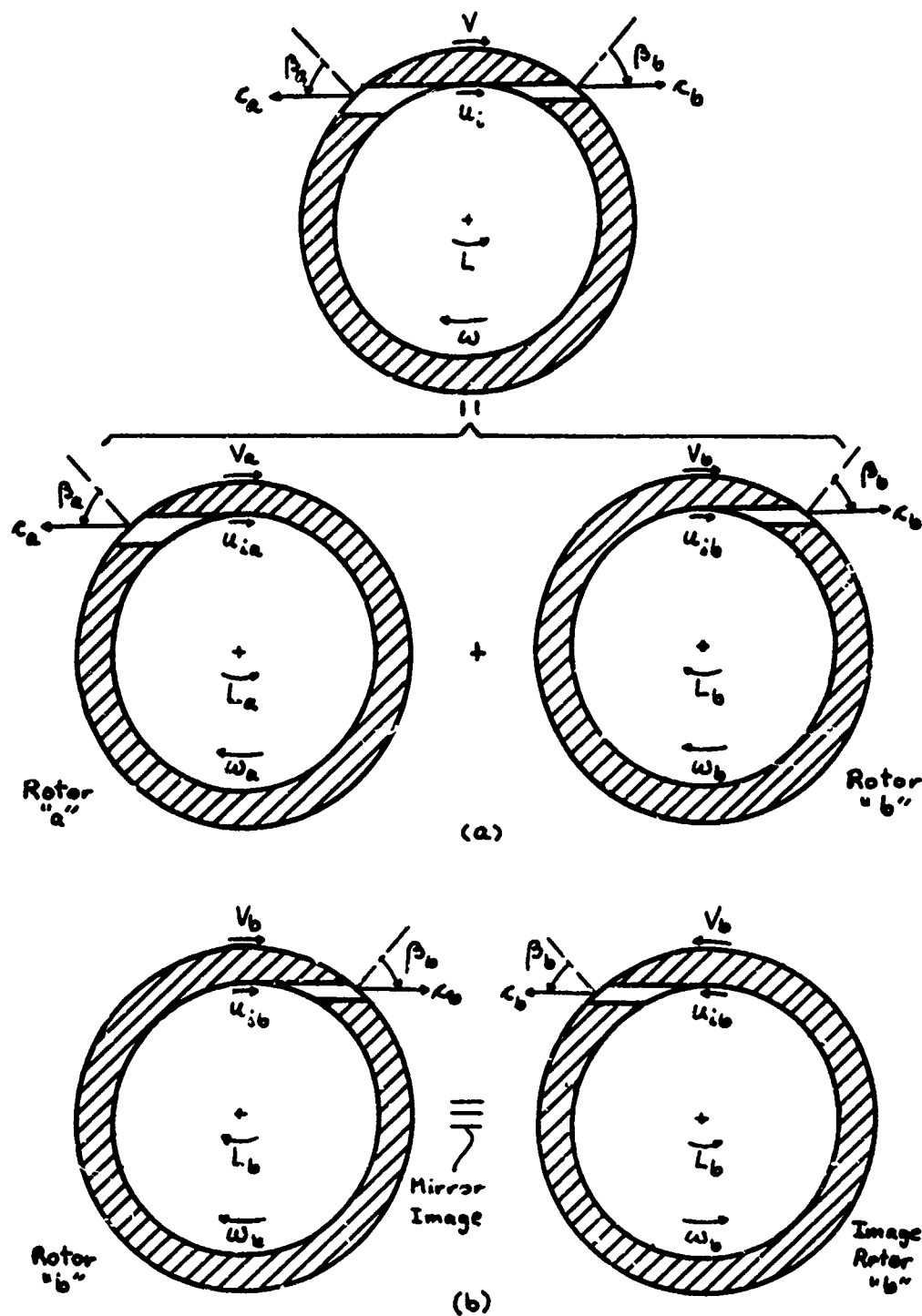


Figure 43  
Equivalence of Internal-Separation Rotor to  
Back-to-Back External-Separation Rotors

due to mixing and other effects may take place within the collector, thereby reducing the total pressure at the collector exhaust port. An understanding of the behavior of the impingement-deflection pattern gained in the external-separation context thus would provide an important starting point for analysis of collection effects in this type of internal-separation FES. Should such losses prove significant, one corrective measure would be simply to have many nozzles (or in the limit, an airfoil cascade) arranged around the rotor, so as to eliminate the impingement-deflection flow pattern.

Continuing now with the derivation of the internal-separation tangential momentum equation, it may be seen that for image rotor "b",

$$\omega_b = -\omega$$

$$V_b = -V$$

$$u_{i,b} = -u_i$$

$$L_b > 0$$

(torque is in "resisting" sense)

Rotor "a" is already oriented properly in Figure 43(a) for comparison with the definitions of Figure 29, and it is seen that

$$\omega_a = \omega$$

$$V_a = V$$

$$u_{i,a} = u_i$$

$$L_a > 0$$

(torque is in "resisting" sense)

Tangential momentum equation (2'), developed for the external-separation analysis, may now be applied to each of the components, rotor "a" and image rotor "b". Assuming that the flow from each nozzle discharges in the plane of rotation,  $\epsilon = 0$  for both component rotors. Also, the mean flow conditions at the nozzle exit, denoted in the external-

separation analysis by  $( )_n$ , are exactly what are desired here for each nozzle, so the  $( )_n$  notation may be replaced by  $( )_a$  and  $( )_b$  respectively. Then:

$$\frac{c_a V_a}{u_{oa}^2} \sin \beta_a - \left( \frac{V_a}{u_{oa}} \right)^2 + \frac{u_{ia} V_a}{u_{oa}^2} = \frac{1}{2} \gamma_a \lambda_a$$

$$\frac{c_b V_b}{u_{ob}^2} \sin \beta_b - \left( \frac{V_b}{u_{ob}} \right)^2 + \frac{u_{ib} V_b}{u_{ob}^2} = \frac{1}{2} \gamma_b \lambda_b$$

or

$$\frac{c_a V}{u_{oa}^2} \sin \beta_a - \left( \frac{V}{u_{oa}} \right)^2 + \frac{u_{ia} V}{u_{oa}^2} = \frac{1}{2} \gamma_a \lambda_a \quad (2'a)$$

$$- \frac{c_b V}{u_{ob}^2} \sin \beta_b - \left( \frac{V}{u_{ob}} \right)^2 + \frac{u_{ib} V}{u_{ob}^2} = \frac{1}{2} \gamma_b \lambda_b \quad (2'b)$$

The internal-separation tangential momentum equation is to be obtained by combining equations (2'a) and (2'b) according to the torque relationship that exists between the two components. From the definition in equation (5d),

$$\lambda_a = \frac{L_a \omega_a / m_a}{h_i^a - h_a} = \frac{L_a \omega / m_a}{h_i^a - h_a}$$

$$\lambda_b = \frac{L_b \omega_b / m_b}{h_i^b - h_b} = \frac{L_b (-\omega) / m_b}{h_i^b - h_b}$$

The net torque  $L$  experienced by the internal-separation rotor at the

top of Figure 43(a) is

$$L = L_a - L_b$$

or

$$L_b = L_a - L$$

Substituting for  $L_b$  and introducing  $\mu = \frac{m_b}{m_a}$ ,  $\lambda_b$  becomes

$$\lambda_b = -\frac{1}{\mu} \frac{h_i^0 - h_a}{h_i^0 - h_b} \left[ \frac{L_a \omega / m_a}{h_i^0 - h_a} - \frac{L \omega / m_a}{h_i^0 - h_a} \right]$$

or, defining the overall torque parameter for the internal-separation rotor as

$$\lambda \equiv \frac{L \omega / (m_a + m_b)}{h_i^0 - h_a}$$

one obtains for  $\lambda_b$

$$\lambda_b = -\frac{1}{\mu} \frac{h_i^0 - h_a}{h_i^0 - h_b} \left[ \lambda_a - (1 + \mu) \lambda \right]$$

or alternatively, for  $\lambda_a$

$$\lambda_a = -\mu \frac{h_i^0 - h_b}{h_i^0 - h_a} \lambda_b + (1 + \mu) \lambda$$

Substituting for  $\lambda_a$  in equation (2'a) gives

$$\frac{\kappa_a V}{u_{oa}^2} \sin \beta_a - \left(\frac{V}{u_{oa}}\right)^2 + \frac{u_i V}{u_{oa}^2} = -\mu \frac{h_i^\circ - h_b}{h_i^\circ - h_a} \frac{\eta_a}{\eta_b} \left(\frac{1}{2} \eta_b \lambda_b\right) + \frac{1}{2} \eta_a (1+\mu) \lambda$$

Replacing  $\frac{1}{2} \eta_b \lambda_b$  by its equivalent by means of (2'b) and rearranging, one may obtain

$$\frac{\kappa_a V}{u_{oa}^2} \sin \beta_a \left(1 - k \mu \frac{\kappa_b \sin \beta_b}{\kappa_a \sin \beta_a}\right) - \left(\frac{V}{u_{oa}}\right)^2 (1 + k \mu) + \frac{u_i V}{u_{oa}^2} (1 + k \mu) = (1 + \mu) \left(\frac{1}{2} \eta_a \lambda\right) \quad (22)$$

where

$$k \equiv \frac{h_i^\circ - h_b}{h_i^\circ - h_a} \frac{\eta_a}{\eta_b} \left(\frac{u_{oa}}{u_{ob}}\right)^2$$

But with the definition of nozzle efficiency, equation (5c), one may write

$$\frac{\eta_a}{\eta_b} = \frac{h_i^\circ - h_a}{h_i^\circ - h_b} \cdot \frac{\frac{1}{2} u_{ob}^2}{\frac{1}{2} u_{oa}^2}$$

whence  $k = 1$ . Thus, the internal-separation tangential momentum equation is

$$\left(\frac{1 - \mu \frac{\kappa_b \sin \beta_b}{\kappa_a \sin \beta_a}}{1 + \mu}\right) \frac{\kappa_a V}{u_{oa}^2} \sin \beta_a - \left(\frac{V}{u_{oa}}\right)^2 + \frac{u_i V}{u_{oa}^2} = \frac{1}{2} \eta_a \lambda \quad (22')$$

The relationship between stagnation enthalpy in  $F_S$  and that in  $F_U$  led, in the external-separation analysis, to equation (3'). The analogous equation needed for the internal-separation configuration may be obtained by again noting Figure 43 and writing for component rotor "a"

$$\left(\frac{\kappa_a}{u_{oa}}\right)^2 = \eta_a + \left(\frac{V_a}{u_{oa}}\right)^2 - 2 \frac{u_{ia} V_a}{u_{oa}^2}$$

or

$$\left(\frac{\kappa_a}{u_{oa}}\right)^2 = \eta_a + \left(\frac{V}{u_{oa}}\right)^2 - 2 \frac{u_i V}{u_{oa}^2} \quad (23)$$

The total enthalpy sum equation is arrived at just as in the external-separation case by noting first that

$$h_a^o = h_a + \frac{u_a^2}{2}$$

$$h_b^o = h_b + \frac{u_b^2}{2}$$

where from the internal-separation geometry,

$$\vec{u}_a = \hat{e}_x (-\kappa_a \sin \beta_a + V) + \hat{e}_r (\kappa_a \cos \beta_a)$$

$$\vec{u}_b = \hat{e}_x (+\kappa_b \sin \beta_b + V) + \hat{e}_r (\kappa_b \cos \beta_b)$$

where the unit vectors  $\hat{e}_x$  and  $\hat{e}_r$  are in the direction of the rotor velocity  $\vec{V}$  and in the positive radial direction, respectively. With  $u^2 = \vec{u} \cdot \vec{u}$  and proceeding as before, there follows

$$h_b^o + h_a^o = 2(h_i^o + V^2 - u_i V) + \kappa_a V \sin \beta_a \left( \frac{\kappa_b}{\kappa_a} \frac{\sin \beta_b}{\sin \beta_a} - 1 \right) \quad (24)$$

Equations (22') and (23) must be solved for  $\frac{V}{u_{oa}}$  and  $\frac{\kappa_a}{u_{oa}}$ .

This parallels completely the external-separation analysis, and the manner of solution is the same. One obtains a pseudo-quadratic in  $\left(\frac{V}{u_{oa}}\right)^2$ ,

$$\left(\frac{V}{u_{0a}}\right)^2 (1 - B_i^2 + D_i) + \left(\frac{V}{u_{0a}}\right)^2 [\eta_a (\lambda - B_i^2) - C_i] + \frac{1}{\eta_a} \eta_a^2 \lambda^2 = 0 \quad (25)$$

where

$$B_i \equiv \left( \frac{1 - \mu \frac{\kappa_b \sin \beta_b}{\kappa_a \sin \beta_a}}{1 + \mu} \right) \sin \beta_a$$

$$C_i \equiv \left(\frac{u_i}{u_{0a}}\right)^2 + 2 B_i \frac{u_i}{u_{0a}} \sqrt{\eta_a + \left(\frac{V}{u_{0a}}\right)^2} - 2 \frac{u_i V}{u_{0a}^2}$$

$$D_i \equiv 2 B_i^2 \frac{(u_i/u_{0a})}{(V/u_{0a})}$$

Defining also

$$\bar{M}_i \equiv \frac{(B_i^2 - \lambda) + \frac{C_i}{\eta_a} + B_i \sqrt{(1 - \lambda)^2 - (1 - B_i^2) + 2(B_i^2 - \lambda) \frac{C_i}{\eta_a} + \left(\frac{C_i}{\eta_a}\right)^2} - D_i \lambda^2}{2(1 - B_i^2 + D_i)}$$

the solution of equation (25) is

$$\left(\frac{V}{u_{0a}}\right)^2 = \eta_a \bar{M}_i \quad (26)$$

whence also, using (23),

$$\left(\frac{\kappa_a}{u_{0a}}\right)^2 = \eta_a (1 + \bar{M}_i) - 2 \frac{u_i}{u_{0a}} \sqrt{\eta_a \bar{M}_i} \quad (27)$$

Dividing equation (21) by  $u_{0a}^2$  gives

$$\frac{h_b^0 - h_a^0}{u_{0a}^2} = \left(1 + \frac{\kappa_b \sin \beta_b}{\kappa_a \sin \beta_a}\right) \frac{\kappa_a}{u_{0a}} \frac{V}{u_{0a}} \sin \beta_a \quad (21')$$



and similarly equation (24) gives

$$\frac{h_b^0 + h_a^0}{u_{oa}^2} = \frac{h_i^0}{\frac{1}{2}u_{oa}^2} + 2\left(\frac{V}{u_{oa}}\right)^2 - 2\frac{u_i V}{u_{oa} u_{oa}} + \frac{\kappa_a}{u_{oa}} \frac{V}{u_{oa}} \sin \beta_a \left(\frac{\kappa_b \sin \beta_b}{\kappa_a \sin \beta_a} - 1\right) \quad (24')$$

Adding equations (21') and (24') and subtracting  $\frac{h_i^0}{\frac{1}{2}u_{oa}^2}$ ,

$$\frac{h_b^0 - h_i^0}{\frac{1}{2}u_{oa}^2} = 2\left[\left(\frac{V}{u_{oa}}\right)^2 - \frac{u_i V}{u_{oa}^2} + \left(\frac{\kappa_b \sin \beta_b}{\kappa_a \sin \beta_a}\right) \frac{\kappa_a V}{u_{oa}^2} \sin \beta_a\right] \quad (28)$$

Subtracting equation (21') and  $\frac{h_i^0}{\frac{1}{2}u_{oa}^2}$  from (24'),

$$\frac{h_a^0 - h_i^0}{\frac{1}{2}u_{oa}^2} = 2\left[\left(\frac{V}{u_{oa}}\right)^2 - \frac{u_i V}{u_{oa}^2} - \frac{\kappa_a V}{u_{oa}^2} \sin \beta_a\right] \quad (29)$$

Finally, dimensionless energy separation referenced to inlet stagnation conditions is found from (28) and (29) together with

$$\frac{h_j^0 - h_i^0}{h_i^0} = K_{OPR} \frac{h_j^0 - h_i^0}{\frac{1}{2}u_{oa}^2} \quad (30)$$

where "j" may refer to either flow "a" or "b" and  $K_{OPR} = \frac{\frac{1}{2}u_{oa}^2}{h_i^0}$  is plotted in Figure 34.

It is instructive to pause here to take note of the extent to which the internal-separation analysis draws upon and parallels that for the external-separation configuration, as this illustrates the basic equivalence of the two devices. The physical equivalence of the external-separation device to an internal-separation device with  $\beta_a = \beta_b = 90^\circ$  and the same  $\mu$  was noted in the INTRODUCTION; an inverse equivalence relationship described in Figure 43 has been utilized in the internal-

separation analysis. Also, the analyses progress in exactly similar ways, as can be seen by comparing equations (1) through (10') with equations (21) through (30). Equations (26) and (27) are identical in form to equations (6) and (7); the groupings  $C_i$ ,  $D_i$ , and  $\bar{M}_i$  are identical in form to  $C_e$ ,  $D_e$ , and  $\bar{M}_e$ , while  $B_i$  has a different appearance from  $B_e$  but plays exactly the same role. Indeed,  $\sin \beta_a$  in the definition of  $B_i$  has the same physical significance as  $\cos \epsilon$  in  $B_e$ ; the ratio  $\frac{\sin \beta_b}{\sin \beta_a}$  would correspond to considering  $\epsilon_a \neq \epsilon_b$  in the external-separation analysis (which was not done); and the presence of  $\frac{\kappa_b}{\kappa_a}$  reflects the fact that the internal-separation analysis is not restricted to small differences in  $\kappa_a$  and  $\kappa_b$  and the fact that the reference discharge condition is "a" rather than a mean condition "n" between discharges "a" and "b". This last item is also responsible for the asymmetry in the last terms of equations (28) and (29).

As in the external-separation analysis, the solution of (26) for  $\frac{V}{u_{oa}}$  is iterative if prerotation  $u_i$  is nonzero, through the entrance of groupings  $C_i$  and  $D_i$  in  $\bar{M}_i$ . Additionally, the internal-separation solution becomes iterative even for zero prerotation if  $\frac{\kappa_b}{\kappa_a} \neq 1$ : applying equation (3') to the component rotors one has

$$\left(\frac{\kappa_a}{u_{oa}}\right)^2 = \gamma_a + \left(\frac{V}{u_{oa}}\right)^2 - 2 \frac{u_i V}{u_{oa}^2}$$

$$\left(\frac{\kappa_b}{u_{ob}}\right)^2 = \gamma_b + \left(\frac{V}{u_{ob}}\right)^2 - 2 \frac{u_i V}{u_{ob}^2}$$

from which one may obtain

$$\frac{C_b}{C_a} = \sqrt{1 + \frac{\eta_a}{(C_a/u_{oa})^2} \left[ \frac{\eta_b}{\eta_a} \left( \frac{u_{ob}}{u_{oa}} \right)^2 - 1 \right]} \quad (31)$$

It is seen from (31) that if there is a difference in discharge pressures ( $u_{ob}/u_{oa} \neq 1$ ) or a difference in nozzle efficiencies ( $\eta_b/\eta_a \neq 1$ ),  $\frac{C_b}{C_a}$  becomes a function of  $C_a/u_{oa}$ , which by equation (23) is a function of  $\frac{V}{u_{oa}}$ , this of course being the item to be solved for by equation (26).

Baseline performance. Following the pattern of the external-separation analysis, the basic characteristics of the internal-separation device will be presented for a set of "baseline" conditions, after which departures from baseline conditions will be examined. The equations as developed allow simultaneous inclusion of all the effects treated, with full inclusion of the nonlinear interactions among variables. These interactions can be expected to be of considerable practical importance in design optimization, but for present purposes only the most fundamental effects will be explored by presenting the effect of perturbing each parameter alone from its baseline value. It should be mentioned here that Foa previously has carried out unpublished analyses which assess the individual effects of nozzle inclination, prerotation, and differences between nozzles "a" and "b" with respect to inclination, distance from the center of rotation, and discharge pressure;<sup>37</sup> however, no analysis has been available heretofore enabling examination of the nonlinear interactions cited above. It may also be noted that inclusion of effects in addition to those considered herein--e.g.,  $R_a \neq R_b$ ,  $u_{ia} \neq u_{ib}$ --would represent a straightforward extension of the analysis utilizing the equivalency concepts of Figure 43.

Baseline conditions for the internal-separation configuration will be defined as follows:

Nozzle inclinations	$\beta_a = \beta_b$	} (32)
Prerotations	$u_i = 0$	
Nozzle efficiencies	$\eta_a = \eta_b = 1$	
Torque	$L = 0$	
Discharge pressures	$p_a = p_b$	

It will be noticed below that for  $\beta_a = \beta_b = 90^\circ$ , the performance is identical to the baseline performance for the external-separation device, as it should be since the internal-separation nozzle inclination is really analogous to the external-separation offset angle. One might therefore reasonably choose  $\beta_a = \beta_b = 90^\circ$  as part of the baseline definition, noting that then the baseline would be the same for the internal- and external-separation configurations. However, from the standpoint of actual fabrication, the nozzle inclination is just as relevant in the internal- as in the external-separation configuration:  $\beta = 90^\circ$  in a flush-exit nozzle can be approached no more closely in real internal-separation hardware than in real external-separation hardware of the same family (consider Figure 43). Therefore, a family of "baseline" curves will be considered in the case of internal separation, there being such a curve for every value of nozzle inclination.

Figures 44(a,b) present baseline energy separation and rotor velocity curves for the internal-separation configuration. As already noted, the curves for  $\beta_a = \beta_b = 90^\circ$  are identical to the external-separation baseline curves, Figures 33(a,b). Curves for lesser values of nozzle inclination exhibit reduced performance, behaving like the

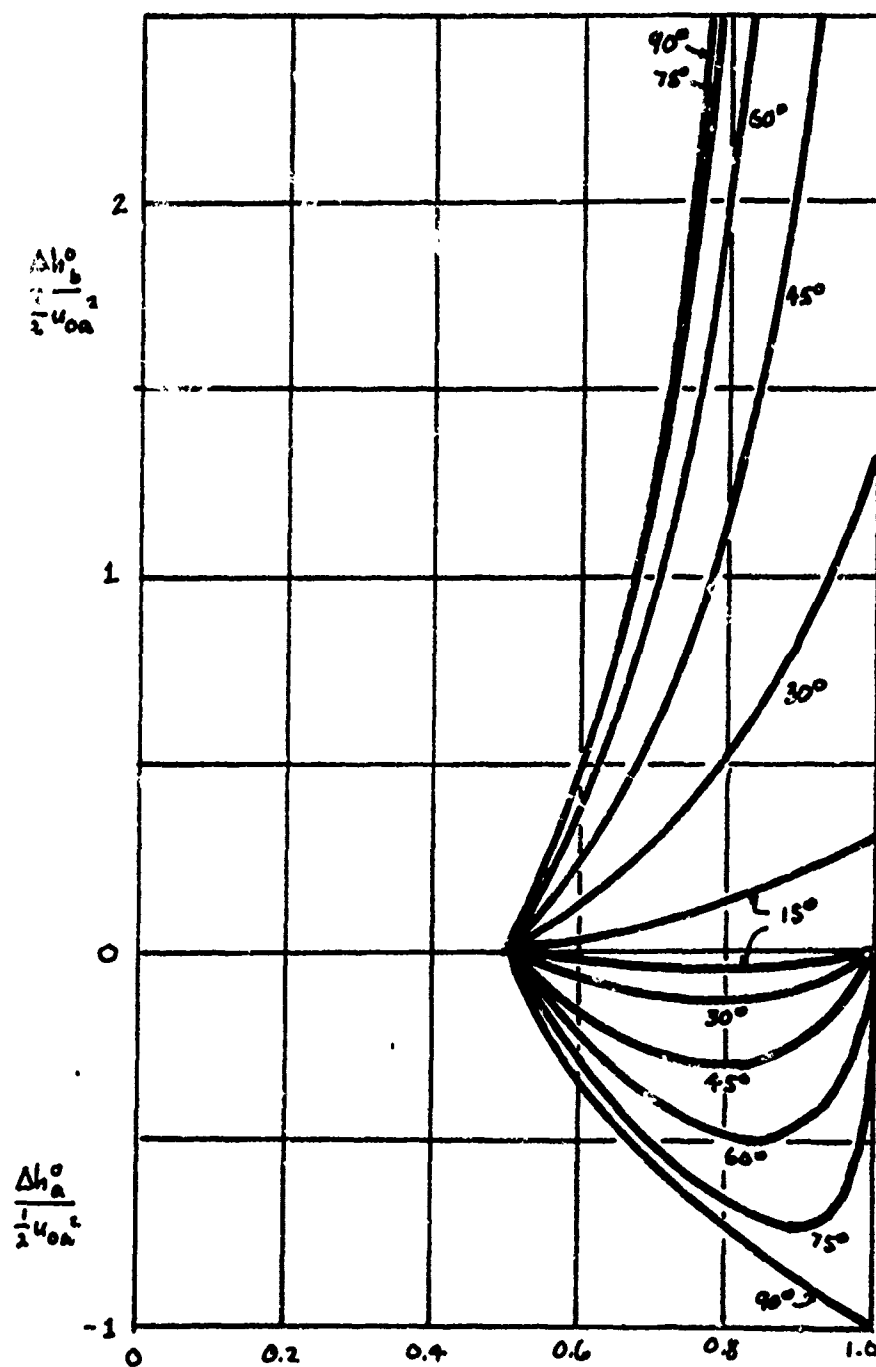


Figure 44(a)  
Baseline Energy Separation for Internal-Separation FES

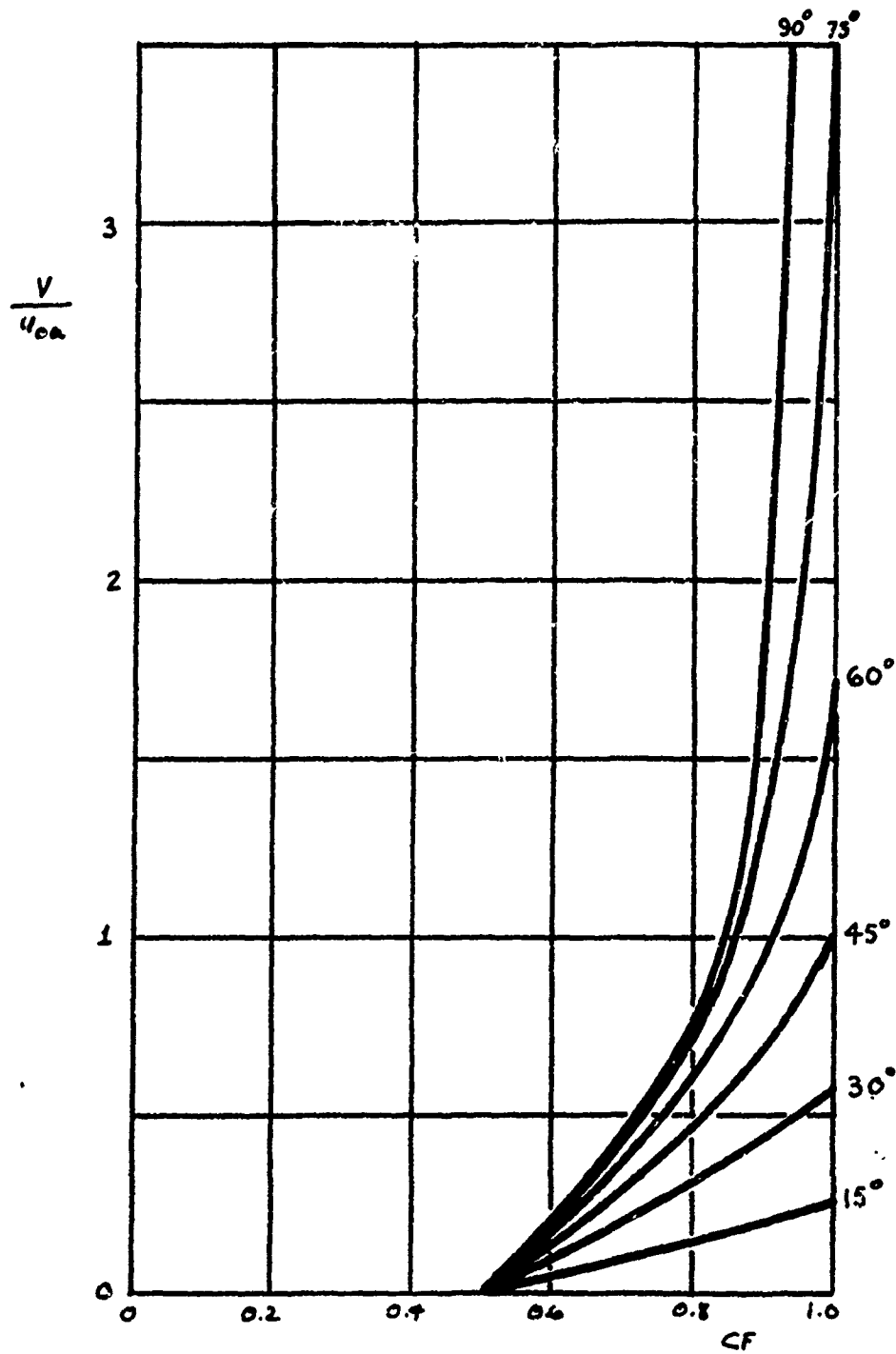


Figure 44(b)  
Baseline Rotor Velocity for Internal-Separation FES

external-separation curves of constant offset angle to which they are equivalent, Figure 38.

Figures 44(a,b) are drawn for completeness to include the whole range of nozzle inclinations from  $0^\circ$  to  $90^\circ$ , at  $15^\circ$  intervals. However, it is clear that the largest possible nozzle inclination should be used, so the curves for small inclinations are of minor practical interest. At the same time, it is also clear that the  $90^\circ$  curve cannot be reached physically with a flush-exit nozzle except perhaps with the aid of the Coanda effect. (The latter possibility has not been investigated.) Thus, of the curves included, those for  $75^\circ$  in Figures 44(a,b) are perhaps in the range of greatest practical interest for a flush-exit nozzle design; it is relevant to note, indeed, that an axial-flow internal-separation FES has been built which in fact has  $\beta_a = \beta_b = 75^\circ$ . The case of  $75^\circ$  will therefore be used to exemplify the effects of perturbations from the baseline conditions of equations (32). As was done in the external-separation case, discussion of these perturbations will center around the cold output curves.

Effect of prerotation. Figure 45 illustrates the effect of prerotation on performance, which is seen to be very strong and basically favorable. The maximum temperature drop increases dramatically, from 0.74 to 0.80 in dimensionless terms, with introduction of the relatively small dimensionless prerotation value of  $\frac{u_i}{u_{oa}} = 0.1$ . Further substantial gains accrue with increasing prerotation, though at a decreasing rate. The beneficial effect on maximum temperature drop is accompanied by a tendency for the cold fraction at maximum temperature drop to decrease, this effect

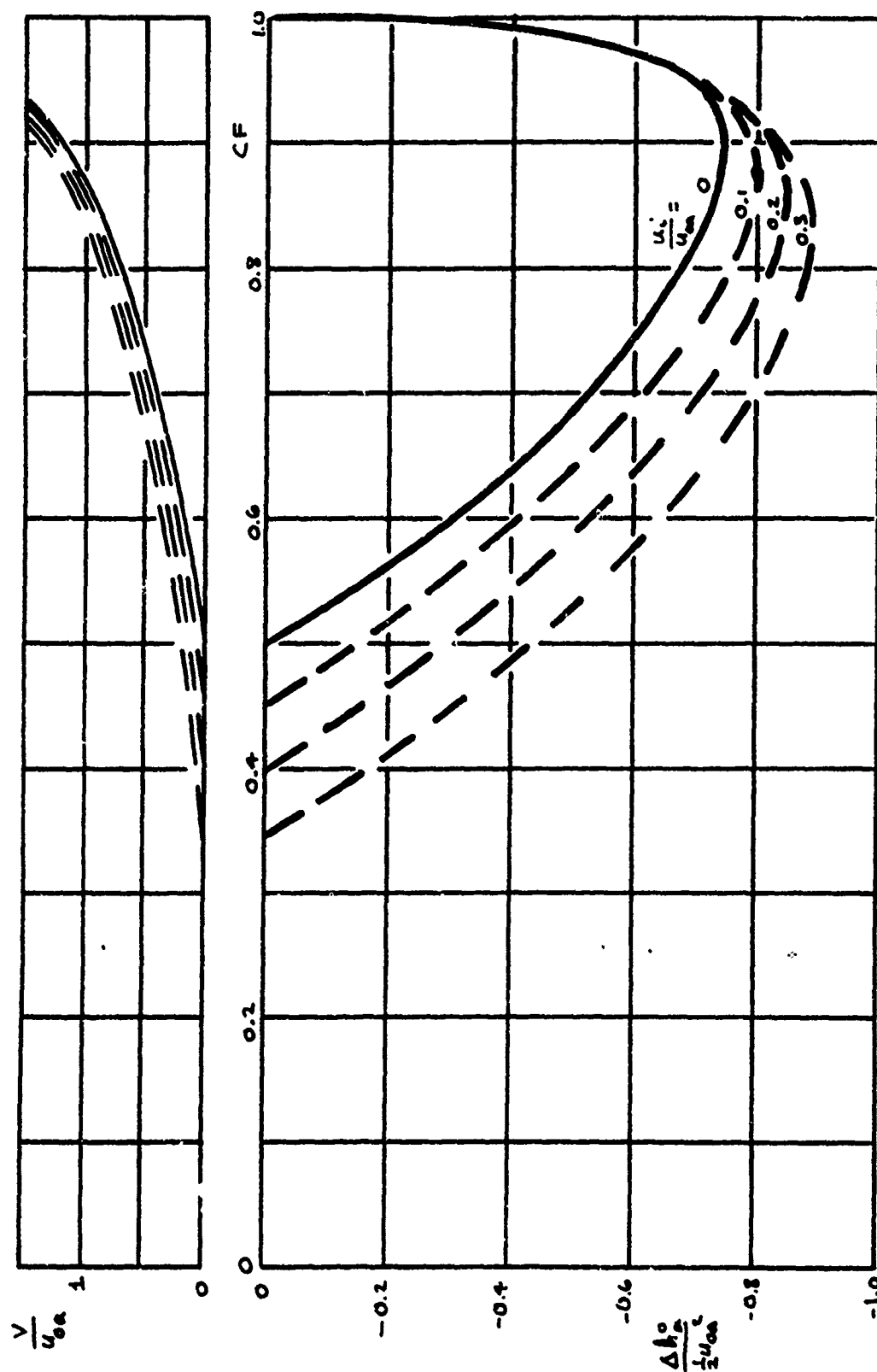


Figure 45  
Effect of Prerotations (Internal Separation)



becoming more pronounced at the higher values of prerotation. It will be noted that, for any given cold fraction (i.e., ratio of nozzle areas) there is an optimum prerotation just as in the external-separation case; for  $CF = 0.90$ , where the temperature drop without prerotation is greatest, this optimum prerotation would appear to be in the neighborhood of  $\frac{u_i}{u_{oa}} = 0.3$ .

It will also be noted that whereas the minimum CF achievable under baseline conditions is 0.5 (corresponding to  $\mu = 1.0$ , equal nozzle areas), prerotation causes the minimum CF to drop to something less than 0.5. This is of little practical concern in the present discussion, wherein maximum refrigeration capabilities are the focus, but might be of interest in applications utilizing the "b" flow, wherein a large hot fraction (hence small cold fraction) might be desirable. It should be noted here and in subsequent curves for which  $CF_{min} < 0.5$ , detailed calculations have been carried out only over the range  $0.5 \leq CF \leq 1.0$ , and  $CF_{min}$  found by using the momentum equation (22') to find  $\mu_{max}$  (where  $\frac{V}{u_{oa}} = 0$ ).

The effect of prerotation is not, of course, all "gravy." One naturally pays a price for increased performance, and this is seen in the auxiliary plot of rotor velocity in Figure 45: prerotation has the effect of increasing rotor speed, which is unfavorable structurally. Structural considerations can therefore be expected to impose limitations upon the amount of prerotation that can be used.

Effect of nozzle efficiencies. Departure from the baseline condition of  $\eta_a = \eta_b = 1.0$  can come about (i) as  $\eta \neq 1.0$ , (ii) as  $\eta_a \neq \eta_b$ , or of course (iii) as a combination of (i) and (ii). Figure 46 illustrates all three cases. The effect of overall efficiency level is as

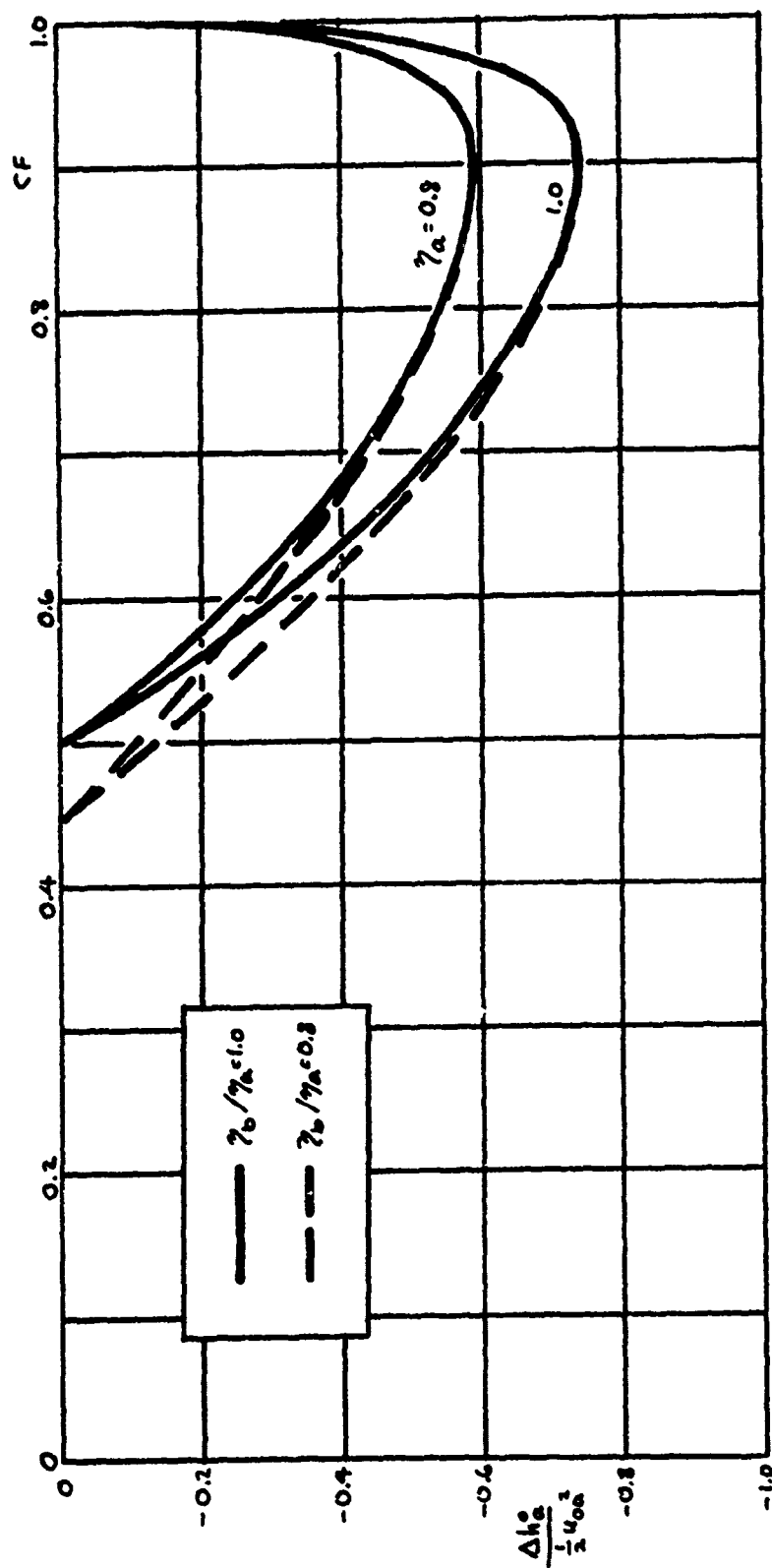


Figure 46  
Effects of Nozzle Efficiencies (Internal Separation)

before, performance being directly proportional to nozzle efficiency; this holds provided the ratio  $\frac{\eta_b}{\eta_a}$  is held constant, whether or not this ratio is unity. The effect of  $\frac{\eta_b}{\eta_a} \neq 1.0$  is seen as a shifting of the minimum CF, with the rest of the curve up to about the point of maximum temperature drop adjusting accordingly; for cold fractions corresponding roughly to the maximum temperature drop and larger, the effect of  $\frac{\eta_b}{\eta_a} \neq 1.0$  ceases to be discernible.

It will be noted that only the case of  $\frac{\eta_b}{\eta_a} < 1$  is assessed in Figure 46; the rationale here is that if one rides on the rotor, he observes the flow entering nozzle "a" without any great fuss, but having to negotiate a near reversal of direction in order to exit through the "b" nozzle. Thus, while there is no reason to anticipate difficulty in achieving high "a" nozzle efficiency, there could prove to be significant limitations on "b" nozzle efficiency.

Figure 46 shows that if the nozzles are sized such that the CF obtained corresponds to the maximum temperature drop as calculated for  $\frac{\eta_b}{\eta_a} = 1$ , there will be no noticeable effect on performance if the "b" nozzle actually has a lower efficiency. Indeed, it is seen that at lower cold fractions the performance is actually increased somewhat relative to the equal-efficiency case, a result which sounds strange: one expects to pay a penalty somehow for such inefficiency. And one does, but the penalty is a structural one rather than a direct performance effect: the lowered efficiency of the "b" nozzle results in a higher rotor speed than would occur for  $\eta_b = \eta_a$ . However, if structural considerations are not a dominant factor, the net observation to be made is that inefficiency in the "b" nozzle is of little importance to cold output performance.

The initial stipulation of the preceding paragraph concerning proper sizing of the nozzles must be noted carefully, as it implies that whatever  $\eta_b$  turns out to be, it is taken account of in the design. If this is not done, the results will be very different. For example, suppose one were to build a device with  $\beta_a = \beta_b = 75^\circ$  and with the nozzles sized so as to give  $CF = 0.90$ , with the assumption that the nozzle efficiencies were equal. If it should turn out that in fact  $\eta_b < \eta_a$ , the inefficiency of nozzle "b" will be reflected also in decreased "b" mass flow. Thus,  $F$  obtained experimentally will rise above the design value of 0.90. This will be accompanied not only by a rise in rotor speed but, as seen from the shape of the curve in Figure 46, a decrease in temperature drop as well. To rectify the situation, the "b" nozzle area must be increased, so as to reduce  $CF$  back to the proper value.

Effect of unequal nozzle inclinations. While efficiency of the "b" nozzle was seen above to have little impact on cold output performance capabilities, it is obviously very relevant if the total pressure of the "b" output flow is of interest, as it would be in pressure-boosting applications. One way of increasing "b" nozzle efficiency if turning losses should indeed prove important would be to reduce  $\beta_b$ , thereby reducing the extent of turning undergone by the flow discharged through the "b" nozzle. It is therefore of some interest to consider the effect on performance of choosing  $\frac{\beta_b}{\beta_a} < 1$ . (Since  $\beta_a$  should be made as large as possible, the opposite situation of  $\frac{\beta_b}{\beta_a} > 1$  does not appear to have much practical relevance.)

Figure 47 shows performance as modified by reduction of  $\beta_b$  to  $60^\circ$ ,  $45^\circ$ , and--as an extreme case-- $0^\circ$ . Qualitatively, the effect is

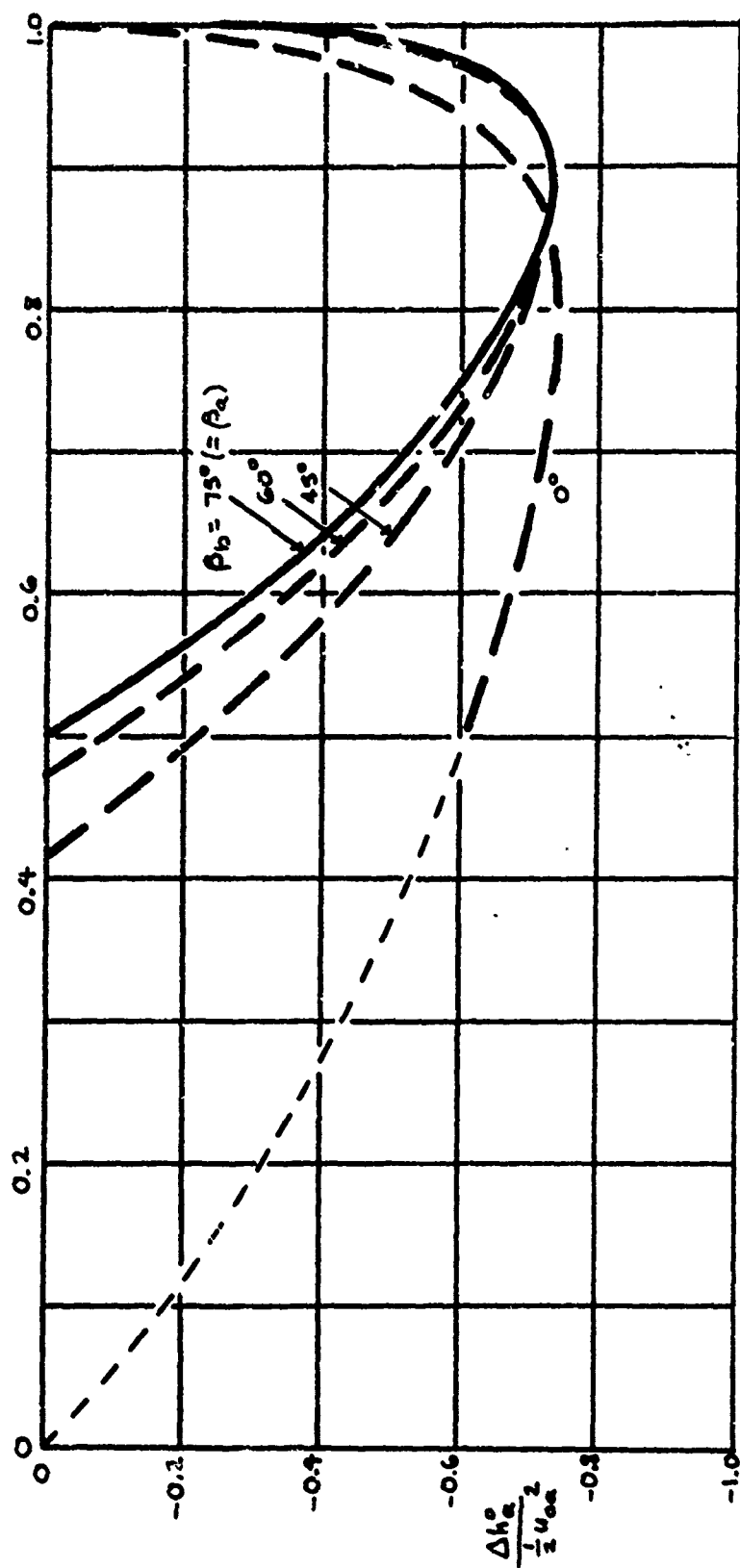


Figure 47  
Effect of Unequal Nozzle Inclinations (Internal Separation)

similar to that of having an inefficient "b" nozzle, which is reasonable since in both cases the tangential momentum of the "b" flow is reduced below baseline values. The maximum temperature drop is neither improved nor degraded, and the cold fraction for which it occurs is not altered greatly; such effect as does exist, however, is to decrease the optimum CF. It is interesting to note, again with possible uses of the "b" flow in mind, that by reducing  $\beta_b$  it is possible to maintain good energy separation performance at much lower values of CF than is obtained with equal angles: for example, with  $\beta_b = 0^\circ$ , the temperature drop at CF = 0.5 is still 83% of the maximum drop, whereas with equal angles the temperature drop at CF = 0.5 is zero. Indeed, for  $\beta_b = 0^\circ$ ,  $CF_{min} = 0$ ; the broken part of the curve indicates the presumed qualitative behavior over the range  $0 \leq CF \leq 0.5$ , but as mentioned earlier detailed calculations were not carried out in this range.

Effect of unequal discharge pressures. The effect of unequal discharge pressures is shown in Figure 48. As was done for the external-separation case, the discharge pressure differential is reflected in the ratio  $\left(\frac{u_{ob}}{u_{oa}}\right)^2$ ; Figure 39 may be used to relate the curves to corresponding values of  $\frac{p_b - p_a}{p_a}$  at any given driving pressure ratio. Also as in the external-separation case, only  $\frac{p_b}{p_a} > 1$  is considered in the curves, this corresponding to inducing an elevated back pressure on the "b" flow. It is seen that the qualitative effect is similar to those found earlier in connection with unequal nozzle inclinations and efficiencies: the effect on maximum temperature drop is nil, but the curves are shifted to the left of the maximum temperature drop. The physical common denominator in all these cases is the reduction of tangential momentum of the exiting

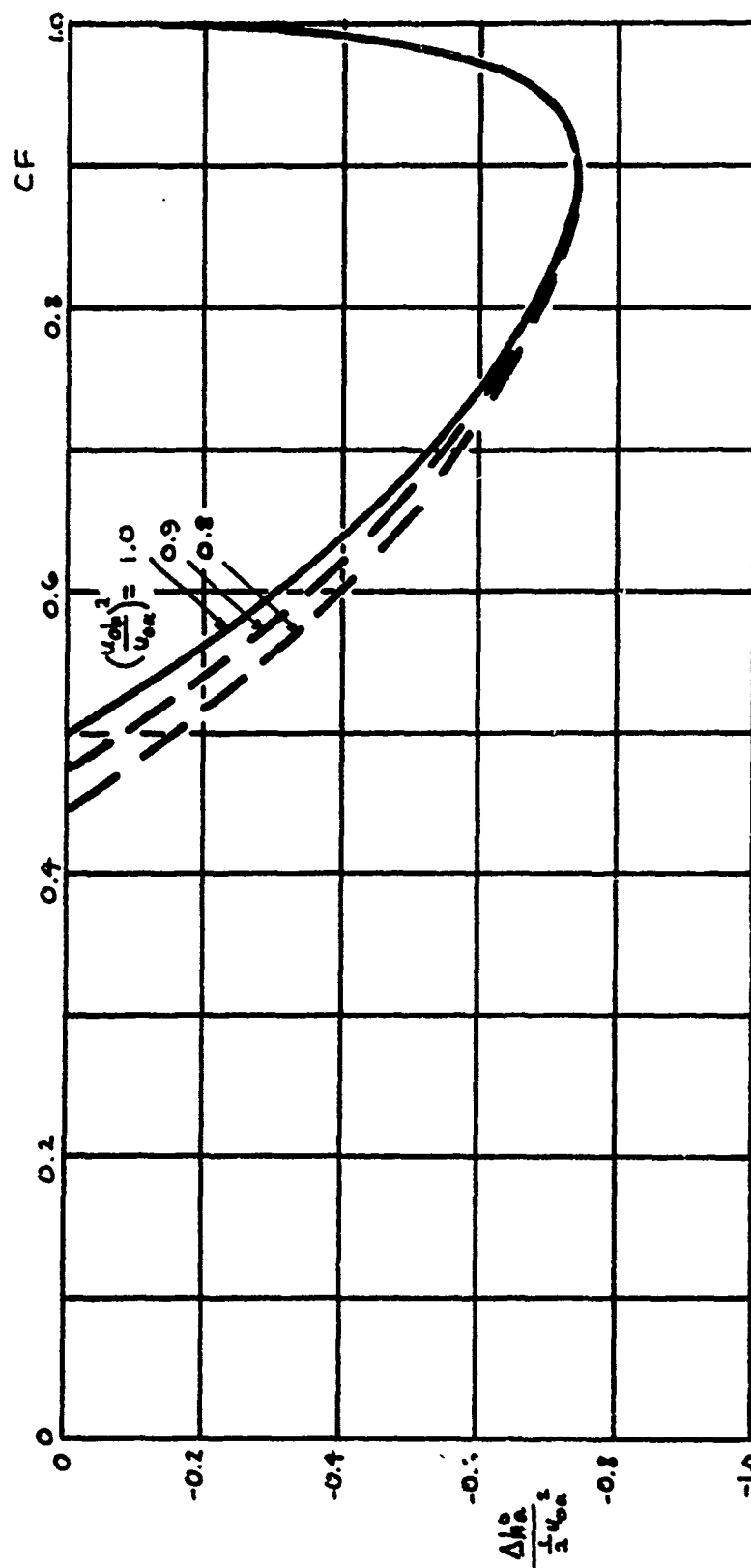


Figure 48  
Effect of Unequal Discharge Pressures (Internal Separation)

"b" flow, which causes the rotor to speed up and also enables operation at  $CF < 0.5$ .

It should be noticed that the effect of a differential in the discharge pressures is not the same for the internal-separation and external-separation configurations: compare Figure 41. In the external-separation case, the rotor velocity is governed by the average discharge pressure at the exit of the single nozzle; this is raised with an increase in  $p_b$ , causing rotor velocity to decrease rather than increase, contrasting with the internal-separation device. Thus, while  $CF$  is increased by  $p_b > p_a$  in both devices, the effect on output temperature is different.

Effect of rotor torque. The effect of resisting torque is presented in Figure 49, the behavior of which is generally similar to that for the external-separation configuration, Figure 37. Several lines of constant  $\lambda$  are shown; the higher values of  $\lambda$  give curves further to the right in the plot, reflecting the fact that as the ratio of "a"- to "b"-nozzle area is increased a higher level of torque can be tolerated. As before, the constant- $\lambda$  curves are carried only for the low-torque branch of the power extraction curve, as described for the external-separation case in Figure 37.

It will be noted in Figure 49 that the maximum temperature drop obtainable in the presence of a resisting torque is scarcely different from that with perfect, frictionless bearings, but the  $CF$  at which this maximum drop is attained is increased. However, the shape of the curves in the vicinity of the maximum temperature drop is such that little penalty in temperature drop is suffered even if the design assumes zero rotor torque and there turns out to be significant friction: at  $CF = 0.90$ , the



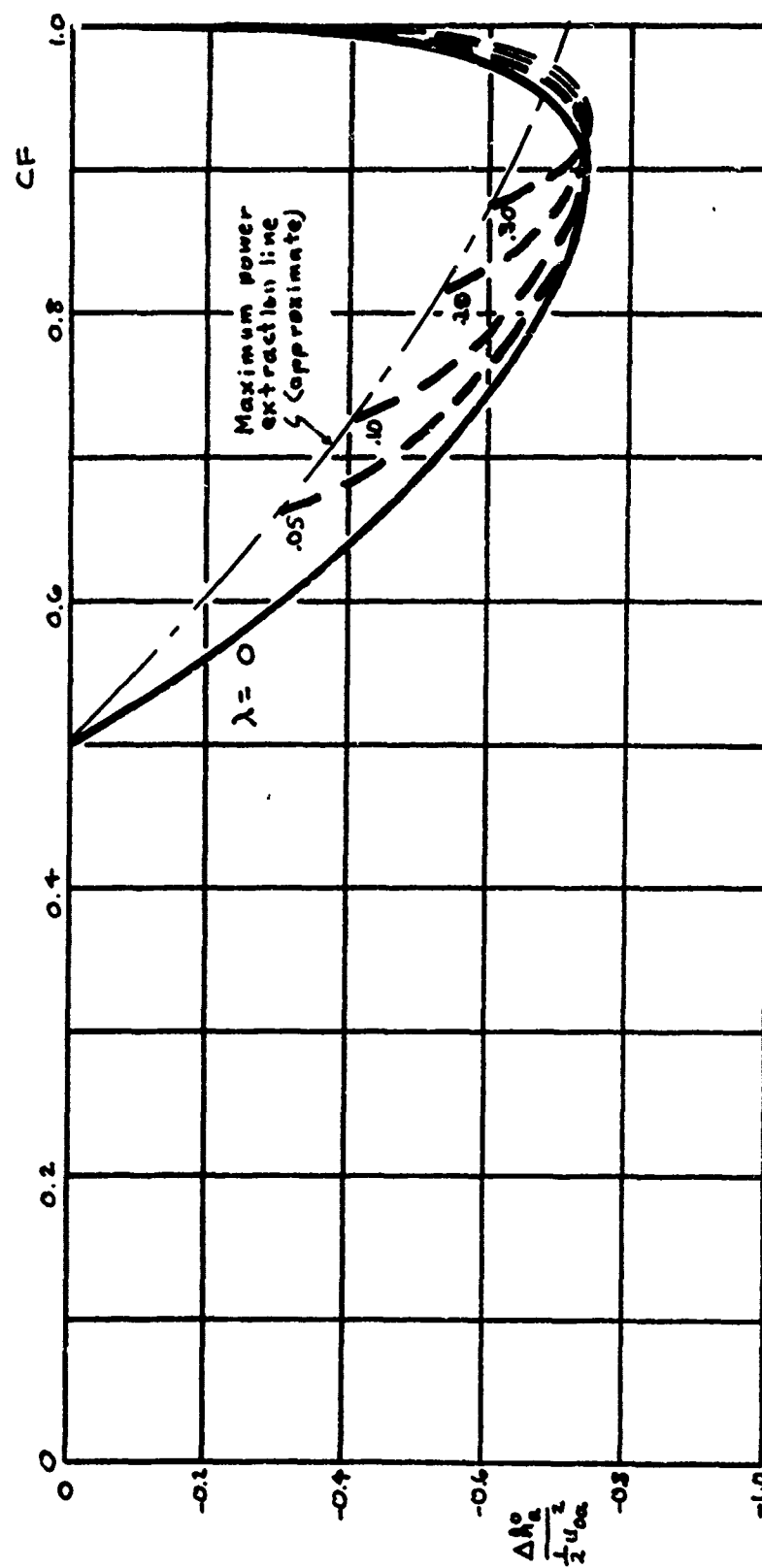


Figure 49  
Effect of Rotor Torque (Internal Separation)

temperature drop is not greatly affected even with  $\lambda$  as large as 0.3. Thus, it is seen that perfect bearings are by no means essential to acceptable FES performance.

### C. Collection Effects

#### 1. Selection of Effects to be Examined

A wide variety of FES configurations and applications are possible,<sup>10</sup> and in the case of the internal-separation design at least, there is no rigid prescription as to the technique that must be used in flow collection. External separation, however, involves the impingement-deflection process which, as pointed out in the INTRODUCTION, causes output flow generation and collection to be linked intimately. Accordingly, two output collection effects of general significance for external separation are treated below.

The collection process may be steady, if the "a" and "b" flows are led into separate collection spaces by guiding surfaces mounted on the rotor; the offset-channel scheme of Figure 29 is one configuration which accomplishes this. With steady collection, the deflected flows of Figure 31 will tend to mix with the regions of deadwater (in  $F_5$ ) alongside them; if the confining channel is sufficiently long, this may bring about viscous reattachment and uniformization of the "a" and "b" flows, with potentially marked influence on performance. If the flows are diverted by vanes mounted on the casing, however, unsteadiness must result. One particularly simple flow collection scheme for the external-separation design utilizes such stationary vanes, and the character and significance of the resultant unsteadiness is analyzed.

## 2. Viscous Reattachment Effects on External-Separation FES Performance

Introduction. If the impingement/collection channel mounted on the rotor of an external-separation FES is long enough, significant mixing of each deflected jet with the region of deadwater (in  $F_S$ ) beside it will occur. Figure 50(a) illustrates the limiting case in which the flow on each side becomes reattached to the channel wall containing the nozzle and--assuming frictionless walls--terminates in a uniform exit flow.

The present simplified analysis has been carried out in order to obtain a grasp of the physical essentials of the problem, and to determine whether such mixing effects are beneficial or detrimental to performance and how major they may be. An incompressible treatment is used, and the offset angle  $\epsilon$  between the plane of Figure 50(a) and the plane of rotation is neglected.

Analysis. Denoting stagnation quantities in  $F_U$  and  $F_S$  respectively by  $( )^0$  and  $( )^\bullet$ , one may write for a given point  $j$  in either flow:

$$T_j^0 = T_j + \frac{u_j^2}{2c_p}$$

$$T_j^\bullet = T_j + \frac{c_j^2}{2c_p}$$

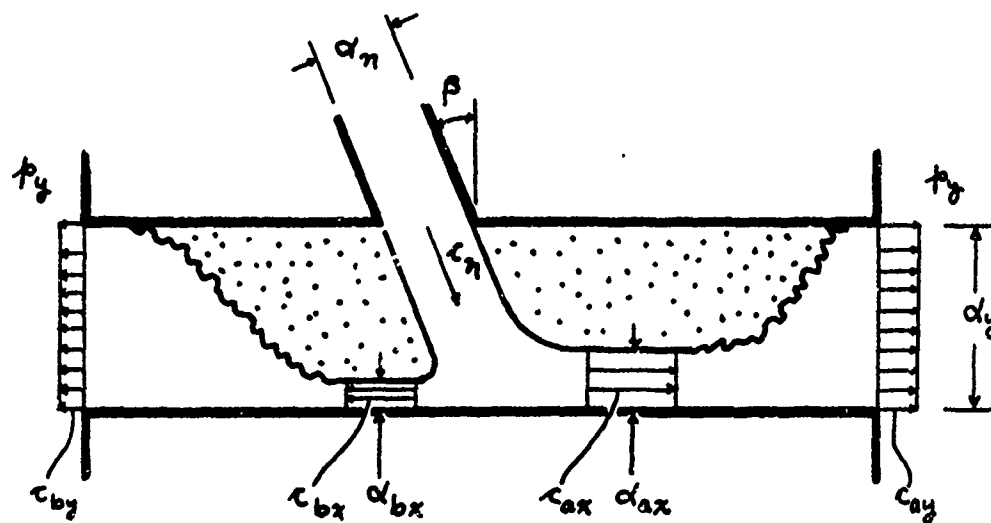
where  $u_j$  and  $c_j$  denote the fluid velocity at point  $j$  as measured in  $F_U$  and  $F_S$  respectively, these velocities being related through

$$\vec{u} = \vec{c} + \vec{v}$$

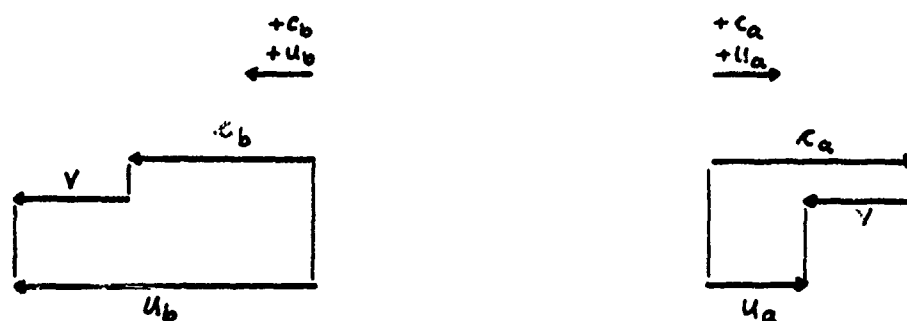
Adopting the conventions noted in Figure 50(b), this gives

$$u_a = c_a - v$$

$$u_b = c_b + v$$



(a)



(b)



(c)

Figure 50  
Analytical Model for Viscous Reattachment

At any point in the "a" flow, therefore:

$$\begin{aligned} T_{aj}^{\circ} &= T_{aj} + \frac{u_{aj}^2}{2c_p} \\ &= \left[ T_{aj} + \frac{c_{aj}^2}{2c_p} \right] + \frac{V^2}{2c_p} - \frac{c_{aj}V}{c_p} \\ &= T_{aj}^{\circ} + \frac{V^2}{2c_p} - \frac{c_{aj}V}{c_p} \end{aligned}$$

and similarly in the "b" flow:

$$T_{bj}^{\circ} = T_{bj}^{\circ} + \frac{V^2}{2c_p} + \frac{c_{bj}V}{c_p}$$

Due to conservation of energy in  $F_S$ ,

$$T_{aj}^{\circ} = T_{bj}^{\circ} = T_n^{\circ}$$

where  $( )_n$  refers to the jet issuing from the nozzle [Figure 50(a)]. Also, in the absence of prerotation, the change of reference frame from  $F_U$  to  $F_S$  gives according to equation (3)

$$T_n^{\circ} = T_i^{\circ} + \frac{V^2}{2c_p}$$

where  $( )_i$  refers to the flow introduced to the rotor. Thus:

$$T_{aj}^{\circ} = T_i^{\circ} + \frac{V^2}{2c_p} - \frac{c_{aj}V}{c_p}$$

or

$$\Delta T_{aj}^{\circ} \equiv T_{aj}^{\circ} - T_i^{\circ} = \frac{V^2}{c_p} \left( 1 - \frac{c_{aj}}{V} \right) \quad (33a)$$

and similarly

$$\Delta T_{bj}^o \equiv T_{bj}^o - T_i^o = \frac{V^2}{c_p} \left( 1 + \frac{c_{u1}}{V} \right) \quad (33b)$$

In the case of no mixing, which will be denoted  $( )_0$ , there is obtained at a given pressure ratio  $\frac{p_i^o}{p_o}$  [ $p_o$  being the discharge pressure, Figure 50(a)] a rotor velocity  $V_o$  and fluid velocities in  $F_S$   $c_{a0} = c_{b0} = c_o$ . If there is neither prerotation nor rotor torque, one may write from the velocity triangle of Figure 50(c), with or without mixing:

$$\frac{c_m}{V} = \frac{1}{\sin \beta}$$

Thus, one has for the case of zero mixing:

$$\Delta T_{a0}^o = \frac{V_o^2}{c_p} \left( 1 - \frac{c_o}{V_o} \right) = \frac{V_o^2}{c_p} \left( 1 - \frac{1}{\sin \beta} \right) \quad (33a')$$

$$\Delta T_{b0}^o = \frac{V_o^2}{c_p} \left( 1 + \frac{1}{\sin \beta} \right) \quad (33b')$$

In the opposite case of complete constant-area uniformization, Figure 50(a), the output temperature increments obtained at the same pressure ratio are

$$\Delta T_{aj}^o = \frac{V^2}{c_p} \left( 1 - \frac{c_{u2}}{V} \right) \quad (33a'')$$

$$\Delta T_{bj}^o = \frac{V^2}{c_p} \left( 1 + \frac{c_{u2}}{V} \right) \quad (33b'')$$

where both the rotor velocity and the fluid velocities will in general differ from the zero-mixing values. Focusing attention on the cold output, (33a") may be rewritten:

$$\begin{aligned}\Delta T_{oy}^{\circ} &= \left(\frac{V}{V_o}\right)^2 \frac{V_o^2}{c_p} \left(1 - \frac{c_{ay}}{c_{ax}} \frac{c_{ax}}{V}\right) \\ &= \left(\frac{V}{V_o}\right)^2 \frac{V_o^2}{c_p} \left(1 - \frac{c_{ay}}{c_{ax}} \frac{c_{ax}}{c_n} \frac{c_n}{V} \frac{V}{V_o}\right)\end{aligned}$$

The factor  $\frac{c_{ax}}{c_n} = 1$  if the jet pressure differential,  $\delta p = p_{bx} - p_{ax}$ , is zero. Looking at Figure 50(a), one can see that  $\delta p$  cannot in fact be expected to be strictly equal to zero in general, since the "a" and "b" flows undergo different area changes during the transition from stations "x", where they have the same total pressure in  $F_S$ , to stations "y", where they have the same static pressure  $p_y$  (considering only the case of subsonic terminal flows). Furthermore, it is possible for  $\delta p$  to be either positive or negative, depending upon the particular combination of  $\beta$  and  $\frac{\alpha_y}{\alpha_n}$  considered. However, it is to be expected that within some domain of geometric combinations  $\delta p$  will be small compared to the nozzle pressure drop,  $p_i^{\circ} - p_n$ : for example, the smaller  $\beta$  becomes, the more nearly equal  $\alpha_{ax}$  and  $\alpha_{bx}$  become, which implies that  $p_{ax}$  and  $p_{bx}$  also become more nearly equal to the mean nozzle-exit pressure  $p_n$ . Or, if  $\beta$  is large but  $\frac{\alpha_{ax}}{\alpha_y}$  is not too much less than unity,  $\frac{\delta p}{p_n}$  is again small. Therefore, for the present rough analysis, the approximation will be used that

$$\frac{c_{ax}}{c_n} \doteq 1$$

Also, from incompressible continuity,

$$\frac{c_{ay}}{c_{ax}} = \frac{\alpha_{ax}}{\alpha_y}$$

Therefore, noting also the velocity triangle again,

$$\Delta T_{ay}^o = \left(\frac{V}{V_o}\right)^2 \frac{V_o^2}{c_p} \left(1 - \frac{\alpha_{ax}}{\alpha_y} \frac{V}{V_o} \frac{1}{\sin \beta}\right) \quad (33a''')$$

Dividing equation (33a''') by equation (33a') gives

$$\begin{aligned} F_{temp} &\equiv \frac{\Delta T_{ay}^o}{\Delta T_{ao}^o} \\ &= \frac{\left(\frac{V}{V_o}\right)^2 \frac{V_o^2}{c_p} \left(1 - \frac{\alpha_{ax}}{\alpha_y} \frac{V}{V_o} \frac{1}{\sin \beta}\right)}{\frac{V_o^2}{c_p} \left(1 - \frac{1}{\sin \beta}\right)} \end{aligned}$$

or

$$F_{temp} = \frac{\Delta T_{ay}^o}{\Delta T_{ao}^o} = \frac{\left(\frac{V}{V_o}\right)^2 \left(1 - \frac{\alpha_{ax}}{\alpha_y} \frac{V}{V_o} \frac{1}{\sin \beta}\right)}{\left(1 - \frac{1}{\sin \beta}\right)} \quad (34)$$

where  $F_{temp}$  is the ratio of cold-output temperature drop with reattachment to that obtained in the inviscid case.

It will be convenient below to use the abbreviated notation

$$\mathcal{V} \equiv \frac{V}{V_o}$$

$$\mathcal{X} \equiv \frac{\alpha_{ax}}{\alpha_y}$$



in terms of which equation (34) may be rewritten as

$$F_{temp} = \frac{(\mathcal{X}\mathcal{V} - \sin \beta)}{(1 - \sin \beta)} \mathcal{V}^2 \quad (34')$$

Note that:

$F_{temp} > 1$  indicates that viscous reattachment is beneficial to performance

$F_{temp} < 1$  indicates that viscous reattachment is detrimental to performance

insofar as cold-output temperature is concerned.

If  $\mathcal{X} = \frac{a_{ax}}{a_y} = 1$ , the "ax" flow fills the duct, and there is no chance for mixing in the "a" flow. In this case,  $\mathcal{V} = \frac{v}{v_0} = 1$ , and equation (34') gives  $F_{temp} = 1$ --i.e., "no-mixing" performance is obtained, as it should be according to the present simplified model. Decreasing  $\mathcal{X}$  to some value slightly less than unity will cause  $\mathcal{V}$  to rise, thanks to the depressed static pressure at the nozzle exit and the resultant higher discharge velocity  $u_n$ ; however, the product  $\mathcal{X}\mathcal{V}$  would presumably change relatively little. Thus,  $F_{temp} > 1$  is expected when  $\mathcal{X}$  is less than, but close to, unity: that is, viscous reattachment should enlarge the cold-output temperature drop.

To verify this, and to carry the analysis further, it is necessary to have more information on the effect of  $\mathcal{X}$  on  $\mathcal{V}$ . This is therefore examined next.

Referring again to Figure 50(c), one may write

$$\mathcal{V} = u_n \tan \beta$$

and hence

$$\frac{v}{v_0} = \frac{u_n}{u_{n0}}$$

For incompressible flow without nozzle losses, the Bernoulli equation gives

$$p_i^0 - p_n = \frac{1}{2} \rho u_n^2$$

or, with the notation  $\Delta p_j \equiv p_i^0 - p_j$ ,

$$u_n = \sqrt{\frac{2 \Delta p_n}{\rho}}$$

Hence,

$$v = \frac{v}{v_0} = \sqrt{\frac{\Delta p_n}{\Delta p_y}} \quad (35)$$

since the nozzle-exit pressure is  $p_y$  in the absence of mixing.

In order to be able to calculate  $\frac{\Delta p_n}{\Delta p_y}$ , the manner in which mixing causes  $p_n$  to differ from  $p_y$  must be known. To this end, consider the mixing of the "a" flow, referring to Figure 50(a). The momentum equation is:

$$p_{ax} + \rho c_{ax}^2 \frac{d_{ax}}{d_y} = p_y + \rho c_{ay}^2$$

or

$$p_y - p_{ax} = \rho c_{ax}^2 \left[ \frac{d_{ax}}{d_y} - \left( \frac{c_{ay}}{c_{ax}} \right)^2 \right]$$

Continuity gives

$$\frac{r_{ay}}{r_{ax}} = \frac{d_{ax}}{d_y}$$

substitution of which into the momentum equation gives:

$$p_y - p_{ax} = \rho r_{ax}^2 \frac{d_{ax}}{d_y} \left(1 - \frac{d_{ax}}{d_y}\right) \quad (36)$$

Now,

$$p_i^0 - p_{ax} = (p_i^0 - p_y) + (p_y - p_{ax})$$

or, with (36),

$$\Delta p_{ax} = \Delta p_y + \rho r_{ax}^2 \frac{d_{ax}}{d_y} \left(1 - \frac{d_{ax}}{d_y}\right) \quad (37)$$

The Bernoulli equation in  $F_S$  gives

$$p_m^0 = p_{ax}^0 = p_{ax} + \frac{1}{2} \rho r_{ax}^2$$

while the change of reference frame gives

$$p_m^0 = p_i^0 + \frac{1}{2} \rho V^2$$

Therefore,

$$\begin{aligned} \Delta p_{ax} &= (p_m^0 - p_{ax}) - (p_m^0 - p_i^0) \\ &= \frac{1}{2} \rho r_{ax}^2 - \frac{1}{2} \rho V^2 \\ &= \frac{1}{2} \rho r_{ax}^2 \left[1 - \left(\frac{V}{r_{ax}}\right)^2\right] \\ &= \frac{1}{2} \rho r_{ax}^2 (1 - \sin^2 \beta) \end{aligned}$$

where the velocity triangle and the approximation  $\frac{c_{ax}}{c_m} \doteq 1$  have again been used. Rearranging,

$$\rho c_{ax}^2 = \frac{2 \Delta p_{ax}}{1 - \sin^2 \beta}$$

and substituting into (37),

$$\Delta p_{ax} = \Delta p_y + \frac{2 \Delta p_{ax}}{1 - \sin^2 \beta} \frac{d_{ax}}{d_y} \left( 1 - \frac{d_{ax}}{d_y} \right)$$

or

$$\frac{\Delta p_{ax}}{\Delta p_y} = 1 + \frac{2}{1 - \sin^2 \beta} \frac{d_{ax}}{d_y} \left( 1 - \frac{d_{ax}}{d_y} \right) \frac{\Delta p_{ax}}{\Delta p_y}$$

Solving for  $\frac{\Delta p_{ax}}{\Delta p_y}$  gives:

$$\frac{\Delta p_{ax}}{\Delta p_y} = \frac{1}{1 - \frac{2}{1 - \sin^2 \beta} \frac{d_{ax}}{d_y} \left( 1 - \frac{d_{ax}}{d_y} \right)} \quad (38)$$

In order to relate  $\frac{\Delta p_m}{\Delta p_y}$  to  $\frac{\Delta p_{ax}}{\Delta p_y}$ , consider two extreme cases:

A. Small  $\beta$ .

As  $\beta \rightarrow 0$ , the flow pattern in Figure 69(a) approaches a symmetric condition, with  $p_{ax} = p_{bx}$ . Therefore, take

$$\frac{\Delta p_m}{\Delta p_y} \doteq \frac{\Delta p_{ax}}{\Delta p_y} \quad (39A)$$

for the "small  $\beta$ " case.

B. Large  $\beta$ .

At large values of  $\beta$ ,  $\mu$  tends toward zero if  $\delta p = 0$ ;

therefore,  $\frac{\alpha_{bx}}{\alpha_y}$  becomes very small and the pressure rise from station "bx" to station "by" becomes negligible.\* Therefore, take

$$p_n \doteq \frac{1}{2} (p_{ax} + p_{ay})$$

for the "large  $\beta$ " case. This leads to:

$$\begin{aligned} \Delta p_n &= p_i^0 - \frac{1}{2} (p_{ax} + p_{ay}) \\ &= \frac{\Delta p_y + \Delta p_{ax}}{2} \end{aligned}$$

or

$$\frac{\Delta p_n}{\Delta p_y} = \frac{1}{2} \left( 1 + \frac{\Delta p_{ax}}{\Delta p_y} \right) \quad (39B)$$

Using the  $\mathcal{V}$  and  $\mathcal{X}$  notation and defining also

$$k_\beta \equiv \frac{1}{1 - \sin^2 \beta}$$

$$\phi \equiv \frac{\Delta p_{ax}}{\Delta p_y}$$

equation (38) becomes

$$\phi = \left[ 1 - 2 k_\beta \mathcal{X} (1 - \mathcal{X}) \right]^{-1} \quad (38')$$

---

\*Note, therefore, that there is in this case a  $\delta p > 0$ --a condition tending to further reduce the amount of "b" flow. Hence, the "large  $\beta$ " solution probably is approached even at nozzle inclinations as moderate as, say,  $30^\circ$ .

From equations (35) and (39A),

$$v_A = \varphi^{\frac{1}{2}} \quad (40A)$$

while from (35) and (39B),

$$v_B = \left( \frac{1+\varphi}{2} \right)^{\frac{1}{2}} \quad (40B)$$

Consider now the situation in which  $x = 1 + \Delta x$ , where  $\Delta x$  is negative and  $|\Delta x| \ll 1$ . One may write

$$\frac{dv}{dx} = \frac{dv}{d\varphi} \cdot \frac{d\varphi}{dx} \quad (41)$$

With (38'),

$$\begin{aligned} \frac{d\varphi}{dx} &= (-1) \left[ 1 - 2k_B x(1-x) \right]^{-2} \cdot (-2k_B)(1-2x) \\ &= 2k_B(1-2x)\varphi^2 \end{aligned}$$

Using (40A),

$$\frac{dv_A}{d\varphi} = \frac{1}{2} \varphi^{-\frac{1}{2}}$$

while from (40B),

$$\frac{dv_B}{d\varphi} = \left( \frac{1}{2} \right)^{\frac{3}{2}} (1+\varphi)^{-\frac{1}{2}}$$

Therefore,

$$\begin{aligned} \frac{dv_A}{dx} &= \frac{1}{2} \varphi^{-\frac{1}{2}} \cdot 2k_B(1-2x)\varphi^2 \\ &= k_B(1-2x)\varphi^{\frac{3}{2}} \end{aligned} \quad (41A)$$

and

$$\begin{aligned}\frac{dv_B}{d\chi} &= \left(\frac{1}{2}\right)^{\frac{3}{2}} (1+\phi)^{-\frac{1}{2}} \cdot 2 k_\beta (1-2\chi) \phi^2 \\ &= (2)^{-\frac{1}{2}} k_\beta (1-2\chi) \phi^2 (1+\phi)^{-\frac{1}{2}}\end{aligned}\quad (41B)$$

Evaluating at  $\chi = 1$ , note from (38') that

$$\phi \Big|_{\chi=1} = 1$$

so that:

$$\begin{aligned}\frac{dv_A}{d\chi} \Big|_{\chi=1} &= k_\beta (1-2)(1) \\ &= -\frac{1}{1 - \sin^2 \beta}\end{aligned}\quad (41A')$$

and

$$\begin{aligned}\frac{dv_B}{d\chi} \Big|_{\chi=1} &= (2)^{-\frac{1}{2}} k_\beta (1-2)(1)(2)^{-\frac{1}{2}} \\ &= -\frac{1}{2} \frac{1}{1 - \sin^2 \beta}\end{aligned}\quad (41B')$$

In the vicinity of  $\chi = 1$ , one may write in approximation:

$$v \doteq 1 + \left(\frac{dv}{d\chi}\right)_{\chi=1} \cdot \Delta\chi \quad (42)$$

Referring to equation (34"), it is clear first that  $v^2 > 1$  if  $\chi < 1$ , as expected, since  $\Delta\chi$  is necessarily negative ( $\alpha_{ax}$  cannot exceed  $\alpha_y$ ) and  $\left(\frac{dv}{d\chi}\right)_{\chi=1}$  is negative for both cases A and B by equations

(41A') and (41B'). As for  $\chi v$ , one has

$$\begin{aligned}\chi v &= [1 + \Delta \chi] \left[ 1 + \left( \frac{dv}{d\chi} \right)_{\chi=1} \Delta \chi \right] \\ &\doteq 1 + \left[ 1 + \left( \frac{dv}{d\chi} \right)_{\chi=1} \right] \Delta \chi\end{aligned}\quad (43)$$

For case A (small  $\beta$ ), equation (43) gives:

$$\begin{aligned}(\chi v)_A &= 1 + \left[ 1 - \frac{1}{1 - \sin^2 \beta} \right] \Delta \chi \\ &= 1 - \frac{\sin^2 \beta}{1 - \sin^2 \beta} \Delta \chi\end{aligned}\quad (43A)$$

According to (43A),  $(\chi v)_A$  is close to unity since  $\Delta \chi$  has been chosen small and the solution itself is for small  $\beta$ . Therefore, for case A, equation (44') gives in the vicinity of  $\chi = 1$ :

$$\begin{aligned}(\text{Ftemp})_A &\doteq \frac{v_A^2 (1 - \sin \beta)}{(1 - \sin \beta)} \\ &= v_A^2 > 1 \quad \text{when } \chi < 1\end{aligned}$$

The expected favorable effect of viscous reattachment is thus seen for case A.

For case B, equation (43) gives:

$$\begin{aligned}(\chi v)_B &= 1 + \left[ 1 - \frac{1}{2} \frac{1}{1 - \sin^2 \beta} \right] \Delta \chi \\ &= 1 + \frac{1 - 2 \sin^2 \beta}{2(1 - \sin^2 \beta)} \Delta \chi\end{aligned}\quad (43B)$$

For a given  $\beta < 90^\circ$ ,  $\Delta \chi$  may be chosen small enough to give  $(\chi v)_B \approx 1$ , which therefore leads to



$$(F_{temp})_B \doteq V_0^2 > 1 \quad \text{for} \quad \chi < 1$$

confirming that here again the effect, at least for  $\chi$  near unity, is favorable.

However, with continued reductions in  $\chi = \frac{\alpha_x}{\alpha_y}$  (or equivalently, increases in the channel-height factor  $\frac{\alpha_y}{\alpha_n}$ ), it is clear that the effect of mixing cannot remain favorable indefinitely. The physical reason for the beneficial effect of viscous reattachment is that the kinetic energy in  $F_U$  of flow "a" is reduced:  $u_{ay} = c_{ay} - V$  is reduced below the zero-mixing value  $u_{ao}$  both because  $V$  is increased and because the fluid velocity in  $F_S$ ,  $c_{ay}$ , is reduced. The optimum condition would therefore presumably be that for which  $c_{ay} = V$ , giving  $u_{ay} = 0$ . Beyond that point,  $u_{ay}$  would become negative as defined, but of course the kinetic energy per unit mass  $\frac{1}{2} u_{ay}^2$  would again rise.

The present analysis yields results that are in agreement with these physical expectations. The cold-output temperature factor,  $F_{temp}$ , may be calculated as a function of  $\beta$  and  $\chi = \frac{\alpha_x}{\alpha_y}$  by means of equations (44'), (48'), and either (40A) for "small  $\beta$ " or (40B) for "large  $\beta$ ." The small- $\beta$  solution is likely to be valid only for nozzle inclinations of a few degrees, since the splashing pattern described by equation (16) departs very rapidly from a symmetric condition as  $\beta$  is increased. For some range of  $\beta$  values, the solution would presumably tend to lie between the small- $\beta$  and large- $\beta$  solutions, with the latter probably being reasonably accurate by the time  $\beta$  reaches  $30^\circ$  or so, as already noted. Figure 51 presents the results obtained at  $30^\circ$

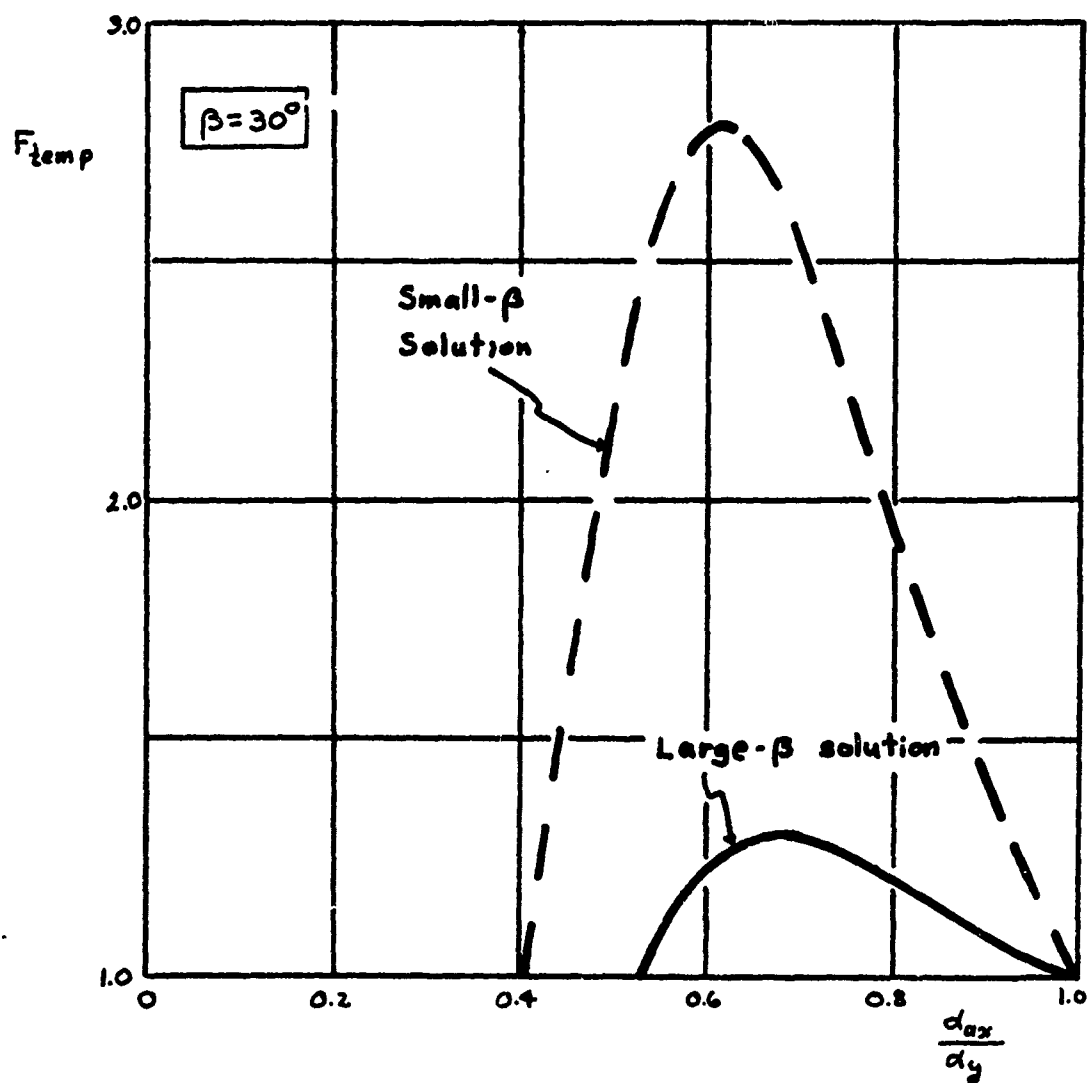


Figure 51  
Effect of Viscous Reattachment on Cold-Output Temperature Drop

according to both solutions; only the large- $\beta$  solution is considered meaningful here, but the small- $\beta$  solution is also presented for qualitative comparison. The small- $\beta$  solution predicts a more pronounced effect of mixing on temperature drop than does the large- $\beta$  solution because the static pressure is lowered on both sides of the nozzle exit in the first case, whereas in the second it is essentially lowered on only one side.

Whichever solution is considered, it is seen (i) that the peak beneficial effect is rather sharply defined, and (ii) that reduction of  $\frac{\alpha_{ax}}{\alpha_y}$  (or increasing the channel-height factor  $\frac{\alpha_y}{\alpha_n}$ ) very much beyond the value corresponding to peak benefit can result in serious net degradation of performance. As for the magnitude of the peak benefit, it should be noted first that for  $\beta = 30^\circ$  the "baseline" performance without mixing [Figure 33(a)] is two-thirds of the isentropic temperature drop associated with a given DPR; therefore, values of  $F_{temp}$  up to 1.5 are not ruled out thermodynamically. The small- $\beta$  solution violates this thermodynamic barrier grossly, which is not surprising since the small- $\beta$  solution is not valid at this large an angle. The large- $\beta$  solution, however, should be meaningful in an order-of-magnitude sense, and the bound is not violated in this case. It is interesting to note that the peak value of  $F_{temp}$  from the large- $\beta$  solution is about 1.3, or roughly halfway between "baseline" (inviscid) performance and the thermodynamic limit.

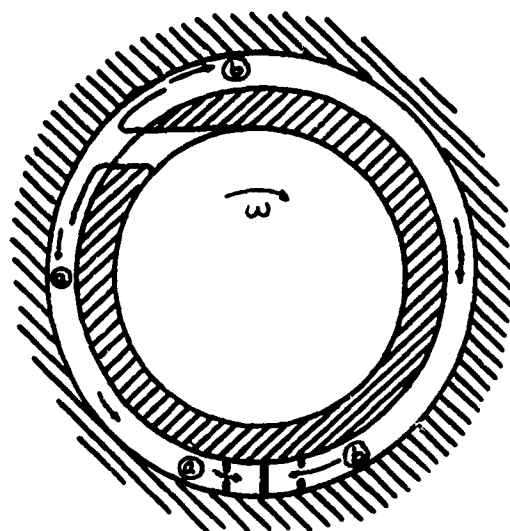
Thus, the conclusion which emerges from the present simple analysis is that viscous reattachment potentially can improve the cold-output performance of a given external-separation geometry, but that use of too

large a channel height can lead instead to detrimental performance effects. It should be noted, however, that the performance improvement is associated with increased rotor velocity and a decrease in  $\mu$ , the former effect being undesirable (for structural reasons) while the latter is favorable (to refrigeration capacity) provided the "b" flow does not disappear altogether due to the effect of  $S_p$  [equation (16)]. Therefore, it would appear that further study of the viscous reattachment effect is in order.

### 3. Nonsteady Collection Effects on External-Separation FES Performance

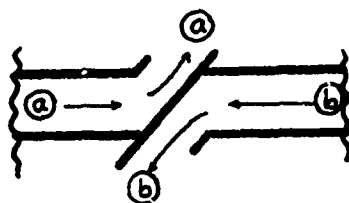
Introduction. Up to here, it has been assumed both in developing the core performance equations and in the consideration of collection effects that the flow is cryptosteady--that is, steady as viewed in the special reference frame  $F_S$  attached to the rotor. However, at least one collection scheme is attractive for its great mechanical simplicity wherein the strictly cryptosteady flow pattern is not maintained, the flow instead being interrupted by turning vanes mounted in  $F_U$  whose purpose is to lead flows "a" and "b" into separate discharge regions. This configuration is depicted in Figure 52.

As shown in Figure 52(a), the flow enters an external-separation rotor, is discharged through a nozzle lying in the plane of rotation, and is collected in an annular channel as shown. The oppositely deflected flows "a" and "b" proceed in opposite directions in the channel toward their respective exit ports, which are located on opposite sides of a baffle at a "flow extraction station," which is shown in Figure 52(b) as it would appear viewed from the center of the rotor. Only a single nozzle

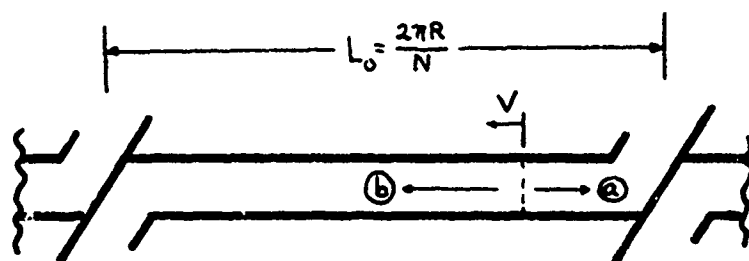


(a)

Flow Extraction Station



(b)



(c)

Figure 52  
External-Separation FES with Interrupted Collector Channel

and flow extraction station are indicated in Figure 52; an actual device could of course have several such nozzles and extraction stations arranged around the periphery, but its behavior would be the same.

Every time the nozzle travels a distance of  $L_0 = 2\pi R/N$ , where  $R$  is the rotor radius and  $N$  is the number of extraction stations (which will be assumed equal to the number of nozzles in the nonsteady flow analysis), it passes a flow extraction station. Thus, unwrapping the collector into its linear equivalent gives a picture like that in Figure 52(c); note that if there is only one extraction station, both ends of the cell shown in Figure 52(c) are actually the same station. Using as a marker for nozzle position the stagnation line which the impinging flow would have if unperturbed (c.f. Figure 31), one notes that the nozzle region looks rather like a two-directional source, moving along the duct at the rotor tangential velocity  $V$ . This "source" enters the duct from the left, traverses it to the right, and exits at the right while simultaneously re-entering at the left.

For the present analysis, no attempt will be made to treat explicitly the effects of flow turning at each end, nor to assess the wave-reflecting characteristics of the port-and-baffle region (presumably a function of baffle angle and port size). Rather, the nonsteady duct flow analyses which will be presented involve as a parameter the "effective" port areas for flows "a" and "b". In general, these effective port areas may differ from the duct area; however, the basic wave-diagram analyses are carried out assuming they are equal to the duct area. Based upon the insights thereby obtained, it is possible to discern the qualitative

effects which would be produced by ports having areas different from that of the duct.

In order to see how nonsteady effects come about in the collection process, consider Figure 53, which depicts an initial sweep of the source through the duct and the beginning of a second sweep, as seen in both reference frames. The progression of events is presented in a pair of pictorialized time-distance diagrams, since the analytical version of such diagrams will be used below.

The first sweep of the source is assumed to be purely crypto-steady, after which the second sweep is examined to see whether it too could possibly be free of nonsteady effects, and if not, the nature of the necessary nonsteady phenomena. Focusing attention on Figure 53(a), the source is seen to travel to the right at a steady velocity  $V$ , arriving at the right end of the duct ( $x = L_0$ ) at the end of the first cycle ( $t = t_{c_1}$ ). As it leaves the right end of the duct, it leaves behind a slug of fluid which fills the duct and is moving leftward uniformly at the velocity  $u_{a0}$ .

An instant later, the source enters the duct again from the left, and is no longer present at the right end. An "initial transient" pattern ensues, consisting of a shock at the left end and a rarefaction accompanied by inflow at the right. The shock is clearly necessary because the source, which is trying to eject "b" fluid to the right, is confronted head-on by a leftward-rushing slug of fluid moving at the velocity (in  $F_0$ ) of  $u_{a0}$ . The inflow is necessary in order to fill up the void that would otherwise develop at the right end of the duct as the slug moves off to the left, and a rarefaction occurs which both accelerates the ambient fluid in

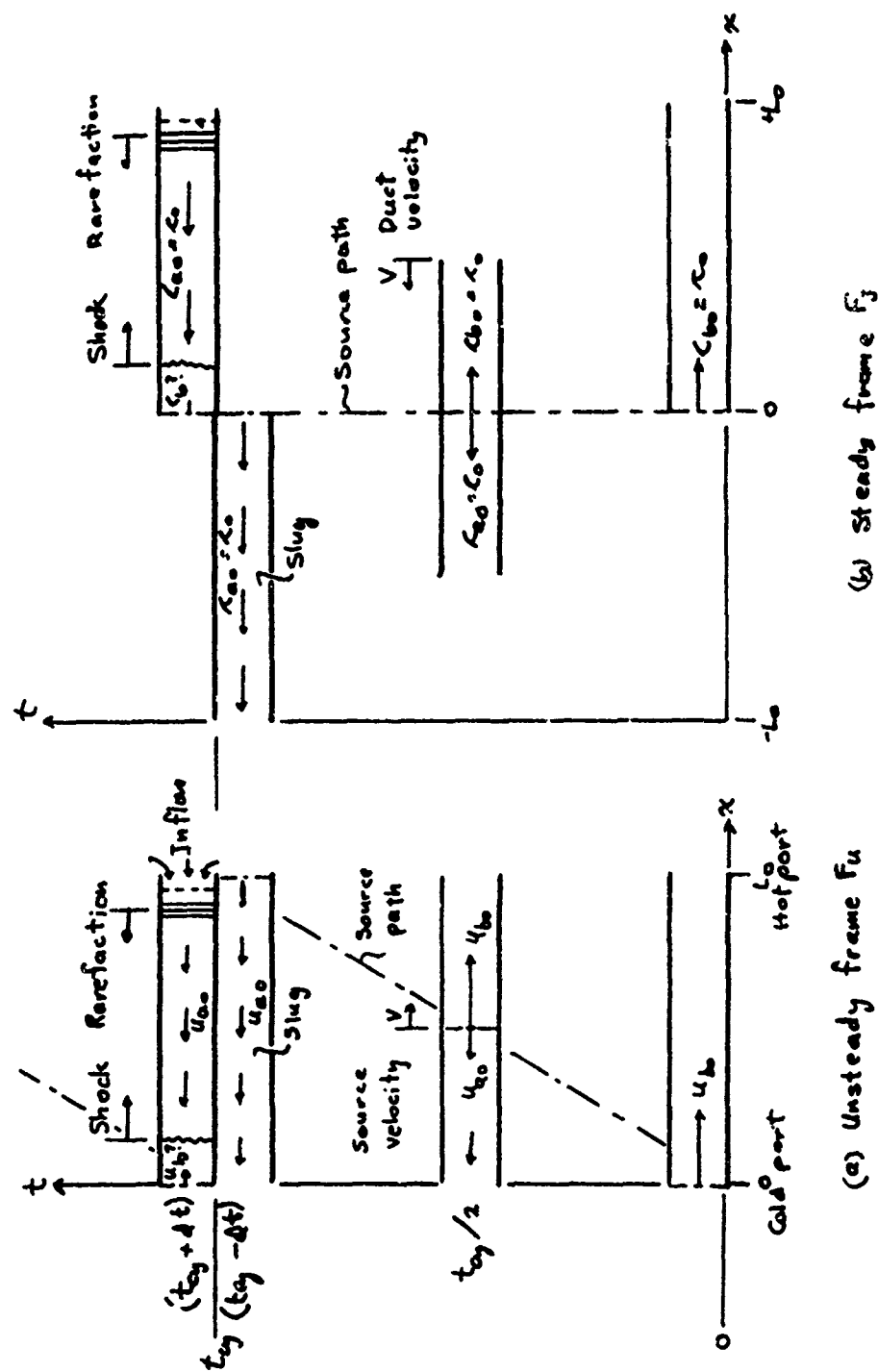


Figure 53  
Initiation of Nonsteady Collection Process



through the right-hand port and also decelerates the rightmost elements of the slug to make their velocity match that of the leading elements of the inflow.

The character of the initial shock and the accompanying perturbation of the source-region flow can be ascertained most readily by referring to Figure 53(b). As viewed in  $F_S$ , the source is stationary while the duct moves leftward at the constant velocity  $V$ . At the end of the first cycle, the entire duct is to the left of the source, and is filled with fluid moving uniformly at the velocity  $c_{a0}$ , which is the same as the velocity  $c_0$  of the fluid ejected from the nozzle. An instant later, this same duct full of leftward-rushing fluid lies ahead of the source, and the aforementioned initial shock forms. Now, to determine whether the source still succeeds in generating any "b" flow behind the shock, consider the possibility that a hammer shock forms, so that no "b" flow emerges but the slug fluid is arrested by the source. In this case,  $p_b^* = p_b = p_h$ , where  $p_h$  is the hammer pressure. But, if the Mach number  $M_{a0} = \frac{c_0}{a_0}$  of the slug is not excessive (larger than about 2.14 for air),  $p_h > p_{a0}^*$ , which implies  $p_b^* > p_{a0}^*$ . This contradicts the known fact that  $p_b^* = p_{a0}^* = p_h^*$ , which is based on the isentropic, isoenergetic (in  $F_S$ ) splashing of the nozzle flow into the deflected flows "a" and "b". Therefore, it is clear that the shock cannot be as strong as a hammer shock, which means that while the slug fluid is decelerated, it is not brought to rest in  $F_S$ : some slug fluid must leak leftward through the source. Thus, the splashing regime of Figure 31 is replaced by one in which the flow from the nozzle is totally swept in

the "a" flow direction, with leakage flow from the slug passing between the deflected jet and the impingement wall.\*

It is thus seen that a cryptosteady collection flow could not be maintained with the present collection geometry even if it could be initiated, and that the nonsteady perturbations are not minor ones. The nonsteady collection analysis presented herein deals with the "second cycle" which theoretically would follow such a cryptosteady first cycle. As will become apparent, this "second cycle" analysis enables one to identify all of the most basic phenomena which would be present in subsequent cycles, and therefore to arrive at meaningful conclusions concerning the impact of nonsteady collection on external-separation FES performance.

Nature and scope of the nonsteady collection analysis. As with the effects of boundary layer and mixing, the orientation of the nonsteady collection analysis is toward evolution of a physical grasp of the nonsteady effects and their impact on performance, including some estimation of the possible magnitude of these effects and their dependence on salient variables. To this end, it is evident from Figure 53 and the discussion thereof that the most appropriate analytical tool is that of one-dimensional nonsteady flow analysis, and this is utilized. However, noting from Figure 31 that the flow in the channel is not really one-dimensional, there are clear limitations on the quantitative accuracy to be expected

-----

\*The conclusion concerning the shock strength and leakage through the source was arrived at here on a one-dimensional basis. If account is taken of the non-one-dimensionality of the separated flows in the channel (Figure 31), the conclusion is reinforced: in  $F_S$ , the larger "a" flow has more momentum than, and hence overwhelms, the "b" flow trying to emerge from the source region.

of the analytical results. With this in mind, finite-wave diagrams have been used, rather than characteristics diagrams which would take account of wave spreading and the distributed nature of some compression waves.

The crux of the nonsteady collection process is the interaction between the fluid already in the duct and that issuing from the nozzle, and an appropriate description of this interaction is therefore also the key to the analytical treatment. Once this is available, the wave diagram analysis can proceed in relatively straightforward fashion. Therefore, the analysis of this source-region interaction with the duct flow and translation of the results into a format convenient for wave diagram analysis will be described in some detail. It is worth noting that the source-region analysis is carried out in  $F_S$ , whereas the nonsteady duct flow is analyzed in  $F_U$ , to which Figure 53(a) pertains; as a result, a change of reference frame is incorporated into the auxiliary curves which are ultimately generated for use in the nonsteady flow analysis. The detailed steps in the wave diagram analysis will not be recounted, as these merely represent an application of the techniques described in Foa,<sup>31</sup> Chapter 6, and in Rudinger;<sup>38</sup> the diagrams themselves, however, are included as Appendix B, and their features will be discussed in connection with the description of the nonsteady collection process that emerges from the analysis.

As already mentioned, the wave-diagram analysis focuses on the "second cycle" which follows an alleged cryptosteady first cycle. As may be seen in Figure 53(a), the source path as viewed in  $F_U$  divides the time-distance plane into triangular halves. The right side pertains to fluid lying between the source and the port for the "b" flow, which will be

referred to as the "hot" port; as is clear from the "initial transient" which starts off the second cycle, this region on the "hot" side of the source experiences pronounced nonsteady phenomena. The region on the left side of the source contains fluid on its way from the source to the "a" or "cold" port; the principal nonsteady effect which occurs here is a depression of the static pressure below ambient. This effect arises specifically because the flow is not in fact one-dimensional, and is a consequence of a retreating-piston effect of the jet issuing from the moving nozzle. The pressure depression effect is not incorporated into the wave-diagram analyses, which focus on the strong nonsteady phenomena on the "hot" side; with the results of these analyses in hand, however, an assessment is made of the pressure depression effect so that this could in principle be accounted for iteratively in constructing subsequent cycles.

The overall thermodynamic cycle of the FES as a whole is taken in all cases to be such that the total temperature  $T_i^o$  of the air introduced into the center of the rotor is equal to ambient. Prerotation and rotor torque are considered to be absent, while the nozzle efficiency is taken to be unity. A set of 27 candidate "cases"--combinations of nozzle inclination  $\beta$  (Figure 29), channel height factor  $\frac{\alpha_d}{\alpha_n}$  (Figure 31), and nozzle-exit Mach number  $M_n$  (Figure 31)--is presented in Table 1 which constitutes the catalog of conditions to be addressed analytically. Note that if  $\beta$  and  $M_n$  chosen, the nozzle pressure ratio  $NPR = \frac{p_o}{p_n}$  is also defined: considering the velocity triangle of Figure 50(c), one may write

$$NPR = \left(1 + \frac{\gamma-1}{2} M_n^2 \cos^2 \beta\right)^{\frac{\gamma}{\gamma-1}}$$

TABLE 1

Combinations of  $\beta$ ,  $\frac{d_d}{d_n}$ ,  $M_o$  to be Analyzed

CASE	Nozzle Inclination $\beta$	Channel-Height Factor $d_d/d_n$	Nozzle Mach Number $M_o$
1 2 3	30°	1.0	0.50 0.75 1.00
4 5 6		1.5	0.50 0.75 1.00
7 8 9		2.0	0.50 0.75 1.00
10 11 12	45°	1.0	0.50 0.75 1.00
13 14 15		1.5	0.50 0.75 1.00
16 17 18		2.0	0.50 0.75 1.00
19 20 21	60°	1.0	0.50 0.75 1.00
22 23 24		1.5	0.50 0.75 1.00
25 26 27		2.0	0.50 0.75 1.00

This equation is plotted in Figure 54 for  $M_\infty = 1.0$ ; it is seen that all of the cases analyzed correspond to a low-to-moderate range of pressure ratios.

"Source" boundary condition on duct flow. Figure 55 illustrates the manner in which the source region is visualized to interact with the duct flow to its right. The flow in the duct is of course nonsteady, but the flow within the source region is assumed to be quasi-steady in  $F_S$ . This assumption is analogous to that employed in the more common case in which the end of the duct is open to ambient conditions, with or without a constriction.

Three source flow regimes are depicted in Figure 55. Part (a) illustrates the supercritical regime, wherein the jet is swept leftward and is accompanied by some "bypass" flow coming from the right; as discussed above, this regime is established by the initial shock. However, the high pressure in the right side of the duct is eventually reduced by wave processes; hence, at some point critical flow occurs wherein the jet just seals the duct [Figure 55(b)], after which further lowering of pressure  $p_b$  allows the normal subcritical or "splashing" flow of Figure 55(c) to reassert itself.

Regardless of the source flow regime, two conditions must hold at every instant:

$$p_b = p_\infty \quad (44a)$$

$$\dot{m}_b = \dot{m}_\infty \quad (44b)$$

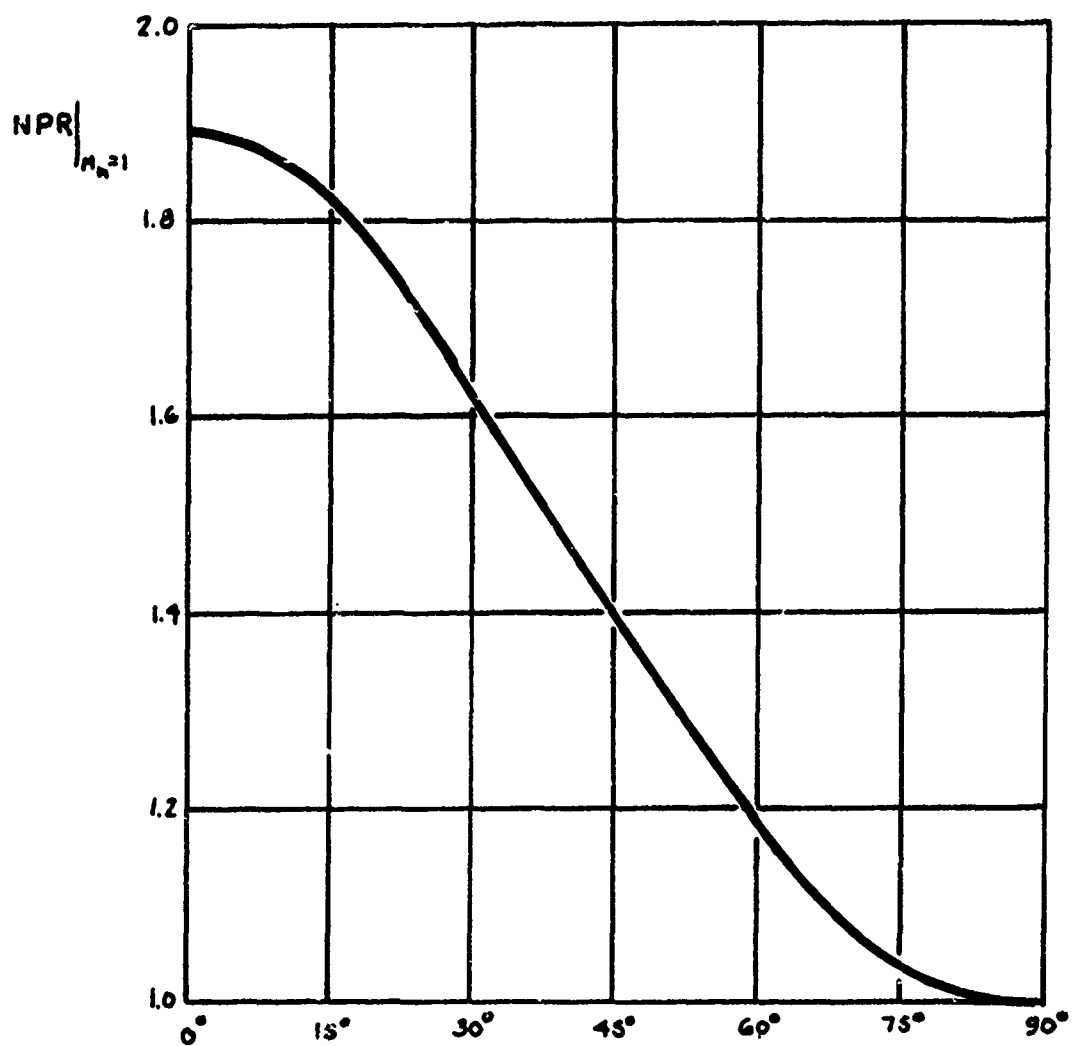


Figure 54  
Nozzle Pressure Ratio Required for  $M_n = 1$

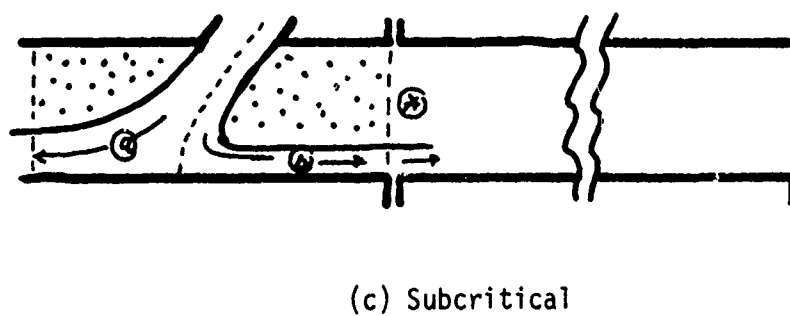
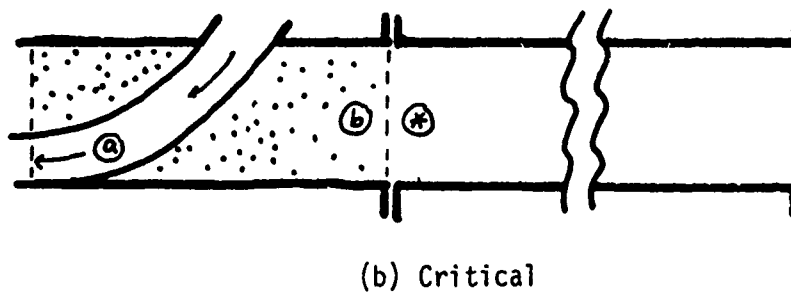
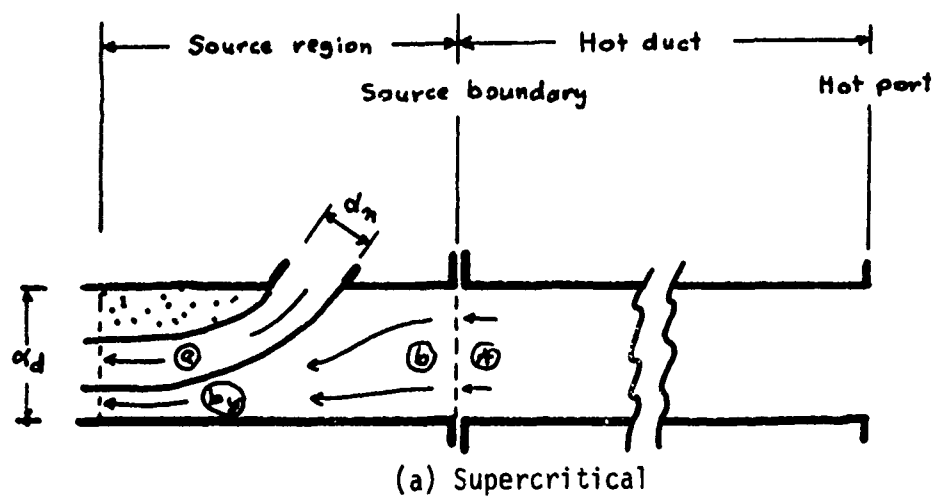


Figure 55  
Flow Regimes for "Source" Boundary of Hot Duct



where "b" denotes the right-hand portion of the source region and "\*" denotes the boundary between the nonsteady duct flow region and the source. This pair of specifications constitute what will be referred to as the "massflow compatibility" boundary condition at the source end of that portion of the duct lying between the source and the hot port. (For brevity, this segment of duct will be referred to below as the "hot duct.") Notice that during outflow of fluid from the left end of the hot duct through the source region, Figure 55(a), it is as if the left end of the duct is open to a back pressure which is not constant, but which instead is dependent upon the amount of outflow taking place. This contrasts with the more usual situation of open end with subsonic outflow, wherein if  $p_b$  is the back pressure surrounding the duct exit, equation (44a) still applies but (44b) is replaced by  $p_b = \text{constant}$ .

That the massflow compatibility condition of equations (44a, b) will indeed lead to a solution in particular for the initial shock and associated bypass flow is readily seen physically. For a given nozzle Mach number  $M_0$  (and hence slug Mach number,  $M_{00} = \frac{c_{00}}{a_{00}} = M_0$ ) and geometry, it is clear that the leftward flow through the source region  $\dot{m}_b = \dot{m}_s$  increases with increasing  $p_b$ , whereas the amount of mass-flow that is able to exit leftward from the hot duct through station "\*" decreases due to increasing strength of the initial shock. Therefore, some unique nonzero value of  $p_b = p_x$  is required in order for equations (44a, b) to be satisfied.

Analysis of supercritical flow in source region. An analysis has already been carried out for the subcritical flow regime of Figure 55(c), in connection with Figure 31. This cannot be applied to the

supercritical regime of Figure 55(a), however, and a new analysis for this regime is therefore needed.

Figure 56 depicts the analytical model employed for the supercritical analysis. It is assumed that a uniform pressure  $p_a$  exist on the left plane of the control volume, while a higher uniform static pressure  $p_b$  exists on the right boundary. Also, in order to calculate the jet momentum and massflow injected through the nozzle, the local static pressures on either side of the nozzle exit must be specified, and these are also taken to be  $p_a$  and  $p_b$  respectively. Note that on the left side, fluid which is stagnant in  $F_S$  is assumed to fill the space next to the upper wall, and since viscous effects are ignored, the assumption that local nozzle-exit pressure is  $p_a$  on this side is natural. On the right side, the pressure felt in the corner formed by the upper wall and right edge of the jet would be  $p_b^*$  in inviscid flow, but as  $M_b$  is always small, the error this introduces is insignificant for present purposes.

Development of a simple, closed-form solution for  $\dot{m}_{bz}$  as a function of  $\delta p$  and the other controlling variables is facilitated if the perturbations in nozzle massflow and mean exit velocity due to  $\delta p$  are ignored. That is, take

$$\dot{m}_n \doteq \dot{m}_{n0}$$

$$K_n \doteq K_{n0}$$

This is consistent with taking  $p_n \doteq p_a$ , noting which one may additionally write:



$$\alpha_a \doteq \alpha_n$$

$$c_n \doteq c_a$$

$$M_n \doteq M_a$$

The overall effect of this approximate approach is to treat the jet as if it were somewhat "stiffer" than it really is--that is, able to withstand larger values of the pressure differential  $\delta p$  for a given bypass mass-flow than is actually the case. The resultant quantitative errors, which for the most part are not large, are in the direction of overestimating the strength of the nonsteady processes; therefore, there is no danger of being led into incorrect qualitative conclusions due to effectively "assuming away" some nonsteady phenomena.

The continuity equations for the nozzle flow and bypassed flow are

$$\dot{m}_a = \dot{m}_n \quad (45a)$$

$$\dot{m}_b = \dot{m}_{by} \quad (45b)$$

The momentum equation for the control volume is, neglecting wall friction,

$$F_A - F_B = -\dot{m}_n c_n \sin \beta$$

where  $F_A$  and  $F_B$ , the values of the stream force at stations "A" and "B", are

$$F_A = p_a \alpha_d + \dot{m}_a c_a + \dot{m}_{by} c_{by}$$

$$F_B = p_b \alpha_d + \dot{m}_b c_b$$

With the continuity equations (45a,b) and the "stiff" jet assumptions,

$$(p_b - p_a)\alpha_d + \dot{m}_{by}(\kappa_b - \kappa_{by}) = \dot{m}_a \kappa_a (1 - \sin\beta) \quad (46)$$

The energy equation for the bypass flow is

$$c_p T_b + \frac{\kappa_b^2}{2} = c_p T_{by} + \frac{\kappa_{by}^2}{2}$$

or, noting that

$$p_{by} = p_a$$

$$\frac{T_{by}}{T_b} = \left(\frac{p_{by}}{p_b}\right)^{\frac{\gamma-1}{\gamma}}$$

one has

$$\kappa_{by}^2 = \kappa_b^2 + 2c_p T_b \left[ 1 - \left(\frac{p_a}{p_b}\right)^{\frac{\gamma-1}{\gamma}} \right] \quad (47)$$

Equations (46) and (47) are to be solved for  $\dot{m}_{by}$ . Glancing at Figure 56, it is noted that  $\alpha_{by} \ll \alpha_d$ , so that  $\kappa_b \ll \kappa_{by}$ . An approximate solution, therefore, may be obtained by neglecting  $\kappa_b$  in comparison to  $\kappa_{by}$ . Equations (46) and (47) give in this case:

$$\dot{m}_{by} = \frac{(p_b - p_a)\alpha_d - \dot{m}_a \kappa_a (1 - \sin\beta)}{\kappa_{by}} \quad (46')$$

$$\kappa_{by} = \sqrt{2c_p T_b \left[ 1 - \left(\frac{p_a}{p_b}\right)^{\frac{\gamma-1}{\gamma}} \right]} \quad (47')$$

Using (47') in (46') gives

$$\dot{m}_{by} = \frac{\left(\frac{p_b}{p_a} - 1\right)p_a \alpha_d - \dot{m}_a \kappa_a (1 - \sin\beta)}{\sqrt{2c_p T_b \left[ 1 - \left(\frac{p_a}{p_b}\right)^{\frac{\gamma-1}{\gamma}} \right]}} \quad (48)$$

For the nonsteady analysis,  $M_b$  is more convenient to use than

$\dot{m}_{by}$  :

$$\begin{aligned}\dot{m}_{by} &= \dot{m}_b = \rho_b c_b \alpha_d \\ &= \sqrt{\frac{\gamma}{R}} \frac{p_b}{\sqrt{T_b}} M_b \alpha_d\end{aligned}$$

$$\begin{aligned}\dot{m}_a c_a &= \rho_a c_a^2 \alpha_a \\ &= p_a \gamma M_a^2 \alpha_n\end{aligned}$$

where  $\alpha_a \doteq \alpha_n$  has been used in the expression for  $\dot{m}_a c_a$ . Substituting for  $\dot{m}_{by}$  and  $\dot{m}_a c_a$  in (48):

$$\sqrt{\frac{\gamma}{R}} \frac{p_b}{\sqrt{T_b}} M_b \alpha_d = \frac{\left(\frac{p_b}{p_a} - 1\right) p_a \alpha_d - p_a \gamma M_a^2 \alpha_n (1 - \sin \beta)}{\sqrt{2 c_p T_b \left[1 - \left(\frac{p_a}{p_b}\right)^{\frac{\gamma-1}{\gamma}}\right]}}$$

which may be rearranged to give

$$M_b = \frac{\sqrt{\gamma-1}}{\gamma} \frac{1 - \frac{1}{(p_b/p_a)} \left\{1 + \gamma M_a^2 \frac{1 - \sin \beta}{(\alpha_d/\alpha_n)}\right\}}{\sqrt{2 \left[1 - \left(\frac{p_a}{p_b}\right)^{\frac{\gamma-1}{\gamma}}\right]}} \quad (49)$$

The value of  $\frac{p_b}{p_a}$  which produces critical flow [Figure 55(b)] is that for which  $M_b = 0$ ; this is found by setting the numerator of the fraction in (49) to zero, since the denominator at the critical condition is nonzero and finite. This gives:

$$\left(\frac{p_b}{p_a}\right)_{cr+} = 1 + \left(\frac{\delta p}{p_a}\right)_{cr+} = 1 + \gamma M_a^2 \frac{1 - \sin \beta}{(d_d/d_m)} \quad (50)$$

where  $( )_+$  indicates that the calculation is as based on the supercritical analysis. With (50), (49) may be rewritten as

$$M_b = \frac{\sqrt{\gamma-1}}{\gamma} \frac{\left[1 - \frac{(p_b/p_a)_{cr+}}{(p_b/p_a)}\right]}{\sqrt{2\left[1 - \left(\frac{p_b}{p_a}\right)^{\frac{\gamma-1}{\gamma}}\right]}} \quad (49')$$

Equation (50) gives  $(p_b/p_a)_{cr+}$  as calculated from the supercritical analysis. A value for  $(p_b/p_a)_{cr+}$  may alternatively be calculated from the subcritical analysis by setting  $\frac{\mu}{\mu_0} = 0$  in equation (16"), which gives (noting that  $M_n$  may be replaced with  $M_a$  in this linearized analysis):

$$\left(\frac{p_b}{p_a}\right)_{cr-} = 1 + \gamma M_a^2 \frac{(1 - \sin^2 \beta)}{(2 \frac{d_d}{d_m} - 1)}$$

or

$$\left(\frac{p_b}{p_a}\right)_{cr-} = 1 + \left(\frac{\delta p}{p_a}\right)_{cr-} = 1 + \frac{\gamma M_a^2}{2(1 + \sin \beta)} \frac{(1 - \sin \beta)}{(\frac{d_d}{d_m} - \frac{1}{2})} \quad (51)$$

where  $( )_-$  identifies the subcritical analysis as the source of this calculation. Comparing (50) and (51), it is seen that the two values for  $(p_b/p_a)_{cr}$  will in general differ somewhat, the tendency being for  $\left(\frac{p_b}{p_a}\right)_{cr-} < \left(\frac{p_b}{p_a}\right)_{cr+}$  but with this being offset to some extent by the

greater sensitivity of  $\left(\frac{p_b}{p_a}\right)_{cr}$  to the channel height factor  $\frac{d_d}{\alpha_m}$ .

Table 2 presents  $\left(\frac{p_b}{p_a}\right)_{cr}$  as calculated from both equations (50) and (51) together with their ratio, and it is seen that while the two analyses do differ at the critical condition (not a surprising result considering that each is a linearized treatment specialized to the regime under consideration), they are in agreement as to general trends and approximate magnitudes.

In the nonsteady analysis, of course, the source region begins the "second cycle" in the supercritical regime and later passes through the critical condition into subcritical flow as wave processes relieve the elevated pressure on the right side of the source. This transition must be accomplished without a discontinuity in  $\left(\frac{p_b}{p_a}\right)_{cr}$  such as would result from using equations (50) and (51) separately for the supercritical and subcritical regimes, respectively. To this end, note that (16") may be written instead as (again using  $M_a$  in place of  $M_m$ )

$$\frac{\mu}{\mu_0} = 1 - \frac{\delta p / p_a}{\left(\delta p / p_a\right)_{cr}} \quad (16''')$$

where  $\left(\frac{\delta p}{p_a}\right)_{cr}$  is as given by equation (51). The basic character of the subcritical flow solution is not changed if  $\left(\frac{p_b}{p_a}\right)_{cr}$  is obtained instead from equation (50), there being merely a minor reduction in the sensitivity to  $\delta p$  that is ascribed to the massflow ratio  $\mu$ . This will therefore be done, so that the behavior of the source over the range of all three regimes in Figure 55 is described by means of equations (16'''), (49'), and (50).



TABLE 2

Values of  $\left(\frac{\delta p}{p_a}\right)_{cr}$  from Subcritical and Supercritical Analyses

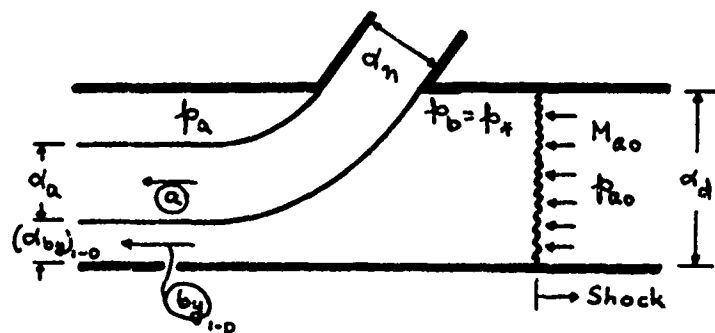
CASE	$\frac{a_{ao}}{a_d}$	$\left(\frac{\delta p}{p_a}\right)_{cr-}$	$\left(\frac{\delta p}{p_a}\right)_{cr+}$	$\frac{(\delta p/p_a)_{cr-}}{(\delta p/p_a)_{cr+}}$
1 2 3	0.75	0.26 0.59 1.05	0.26 0.59 1.05	1.00
4 5 6	0.50	0.13 0.30 0.52	0.18 0.39 0.70	0.75
7 8 9	0.38	0.088 0.20 0.35	0.13 0.30 0.52	0.67
10 11 12	0.85	0.18 0.39 0.70	0.18 0.39 0.70	1.00
13 14 15	0.57	0.088 0.20 0.35	0.12 0.26 0.47	0.75
16 17 18	0.43	0.058 0.13 0.23	0.088 0.20 0.35	0.67
19 20 21	0.93	0.088 0.20 0.35	0.088 0.20 0.35	1.00
22 23 24	0.62	0.044 0.098 0.18	0.058 0.13 0.23	0.75
25 26 27	0.47	0.029 0.066 0.12	0.044 0.098 0.18	0.67

Initial shock conditions. The initial shock conditions are determined on the basis of massflow compatibility, with the assumption that the entire duct to the right of the source is filled with leftward-moving "cold slug" fluid (see Figure 53), i.e. that the duct flow is one-dimensional; this assumption also applies to the construction of the wave diagrams which describe the ensuing nonsteady duct flow phenomena. Thus, the determination of initial shock strength is illustrated in Figure 57(a). Of course, the slug does not in fact fill the duct; therefore, the amount of massflow calculated to bypass through the source region must in effect contain a correction to satisfy continuity requirements as depicted in Figure 57(b), which amounts to multiplying  $\dot{m}_b$  (hence  $\dot{m}_{by}$ ) by the ratio  $\frac{\alpha_{so}}{\alpha_d}$ . Ordinarily, this continuity correction takes care of itself in the wave diagrams, since only a certain fraction of the leftward-flowing "cold slug" succeeds in exiting through the source region and the duct area does not enter explicitly at all. However, if the duct height is small enough, the leftward-swept jet issuing from the nozzle is forced to adhere to the wall as shown in Figure 57(c); the shock strength must in such a case reflect the area constraint on the leftward flow from the source region, and in accounting for this area constraint it is necessary to consider the continuity correction of Figure 57(b) explicitly.

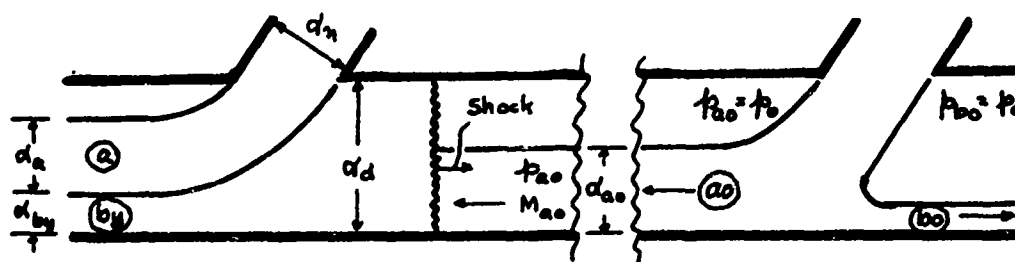
Consider now Figure 57(a) and the determination of initial shock conditions by application of the massflow compatibility boundary condition. As depicted in Figure 55, a station "\*" will be thought of as the junction between the source region to the left and the "hot duct" to the right.

On the source side, equations (49') and (50) describe the manner in which

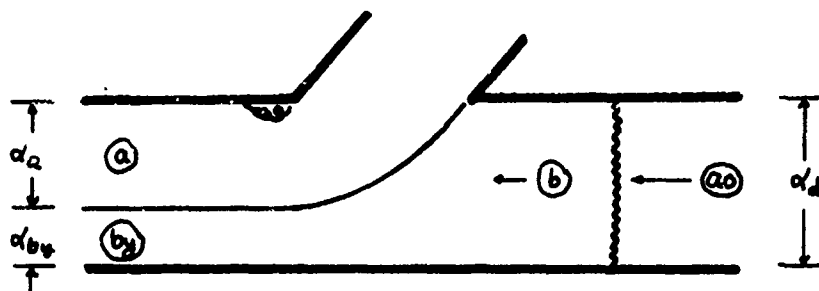
$\dot{M}_b$  depends upon  $\frac{p_0}{p_a}$ ; note that all dependence upon configuration



### (a) One-dimensional Massflow Compatibility



### (b) Continuity Correction



(c) Area-constrained Condition

**Figure 57**  
**Supercritical Flow and Initial Shock Conditions**

( $\beta$ ,  $\frac{a_d}{a_m}$ ) and operating condition ( $M_a$ ) is contained in the expression for  $(\frac{p_b}{p_a})_{sh}$ , equation (50), so that a set of generalized curves may be generated for various values of  $(\frac{p_b}{p_a})_{sh}$ , after which these may be entered for any given combination of  $\beta$ ,  $\frac{a_d}{a_m}$ , and  $M_a$ . On the duct side, define:

$a_{ref}$  = a reference speed of sound

$A_{ao}$  = dimensionless speed of sound in the cold slug,  $a_{ao}/a_{ref}$

$u_{ao}^{(s)}$  = dimensionless velocity in  $F_S$  of the cold slug,  $-c_{ao}/a_{ref}$

$u_b^{(s)}$  = dimensionless velocity in  $F_S$  of the flow exiting from the duct through plane "\*",  $-c_b/a_{ref}$

Note that  $u_{ao}^{(s)}$  and  $u_b^{(s)}$  are defined as algebraic quantities, whereas  $c_{ao}$  and  $c_b$  are just magnitudes of velocity; hence the minus signs enter, reflecting the sign convention of velocity positive to the right (in the direction of the "hot" port). If  $a_{ref}$  is chosen as  $a_{ao}$  and  $\Delta u^{(s)} = u_b^{(s)} - u_{ao}^{(s)}$ , then one may readily obtain

$$u_b^{(s)} = -M_a + \frac{|\Delta u|}{A}$$

or, with  $M_b = -u_b^{(s)}$ ,

$$M_b = M_a - \frac{|\Delta u|}{A} \quad (52)$$

The magnitude of the dimensionless velocity change across the shock,  $\frac{|\Delta u|}{A}$ , may be found as a function of  $\frac{p_b}{p_a}$  from tabulations in Rudinger,<sup>38</sup> the case of  $\gamma = 1.4$  being presented in Table 1a.

Using equations (49') and (50) for the source-region flow and equation (52) together with Table 1a of Rudinger for the initial shock, the curves in Figure 58 may be generated for the cases in Table 1 wherein

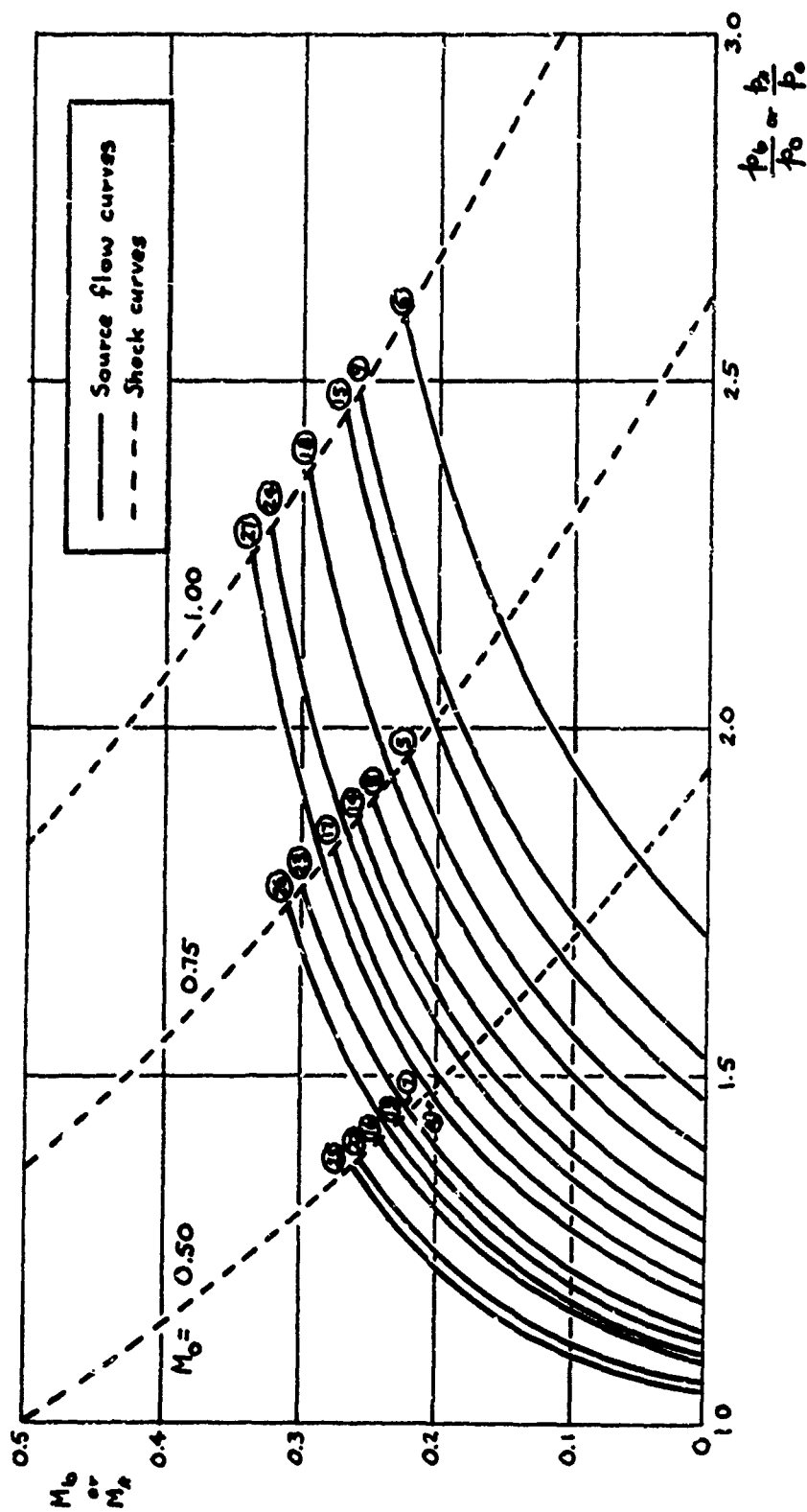


Figure 58  
Constraint-Free Source Flow Curves

the area constraint is absent. For each case, the intersection of the source-region curve with the initial-shock curve for the given value of  $M_a$  gives the initial shock solution. The case corresponding to each solution is indicated.

Consider now the area-constrained circumstance, which occurs when  $\frac{d_d}{d_m}$  is in the neighborhood of unity. Generally, an area-constrained flow pattern might occur for  $\frac{d_d}{d_m} = 1.25$ , say, but by the time the channel height factor is as large as 1.5 it no longer occurs. Therefore, of the cases in Table 1, only those with  $\frac{d_d}{d_m} = 1.0$  happen to be affected.

The general requirement which must be met by flows "a" and "by" is that

$$\frac{d_{ao}}{d_d} + \frac{d_{by}}{d_d} \leq 1 \quad (53)$$

If a separated region is left above the flows as in Figure 57(b), the inequality applies, and the duct area is irrelevant. If the situation of Figure 57(c) occurs, however, the equality applies in equation (53), and in general this will cause the bypass flow to be less--and the initial shock stronger--than would be the case if the area constraint were not present.

The following procedure has been used to account in a rough way for the area constraint effect, which is incorporated into adjusted source flow curves.

(1) Calculate

$$R_d = \frac{d_{ao}}{d_d} + \frac{d_{by}}{d_d}$$

or

$$k_\alpha = \frac{\alpha_{ao}}{\alpha_d} \left[ 1 + \left( \frac{\alpha_{by}}{\alpha_d} \right)_{1-D} \right]$$

where the continuity correction of Figure 57(b) is applied and  $\left( \frac{\alpha_{by}}{\alpha_d} \right)_{1-D}$  is as obtained from continuity for Figure 57(a).

$$\left( \frac{\alpha_{by}}{\alpha_d} \right)_{1-D} = \frac{D_b}{D_{by}}$$

Note that

$$D_{by} = D \left( \frac{p_{by}}{p_a} \right) \doteq D \left( \frac{p_b}{p_a} \right)$$

since  $p_{by} = p_a$ ,  $p_{by}^* = p_b^* \doteq p_b$  due to  $M_b$  small.

(2) If  $k_\alpha \leq 1$ , there is no problem. If  $k_\alpha > 1$ , assume that the "a" and "by" flows are in the same proportion as they would be if unconstrained, but that both flows are reduced in area--hence, flow rate--by the factor  $\frac{1}{k_\alpha}$ . Since  $M_b$  is small, one has at any given value of  $\frac{p_b}{p_a}$ :

$$\frac{M_b'}{M_b} \doteq \frac{m_{by}'}{m_{by}}$$

where primes denote values adjusted to account for the area constraint; or

$$M_b' \doteq \frac{M_b}{k_\alpha}$$

It is seen that in the area-constrained case,  $M_b$  will be smaller at any given value of  $\frac{p_b}{p_a}$  than would occur without area constraint.

(3) The intersection of the area-constrained source flow curve with the appropriate initial shock curve gives the initial shock solution

in a manner similar to Figure 58.

In the present analysis, the only area-constrained cases are those with  $\frac{\alpha_d}{\alpha_n} = 1.0$ . Since the approximate analysis used for the source region takes  $\alpha_a = \alpha_n$ , this implies that if any bypass flow occurs at all, an area constraint adjustment must be applied in these cases. Now,  $\alpha_{by}$  is proportional to  $\dot{m}_{by}$  and hence to  $M_b$ ; therefore, for the present analysis with  $\frac{\alpha_d}{\alpha_n} = 1.0$ , one has

$$k_\alpha = 1 + (\text{const}) M_b$$

The constraint correction curve is similar in shape, in other words, to the unconstrained source flow curve involved in step (1). The resultant area-constrained source flow curves and corresponding shock solutions are presented in Figure 59, and it will be noticed that the curves in Figure 59 are flatter than those in Figure 58.

Figure 60 summarizes the initial shock solutions obtained from the intersections in Figures 58 and 59. It is seen that the Mach number  $M_0$  (to which  $M_n$ ,  $M_a$ , and  $M_{ao}$  are all equal in the present analysis) is the most important variable in determining the shock strength. Channel height also has an appreciable influence, whereas the effect of nozzle inclination is relatively weak.

Perturbation relief transient: supercritical phase. Conditions

the right-hand boundary of the source region will correspond to the initial shock solution until subsequent waves arrive from the right to alter conditions there. For the situation being analyzed, wherein the effective "hot port" area is equal to the duct area, a rarefaction is generated at the port as part of the initial transient, Figure 53, and



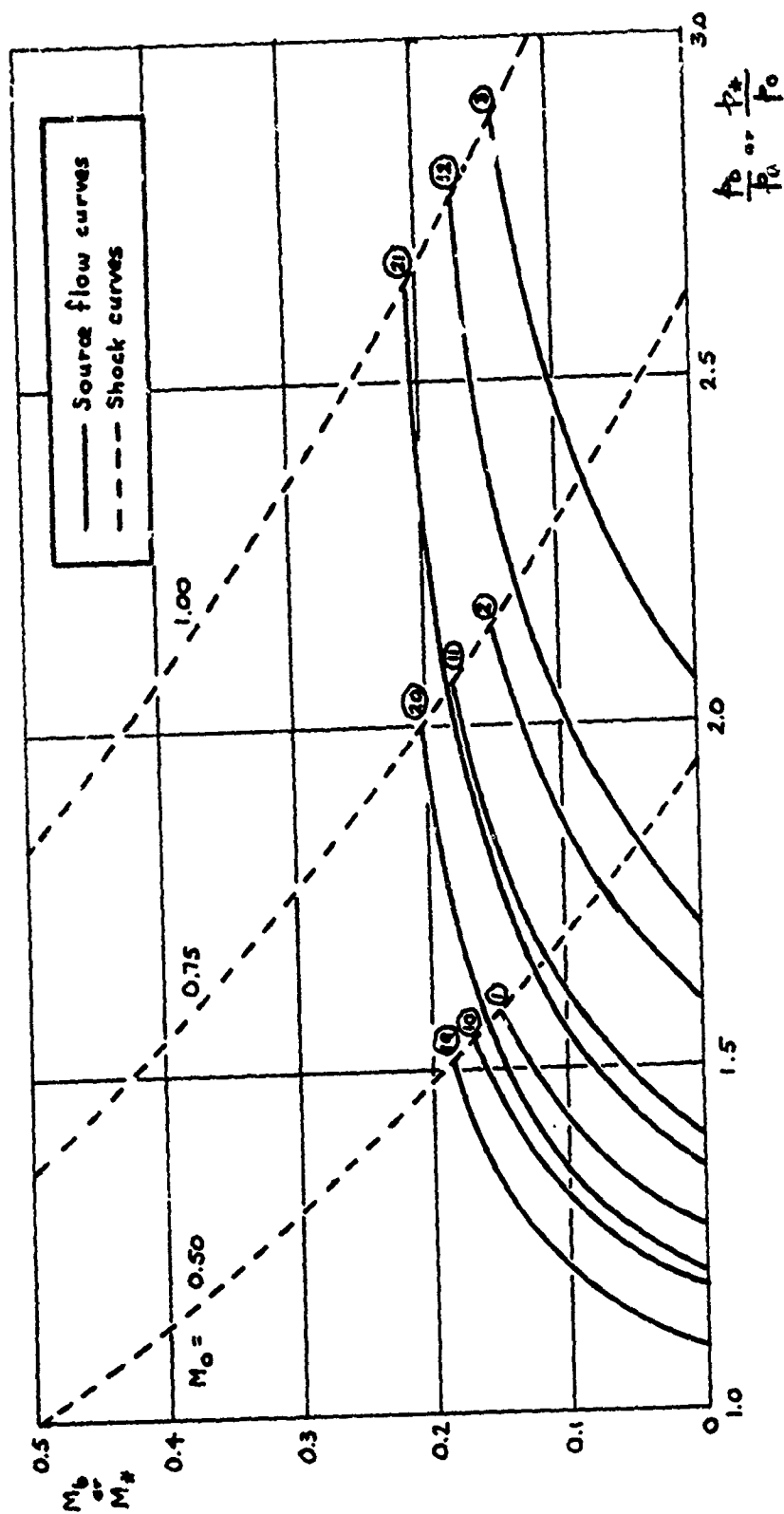


Figure 59  
Area-Constrained Source Flow Curves

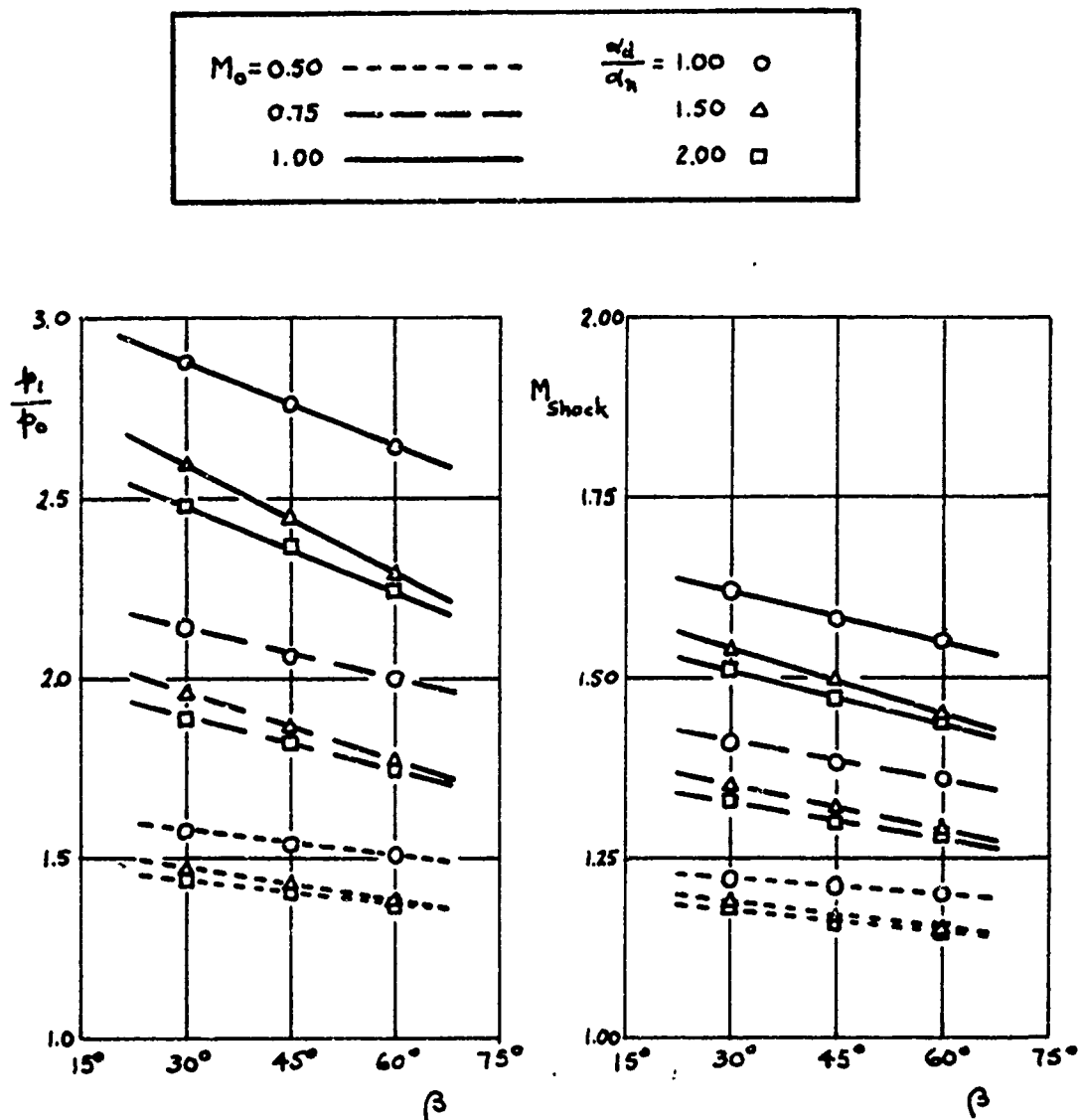


Figure 60  
Initial Shock Solutions

this will begin reducing the pressure  $p_*$ . The initial shock, when it arrives at the hot port, will be reflected as a strong rarefaction, and when it arrives at the source sometime later it will further reduce  $p_*$ . Referring to Figures 58 and 59, then, rarefactions will cause the source flow condition to depart from the initial shock solution and move leftward down the source flow curve that corresponds to any given case, reaching the intersection of the curve with the  $M_b = 0$  axis when  $p_*$  is reduced to the critical value.

To analyze this transient, it is necessary to carry out a wave diagram analysis of the phenomena in the hot duct. This is best done by expressing the characteristics of the source region in terms of auxiliary curves analogous to those commonly used for outflow through a partially open end. Define:

- $p_o$  = ambient pressure, to which the pressures  $p_{ao}$  of the "cold slug" and  $p_a$  in the cold duct (to left of source) are assumed equal
- $p_i$  = value of  $p_*$  established by initial shock
- $p_{cr}$  = value of  $p_*$  for which source flow is critical
- $a_o$  = reference speed of sound, taken equal to that of the "cold slug"
- $A$  = dimensionless speed of sound,  $a/a_o$  (54)
- $u^{(s)}$  = dimensionless velocity in  $F_S$ ,  $u/a_o$
- $u^{(u)}$  = dimensionless velocity in  $F_U$ ,  $u/a_o$
- $P, Q$  = Riemann variables
- $\xi$  = dimensionless distance,  $x/L_o$
- $\tau$  = dimensionless time,  $a_o t/L_o$

The Riemann variables are defined by

$$P = \frac{2}{\gamma-1} A + U \quad (55)$$

$$Q = \frac{2}{\gamma-1} A - U \quad (56)$$

During outflow from the hot duct through the supercritical source,

$$U_b^{(s)} = -M_b A_*$$

with which the Riemann variables in  $F_S$  may be written at station "\*" as

$$P_*^{(s)} = \frac{2}{\gamma-1} A_* \left(1 - \frac{\gamma-1}{2} M_b\right) \quad (55')$$

$$Q_*^{(s)} = \frac{2}{\gamma-1} A_* \left(1 + \frac{\gamma-1}{2} M_b\right) \quad (56')$$

The alteration of the pressure  $p_*$  from its initial value  $p_i$ , behind the initial shock to a subsequent value takes place as the result of a series of isentropic disturbances, whence

$$A_* = A_i \left(\frac{p_*}{p_i}\right)^{\frac{\gamma-1}{2\gamma}}$$

Therefore,

$$P_*^{(s)} = \frac{2}{\gamma-1} A_i \left(\frac{p_*}{p_i}\right)^{\frac{\gamma-1}{2\gamma}} \left(1 - \frac{\gamma-1}{2} M_b\right) \quad (55'')$$

$$Q_*^{(s)} = \frac{2}{\gamma-1} A_i \left(\frac{p_*}{p_i}\right)^{\frac{\gamma-1}{2\gamma}} \left(1 + \frac{\gamma-1}{2} M_b\right) \quad (56'')$$

Note in particular that critical source flow occurs when the Q-characteristic arrives which produces  $p_* = p_{0R}$  and hence  $M_b = 0$ . For a

given case being analyzed, this characteristic may be identified as

$$Q_{CR}^{(s)} = \frac{2}{\gamma-1} A_1 \left( \frac{p_{CR}/p_0}{p_1/p_0} \right)^{\frac{\gamma-1}{2\gamma}}$$

Finally, note that

$$A^{(u)} = A^{(s)}$$

$$U^{(u)} = U^{(s)} + U_*$$

where  $U_*$  is the dimensionless rotor velocity as measured in  $F_U$ ,

$$\begin{aligned} U_* &= \frac{V}{a_0} \\ &= \frac{V}{c_m} \frac{c_m}{a_0} \\ &= M_0 \sin \beta \end{aligned}$$

Applying the Riemann variable definitions in  $F_U$ , one therefore obtains with equations (55") and (56") and the change of reference frame,

$$P_*^{(u)} = \frac{2}{\gamma-1} A_1 \left( \frac{p_*}{p_1} \right)^{\frac{\gamma-1}{2\gamma}} \left( 1 - \frac{\gamma-1}{2} M_0^2 \right) + M_0 \sin \beta \quad (57)$$

$$Q_*^{(u)} = \frac{2}{\gamma-1} A_1 \left( \frac{p_*}{p_1} \right)^{\frac{\gamma-1}{2\gamma}} \left( 1 + \frac{\gamma-1}{2} M_0^2 \right) - M_0 \sin \beta \quad (58)$$

Using equations (57) and (58) together with Figures 58 and 59, an auxiliary plot of  $P_*^{(u)}$  versus  $Q_*^{(u)}$  may be generated for each case to be analyzed, covering the supercritical transition from the initial shock to the condition of critical source flow. Figure 61 presents these auxiliary curves for all of the cases in Table 1. Their most outstanding

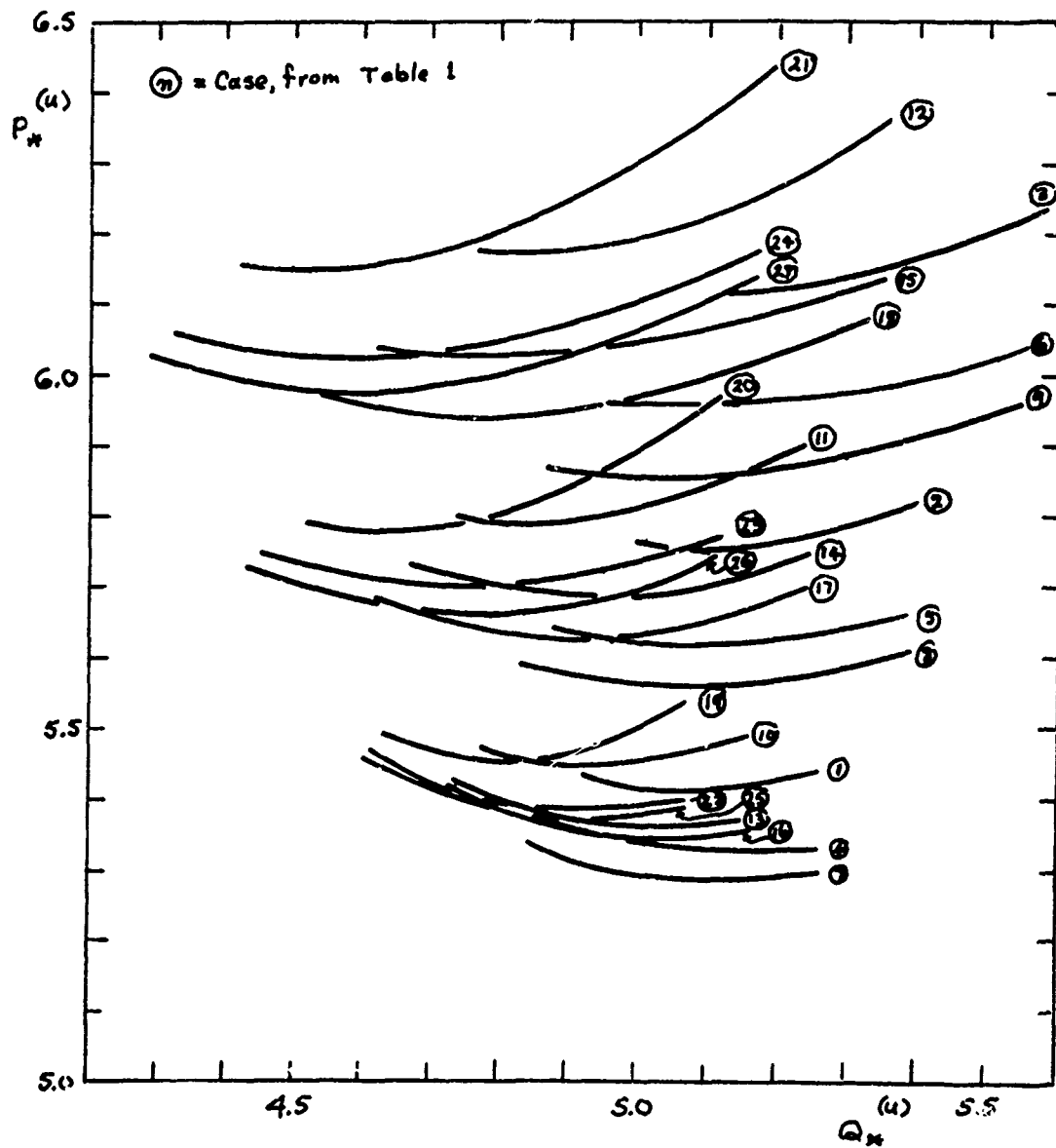


Figure 61  
Auxiliary Plots for Supercritical Perturbation Relief Transients

feature is their shallowness: the change in  $P_*^{(u)}$  that is occasioned by a given change in  $Q_*^{(u)}$  is small. In other words, any incipient wave from the right is reflected only very weakly. This is analogous to the situation wherein a partially open end of a duct can reflect an incipient wave weakly or not at all if the opening is sized properly; in the present case, the qualitative tendency of the source is to continuously adjust itself so that the effective opening (the bypass flow area) results in very little wave reflection.

Perturbation relief transient: subcritical phase. The supercritical phase of the relief transient begins after the initial shock has established supercritical flow, Figure 55(a), and terminates with the condition of critical flow, Figure 55(b). Further lowering of  $P_*$  leads to a re-emergence of the "b" flow from the source region, as shown in Figure 55(c).

At the critical flow condition, Figure 55(b), the boundary condition on particles just to the right of the jet is that they move at the velocity of the source,  $V$  (or in dimensionless terms,  $U_*$ ). Reestablishment of the "b" flow as shown in Figure 55(c) causes a thin layer of fluid to be sliding along the wall underneath the main column of fluid, but the left end of this column still abuts the main jet issuing from the nozzle. Thus, so long as wave effects do not raise  $P_*$  back up to a high enough level to reestablish supercritical flow, the boundary condition which the source provides for the main column of fluid in the hot duct is that of a piston.

Thus, as the source travels from left to right through the duct, it starts out as a leaky piston thanks to the disturbance associated

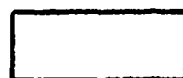
with the initial shock. It becomes less leaky as it progresses to the right, due to the action of rarefaction waves from the right which lower  $p_*$ , and eventually it becomes equivalent to a solid piston. Simultaneous with this development, it begins ejecting "b" fluid which, according to the present model wherein viscous effects are not considered, slides along the wall without greatly influencing the continued wave phenomena taking place in the main column of gas in the hot duct.

Description of the nonsteady collection process. The physical picture of the nonsteady collection process that emerges from the analysis is portrayed in Figure 62, while Figure 63 illustrates the wave diagrams developed in the course of the analysis; the actual diagrams are contained in Appendix B. A number of key phenomena are noted in both Figures 62 and 63(a) to help in grasping the nature of the process.

In Figure 62, sketches (a) through (d) illustrate the cryptosteady first cycle that is assumed to occur. As indicated in 62(a), subcritical (splashing) flow exists in the source region, and the pressure in the duct is  $p_0$ , the ambient pressure; primary attention, however, is focused on what is happening on the left side of the source. Since the leftward-flowing jet does not fill the duct, it follows that the region above the jet must be filled by fluid which, in  $F_S$ , is "deadwater." However,  $F_S$  is attached to the source which is moving to the right at the velocity  $V$  (or, in dimensionless terms,  $U_A$ ); hence the deadwater is moving to the right at velocity  $U_A$  in  $F_U$ , as indicated in 62(b). The jet itself, of course, has a net leftward dimensionless velocity  $U_{A0}$  in  $F_U$ , as is also indicated in 62(b). Finally, the height of the jet is  $d_{A0} = d_n \frac{1 + \sin \beta}{2}$ , as obtained from equation (15') of the splashing



Legend for Figure 62



Cryptosteady flow



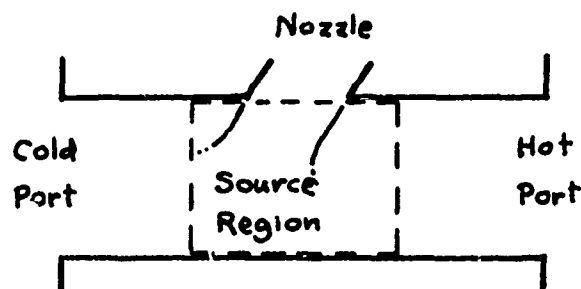
Nonsteady flow which originated at the source (nozzle)



Nonsteady flow drawn in through the hot port



Pumped flow



- (ac) Cryptosteady cold flow
- (au) Unsteady cold flow
- (ap) Pumped cold flow
- (bc) Cryptosteady hot flow
- (bu) Unsteady hot flow
- (bu') Additional unsteady hot flow (inflow/outflow)
- (bp) Pumped hot flow

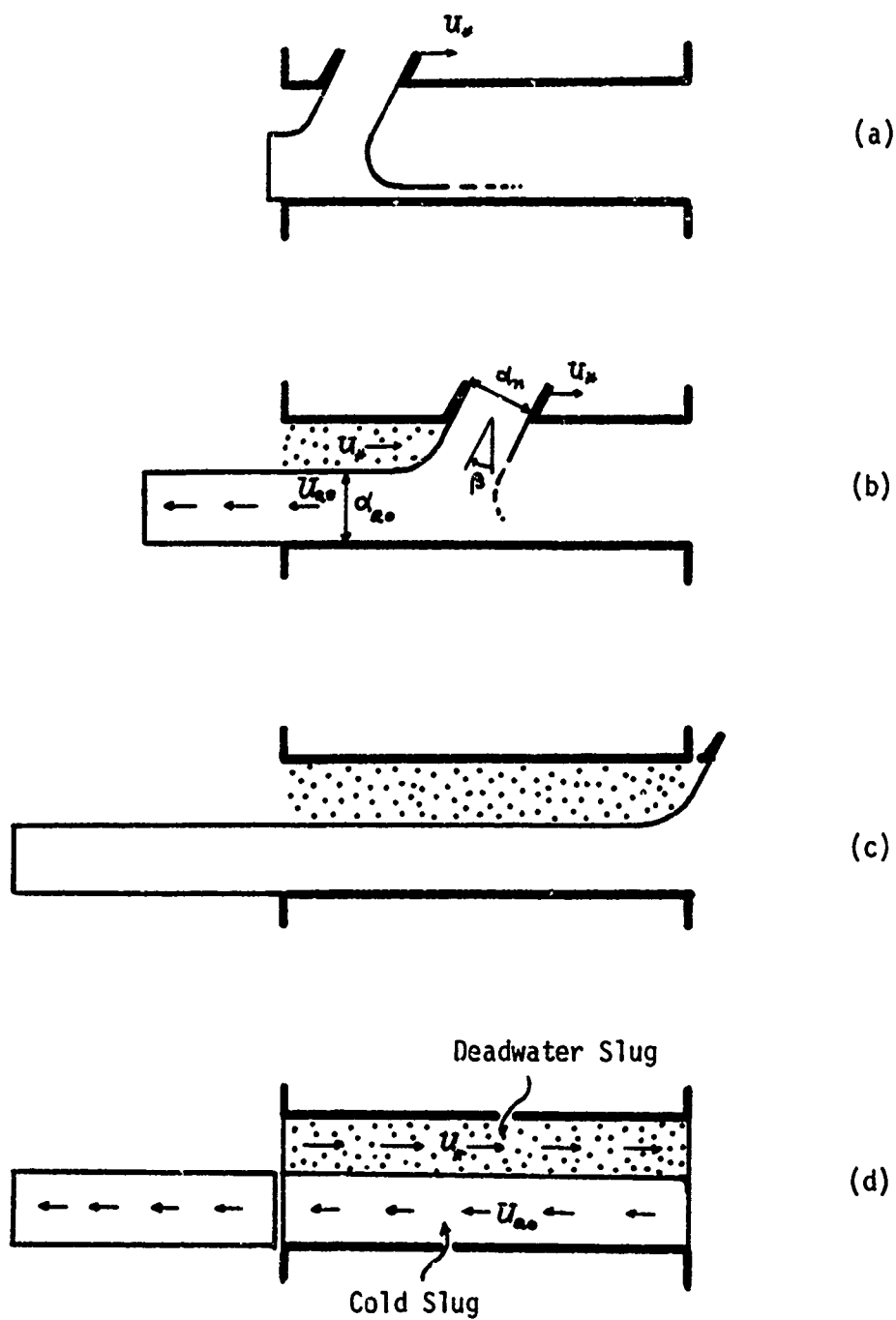


Figure 62  
Visualization of Nonsteady Collection Process

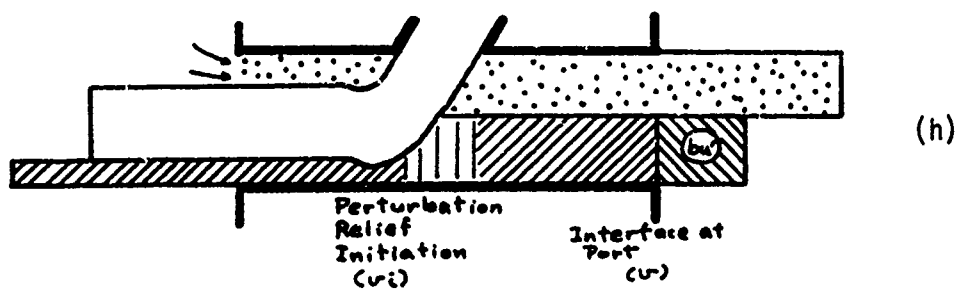
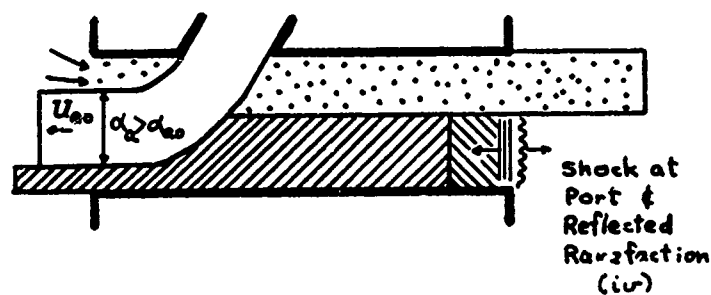
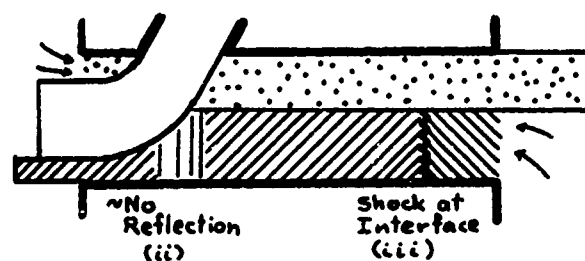
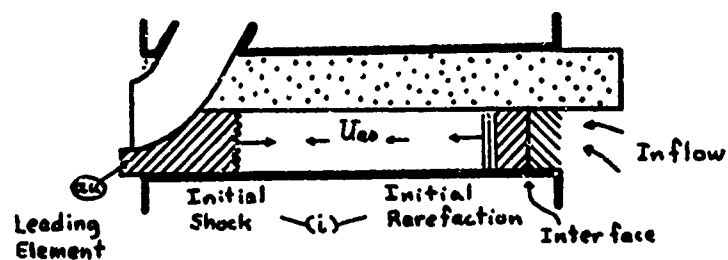
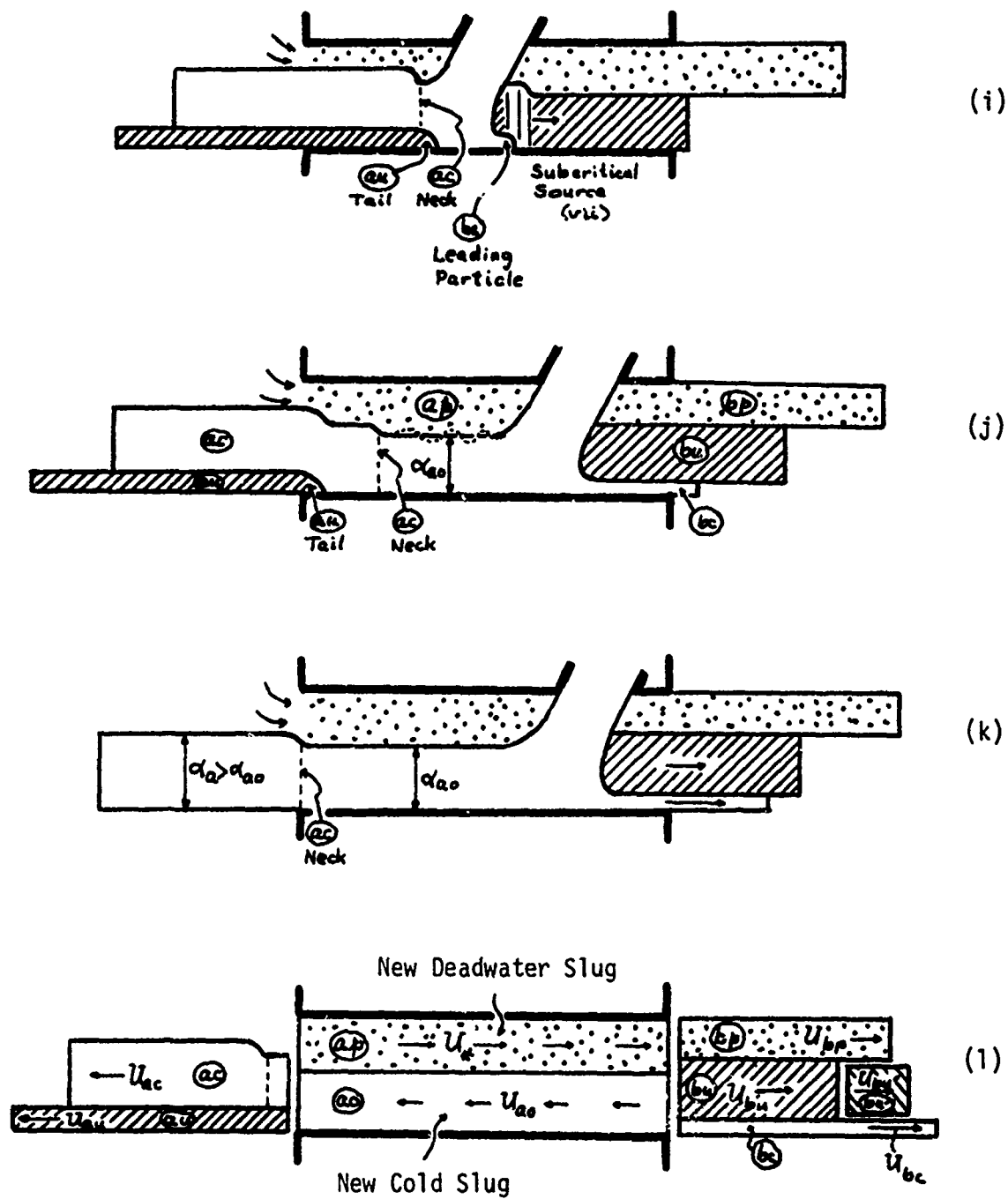









Figure 62  
(continued)



Legend for Figure 63

	Rarefaction
	Compression or shock
	Quasi-cryptosteady particle path
	Nonsteady particle path
	Interface between "cold slug" and inflow fluid
	Source (nozzle) path
	Inflow fluid

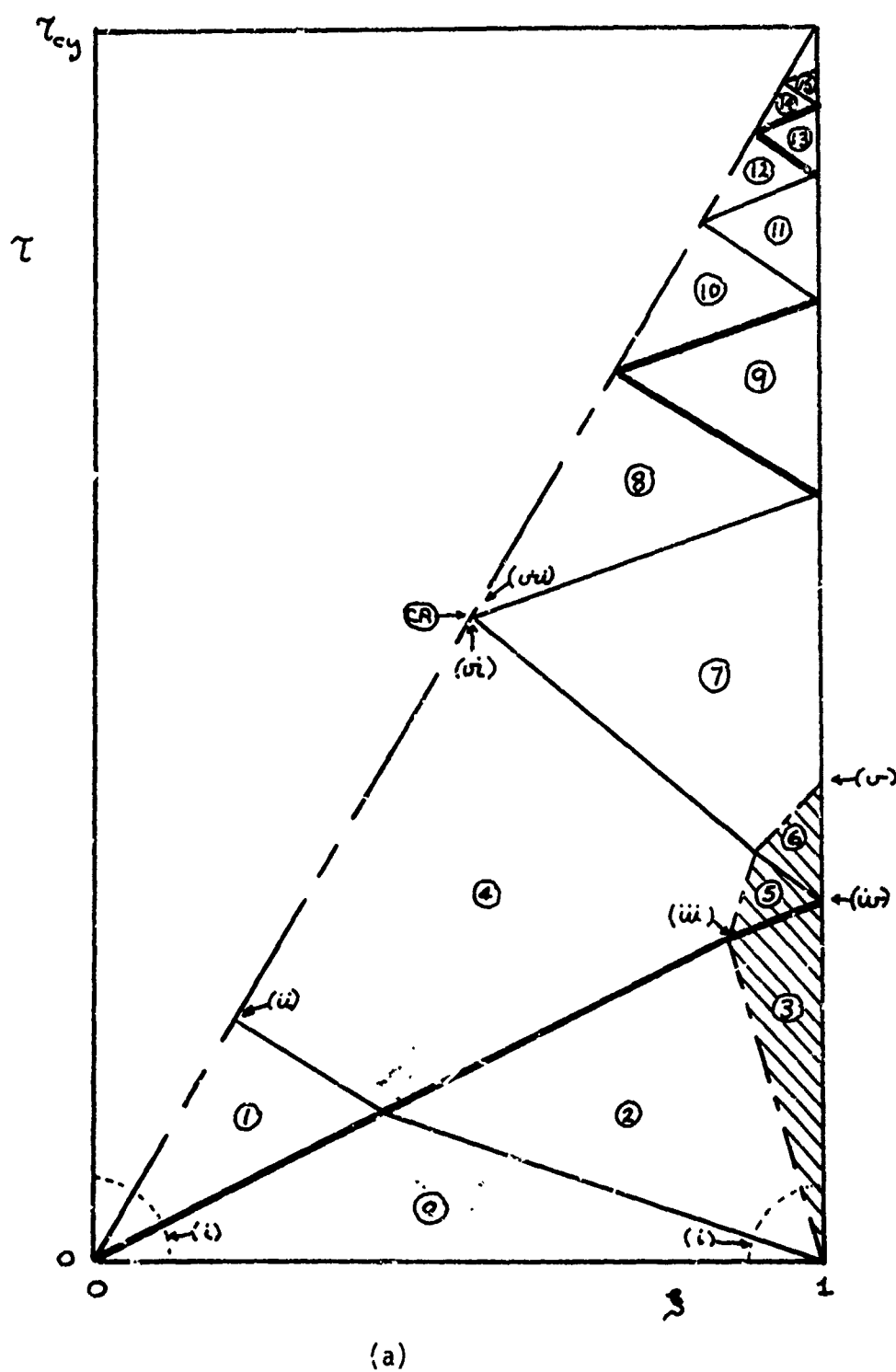


Figure 63

Description of Nonsteady Collection Wave Diagram

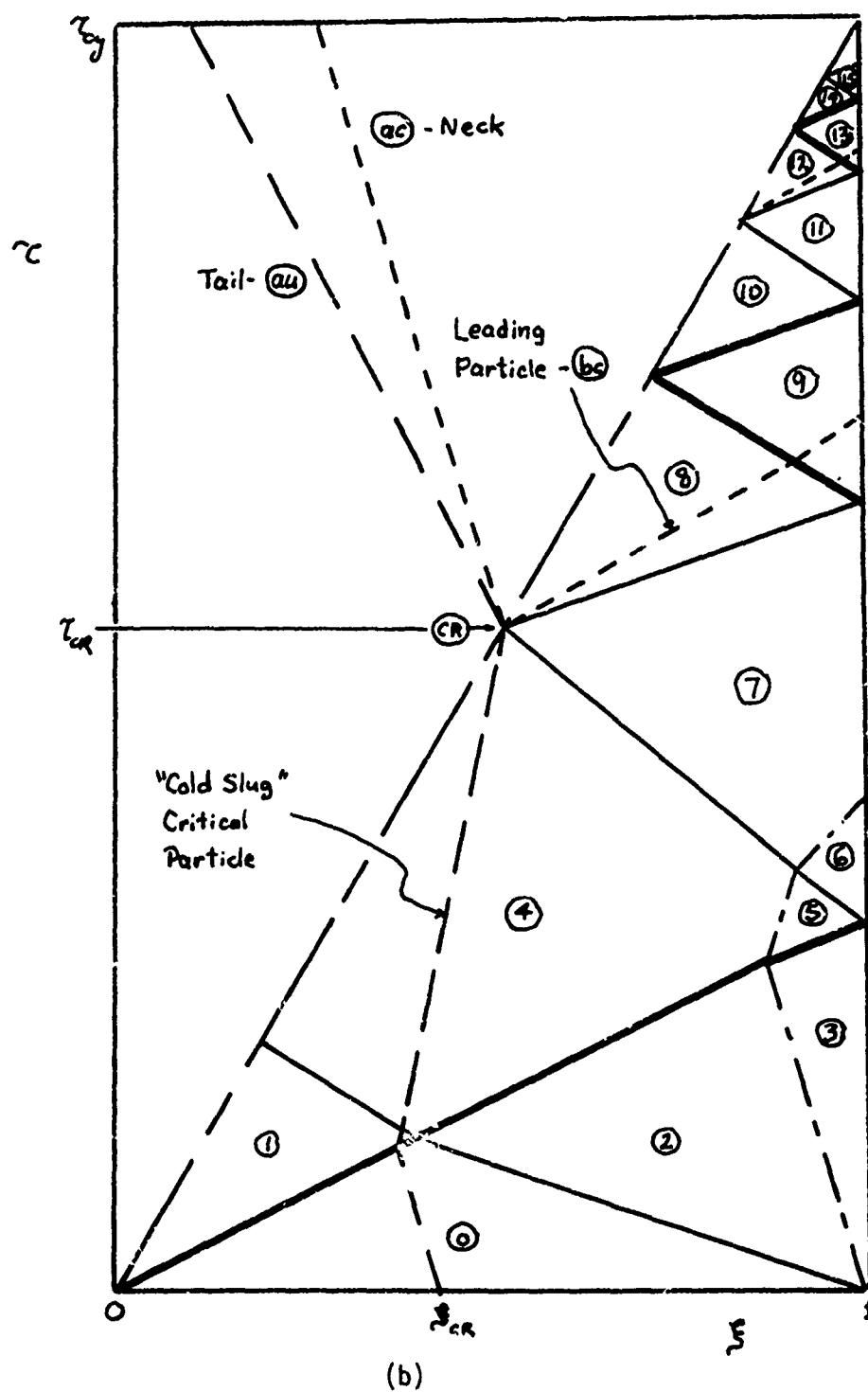


Figure 63  
(continued)

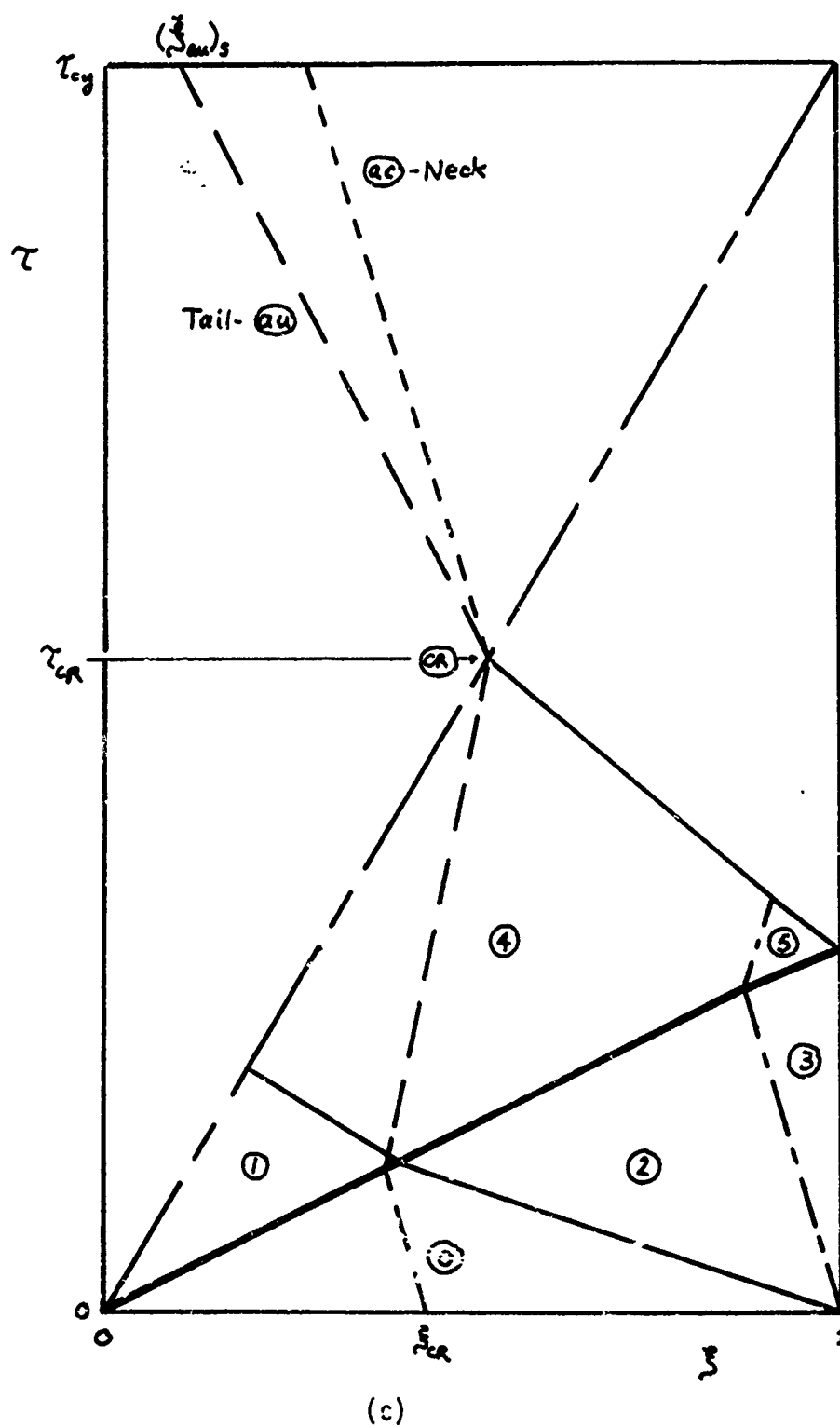


Figure 63  
(continued)



analysis for the case of  $\delta p = 0$  (no pressure differential across the jet). In 62(c), the source is just exiting from the duct, so that at the end of the cycle the situation is as picture 62(d): the lower portion of the duct is filled with a slug of fluid produced by the source and flowing leftward, while the upper portion contains a slug of fluid which is stagnant in  $F_S$ , hence rightward-moving in  $F_U$ . The top slug will be termed the "deadwater slug," while the lower body of fluid will be referred to as the "cold slug" since its properties are the same as those of the cold fluid which has been ejected out the left port.

The remainder of Figure 62--parts (e) through (l)--depict the sequence of events comprising the "second cycle." Figure 63 also pertains to this "second cycle," and it will be useful to correlate the phenomena shown in Figure 62 with the corresponding features of the wave diagram. The diagram is divided by the source path into two regions--one ahead of the source and the other behind it; the region ahead of the source will be referred to as the "hot" side and that behind it as the "cold" side. The "hot duct"--that is, the region ahead of the source--is where the strong and significant wave processes occur; hence the lower-right half of the  $\xi-\tau$  plane is explored by wave diagram techniques. Figure 63(a) illustrates the basic wave diagram that emerges, with regions of uniform flow labelled and with attention drawn to several points in the diagram which will be correlated with Figure 62. Figure 63(b) repeats 63(a), but adds several particle path lines (including two on the cold side) that have special significance. Figure 63(c) is a truncated version of Figure 63(b), and--with the aid of insight gained from the more complete diagram--is all that is needed for a rough estimation of performance.

In Figure 63(a), attention is first called to the initial transients at both ends of the duct, this being item (i); these events are also depicted in Figure 62(e). At the left end, the source appears and is moving rightward at the velocity  $U_*$ ; it is producing a jet which encounters the leftward-rushing "cold slug," with the result that a shock is produced whose strength is dependent upon the "massflow compatibility" boundary condition discussed earlier. At the right end, inflow must occur to prevent the development of a vacuum behind the right end of the "cold slug" as it travels to the left; the initiation of this inflow is accompanied by a rarefaction. Thus, it is seen in Figure 62(e) that a shock has begun moving rightward into the (leftward-moving) "cold slug" while a rarefaction is moving into the slug from the opposite end, which is adjacent to a body of foreign fluid drawn into the duct through the hot port. The unshaded portion of the "cold slug" still possesses properties identical to those of the cryptosteady cold flow; the shaded portions, however, have undergone nonsteady effects which have altered conditions there. Also, note in Figure 62(e) that the shaded portion to the left of the shock is squashing down against the lower wall and sliding past the jet; due to the pressure rise behind the shock, which is weaker than a hammer wave but qualitatively similar, this shaded flow has a higher total pressure than the cryptosteady jet and hence expands to a higher velocity. Finally, an additional item is present which lies outside the scope of the wave diagram--i.e., the pumped flow which is being forced out ahead of the cryptosteady jet. No attempt is made to take account of the detailed history of its passage, but it is clear that it must exit via the hot port, and that it must do so at a velocity which is of the order of the source

velocity  $u_x$ . In the sketches, it is merely treated as if it were pushed out at a continued uniform velocity  $u_x$ .

Item (ii) highlighted in the wave diagram, Figure 63(a), is the arrival of the initial rarefaction at the source; this is also shown in Figure 62(f). The initial rarefaction is a weak one, and the supercritical source reflects any incident wave very weakly, behaving rather like a conventional partially-open duct end (see Figure 61). As a result, the reflection is so weak that it is neglected.

Item (iii), also shown in Figure 62(f), is the arrival of the shock at the interface. The shock is strong enough to reverse the direction of travel of the interface, so that this point marks the maximum penetration of the duct by inflow. It will be noted that no reflected (Q) wave is drawn where the shock strikes the interface; this is because the strength of this reflected wave (a rarefaction) is negligible for present purposes.

Of course, it is not until the arrival of the shock at the hot port--item (iv)--a short time later that the fluid surrounding the port gets the news that it is no longer welcome. At this point inflow is replaced by outflow and the shock is reflected as a strong rarefaction. As with the shock, the reflected wave at the interface is neglected.

Item (iv) is pictured in Figure 62(a).

The timing of items (v) and (vi) may be as shown in Figure 63(a), or reversed, or about equal, depending on the combination of  $\beta$ ,  $\frac{d\beta}{dm}$ , and  $M_0$ ; therefore, they are depicted together in Figure 62(h). Item (v) is the arrival of the interface at the hot port, at which point reexpulsion of the inflow fluid has been completed and the basic nonsteady hot

flow is about to emerge. Item (vi) is the arrival of the leading elements of the reflected rarefaction, which begin to "relieve" the high pressure prevailing to the right of the source and thereby cause the flow pattern in the source region to start changing in the direction of critical flow (leftward-swept jet just sealing the duct).

The strength of the rarefaction and its effect on the source can be appreciated by noting that region 4, Figure 63(a), is little different from region 1 (conditions behind the initial shock), whereas if the exit flow is subsonic, region 7 is at ambient pressure  $p_0$ . Therefore, subcritical or "splashing" flow is reestablished partway through the rarefaction/source interaction--item (vii)--with the remainder of the rarefaction being fully reflected from the side of the jet issuing from the source, which now behaves essentially as if it were a solid piston with respect to incident waves. (So long as subsequent wave action does not raise the pressure to the right of the source above the critical level, it will continue to be true that fluid on the right side of the source and experiencing wave phenomena cannot pass through the source region, and hence the source will behave as a "closed end" in  $F_S$ , which is the same thing as a piston with velocity  $U_x$  in  $F_U$ . If the pressure  $p_x$  ever is raised back above the critical level, then of course the "piston" condition breaks down, and supercritical-flow source behavior obtains instead.)

Figure 62(i) illustrates the freshly reestablished subcritical flow condition and what amounts to a partial reflection of the overall incident rarefaction. For correlation purposes, one may shift attention from Figure 63(a) to 63(b) and note that point "CR" is a singular point on the wave diagram where a number of important things happen. Events (vi)

and (vii), which are separated in reality by a finite time, are compressed analytically into the same point since a finite-wave diagram is in use rather than a characteristics diagram. In this representation, then, comparison of Figures 62(h) and 62(i) reveals that the body of fluid which started out as the "cold slug" is in effect chopped in two at point "CR". This phenomenon will be a basic ingredient in the final conclusion of the present analysis that nonsteady collection has an inherently detrimental effect on external-separation FES performance.

Looking at Figure 63(b), notice that point "CR" is common to all four of the particle paths which are sketched in addition to the interface path. Consider first the nonsteady particle paths (long-dash lines): "CR" is the destination of the "cold slug" critical particle, and the origination point for the "tail" of the "au" slug. Looking at Figures 62(h) and 62(i), it can be seen that the critical particle path pertains to the point in the "cold slug" at which the slug is destined to be chopped in two after undergoing some wave processes. Looking at Figure 62(i), it is clear that the particle just to the right of this dividing line leaves the "CR" point adjacent to the jet, and its particle path is therefore identical with the source path. The particle just to the left of the dividing line, however, is the "tail" of the "au" slug, marked in Figure 62(i) and Figure 63(b).

As for the two cryptosteady paths (short-dash lines), look again at Figure 62(i). Subcritical flow is established at point "CR"; hence, the leading particle of the "bc" flow emerges from point "CR" en route to the hot port, as shown in Figure 63(b). At the same time, the area of the cold flow is decreased, since the jet is no longer totally swept to the

left; this is represented in Figure 62(i) as a "neck" in the "ac" flow, and it is the path of this "neck" that is traced in Figure 63(b).

Figures 62(j), (k), and (l) illustrate the situation in which both the "au" "tail" and the "ac" "neck" leave the cold port before the end of the cycle, the "au" "tail" being the first to leave due to the higher velocity of the "au" flow. (Note that in this simplified analysis, the "au" slug is treated as if it were a solid body moving at the uniform speed  $U_{au}$  which characterizes the majority of the slug. The elements near the tail doubtless move at a reduced velocity, but accounting for this effect would introduce considerable complication without enhancing physical insight and probably without greatly affecting the quantitative outcome of performance calculations.) If the "au" "tail" and "ac" "neck" do indeed depart before the end of the cycle, it is seen that the final state in the duct, Figure 62(l), is qualitatively similar to that following the (fictitious) cryptosteady first sweep, Figure 62(d); and indeed if the pressure-depression effect associated with the inflow of "ap" fluid is neglected, they are exactly the same. In this case, to the extent that the simplifications of the analysis itself can be accepted, the "second cycle" performance calculations provide a good measure of the cyclically "steady" state performance. It turns out that for small  $\beta$  ( $\lesssim 30^\circ$ ) these conditions are approximately satisfied, though there is some adverse effect of  $M_o$ .

For larger  $\beta$ , however, the situation is more as pictured in Figure 63(b). Here, the intersection of the "ac" path with the  $\mathcal{Z} = \mathcal{Z}_{cy}$  line at a positive value of  $\xi$  indicates that a segment of the thickened portion of the "ac" jet, generated during the supercritical flow regime,

is trapped within the duct. If this occurs, the mass of the cold slug at the end of the second cycle exceeds that deposited by the first sweep. Therefore, the next interaction between the jet and the slug, Figure 62(e), will be altered (shock strength and bypass flow increased), and it follows that the third cycle will differ somewhat from the second. However, it would appear that a moderate amount of this effect can be tolerated without drastically altering performance. Matters rapidly become more complex if in addition the "au" slug fails to be fully ejected, indicated similarly by intersection of the particle path at a positive  $\xi$  on the  $\tau = \tau_0$  line. The relatively simple situation of Figure 62(e) is replaced by one in which the jet issuing from the nozzle encounters both a thickened "cold slug" and an underlying, high-energy layer of "au" fluid during the early portion of the cycle, with this tapering down to the basic "cold slug" toward the right end of the duct. This situation is clearly more severe than that of the second cycle, and more complicated as well.

If either or both of these effects occur, obviously there is more mass (ignoring pumped fluid) in the duct at the end of the second cycle than at the end of the first: in other words, some net mass storage has taken place. This implies some adjustment in the nonsteady flow processes during the third cycle, probably with some additional net mass storage, and so on until a cyclic "steady" state is reached in which no further net mass storage occurs and the pattern of mass storage is the same for succeeding cycles. Therefore, a check on the probable quantitative significance of the "second cycle" performance calculations is provided by calculating the net mass storage during that cycle: if it is negligible, the calculations probably provide a good approximation to "steady" state

performance (within the limitations of the analytical model), whereas if it is large the approximation is doubtless correspondingly poor.

With reference to the performance calculation problem, consider again Figure 63(b), which presents the typical or basic wave diagram structure as it emerges from the nonsteady analysis. Above point "CR" a succession of compressions and rarefactions is seen to occur in the "hot duct" (to the right of the source).<sup>\*</sup> In the basic pattern which occurs at low to moderate values of  $M_0$ , regions 8-9-10-11 constitute a sequence which is then repeated in diminishing scale for the rest of the cycle; it will therefore be termed the "terminal sequence." Region 8 is below ambient pressure  $p_0$ , so that  $\mu > \mu_0$ ; region 9 is at  $p_0$ , region 10 is above  $p_0$  so that  $\mu < \mu_0$ , and region 11 is again at  $p_0$ . Considering regions 8 and 10, it turns out that even if the magnitude of the pressure fluctuations about  $p_0$  is large, the fraction of the total nozzle flow that emerges during the "terminal sequence" is essentially equal to the cold fraction in unperturbed crytosteady operation,  $CF_0 = \frac{1+\sin\beta}{2}$ .

As  $M_0$  increases, the wave processes become more violent, this being accentuated if the channel height factor is small. Indeed, for  $\frac{\alpha_d}{\alpha_m} = 1.0$ , the wave diagram analysis indicates in some cases that the pressure in region 10 rises back up to a value slightly in excess of the critical value, therefore reestablishing supercritical source flow. Whether this is a real effect or simply a consequence of analytical approximations has not been determined, but its impact on performance is insignificant in

-----

<sup>\*</sup>The ripples these would cause in the "ac" flow [broken wavy line, Figure 62(j)] are ignored in the present analysis.



any case: the source is just barely supercritical and the total leakage corresponding to region 10 is negligible, and the flow adjustment accomplished by this slight leakage is such that supercritical flow does not recur in subsequent cycles. Therefore, the estimate of bypassed flow "au" obtained as shown in Figure 63(b) is still very nearly correct, and the average rate of "ac" flow emerging from the source is still reasonably estimated by  $CF_0$ .

Finally, if  $\beta$  and/or  $M_0$  are large enough, sonic outflow occurs in region 7 and the simple "terminal sequence," if it occurs at all, does not occur until a long period of adjustment whose description would require a full-fledged characteristics analysis. In this case, point "CR" is located as the point reached by the "critical ray" of the Q-rarefaction which extends from region 4 all the way to the exit plane ( $\xi = 1.0$ ); determination of this critical ray is based upon knowledge of the value of Q needed to produce critical flow at the source following the initial shock. In this situation,  $\mathcal{Z}_{CR}$  proves to be such a large fraction of  $\mathcal{Z}_{cy}$  that the outcome of the performance calculations is not too sensitive to the precise value of CF attributed to the source for the short period from "CR" to the end of the cycle; accordingly,  $CF_0$  is used in this case also.

Having decided that  $CF_0$  is to be used to estimate the fraction of source flow directed in the cold-port direction from point "CR" onward, the details of the wave diagram beyond point "CR" are no longer needed. Indeed, if the performance analysis is carried out using information at the cold port, the only data needed from the wave diagram prove to be  $\mathcal{Z}_{CR}$ ,  $\xi_{CR}$ , and mass storage information from the "ac" "neck" and "au" "tail" particle paths. Accordingly, the  $\xi - \mathcal{Z}$  diagrams developed for

the actual performance analyses (Appendix B) are in the truncated form indicated in Figure 62(c).

It may also be observed that the only effect of the interface on the data needed from the wave diagram is due to wave refraction, which is slight; these diagrams are therefore drawn with the initial shock having its initial slope all the way to the hot port, and with the reflected rarefaction having a uniform slope equal to that bounding region 4. Thus, even regions 3 and 5 need not be shown or analyzed; however, the interface path is included as shown in Figure 63(c) to avoid possible confusion in physical interpretation of the diagrams.

The performance analysis, then, utilizes a wave diagram in the highly simplified form of Figure 63(c). The flows, or better the slugs of fluid, defined in Figure 62(1) are also elements of the analysis; the cold flows "ac", "au", and "ap" are used for the basic analysis, while discussion of the effects seen at the hot port naturally takes flows "bc", "bu", "bu'", and "bp" into account.

Performance analysis. Before presenting a synopsis of the procedure used for quantitative performance estimation, a few key observations are possible which lead one to the conclusion that nonsteady collection is inherently detrimental to performance.

Consider first the effect on cold fraction, CF. As illustrated in Figure 62, a large fraction of the fluid which leaves the source region in the "a" direction as the source sweeps along the duct does not escape out the cold port, but instead is trapped within the duct at the end of the cycle. This leftward-moving "cold slug" is then confronted with the source as it reappears at the left, with resultant strong nonsteady effects.

The overall effect of these nonsteady phenomena (as far as massflow is concerned) is that this slug is chopped about in half, after which one portion leaves via the cold port--its original destination--and the other portion is forced instead to leave through the hot port. Obviously, this phenomenon tends to reduce the fraction of the total flow that exits via the cold port--i.e., the cold fraction. Admittedly, if one compares Figures 62(d) and 62(l), a countervailing effect caused by supercritical flow can be discerned: the "ac" slug in Figure 62(l) has a greater mass than that which one would calculate from Figure 62(d), in which the slug has its normal (cryptosteady) height but is merely reduced in length. However, this compensatory effect of supercritical flow is much smaller than the mass storage effect, and so the net effect on cold fraction is still to reduce it below the cryptosteady level.

In addition to the storage effect, if the channel height factor  $\frac{\alpha_d}{\alpha_n}$  is appreciably greater than unity, there is a "pumping" effect by which cold fluid is transported to the hot port instead of the cold port. This acts to further reduce the cold fraction.

The temperature drop in the cold output is also degraded. The two fragments into which the cold slug is divided emerge as flows "au" and "bu" [Figures 62(j,l)], and these flows contribute less effectively to energy separation than the basic, cryptosteady flows "ac" and "bc". On the cold side, denoting stagnation quantities in  $F_S$  by  $( )^\circ$ ,  $p_{au}^\circ > p_{ac}^\circ$  due to the initial shock which creates supercritical flow in the source region. However, the entropy  $s_{au} = s_{ac} = s_o$  by virtue of the isentropic shock, and therefore  $a_{au} = a_{ac} = a_o$ . Since the "au" flow has the same speed of sound as the "ac" flow but a higher Mach number due

to higher total pressure,  $\tau_{au} > \tau_{ac}$  and hence  $U_{au} > U_{ac}$ . Noting that  $U_{ac}$  and  $U_{au}$  are equal to the Mach numbers in  $F_U$  of the respective flows ( $q_0$  being used to nondimensionalize velocities), one has

$$\frac{T_{au}^0}{T_{au}} = \frac{T_{au}^0}{T_0} = 1 + \frac{\gamma-1}{2} U_{au}^2$$

$$\frac{T_{ac}^0}{T_{ac}} = \frac{T_{ac}^0}{T_0} = 1 + \frac{\gamma-1}{2} U_{ac}^2$$

Clearly,  $T_{au}^0 > T_{ac}^0$ ; therefore, the net cold flow which is a mixture of the "ac" and "au" flows cannot be as cold as the basic cryptosteady flow "ac" alone.

On the hot side, similarly, flow "bu" achieves a lesser temperature rise than the basic "bc" flow. "Cold slug" fluid is isentropically brought to rest in  $F_U$ , except for pulsations produced by pressure differentials between conditions at the source and the region surrounding the hot port; see Figures 62(i) and 63(a). Thus, the mean velocity of flow "bu" tends to approximate  $U_*$ . Looking at Figure 63(a), one may note that during outflow from region 7 the "bu" exit flow velocity exceeds  $U_*$  by a considerable margin; after that, the mean velocity of flow "bu" is essentially  $U_*$ , although the alternating compressions and rarefactions cause  $U_{bu}$  at any given moment to either exceed or fall short of  $U_*$ . Due to the adjustment period in region 7 and the subsequent pulsations, the effective mass-averaged velocity of the "bu" flow actually exceeds  $U_*$  by some amount, but not enough to change the conclusions being discussed here. For, consider flow "bc", which flows along on the floor of the channel in a quasi-steady manner in the present inviscid model. It maintains  $p_{bc}^0 = \text{constant}$  from the nozzle to the hot port, where it exits

at a velocity corresponding to the local static pressure  $p_0$  --i.e., it exits at the same velocity that would pertain to flow "b" of the corresponding fully cryptosteady device. This velocity is

$$U_{bc} = U_* + C_{bc} \quad (C_{bc} = \frac{C_{bc}}{\alpha_0})$$

and since for  $\lambda = u_i = 0$

$$\frac{U_*}{C_c} = \frac{U_*}{C_{bc}} = \sin \beta$$

there follows

$$U_{bc} = \frac{1 + \sin \beta}{\sin \beta} > 2 U_* \quad \text{for any } \beta < 90^\circ$$

Thus:

$$U_{bu} \approx U_*$$

$$U_{bc} > 2 U_*$$

Since flows "bu" and "bc" exit to the same pressure  $p_0$  with the same entropy, they have the same static temperature. Therefore, since  $U_{bc} > U_{bu}$ , it is seen that  $T_{bu}^0 < T_{bc}^0$  --the nonsteady component of the total "b" flow is not as hot as the basic cryptosteady component.

The qualitative effect of nonsteadiness on performance, then, is not in doubt: it reduces both cold fraction and the magnitude of the temperature drop achieved in the cold output. However, it is still of importance to have some estimate of the magnitude of these performance penalties, and to see how these penalties are affected by geometric and operating variables. The performance analysis described below is addressed

to these quantitative purposes. Major symbols to be used here are as follows:

$m$  = total mass of the subscripted flow involved in a given cycle. Flow "i" is that entering the rotor; other flows are defined in Figure 63(1).

$\Delta T^o$  = total temperature increment relative to rotor inlet conditions,  $(T^o - T^o_i)$

$( )_s$  = measured at the source

$( )_{ex}$  = measured at a port

$( )_s$  = stored during a cycle

$( )_o$  = conditions corresponding to cryptosteady flow discharging to ambient pressure  $p_o$

$( )^o$  = stagnation conditions in  $F_U$

$( )^{\bullet}$  = stagnation conditions in  $F_S$

Three performance measures will be utilized, which present the ratio of net performance with nonsteady collection to performance in normal cryptosteady operation. The performance measures are the following:

COLD TEMPERATURE FACTOR ( $F_{temp}$ )

$$F_{temp} \equiv \frac{(\Delta T_a^o / T^o_i)_{net}}{(\Delta T_a^o / T^o_i)_o}$$

where

$$\left( \frac{\Delta T_a^o}{T^o_i} \right)_{net} = \frac{(m_a)_{ex} \frac{\Delta T_{ac}^o}{T^o_i} + (m_{au})_{ex} \frac{\Delta T_{au}^o}{T^o_i}}{(m_{ac})_{ex} + (m_{au})_{ex}} \quad (59)$$

COLD FLOW FACTOR ( $F_{flow}$ )

$$F_{flow} \equiv \frac{CF_{net}}{CF_o}$$

where

$$CF_{net} = \frac{(m_{ac})_{ex} + (m_{au})_{ex} - m_{ap}}{m_i} \quad (60)$$

#### REFRIGERATION CAPACITY FACTOR ( $F_{capy}$ )

A simple definition for refrigeration capacity is the amount of heat absorbed by the cold flow from the cooled space, per unit of total flow entering the rotor, if the cold flow exits from the cooled region at ambient temperature. Noting that for the present analysis the rotor inlet total temperature  $T_i^o$  is assumed equal to ambient, the refrigeration capacity defined in this manner is modified by the factor

$$F_{capy} = F_{temp} \cdot F_{flow}$$

where  $F_{temp}$  and  $F_{flow}$  are as calculated above.

For actual performance calculations, it proves convenient to nondimensionalize mass flows by  $m_{ao}$ , whence (59) and (60) are replaced by

$$\left(\frac{\Delta T_a^o}{T_i^o}\right)_{net} = \frac{\frac{(m_{ac})_{ex}}{m_{ao}} \frac{\Delta T_{ac}^o}{T_i^o} + \frac{(m_{au})_{ex}}{m_{ao}} \frac{\Delta T_{au}^o}{T_i^o}}{\frac{(m_{ac})_{ex}}{m_{ao}} + \frac{(m_{au})_{ex}}{m_{ao}}} \quad (59')$$

and

$$CF_{net} = \frac{\frac{(m_{ac})_{ex}}{m_{ao}} + \frac{(m_{au})_{ex}}{m_{ao}} - \frac{m_{ap}}{m_{ao}}}{\frac{m_i}{m_{ao}}} \quad (60')$$

Consider the total temperature increments of the "basic" cold-flow components "ac" and "au", which are needed for equation (59'). Flow "ac" is taken to be quasi-steady in  $F_S$  (or quasi-cryptosteady), discharging to  $p_o$  (the cold-side pressure depression effect being neglected).

Then

$$\begin{aligned}\frac{\Delta T_{ac}^o}{T_{oi}^o} &= \left( \frac{\Delta T_a^o}{T_{oi}^o} \right)_o \\ &= \frac{T_{ac}^o}{T_{ac}} \cdot \frac{T_{ac}}{T_{oi}^o} \cdot \frac{T_{oi}^o}{T_{oi}^o} - 1\end{aligned}\quad (61)$$

Now

$$\frac{T_{ac}^o}{T_{ac}} = 1 + \frac{\gamma-1}{2} U_{ac}^2 \quad (62)$$

where the fact that the magnitude of  $U_{ac}$  is the Mach number of flow "ac" in  $F_U$  has been used. Similarly in  $F_S$ ,

$$\frac{T_{oi}^o}{T_{ac}} = \frac{T_{ac}^o}{T_{ac}} = 1 + \frac{\gamma-1}{2} C_{ac}^2 \quad (63)$$

To obtain  $\frac{T_{oi}^o}{T_{oi}^o}$ , note that if there is no prerotation,

$$\begin{aligned}h_{oi}^o &= h_{oi}^o + \frac{v^2}{2} \\ &= h_{oi}^o + \left( \frac{v}{c_n} \right)^2 \frac{c_n^2}{2}\end{aligned}$$

But, since prerotation and rotor torque are both taken to be absent in the present analysis,

$$\frac{v}{c_n} = \frac{U_*}{c_o} = \sin \beta \quad (64)$$



so that

$$h_i^0 = h_i^0 + \frac{\kappa_m^2}{2} \sin^2 \beta$$

or, collecting quantities in  $F_S$  on the same side of the equation,

$$h_i^0 = h_i^0 - \frac{\kappa_m^2}{2} \sin^2 \beta$$

$$\begin{aligned} \frac{h_i^0}{h_i^0} &= 1 - \frac{\kappa_m^2}{2h_i^0} \sin^2 \beta \\ &= 1 - \frac{\frac{\gamma-1}{2} M_0^2}{1 + \frac{\gamma-1}{2} M_0^2} \sin^2 \beta \\ &= \frac{1 + \frac{\gamma-1}{2} M_0^2 (1 - \sin^2 \beta)}{1 + \frac{\gamma-1}{2} M_0^2} \end{aligned}$$

where the fact that  $M_m = M_0$  is assumed for the source-region analysis has been used. Thus,

$$\frac{T_i^0}{T_0^0} = \frac{1 + \frac{\gamma-1}{2} M_0^2}{1 + \frac{\gamma-1}{2} M_0^2 (1 - \sin^2 \beta)} \quad (65)$$

Use of (62), (63), and (65) with (61) gives

$$\frac{\Delta T_{ac}^0}{T_0^0} = \frac{1 + \frac{\gamma-1}{2} U_{ac}^2}{1 + \frac{\gamma-1}{2} C_{ac}^2} \cdot \frac{1 + \frac{\gamma-1}{2} M_0^2}{1 + \frac{\gamma-1}{2} M_0^2 (1 - \sin^2 \beta)} - 1$$

or, noting with the aid of (64) that

$$\begin{aligned} U_{ac} &= C_{ac} + U_k \\ &= -C_0 (1 - \sin \beta) \end{aligned}$$

and that  $\zeta_o = M_o$ , one arrives at:

$$\frac{\Delta T_{ac}^o}{T_i^o} = \left( \frac{\Delta T_a^o}{T_i^o} \right)_o = \frac{1 + \frac{\gamma-1}{2} M_o^2 (1 - \sin^2 \beta)^2}{1 + \frac{\gamma-1}{2} M_o^2 (1 - \sin^2 \beta)} - 1 \quad (61')$$

Flow "au" is considered to depart leftward from the source region with a uniform velocity equal to that corresponding to isentropic, steady flow in  $F_5$  from the conditions just behind the initial shock to the pressure  $p_o$  prevailing to the left of the source; see Figure 62(e). Neglecting the entropy rise across the shock, it is noted that flows "ac" and "au" both have the same entropy  $s_o$ , as well as the same static pressure  $p_o$ ; it follows that they have the same static temperature  $T_o$  also, and it may be observed that

$$\frac{T_{au}}{T_i^o} = \frac{T_{ac}}{T_i^o} = \frac{T_o}{T_i^o}$$

The amount by which the total temperature  $T_{au}^o$  differs from  $T_i^o$  is

$$\frac{\Delta T_{au}^o}{T_i^o} = \frac{T_{au}^o}{T_{au}} \cdot \frac{T_{au}}{T_i^o} \cdot \frac{T_i^o}{T_o} - 1 \quad (66)$$

in which the only factor differing from those in equation (61) is  $\frac{T_{au}^o}{T_{au}}$ :

$$\frac{T_{au}^o}{T_{au}} = 1 + \frac{\gamma-1}{2} U_{au}^2 \quad (67)$$

Therefore, one obtains:

$$\frac{\Delta T_{au}^o}{T_i^o} = \frac{1 + \frac{\gamma-1}{2} U_{ac}^2 \left( \frac{U_{au}}{U_{ac}} \right)^2}{1 + \frac{\gamma-1}{2} \zeta_{ac}^2} \cdot \frac{T_i^o}{T_o} - 1$$

or

$$\frac{\Delta T_{au}^0}{T_0^0} = \frac{1 + \frac{\gamma-1}{2} M_0^2 (1 - \sin^2 \beta) \left( \frac{U_{au}}{U_{ac}} \right)^2}{1 + \frac{\gamma-1}{2} M_0^2 (1 - \sin^2 \beta)} - 1 \quad (66')$$

Comparing equations (61') and (66') and noting that  $\frac{U_{au}}{U_{ac}} > 1$ , it is clear that  $\frac{\Delta T_{au}^0}{T_0^0}$  is more positive, or less negative, than  $\frac{\Delta T_{ac}^0}{T_0^0}$  --i.e., that the "au" fluid is not as cold in  $F_U$  as the "ac" fluid.

Consider now the mass conservation during a cycle. For the cryptosteady fluid:

$$m_i = (m_{ac})_{ex} + (m_{ac})_s + m_{bc} \quad (68)$$

For the cold slug fluid:

$$m_{ao} = (m_{au})_{ex} + (m_{au})_s + m_{bu} \quad (69)$$

For the hot-port inflow fluid:

$$(m_{bu'})_{expelled} - (m_{bu'})_{indrafted} = 0 \quad (70)$$

Note that this flow contributes nothing to the net massflow during a cycle, though it does effect a net transport of energy out the hot port. Finally, for the pumped flow:

$$m_{bp}^{(n)} = m_{ap}^{(n-1)} \quad (71)$$

where  $n$  is the number of the cycle being analyzed.

At the cyclic "steady" state, no net mass storage occurs from one cycle to the next. Specifically:

$$(\dot{m}_{ac})_s = (\dot{m}_{ac})_f - (\dot{m}_{ac})_{ex} = \dot{m}_{ao} \quad (72a)$$

$$(\dot{m}_{au})_s = 0 \quad (72b)$$

$$(\dot{m}_{ap})^{(n-1)} = \dot{m}_{ap}^{(n)} \quad (72c)$$

In the context of the "second cycle" analysis, (72a) states that the cold slug left at the end of the second cycle [Figure 62(1)] has the same mass as that left by the (fictitious) cryptosteady first cycle [Figure 62(d)]; (72b) states that none of the "au" fluid generated during the second cycle is trapped, or stored, within the duct at the end of the cycle; and (72c) expresses the fact that at "steady" state the amount of fluid pumped is the same during each cycle. These conditions are approximately satisfied by the second cycle if  $\beta$  and  $M_o$  are not too large ( $\beta \lesssim 30^\circ$ ,  $M_o \lesssim 0.5-0.75$ ).

Using (72a) with (69) and (72b) in (68) gives the steady-state continuity equation for the "basic" flows--i.e., those which originate strictly as part of the rotor-inlet flow and which are present with or without pumping--as:

$$\dot{m}_i = (\dot{m}_{ac})_{ex} + (\dot{m}_{au})_{ex} + \dot{m}_{bc} + \dot{m}_{bu} \quad (68')$$

or, identifying

$$\dot{m}_{a,basic} = (\dot{m}_{ac})_{ex} + (\dot{m}_{au})_{ex} \quad (73a)$$

and

$$\dot{m}_{b,basic} = \dot{m}_{bc} + \dot{m}_{bu} \quad (73b)$$

one has equivalently

$$\dot{m}_c = \dot{m}_{a, \text{basic}} + \dot{m}_{b, \text{basic}} \quad (68'')$$

Note that each of the two "basic" output flows is comprised of a crypto-steady and a nonsteady component.

For the performance figures to be presented below, one set of calculations in each "case" (combination of  $\beta$ ,  $\frac{d\delta}{\alpha_m}$ ,  $M_o$ ) in effect assumes the absence of mass storage and hence steady state. In addition, wherever equation (72b) is violated according to the  $\xi - \tau$  diagram, a second calculation is carried out in which  $(\dot{m}_{au})_{ex}$  is adjusted to reflect this mass storage. As for violation of equation (72a), this can be noted wherever it occurs in the wave diagrams, but it is not explicitly accounted for because (i) at  $30^\circ$  it is not a major effect according to the "ac" "neck" path lines, and (ii) at higher angles the ratio of cold to total crypto-steady flow is close to unity, so that again the effect is small relative to that of "au" fluid storage.

With regard to the "additive" flows--the pumped flow and the flow which is sucked in through the hot port early in the cycle and then expelled--equation (70) is valid whether or not steady state obtains, while with the steady-state condition (72c), (71) becomes

$$\dot{m}_{bp} = \dot{m}_{ap} \quad (71')$$

The particular massflows needed for use in equations (59') and (60') are  $\frac{(\dot{m}_{ac})_{ex}}{\dot{m}_{ao}}$ ,  $\frac{(\dot{m}_{au})_{ex}}{\dot{m}_{ao}}$ ,  $\frac{\dot{m}_c}{\dot{m}_{ao}}$ , and  $\frac{\dot{m}_{ap}}{\dot{m}_{ao}}$ . The method of calculating these is described next.

$$\frac{(m_{ac})_{ex}}{m_{a0}} :$$

$$(m_{ac})_{ex} = (m_{ac})_x - (m_{ac})_s$$

$$= (m_{ac})_x - m_{a0} \quad (74)$$

where, as already stated, equation (72a) is assumed to hold in all cases for calculation purposes.

Referring to Figure 63(c), assume conditions at the source from  $\tau = 0$  to  $\tau = \tau_{CR}$  to be uniform and equal to those in region 1, behind the initial shock; denote this regime at the source by  $( )_{CR-}$ . Treat conditions at the source from  $\tau = \tau_{CR}$  to the end of the cycle as if they were also constant, and equal to mean conditions there; denote this phase by  $( )_{CR+}$ . Also, denote the total rotor-inlet mass flow that would occur during a cycle with the nozzle-discharge pressure equal to  $p_0$  as  $m_{i0}$ . Then:

$$(m_{ac})_x = \frac{\tau_{CR}}{\tau_{cy}} \frac{(m_{in})_{CR-}}{(m_{in})_0} (CF)_{CR-} \cdot m_{i0} + \left(1 - \frac{\tau_{CR}}{\tau_{cy}}\right) \frac{(m_{in})_{CR+}}{(m_{in})_0} (CF)_{CR+} \cdot m_{i0} \quad (75)$$

Now,

$$\frac{(m_{in})_{CR-}}{(m_{in})_0} = \frac{1}{k_x} \text{ where } k_x = \text{bypass flow area correction factor; see source-region analysis.}$$

$$k_x \geq 1 \text{ if flow to left of source fills duct } \left(\frac{u_d}{a_m} = 1.0 \text{ cases}\right)$$

$$k_x = 1 \text{ otherwise } \left(\frac{u_d}{a_m} = 1.5, 2.0 \text{ cases}\right)$$

$$(CF)_{CR-} = 1 \text{ since nozzle flow is totally swept to left}$$

and from the wave diagram analysis,

$$\frac{(m_n)_{cr+}}{(m_n)_0} = 1$$

$$(CF)_{cr+} = CF_0$$

Thus (75) reduces to

$$\frac{(m_{ao})^*}{m_{io}} = \frac{1}{k_x} \frac{\tau_{ex}}{\tau_{ey}} + CF_0 \left(1 - \frac{\tau_{ex}}{\tau_{ey}}\right) \quad (75')$$

The stored portion  $m_{ao}$  of the total unperturbed flow  $m_{io}$  is given by [see Figure 64(a)]

$$\begin{aligned} \frac{m_{ao}}{m_{io}} &= \frac{V}{\tau_0} CF_0 \\ &= CF_0 \sin \beta \end{aligned} \quad (76)$$

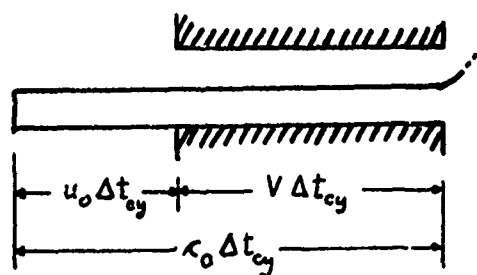
Therefore,

$$\begin{aligned} \frac{(m_{ao})^*}{m_{ao}} &= \frac{(m_{ao})^*/m_{io}}{m_{ao}/m_{io}} \\ &= \frac{\frac{1}{k_x} \frac{\tau_{ex}}{\tau_{ey}} + CF_0 \left(1 - \frac{\tau_{ex}}{\tau_{ey}}\right)}{CF_0 \sin \beta} \end{aligned} \quad (77)$$

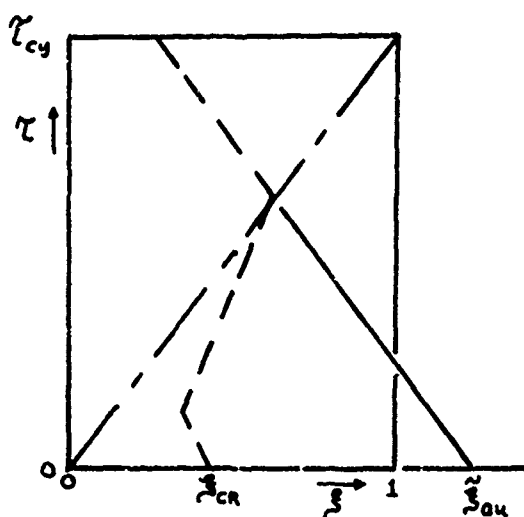
Rewriting (74) as

$$\frac{(m_{ao})_{ex}}{m_{ao}} = \frac{(m_{ao})^*}{m_{ao}} - 1$$

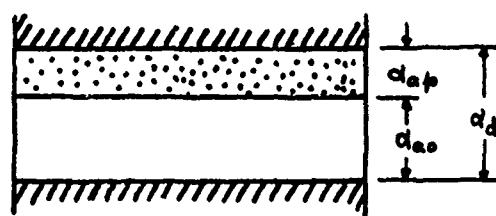
and introducing (77), one obtains



(a) Cold Slug Storage



(b) Expanded Length of "au" Slug



(c) Mass of Pumped Flow

Figure 64  
Auxiliary Sketches for Performance Analysis



$$\frac{(m_{ao})_{ex}}{m_{ao}} = \frac{\frac{1}{k_\alpha} \frac{\tau_{cr}}{\tau_{cy}} + CF_0 (1 - \frac{\tau_{cr}}{\tau_{cy}})}{CF_0 \sin \beta} \quad (78)$$

Note that  $CF_0 = (1 + \sin \beta)/2$ ;  $k_\alpha$  is determined from the massflow compatibility analysis which establishes the initial-shock strength; and  $\tau_{CR}$  and  $\tau_{cy}$  are read from the wave diagram.

$$\frac{(m_{au})_{ex}}{m_{ao}}:$$

Inspecting the wave diagram, e.g. Figure 63(c), one notes that if the "au" fluid all escapes before the end of the cycle--i.e., (72b) is satisfied--one has simply

$$\frac{(m_{au})_{ex}}{m_{ao}} = \frac{m_{au}}{m_{ao}} = \xi_{CR}$$

However, if the "au" "tail" does not escape,  $\frac{(m_{au})_{ex}}{m_{ao}}$  is reduced correspondingly. As shown in Figure 63(c), the dimensionless length of the stored segment of "au" fluid is  $(\tilde{\xi}_{au})_s$ , this being expanded "au" fluid traveling at velocity  $U_{au}$ . The expanded length of the entire "au" slug,  $\tilde{\xi}_{au}$ , is most easily obtained by backward projection of the "au" "tail" path through point "CR" to the  $\tau = 0$  line and reading  $\tilde{\xi}_{au}$  on the  $\xi$  axis, as depicted in Figure 64(b). From the wave diagrams,  $\tilde{\xi}_{au}$  is typically at least twice and often several times  $\xi_{CR}$ .

With the expanded lengths of the complete "au" slug and the stored portion of it determined from the wave diagram along with  $\xi_{CR}$ , one obtains:

$$\frac{(m_{au})_{ex}}{m_{ao}} = \xi_{cr} \left[ 1 - \frac{(\xi_{au})_s}{\xi_{au}} \right] \quad (79)$$

$$\frac{m_i}{m_{ao}} :$$

$$\frac{m_i}{m_{ao}} = \frac{m_i / m_{i0}}{m_{ao} / m_{i0}} \quad (80)$$

The numerator is found in a manner exactly similar to the development of equation (75'), except that this time the cold fraction factor is absent. Thus:

$$\frac{m_i}{m_{i0}} = \frac{1}{k_d} \frac{\tau_a}{\tau_y} + \left( 1 - \frac{\tau_a}{\tau_y} \right)$$

or

$$\frac{m_i}{m_{i0}} = 1 - \frac{\tau_a}{\tau_y} \left( 1 - \frac{1}{k_d} \right) \quad (81)$$

Note that  $\frac{m_i}{m_{i0}} = 1.0$  unless  $k_d$  differs from unity, which occurs in the present approximate analysis only in the cases [Table 1] for which  $\frac{\alpha_d}{\alpha_m} = 1.0$ .

The denominator of (80) is given by (76). Thus:

$$\frac{m_i}{m_{ao}} = \frac{1 - \frac{\tau_a}{\tau_y} \left( 1 - \frac{1}{k_d} \right)}{CF_0 \sin \beta} \quad (82)$$

Considering Figures 62(d) and 64(c), one may write

$$\frac{m_{ap}}{m_{ao}} = \frac{\alpha_{ap}}{\alpha_{ao}} \cdot \frac{\rho_{ap}}{\rho_{ao}} \quad (83)$$

Here, the area assumed to be available for the pumped cold flow "ap" is based on the presence of a cold slug having mass and volume equal to that deposited in the first sweep, which implies no net mass storage and no volume change due to the pressure depression which occurs here on the cold side of the source. (The latter approximation can be supported somewhat by observing that, according to the linearized analysis of the source region in the subcritical or "splashing" regime, the area of the "a" flow is relatively insensitive to small changes in  $\delta p$ , the differential pressure across the jet.)

Now,

$$\frac{\alpha_{ap}}{\alpha_{ao}} = \frac{1 - \frac{\alpha_{ao}}{\alpha_d}}{\frac{\alpha_{ao}}{\alpha_d}}$$

$$\frac{\alpha_{ao}}{\alpha_d} = \frac{1 + \sin\beta}{2} \frac{d_m}{\alpha_d}$$

so that

$$\frac{\alpha_{ap}}{\alpha_{ao}} = \frac{1 - \frac{1 + \sin\beta}{2} \frac{d_m}{\alpha_d}}{\frac{1 + \sin\beta}{2} \frac{d_m}{\alpha_d}} \quad (84)$$

As for the density ratio, consider a model in which the "ap" fluid is drawn in from the surroundings at the cold port, à la Figure 62(b). Then one may write, with  $( )_c$  denoting cold-port ambient:

$$\frac{\rho_{ap}}{\rho_{ao}} = \frac{\rho_{ap}}{\rho_c} \cdot \frac{\rho_c}{\rho_{ao}} \quad (85)$$

Assume isentropic, quasisteady inflow through the port to the uniform internal velocity,  $U_{ap} = U_*$ , and internal pressure  $p_a < p_o$ . From the energy equation:

$$\begin{aligned} T_{ap} &= T_c^o - \frac{V^2}{2c_p} \\ \frac{T_{ap}}{T_c^o} &= 1 - \frac{V^2}{2c_p T_c^o} \\ &= 1 - \frac{\gamma-1}{2} \frac{V^2/a_o^2}{(a_c^o)^2/a_o^2} \\ &= 1 - \frac{\gamma-1}{2} \left( \frac{U_*}{A_c^o} \right)^2 \end{aligned} \quad (86)$$

and since the inflow is assumed isentropic,

$$\frac{p_{ap}}{p_c^o} = \left[ 1 - \frac{\gamma-1}{2} \left( \frac{U_*}{A_c^o} \right)^2 \right]^{\frac{1}{\gamma-1}} \quad (87)$$

Also,

$$\begin{aligned} \frac{p_c^o}{p_{ao}} &= \frac{p_c^o}{p_o} \cdot \frac{T_o}{T_c^o} \\ \frac{p_c^o}{p_{ao}} &= \left( \frac{1}{A_c^o} \right)^2 \end{aligned} \quad (88)$$

Substituting (87) and (88) into (85) gives

$$\frac{p_{ap}}{p_{ao}} = \left( \frac{1}{A_c^o} \right)^2 \left[ 1 - \frac{\gamma-1}{2} \left( \frac{U_*}{A_c^o} \right)^2 \right]^{\frac{1}{\gamma-1}} \quad (89)$$

Using (84) and (89) in (83) gives

$$\frac{\dot{m}_{ap}}{\dot{m}_{ao}} = \left[ \frac{1 - \frac{1 + \sin \beta}{2} \frac{\alpha_m}{\alpha_d}}{1 + \frac{1 + \sin \beta}{2} \frac{\alpha_m}{\alpha_d}} \right] \frac{\left[ 1 - \frac{\gamma - 1}{2} \left( \frac{U_{\infty}}{A_c^*} \right)^2 \right]^{\frac{1}{\gamma - 1}}}{(A_c^*)^2} \quad (90)$$

Note here that

$$\begin{aligned} \left( \frac{1}{A_c^*} \right)^2 &= \frac{1}{(A_{c,i}^*)^2} \left( \frac{A_{c,i}^*}{A_c^*} \right)^2 \\ &= \frac{1}{(T_{c,i}^*/T_o)} \frac{T_{c,i}^*}{T_c^*} \\ &= \frac{1}{\frac{T_{c,i}^*}{T_o} \cdot \frac{T_o}{T_c^*}} \cdot \frac{1}{1 + \frac{\Delta T_c^*}{T_o}} \end{aligned}$$

and

$$\frac{T_{c,i}^*}{T_o} = \frac{1 + \frac{\gamma - 1}{2} M_o^2 (1 - \sin^2 \beta)}{1 + \frac{\gamma - 1}{2} M_o^2} \quad [\text{by equation (65)}]$$

$$\frac{T_{c,i}^*}{T_o} = 1 + \frac{\gamma - 1}{2} M_o^2$$

$$\frac{\Delta T_c^*}{T_{c,i}^*}$$

is selected to reflect the state of the cold pumped fluid; considering the recirculation arguments which will be discussed in connection with Figure 71, the most reasonable choice is probably

$$\frac{\Delta T_c^*}{T_{c,i}^*} = \left( \frac{\Delta T_a^*}{T_{a,i}^*} \right)_{\text{net}}$$

where  $\left( \frac{\Delta T_a^*}{T_{a,i}^*} \right)_{\text{net}}$  is found by use of equation (59').

To summarize, equations (59') and (60') are solved with the aid of the equations whose numbers are indicated:

$$\left(\frac{\Delta T_a^*}{T_i^*}\right)_{net} = \frac{( ) ( ' ) + ( ) ( ' )}{( ) + ( )} \quad (59')$$

$$CF_{net} = \frac{( ) + ( ) - ( )}{( )} \quad (60')$$

Additional performance-perturbing effects. The performance calculations described above neglect the effect of the cold-side pressure depression (except in calculating  $m_{ap}$ ), and also assume that the rotor velocity is unchanged from the value which holds in cryptosteady flow, wherein the nozzle discharge pressure is  $p_o$ . While the impact which these effects would have will not be assessed in terms of quantitative performance changes, an estimate of the magnitudes of the perturbations themselves will be provided.

With respect to the pressure depression, use of the isentropic quasisteady inflow model for the pumped flow gives with the aid of equation (86)

$$\frac{p_{ap}}{p_o} = \left[1 + \frac{\gamma-1}{2} \left(\frac{U_{*}}{A_c}\right)^2\right]^{\frac{\gamma}{\gamma-1}}$$

and since  $p_{ap} = p_a$  and  $p_c^o = p_o$ , there follows:

$$\frac{p_a}{p_o} = \left[1 - \frac{\gamma-1}{2} \left(\frac{U_{*}}{A_c}\right)^2\right]^{\frac{\gamma}{\gamma-1}} \quad (91)$$

A first approximation for the alteration in rotor velocity which is occasioned by departure of the effective nozzle discharge pressure

from its cryptosteady-collection value of  $p_o$  may be obtained as follows:

1. Calculate the time-average value of the mean static pressure at the nozzle exit, where

$$p_m = \frac{p_a + p_o}{2}$$

Note that  $p_b$  exceeds  $p_o$  on the average, due to the initial shock;  $p_a$ , however, is less than  $p_o$  due to the pressure-depression effect.

2. Calculate the value of mean nozzle-discharge velocity  $c_m$  corresponding to the modified value of  $p_m \neq p_o$  calculated above, with rotor velocity still =  $V_o$ , thus:

$$\begin{aligned} \frac{c_m}{c_o} &= \frac{M_m}{M_o} \sqrt{\frac{T_n/T_n^o}{T_o/T_o^o}} \\ &= \frac{M_m}{M_o} \sqrt{\left(\frac{p_m}{p_o}\right)^{\frac{\gamma-1}{\gamma}}} \end{aligned}$$

and

$$M_m = \sqrt{\frac{2}{\gamma-1} \left[ \left(\frac{p_m/p_o}{p_o/p_o}\right)^{\frac{\gamma-1}{\gamma}} - 1 \right]}$$

which leads to

$$\frac{c_m}{c_o} = \frac{\sqrt{\frac{2}{\gamma-1} \left[ 1 + \frac{\gamma-1}{2} M_o^2 - \left(\frac{p_m}{p_o}\right)^{\frac{\gamma-1}{\gamma}} \right]}}{\quad} \quad (92)$$

3. Noting that  $V = c_n \sin \beta$ , take the ratio of perturbed to cryptosteady rotor velocity to be:

$$\frac{V}{V_0} = \frac{c_m}{c_0} = \frac{\sqrt{\frac{2}{\delta-1} \left[ 1 + \frac{\gamma-1}{2} M_0^2 - \left( \frac{p_m}{p_0} \right)^{\frac{\delta-1}{\gamma}} \right]}}{M_0} \quad (93)$$

Results of performance calculations. The "cases" chosen in Table 1 for the study of nonsteadiness effects were selected so as to span a range of values for each variable that appeared to be of practical interest and did not invite obvious analytical complications. The majority of these cases (20) survived all the way through the final performance calculation phase, but most of those having  $\frac{a_d}{a_n} = 1.0$  did not. Cases 1, 2, and 3 were deleted because the simplified analysis for the supercritical source, which overestimates the "stiffness" of the jet relative to its ability to support a pressure differential, leads in these cases to a value for the critical differential-pressure ratio  $\frac{p_0}{p_a}$  that exceeds the total pressure of the nozzle flow (measured in  $F_5$ )--a situation which can be shown to be physically impossible.\* Cases 10 and 19 through 21 are represented by wave diagrams, but did not survive through all the steps of the performance-calculation process. In these cases, the channel-height factor is again 1.0, and the leftward-swept nozzle flow and the bypass flow not only fill the duct but must produce a reduction in nozzle flow rate in the process, according to the source-region model employed. However, a

---

\*It has been confirmed with the aid of a more exact supercritical source analysis that this is strictly the result of errors induced by approximations, rather than any basic difficulty with the physics of the analytical model. The more exact analysis is not included herein because it is considerably more complex, cannot be obtained in closed form (i.e., requires numerical solution by computer), and gives results which do not differ greatly from those of the simplified model on the whole.



rather rough-shod procedure is used to describe this modified situation, and in the face of increasingly severe mass-storage effects as  $\beta$  increases the source-region treatment proves too inaccurate in these cases. In cases 11 and 12, however, results are obtained which do appear meaningful. (Note that in these two cases, the intermediate value of  $\beta = 45^\circ$  is such that mass storage effects are overall much less than at  $60^\circ$ , while the elevated  $M_n$  values of 0.75 and 1.00 are favorable to improved accuracy of the simplified treatment of the source region in supercritical flow.) Copies of the working wave diagrams for all cases except 1, 2, and 3, which were deleted, are presented as Appendix B.

As was pointed out with the aid of Figure 54, the entire set of cases analyzed for nonsteady collection effects pertains to a fairly low range of pressure ratios. The possibility exists that the performance penalties might be less severe at higher pressure ratios than those explicitly analyzed, and indeed the performance data presented below suggest this. However, it must be realized that nonsteady flow collection produces some additional phenomena which have been neglected in the present analysis, but which will also have an effect on performance. Several of these additional phenomena are discussed in a separate section below; taken together, they appear to dim the prospects for substantial performance-penalty reductions at higher pressure ratios.

The basic results were of course obtained as a function of  $\beta$ ,  $\frac{ds}{dn}$ , and  $M_o$  (which is taken to be the value of  $M_n$  in the simplified source-region analysis used). However,  $DPR = \frac{p_o}{p^*}$  is of more direct relevance to performance analysis than  $M_o$ , and plots vs. DPR at constant  $\beta$  have been generated. It will be noted that at  $30^\circ$  a single point

is obtained for each datum, whereas at 45° and 60° some uncertainty is expressed by an error band. The uncertainty springs from the fact that at the higher  $\beta$ 's the mass stored in the duct during the second sweep is calculated to be greater than that stored during the first (assumed cryptosteady) sweep. The two extreme values for a given datum were obtained by ignoring the net-mass-storage effect for one calculation and taking it into account via a correction in the other.

The effect of nonsteady perturbations on temperature drop is shown in Figure 65. In 65(a), the performance factor  $F_{temp}$  is plotted against  $\beta$  at constant  $M_o$  for  $\frac{d_d}{d_m} = 1.5$ ; straight-line fairings are used rather than curves, given the uncertainties in the high- $\beta$  calculations. Using the curve fit values from 65(a), a replot against DPR is obtained as in 65(b) with the aid of  $DPR = \text{function}(\beta, M_o)$  for each point. Figure 65(c) indicates the effect of channel height.

Figure 65(b) indicates that as the pressure ratio increases, the temperature on the cold side tends to approach the value that would be produced in cryptosteady operation. Thus, it would appear that as far as temperature drop is concerned, the penalty associated with nonsteady collection might be tolerable except at very low pressure ratios. In addition, the effect of increasing  $\beta$  at a given pressure ratio is to cause the nonsteady-collection performance to approach the cryptosteady performance more rapidly; hence, the sensitivity of temperature performance to  $\beta$  is even more pronounced with nonsteady collection than with cryptosteady operation. The trends depicted in 65(b), which suggest the qualitative behavior shown in the inset, do not change qualitatively even if quite different

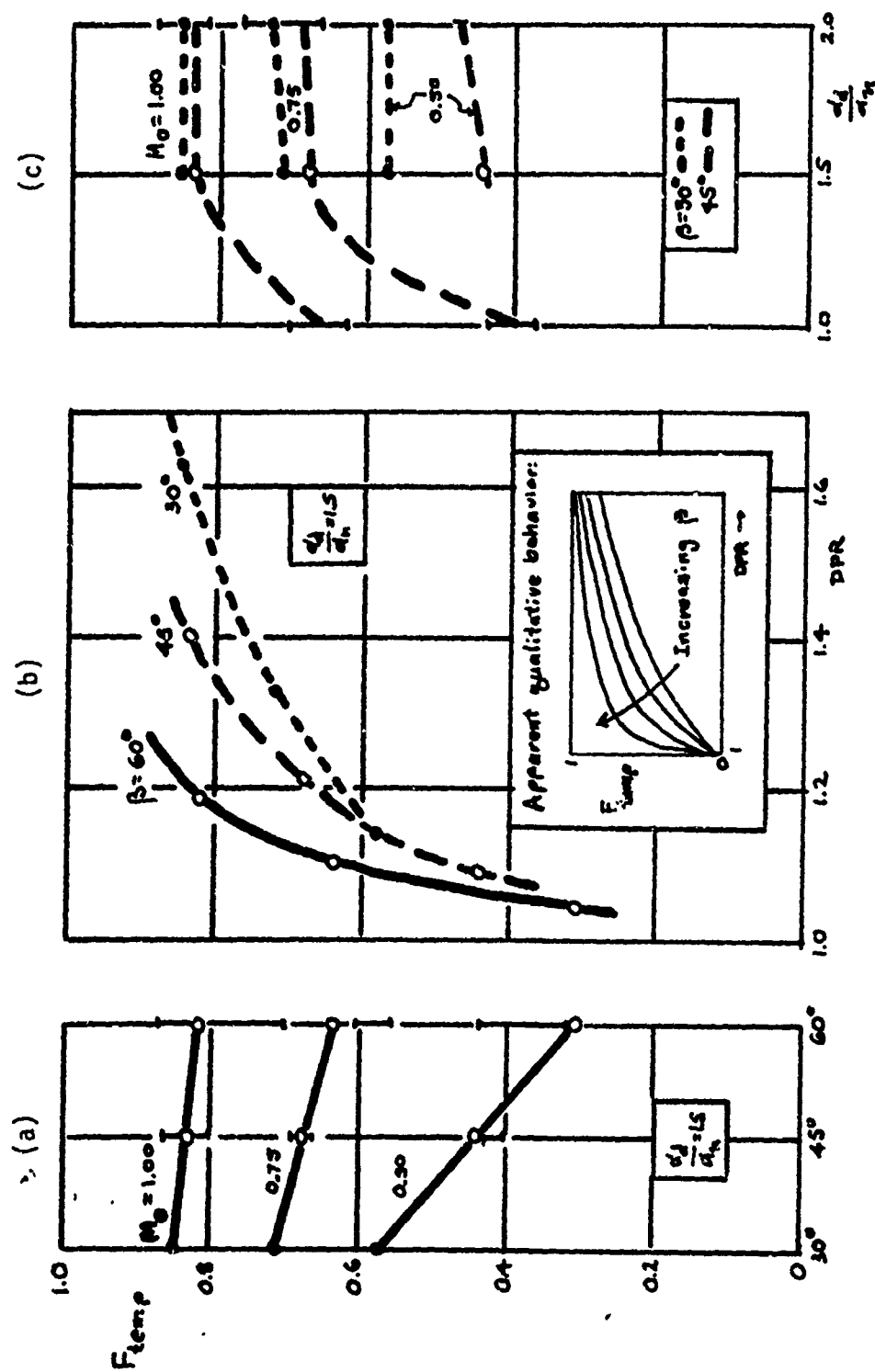


Figure 65  
Effect of Nonsteady Collection on Magnitude of Temperature Drop (Cold Output)

fairings are chosen in 65(a) so long as the fairings themselves look reasonable.

Figure 65(c) indicates that the effect of channel height on  $F_{temp}$  is very weak, unless it is reduced to something close to the nozzle width (measured in the plane of rotation)--at which point  $F_{temp}$  tends to fall off. Noting the  $M_o = 1.00$  curves, however, it would appear that even this effect may be less pronounced as pressure ratio is increased.

The effect on cold fraction is shown in Figure 66, with the presentations in parts (a,b,c) analogous to those in Figure 65 for the case of temperature drop. Two effects are at work to reduce cold fraction: one is that of Figures 62(i,j) wherein the "cold slug" is chopped into components "au" and "bu", the latter portion being obliged to leave via the hot port rather than the cold port. The other effect is that of pumping, which reduces the net flow out the cold port while raising that out the hot port.

Figure 66(b) shows that  $F_{flow}$  gets worse with increasing  $\beta$ , at a given channel-height factor and pressure ratio. The effect of pressure ratio tends to be favorable, but the curve flattens out rapidly toward a value which, for  $\frac{d_d}{d_m} = 1.5$  at least, is well below 1.0. Figure 66(c) shows in addition that reduction of channel height cannot bring  $F_{flow}$  a great deal closer to unity, because as the pumping effect is reduced the nonsteady effect of Figures 62(i,j)--exacerbated by reduction of total nozzle flow due to wall proximity--becomes more serious. Note from Figure 66(c) that there is evidently an optimum channel-height factor insofar as  $F_{flow}$  is concerned; this optimum value of  $\frac{d_d}{d_m}$  is slightly larger than unity (the exact value unquestionably depending upon  $\beta$  and probably DPR),

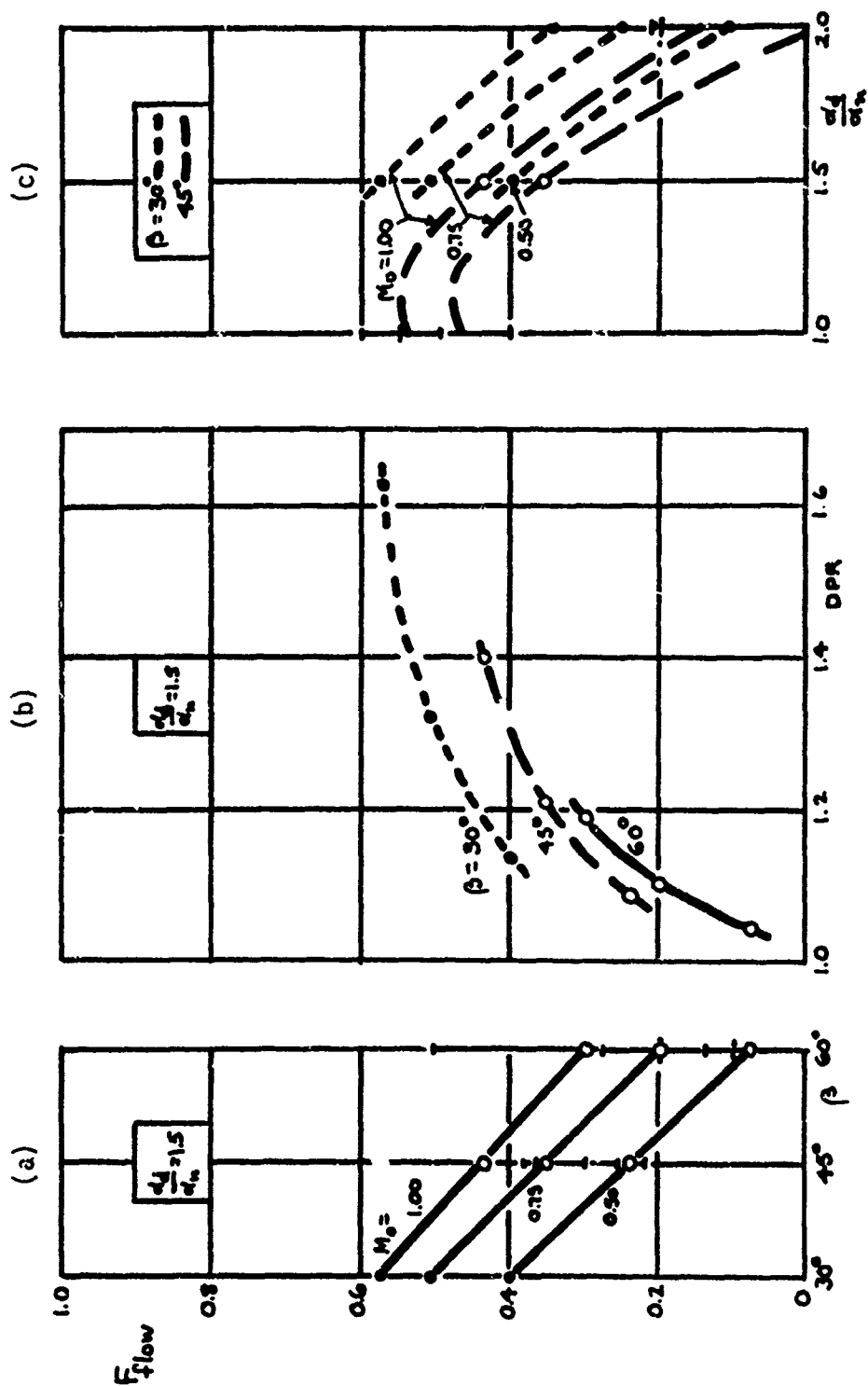


Figure 66  
Effect of Nonsteady Collection on Cold Fraction

and corresponds physically to the condition wherein the impingement wall is close enough to cause the leftward-swept source flow and bypass flow to fill the duct and eliminate pumping, but not so close as to reduce the source flow rate appreciably.

For channel-height factors exceeding the optimum value, the pumping effect is a very strong function of  $\frac{d_d}{\alpha_m}$  : for example, with  $\beta = 45^\circ$  and  $M_o = 1.00$  (i.e., DPR = 1.40), the entire cold flow consisting of "ac" and "au" combined would be lost to the pumping effect at a channel-height factor of around 2.0. A further increase in  $\frac{d_d}{\alpha_m}$  would result in a net pumping of fluid from the "cold" side to the "hot" side.

The manner in which refrigeration capacity is affected by non-steadiness is summarized in Figure 67. Considering Figure 67(b), it is noted that  $F_{\text{capy}}$  is very low at low DPR's, reflecting the behavior of  $F_{\text{temp}}$  [Figure 65(b)], is favorably affected by increasing pressure ratio, but starts levelling off rapidly at a value well below unity, reflecting the behavior of  $F_{\text{flow}}$  [Figure 66(b)]. The qualitative behavior which appears to occur is indicated in the inset of Figure 67(b); however, the sensitivity to  $\beta$  may be noted to be relatively small. Figure 67(c) is dominated in its behavior by massflow effects, and so looks very similar to 66(c). However, the drop-off in  $F_{\text{temp}}$  as  $\frac{d_d}{\alpha_m}$  is decreased toward 1.0 results in shifting the optimum channel-height factor toward a larger value than that indicated in 66(c).

#### Cold-side pressure depression and rotor velocity perturbation.

The depression of the pressure  $p_a$  below the ambient value  $p_o$  may be calculated by means of equation (91). This effect has been accounted for only with regard to estimating the magnitude of the pumping effect, which

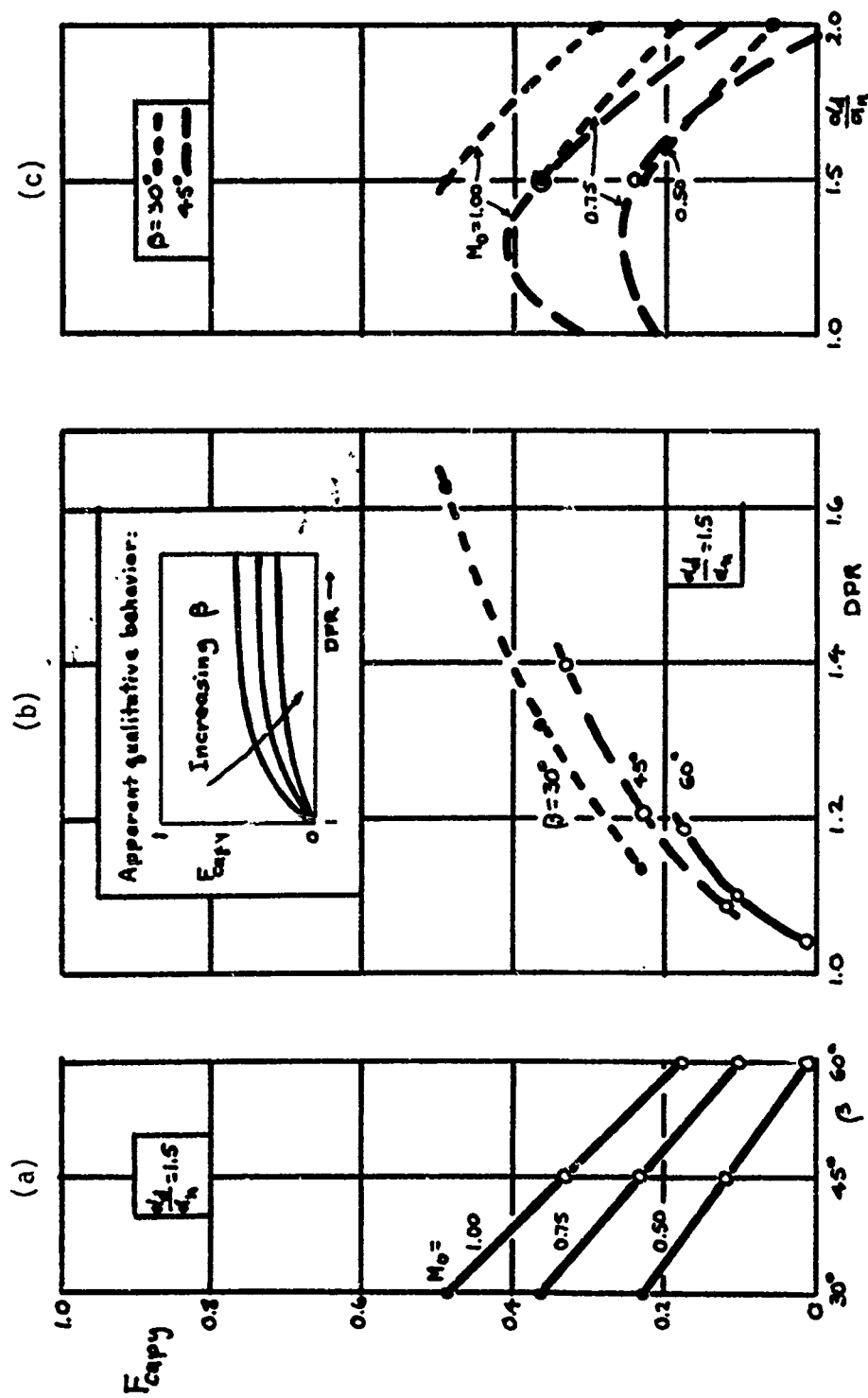


Figure 67  
Effect of Nonsteady Collection on Refrigeration Capacity

was done by assuming isentropic quasi-steady inflow through the port to a uniform velocity equalling that of the source. However, there will in fact be two additional effects, ignored up to here: (i) the net pressure differential  $\delta p$  across the jet in the presence of the initial shock will be increased, thereby causing increased bypass flow, which is undesirable; (ii) the velocities  $c_{ac}$  and  $c_{au}$  of the flows "ac" and "au" in frame  $F_S$  will be increased, leading to higher values of  $T_{ac}^0$  and hence poorer cold-temperature performance.

Figure 68 gives the ratio of the depressed cold-side pressure level  $p_a$  to the nominal (ambient) pressure level  $p_o$ , as a function of  $\beta$  and the nozzle pressure ratio  $NPR = \frac{p_o}{p_m}$ , where  $p_m$  is the effective mean static pressure at the exit of the nozzle. It is seen that the magnitude of the pressure depression is not too severe for small  $\beta$ 's up to moderate NPR's; but as  $\beta$  goes up, the pressure depression effect rapidly becomes a major one. This effect is directly related to that shown in Figure 54: very high rotational speeds are produced at quite low pressure ratios if  $\beta$  is large. -

As for rotor velocity, the nonsteady effects have been analyzed which would follow an ideal, cryptosteady first sweep of the duct by the source, the source velocity being assumed to remain unchanged during the second sweep. However, it must be noted that if the time-averaged value of  $p_m \neq p_o$  during the second sweep, this implies that at cyclically "steady" state the nozzle exit velocity will be changed and the rotor velocity along with it.

The analysis assumes zero prerotation and shaft torque, and under these conditions the rotor velocity  $V$  and the mean nozzle-exit velocity



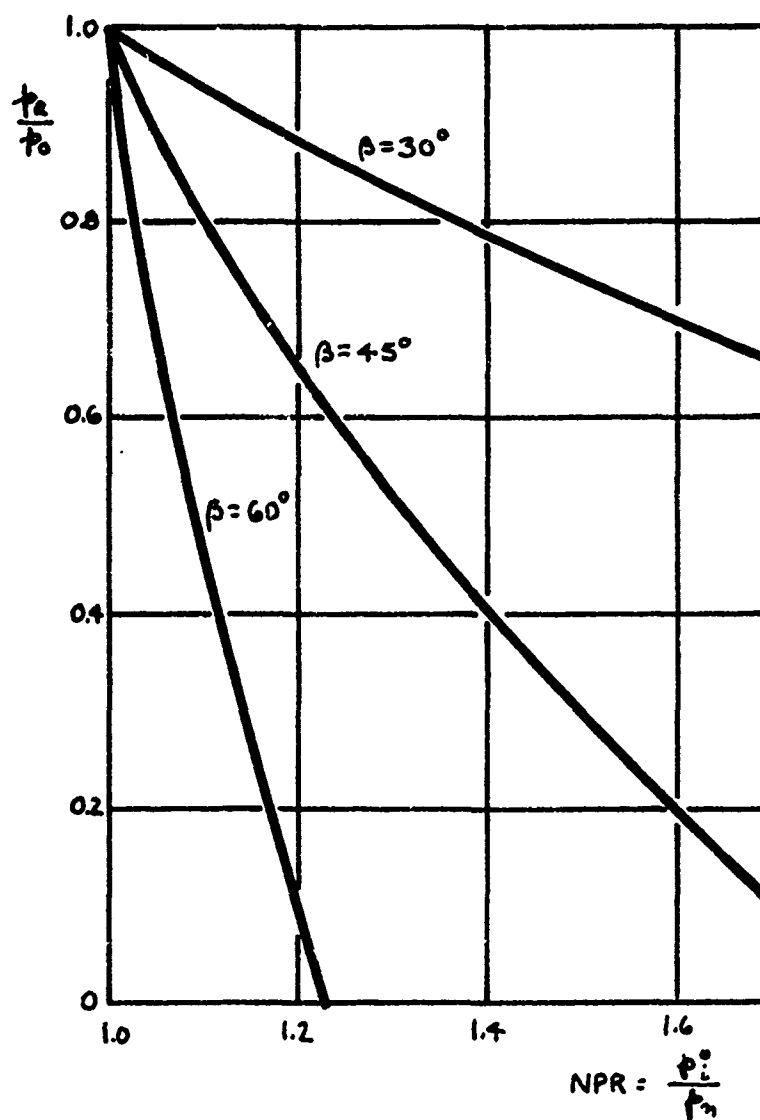


Figure 68  
Cold Side Pressure Depression

$\kappa_m$  are related through

$$V = \kappa_m \sin \beta$$

and hence if the time-average value of  $\kappa_m$  for a whole cycle is used,

$$\frac{V}{V_0} = \frac{\kappa_m}{\kappa_0}$$

A first approximation for the adjustment in  $V$  which must come about is obtained by calculating the time-average value of  $p_m$  during the "second sweep" which has been analyzed and, using the value of  $p_m^*$  that corresponds to  $V = V_0$ , to calculate a value for  $\kappa_m$  to use in the above expression. The reason this is only an approximation is that, as the rotor slows down, the wave processes will be altered and  $p_m^*$  will decrease; nevertheless, this estimate is probably of the correct order of magnitude.

The pressure depression on the cold side (Figure 68) tends to decrease  $p_m$ ; however, this is overbalanced by the very strong increase in  $p_b$  (just to the right of the source) due to the shock as long as supercritical flow exists. When the pressure is at last relieved, it is only relieved sufficiently to give  $\bar{p}_b \doteq p_0$  for the remainder of the cycle. As a result, the net effect averaged over the cycle is a significant increase in  $p_m$  and a concomitant decrease in  $V$ . Figure 69 presents estimates of  $\frac{V}{V_0}$  obtained in the approximate manner mentioned above.

Surprisingly little sensitivity to  $M_0$  (or, for a given  $\beta$ , DPR) emerges, but there is some slight sensitivity to channel height as shown. Clearly, the rotor-velocity effect is a very noticeable--and detrimental--effect, given the fact that FES performance varies roughly as  $V^2$ .

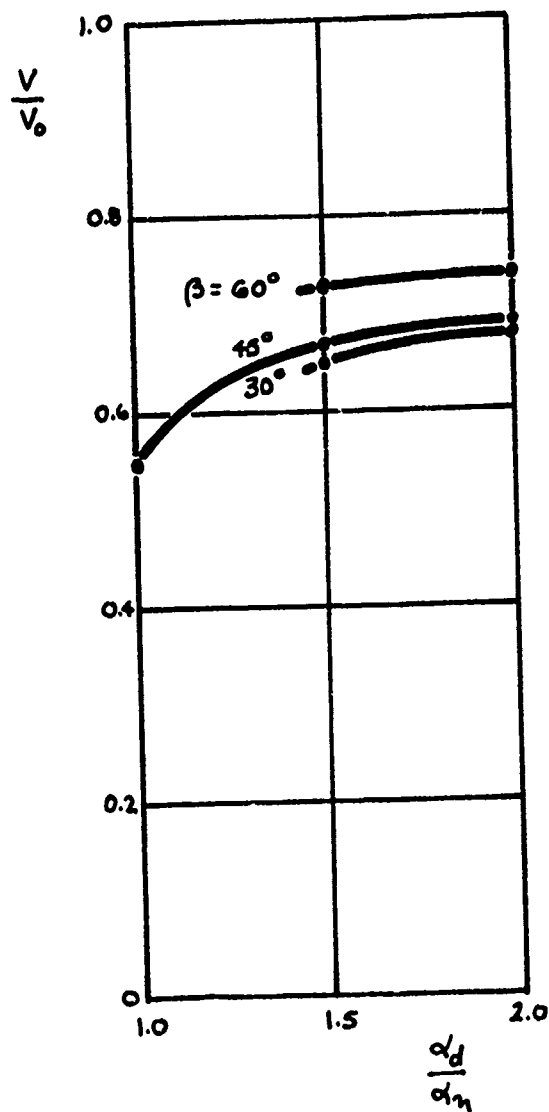


Figure 69  
Rotor Velocity Perturbation

Anticipated effects of exit plenums. The wave diagrams and associated performance analyses were carried out for the case in which the flows discharge to ambient conditions, as might be the case for example in a simple experimental setup. In practice, however, one or both of the outputs may discharge to exit plenums: a confined space to be cooled by the cold output constitutes such a plenum, for example, and a plenum might be used for the hot output to enable mass-average total temperatures to be measured accurately. It is therefore relevant to inquire into the effect these would produce on performance. It will be assumed that the port discharge pressure is  $p_0$ , as would be the case without a plenum; the effects sought are those due to communication of the nonsteady flow patterns with surrounding fluid at an altered temperature level.

**COLD PLENUM.** Physical reasoning suggests strongly that the presence or absence of a plenum on the cold side is of little moment. This is because, although Figure 62 depicts the pumped inflow "ap" as coming from the surroundings whose temperature would be affected by a plenum, in reality this deadwater probably is obtained from recirculation of fluid peeled off from the upper layers of the leftward-moving combined mass of "ac" and "au" flow, as is depicted below in Figure 71. Indeed, this expectation is incorporated into the performance calculations by assuming that  $\frac{\Delta T_c}{T_{c0}} = \left(\frac{\Delta T_c}{T_c}\right)_{net}$ .

**HOT PLENUM.** Based on the physical picture of the nonsteady-collection flow process that emerges from the nonsteady analysis, three mechanisms suggest themselves by which the presence of a hot plenum might affect performance: (1) altered timing of the wave processes; (2) altered strength of the initial rarefaction, which is associated with the inflow through the

hot port; and (3) altered energy transport by the "bu" flow (which is inducted through the hot port, energized, and re-expelled during the earlier portions of the cycle).

(1) Wave-process timing. This is the easiest to dispense with, since as the wave diagrams show, refraction of the incident shock and later the strong reflected rarefaction is so mild that it can be neglected altogether without significantly affecting the timing which is calculated as a result.

(2) Initial rarefaction strength. Here, it should first be noted that the initial rarefaction is quite weak for all the conditions analyzed; its effect is accounted for in the wave diagram through its influence on the interface velocity and the particle velocity in region 4, but the slight pressure reduction at the source is not accounted for in calculating performance. Even so, it is relevant to ascertain the qualitative effect of the plenum on this rarefaction, on the chance that it might make the rarefaction more important.

For this purpose, consider the right end of Figure 62(e). The undisturbed portion of the "cold slug" is moving leftward uniformly at dimensionless velocity  $U_{\infty}$ ; there is however a rarefaction (moving leftward relative to the slug) to the right of which elements of the slug are moving leftward more slowly, at velocity  $U_x$  (the interface velocity), which is equal to the velocity of the elements of inflow to the right of the interface. Pressure at the interface is  $p_2 = p_3 = p_x$ , where subscripts 2 and 3 refer to the corresponding regions of the wave diagram, Figure 63(a). Stagnation temperature in the plenum surrounding the hot port will be denoted  $T_H^0$ .

At the port itself, there is quasi-steady flow from the reservoir surrounding the port to the pressure  $p_3$  and velocity  $u_3$ . Therefore,

$$T_3 = T_H^0 - \frac{u_3^2}{2c_p}$$

or in dimensionless variables,

$$\frac{T_3}{T_H^0} = 1 - \frac{\gamma-1}{2} \left( \frac{u_3}{A_i^0} \right)^2 \frac{T_i^0}{T_H^0}$$

and if the inflow is assumed isentropic,

$$\begin{aligned} \frac{p_3}{p_H^0} = \frac{p_x}{p_0} &= \left[ 1 - \frac{\gamma-1}{2} \left( \frac{u_x}{A_i^0} \right)^2 \frac{T_i^0}{T_H^0} \right]^{\frac{\gamma}{\gamma-1}} \\ &\doteq 1 - \frac{\gamma}{2} \left( \frac{u_x}{A_i^0} \right)^2 \frac{T_i^0}{T_H^0} \end{aligned}$$

where the approximate form is justified by the weakness of the rarefaction.

Now designate conditions without a plenum by ( )' and those with a plenum by ( )". Also, define  $\Delta p_x = p_x - p_0$  and  $\Delta u_x = u_x - u_0$ . Note physically that if  $\Delta p_x = 0$  there is no rarefaction and therefore  $\Delta u_x = 0$ ; conversely, if  $\Delta u_x > 0$ , there has to be a rarefaction and  $\Delta p_x < 0$ --in other words, the magnitudes of  $\Delta u_x$  and  $\Delta p_x$  are directly related. Suppose one were to assume  $u_x'' = u_x'$ : then

$$\frac{\Delta p_x'}{p_0} = -\frac{\gamma}{2} \left( \frac{u_x'}{A_i^0} \right)^2 \frac{T_i^0}{T_H^0} \quad \text{and} \quad \frac{\Delta p_x''}{p_0} = -\frac{\gamma}{2} \left( \frac{u_x'}{A_i^0} \right)^2 \frac{T_i^0}{T_H^0}$$

or

$$\frac{\Delta p_x''}{\Delta p_x'} = \frac{T_i^0}{T_H^0} < 1$$

which implies also that

$$\frac{\Delta u_{\kappa}''}{\Delta u_{\kappa}'} < 1$$

contradicting the assumption  $u_{\kappa}'' = u_{\kappa}'$ . The solution, therefore, is one for which  $\Delta p_{\kappa}''$  has a smaller value than the above and  $\Delta u_{\kappa}'' < \Delta u_{\kappa}'$  --i.e., the rarefaction is weaker with the plenum than without it. (Note, this conclusion is also physically obvious: the fluid surrounding the hot port has the same total pressure with or without the plenum, but a higher total temperature with the plenum; hence, the inflow Mach number engendered by the piston-like action of the right end of the cold slug must be lower.)

Qualitatively, the weakened rarefaction will allow the inflow to penetrate slightly further into the duct before having its direction reversed by the shock; however, since the rarefaction was weak even without a plenum, this further weakening has an insignificant effect quantitatively. There will also be a tendency for the strong supercritical flow at the source to be relieved even less, prior to arrival of the strong rarefaction reflected from arrival of the shock at the hot port, but again this effect is very minor.

(3) Energy transport by inducted flow "bu". Let  $\Delta \mathcal{H}_{bu}^{\circ}$ , denote the net total enthalpy transported out the hot port when it is expelled [region 6 of the wave diagram, Figure 63(a,b)] and use the same notation as before to denote conditions without and with a hot plenum.

Then

$$\frac{(\Delta \mathcal{H}_{bu}^{\circ})''}{(\Delta \mathcal{H}_{bu}^{\circ})'} = \frac{(m_{bu} c_p \Delta T_{bu})''}{(m_{bu} c_p \Delta T_{bu})'}$$

According to the discussion of item (2) above, the distance  $\Delta \xi_3$  to which the inflow penetrates the duct is affected little by the plenum. Also, the strength of the transmitted shock which separates regions 3 and 5 is changed little by the plenum's presence ( $\Delta p_{3-5}$  is increased about 2.5% in Case 6, where this effect is the largest), and hence the reflected rarefaction also maintains about the same strength it had in the absence of a plenum.

There is, to be sure, a slight increase in the exit velocity  $U_6$ ; however, this increase in kinetic energy per unit mass is offset by decreased density, hence less total mass. Tracing this analytically, note that since  $\Delta \xi_3'' \doteq \Delta \xi_3'$  and since the shock strength is essentially unchanged, the interface path is the same as before and therefore

$\Delta \xi_6'' \doteq \Delta \xi_6'$ . Therefore,

$$\frac{(m_{bu})''}{(m_{bu})'} = \frac{\Delta \xi_6''}{\Delta \xi_6'} \frac{\rho_6''}{\rho_6'} \doteq \frac{\rho_6''}{\rho_6'}$$

But

$$\begin{aligned} \frac{\rho_6''}{\rho_6'} &= \frac{p_6''}{p_6'} \cdot \frac{T_6'}{T_6''} \\ &= \frac{(p_6/p_0)''}{(p_6/p_0)'} \cdot \frac{(T_6'/T_i^0)}{(T_6''/T_i^0)} \cdot \frac{T_i^0}{T_i^0} \end{aligned}$$

The first two factors are functions of the change in shock strength, and are therefore essentially unity. Therefore, the density effect is given by

$$\frac{\rho_6''}{\rho_6'} \doteq \frac{T_i^0}{T_i^0}$$



As for  $\Delta T_{bu}'$ , what is needed is the effective or net total-temperature rise above  $T_H^0$ :

$$\begin{aligned}\frac{\Delta T_{bu}'}{T_i^0} &= \frac{T_c^0 - T_H^0}{T_i^0} \\ &= \frac{T_c^0}{T_c} \frac{T_c}{T_H^0} \frac{T_H^0}{T_i^0} - \frac{T_H^0}{T_i^0} \\ &= \left( \frac{T_c^0}{T_c} \frac{T_c}{T_H^0} - 1 \right) \frac{T_H^0}{T_i^0}\end{aligned}$$

The quantity in parentheses is dependent upon the transmitted shock strength, and is therefore essentially the same with or without a plenum. (Note, however, that if the shock strength were accounted for, the effect would be in a favorable sense.) Therefore,

$$\frac{(\Delta T_{bu}')''}{(\Delta T_{bu}')'} = \frac{(\Delta T_{bu}'/T_i^0)''}{(\Delta T_{bu}'/T_i^0)'} = \frac{T_H^0}{T_i^0}$$

is the effect on temperature rise. Bringing together the effects on density and temperature rise, the net effect on total enthalpy transport by flow "bu" is

$$\begin{aligned}\frac{(\Delta \mathcal{H}_{bu}')''}{(\Delta \mathcal{H}_{bu}')'} &= \frac{T_i^0}{T_H^0} \cdot \frac{T_H^0}{T_i^0} \\ &= 1\end{aligned}$$

In other words, to a first approximation, the plenum has no net effect on energy transport by flow "bu".

Thus, the overall conclusion would appear to be that the presence or absence of plenums to receive the hot and/or cold flows is of little importance to the actual performance of the device (though the use of a hot plenum will have a very strong effect on the measured hot-output temperature, serving to make the temperature measurement more meaningful). This is based upon rather rough analysis, but there appears to be little reason to expect the picture to change dramatically with more precise analysis: for example, the slight beneficial effect due to shock strength increase in item (3) would tend to be offset by the minor detrimental effect on flow in the source region due to the weakened rarefaction in item (2).

Anticipated effects of exit port area changes. The wave-diagram and associated performance analyses were done for the case in which the cold and hot exit port areas,  $\alpha_{pa}$  and  $\alpha_{pb}$  respectively, are both equal to the duct area  $\alpha_d$ . Given the complexity of the total flow pattern that occurs with nonsteady collection and the analytical difficulties that arise even in this geometrically simple situation, the effects of altering the exit port areas have not been examined by direct extension of the basic wave-diagram analysis. Instead, qualitative effects of port area are deduced on the basis of the salient physical features of this flow pattern.

**HOT PORT.** If the effective hot-port area  $\alpha_{pb}$  is reduced, the reflected rarefaction produced by arrival of the initial shock is reduced in strength. When it arrives at the source, therefore, it will not reestablish quite as vigorous a subcritical (splashing) flow as occurs with  $\frac{\alpha_{pb}}{\alpha_d} = 1.0$ , and additional wave action will be required to bring the pressure  $p_*$  (immediately to the right of the source) down to  $p_0$ . The

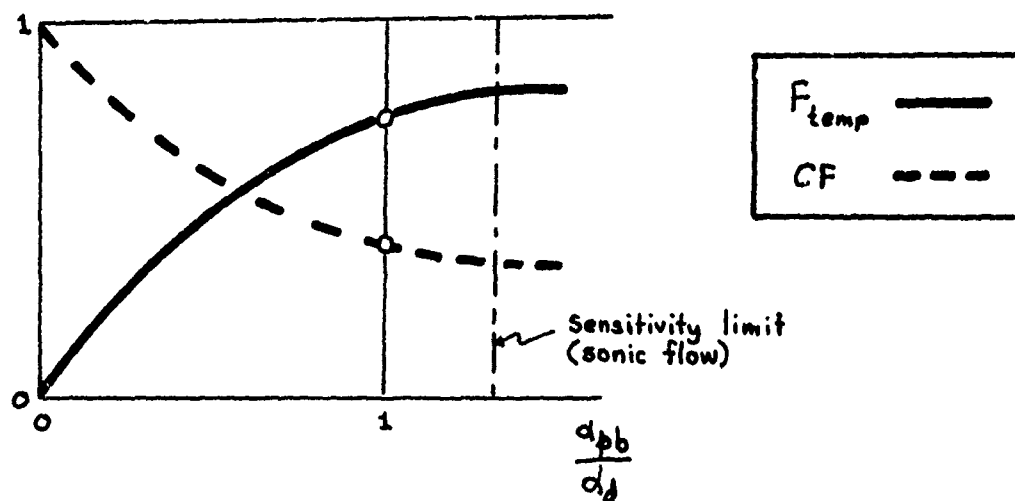
upshot of all this is that the total amount of "bc" flow produced during the cycle will be reduced, degrading performance since "bc" is the most effective of the hot flows. Further reduction in  $\alpha_{pb}$  will so weaken the reflected rarefaction that subcritical flow will not be reestablished at all by its arrival, and further wave action will be needed even to reach the critical condition. This will further reduce the total amount of "bc" flow produced during the cycle and in addition will increase the amount of "au" flow, which pollutes the cold flow. Further reduction in  $\alpha_{pb}$  will cause the shock to be reflected as another shock; when this point is reached, supercritical flow continues for the entire cycle.

The trends corresponding to this process of closing down the hot-port area are clearly decreasing cold-temperature performance (or  $F_{temp}$ ) and increasing cold fraction (CF), the latter because less and less "bc" flow occurs and more and more bypass flow occurs. Conversely, if  $\alpha_{pb}$  is increased by causing the flow to diffuse to a larger area, a reduction in cold fraction and an improvement in cold-temperature performance should result, due to increasing the velocity of the hot flows and biasing the pressure difference across the source in such a way that the average "bc" flow rate after reestablishment of splashing flow is greater than normal. Things can only be carried so far in this direction, however: as soon as sonic flow occurs at the end of the constant-area duct, further changes of port exit area are meaningless. Since sonic outflow occurs after arrival of the shock at the port for many cases examined (involving combinations of the larger  $M_o$  and  $\beta$  values), effective increases in  $\alpha_{pb}$  probably are not possible for most conditions of practical interest.

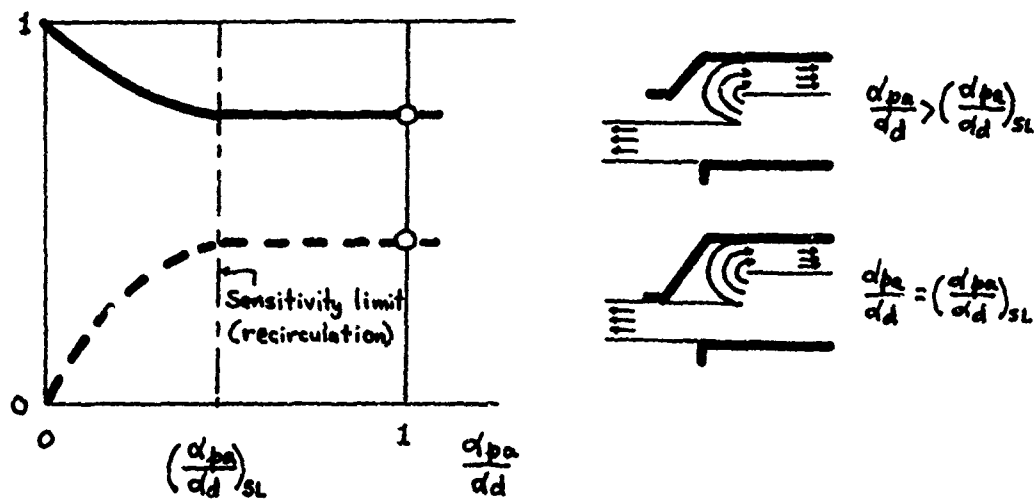
Figure 70(a) illustrates the qualitative effects of hot-port area changes deduced above. Note that the reasoning above with respect to decreasing  $\alpha'_{pb}$  leads, in the limit of  $\alpha'_{pb} = 0$ , to  $CF = 1$  and  $F_{temp} = 0$ . This is clearly the correct limit if the whole energy separator is viewed as an adiabatic black box: fluid is introduced at the center of the rotor and all exits via the cold port, hence  $\frac{m_a}{m_i} = 1$  and  $T_a^o = T_i^o$  (no total-temperature drop).

COLD PORT. If  $\alpha'_{pa}$  is decreased, the recirculation considerations alluded to earlier suggest that there would be a range over which decreases in area would have little effect: one would simply be enclosing the recirculation pattern depicted in the sketch of Figure 70(b). As soon as the port area dropped below that normally occupied by the net exit flow, however, the constriction of the flow would tend to raise the pressure within the duct and to the left of the source. The reduction in available exit flow area would clearly reduce the cold massflow; however, the rise in pressure on the left side of the source would tend to offset the high pressure due to the shock on the right side of the source, thereby reducing the amount of bypass flow and improving cold temperature performance. As the area  $\alpha'_{pa}$  tends toward zero,  $F_{temp}$  should approach 1.0; however, the cold massflow is approaching zero, so that we have the hot fraction (HF) approaching 1.0 and the hot temperature approaching  $T_i^o$ .

To increase the effective value of  $\alpha'_{pa}$ , it would be necessary to contour the exit nozzle in such a way that the net flow shown in the sketch of Figure 70(b) would attach to it, and then diffuse this flow to a larger area; or some sort of ejector effect could be used. However, there would appear to be little incentive to go to such lengths: this



(a) Influence of Hot Port Area



(b) Influence of Cold Port Area

Figure 70  
Effects of Port Area Changes

would depress the pressure in the duct to the left of the source, increasing the net pressure differential  $\delta p$  across the jet produced by the initial shock and resulting in more bypass flow, which is undesirable. Thus, the possibility of increasing  $\alpha_{pa}$  by such means will be ignored.

Figure 70(b) illustrates the qualitative effects of cold-port area changes postulated above. Note that the effect of decreasing area is predicated on the presumption of a recirculatory flow pattern something like that sketched; if instead the pumped flow is largely drawn in from the surroundings with the bulk of the basic cold flow emerging as in Figure 62, decreasing the cold-port area would interfere with this inflow and have quite different effects perhaps. The basic trend once  $\alpha_{pa}$  is less than the net flow area in the sketch of Figure 70(b) should, however, still be valid.

Influence of effects neglected in basic analysis. The present analysis has been simplified in a number of ways, and it is pertinent to ask how the theoretical results thus obtained may be expected to deviate from reality. Several of the more important effects which have not been analyzed explicitly are therefore discussed briefly below.

**MASS STORAGE BUILDUP IN SUBSEQUENT CYCLES.** As pointed out earlier, under certain conditions the mass of the "cold slug" stored during the second sweep of the duct by the source is greater than that during the first (cryptosteady) sweep. Under more severe conditions, there is in addition a failure of the bypassed slug "au" to escape completely out the "a" port, a portion therefore being trapped in the duct at the end of the cycle. If one or both of these effects are present, the total mass of fluid (excluding the pumped flow) present in the duct at the end of the

second cycle is greater than at the end of the first; this implies that the third cycle will have to differ in quantitative terms from the second, probably with a further adjustment in mass storage, and so on until a cyclic recurrence of conditions (dominated by mass storage) signals the attainment of "steady" state.

This mass storage buildup effect increases fairly rapidly with  $M_o$ , and much more rapidly with  $\beta$ : at  $30^\circ$ , it is absent at  $M_o = 0.50$  and  $0.75$ , minimal at  $1.00$ ; but at  $45^\circ$  and especially at  $60^\circ$  it is severe. This effect is the source of the uncertainty bands in Figures 65 through 67.

Qualitatively, referring to Figure 63(a), it may be noted that since more mass which started out life as "ac" flow is being stored, more of it will be transformed into "au" and "bu" flow components; thus, the mass-storage buildup phenomenon would appear to imply deteriorating performance in succeeding cycles as the "steady" state is approached. Therefore, the "second sweep" performance calculations are presumably optimistic wherever this effect is present. Because of this, the favorable influences of  $\beta$  and DPR seen in Figures 65 and 67 are to be accepted with caution:  $45^\circ$  may indeed be better than  $30^\circ$ , but it is entirely possible that by  $60^\circ$  the mass-storage effect wipes out the gains expected on the basis of second-sweep calculations.

ENTROPY INCREMENTS DUE TO SHOCKS. At the conditions considered in the wave-diagram and performance analyses, the shocks produce relatively small entropy increments, and these are therefore ignored. However, consider the "Comparison of Hammer and Stagnation Conditions" on page 157 of Rudinger:<sup>38</sup> two facts stand out. First, note that the largest value of

$M_0$  considered in the present analysis is 1.0, and that the ratio of ( $p_{\text{hammer}}/p_{\text{stagnation}}$ ) is a maximum at approximately this Mach number. As  $M_0$  is increased further, therefore, the decreasing ratio of  $p_1/p_{\text{stagnation}}$  implies that the pressure  $p_0$  established to the right of the source will come closer and closer to the hammer pressure, which implies that the shock is more and more nearly a hammer shock. (Indeed, at  $M_0 = 2.14$ , if the basic splashing pattern still behaved as it did subsonically, the "b" flow would have a total pressure equal to the hammer pressure, and the shock would be exactly a hammer shock. At still higher  $p_0$ ,  $p_1$ , and the shock strength would correspond to that ahead of a piston moving rightward in  $F_5$  from the source toward the leftward-moving cold slug.)

Second, note with the additional aid of Rudinger Table 1a that the entropy increment associated with a hammer shock at (say) Mach 1.5 is several times that at Mach 1.0; thus, shock-produced entropy increments increase to appreciable levels rather rapidly as DPR is increased above the level indicated in Figure 54 for any given  $\beta$ . Looking at Figure 54, these effects could become significant at pressure ratios around 2 to 3, and even much lower for high  $\beta$ 's.

Of course, all of this is only significant if the initial compression formed when the shock appears at the left end of the duct at the beginning of the cycle actually coalesces into a shock. Conceivably, the effect of finite port width in combination with the dynamic behavior of the jet itself could lead to a distributed compression wave which would be isentropic. No detailed or comprehensive investigation in this respect has been carried out, but in the one case in which this was examined ( $30^\circ$ ,  $M_0 = 0.5$ ) it was discovered that coalescence of the shock could not be



completely prevented unless the effective port-opening width amounted to a little over 10% of the complete length of the duct. Realistic numbers would seem to be a fraction of this--say 3-5%--which implies that a considerable amount of shock coalescence is to be expected. In the case cited, full coalescence would appear likely by  $\frac{x}{L} \approx 0.5$  or before.

WAVE PROPAGATION THROUGH STRATIFIED MEDIA. The most basic, pervasive departure of the analytical model from physical reality lies in the application of nonsteady one-dimensional flow analysis techniques to a problem wherein the flow in the duct is actually stratified. This would also be by far the most difficult effect to assess analytically, but it clearly calls for comment. The expectation of the writer is that this effect would not change the qualitative nature of the nonsteady collection process, but that the magnitude of the penalties would not be as large as those which have been calculated. In particular, the flow stratification would presumably lead to formation of what would basically be an oblique initial shock rather than the normal shock implied in the analysis; this would involve a lesser rise in  $p^*$ , and would also lead to somewhat earlier perturbation relief because of higher propagation velocity. Thus, in this respect at least, the results of the present analysis are probably on the pessimistic side.

The general suggestion that emerges from this exploration of effects not included in the basic analysis is that the estimates of performance are probably somewhat on the optimistic side, although the stratified-media wave propagation effect may be an offsetting factor. Furthermore, these additional effects tend to become more important with increasing pressure ratio and especially with increasing  $\beta$ , which implies that

the favorable influence of these factors on performance is not as strong as indicated in Figures 84 and 86 (or more properly for Figure 86, the detrimental effect of  $\beta$  is stronger than that calculated).

Summary of principal nonsteady collection effects on performance.

The basic conclusion reached on the basis of the nonsteady collection analysis is that nonsteadiness in the collection process is inherently detrimental to performance. This conclusion is rooted in the fact that during each cycle, or sweep of the duct by the source, a portion of the "a" flow is trapped in the duct at the end of the cycle. During the next sweep, this slug of fluid is essentially chopped in two by nonsteady effects on the source flow, after which one fragment leaves via the "a" port and the other is forced to leave via the "b" port instead; this reduces the net massflow out the "a" port below the cryptosteady level. Furthermore, the fragment leaving via the "a" port has a higher total enthalpy than the cryptosteady "a" flow, and that leaving via the "b" port has a lower total enthalpy than the cryptosteady "b" flow, with the result that the degree of energy separation effected is reduced. In addition, if the collector channel height is appreciably greater than the nozzle width (measured in the plane of rotation), there is a strong pumping effect which increases the flow out the hot port while reducing that at the cold port.

Figure 71 summarizes salient features of the flow phenomena revealed by the nonsteady-flow analysis. In 71'a), all the flows are depicted except flow "bu'", which is inducted and reexpelled at the hot port during the early portion of the cycle. The source flow "n" is, in effect, divided into four flows--the cryptosteady components "ac" and "bc" and the unsteady components "au" and "bu". Flows "ap" and "bp" are

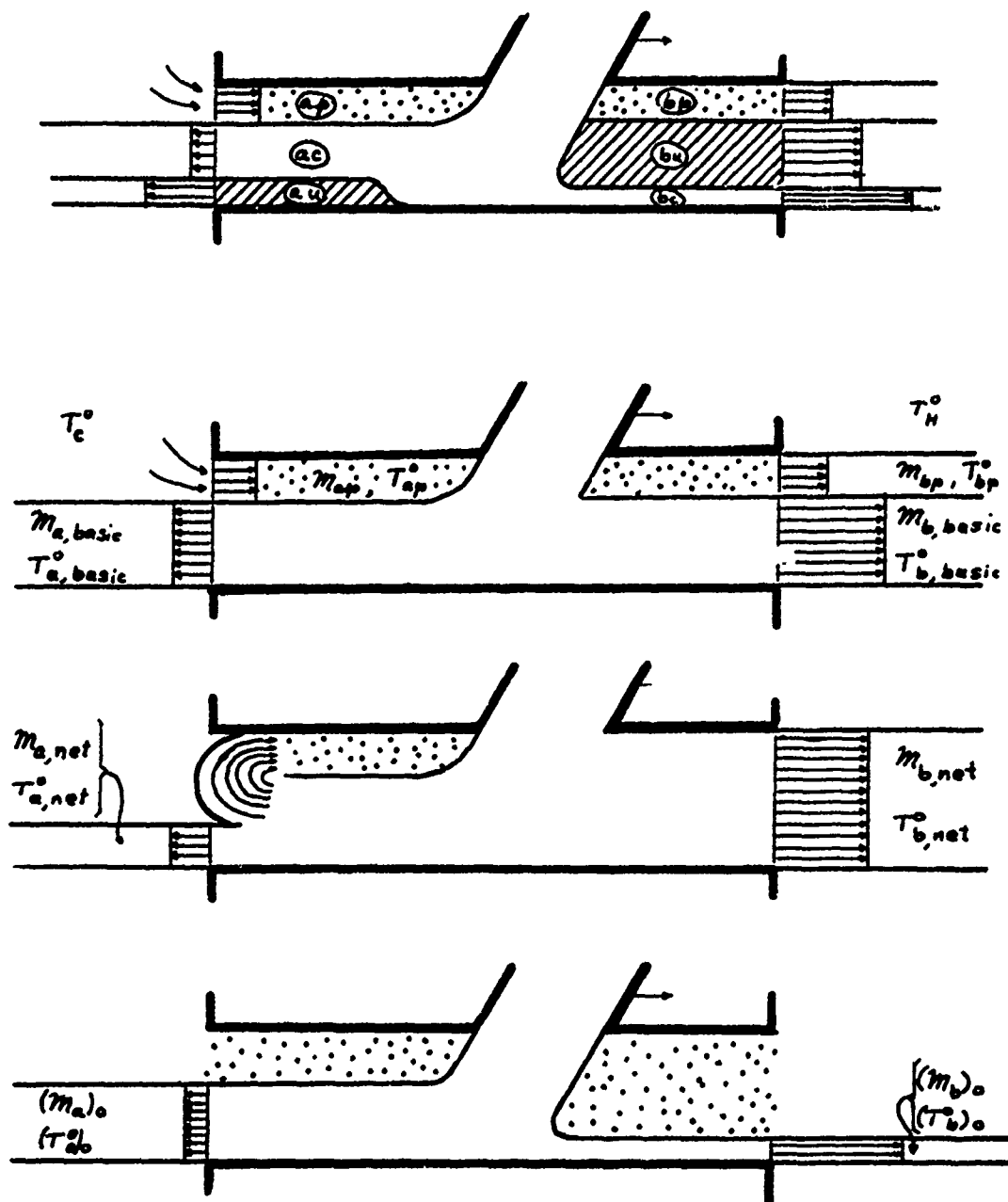


Figure 71  
Summary of Nonsteady Collection Flow Phenomena

"pumped" fluid: the slug "ap" drawn in from the left during one sweep of the source is expelled at the right as slug "bp" in the next sweep.

In Figure 71(b), the flows which originated at the source are lumped into "basic" flows "a" and "b", while the distinct character of the pumped flow is still indicated. Since energy separation is a process in which an initially uniform flow is divided into two (or more) flows having different energy levels, it is clear that the "basic" flows insofar as energy separation is concerned are those so denoted in Figure 71(b). However, the energy level of flow "a, basic" is decreased below that of the fluid introduced into the rotor not only by the energizing of flow "b, basic" but also by two additional effects: (i) the indrafted flow "bu" (not shown in Figure 71) is energized by wave action and therefore transports more energy out than it came in with, and (ii) the portion of the jet between slugs "ap" and "bp" does work on the pumped flow, behaving in that region like a pseudoblade in a bladeless pump.

The cold massflow rate produced is reduced below the cryptosteady value even without pumping, and is reduced a great deal further by pumping. The first statement can be understood by looking at Figure 71(a): the shaded slugs "au" and "bu" would both exit as part of the uniform, cryptosteady "ac" flow in cryptosteady operation, but of course in non-steady operation the "bu" slug is pushed out the hot port instead. As for the effect of pumping, consider Figures 71(b,c). Figure 71(b) depicts the idealized, inviscid situation in which flow "a, basic" leaves while cold-ambient fluid is drawn in next to it to fill the space behind the rightward-moving source. However, it is suspected that in reality the flow pattern is more like that depicted in 71(c)--the upper layers of the

basic jet are peeled off in sufficient quantity to fill the deadwater region, leaving only a fraction of the flow to actually emerge from the port. The picture in 71(b) was used as a model in order to estimate the pumped massflow, with  $T_c$  (the cold-ambient temperature) taken to be equal to the total temperature of the cold flow in  $F_U$ .

Figure 71(c) depicts the "net" flows which appear at the ports and would be measured experimentally. At the cold port, the stratification of flow "a, basic" seen in 71(a) is not accounted for, and therefore  $T_c = T_{a,basic} = (T_a)_{net}$ . (Note that the effect of stratification would be to degrade cold-temperature performance further, since the upper layers which would be peeled off consist of the colder "ac" fluid.) The pumped flow subtracted from the cold flow is added to the hot flow, but its total temperature even after being energized somewhat by the pumping action is much less than  $T_{b,basic}^0$ ; thus, the mass-average temperature  $(T_b)_{net}^0$  of the total flow emerging from the hot port is considerably reduced by dilution.

Finally, then, it is instructive to compare the flow pattern in Figure 71(c) with the pattern in 71(d), which would be obtained in cryptosteady operation. In cryptosteady operation, the cold flow is a large fraction of the total flow entering the rotor, and may fill most of the cold port if  $\frac{\alpha_d}{\alpha_m}$  is small; the hot flow is a small fraction of the total flow, fills only a small fraction of the port, and is very hot. The contrast with the nonsteady situation in 71(c) is dramatic: here, the cold flow is much reduced and occupies a rather small fraction of the port area, while the hot flow fills the port and exhibits a greatly reduced mass-average temperature.

Furthermore, the measurement of this hot output temperature presents a different problem than in the cryptosteady case, because the hot flow is both stratified and undergoing strong wave processes, including an inflow phase. As a result, the wave diagrams show that major errors in hot-temperature estimation can easily result experimentally if the attempt is made to measure temperature with a thermocouple in the exit port--a technique which is quite acceptable for cryptosteady operation (aside from matters of probe error related to heat transfer details). In particular, if the hot port discharges to ambient (rather than a plenum), ambient temperature is felt during the inflow phase, and this further worsens the error in indicated hot output temperature. It is worth noting in this context that when a configuration similar to that of Figure 71 was tested several years ago at Rensselaer Polytechnic Institute, the "a" output was quite cold but the "b" output temperature as measured with a probe in the exit port was anomalously low, relative to what would have been expected on the basis of strictly cryptosteady operation; output massflows, however, were not measured. That relatively good temperature drop on the "a" side should have been obtained together with practically no indicated temperature rise on the "b" side is entirely consistent with the results of the nonsteady collection analysis.

Finally, it is interesting to observe that Figures 71(c) and 71(d) provide a handy physical picture to aid in remembering the effects of port area changes with nonsteady collection. It has been reasoned, on the basis of various details of the flow process, that a small cold port and a large hot port are desirable; and this is exactly the sort of configuration that suggests itself most directly simply by glancing at Figure

71(c). It is also, it should be noted, the exact reverse of what one would have thought on the basis of purely cryptosteady flow, pictured in Figure 71(d).

## PART IV

### DISCUSSION AND CONCLUSIONS

#### A. Review of Principal Findings

The present paper has been devoted primarily to an examination of the performance capabilities of the Foa energy separator (FES). However, an attempt has been made to place this treatment in its proper context within the field of energy separation as a whole by giving attention also to the predecessors of the FES, the Ranque-Hilsch vortex tube (RHT) and the dynamic pressure exchanger "divider" (DPE). In the case of the RHT, this includes a new performance analysis of a sort appropriate for the present contextual interest. A similar treatment of the DPE was infeasible, however, and the open literature on its performance characteristics is quite limited; therefore, the discussion of the DPE is confined to Appendix A, where performance characteristics are transformed from the format usual in DPE literature into one which is more convenient for present purposes.

##### 1. The Ranque-Hilsch Tube

It is of interest in the present case to have an estimate of the performance bounds within which RHT performance can always be expected to lie, in order to permit meaningful comparisons to be made with the present theoretical findings regarding the FES. No theory was found in the literature which would serve this purpose, and a new analysis has therefore been carried out.

In contrast to most previous analyses, the present treatment deals with the uniflow configuration rather than counterflow: it is



observed with the aid of experimental internal flow data reported in the literature that the two devices are basically equivalent, and that such minor differences as do exist probably give a slight performance advantage to the uniflow device. This choice enables an analytical model to be employed wherein--for "upper bound" performance calculation purposes--nothing at all must be assumed about the internal flow details (aside from ignoring the influence of wall friction, the justification for which is discussed). Instead, it is assumed on physical grounds that the terminal flow condition within the tube before flow extraction is that of a turbulent, compressible forced vortex with uniform axial velocity. Then the conservation equations for mass, angular momentum, axial momentum, and energy are applied to relate these terminal conditions to those of the flow entering through the injection nozzle. The axial momentum equation has not been utilized in previous theories, and yet is a fundamental key to defining the relationship between performance and pressure ratio; as a result, earlier theories must supply the missing information by means of questionable assumptions or empirical constants which are not needed here.

Exit losses that are inherent and peculiar to the RHT are also taken into account, after which overall performance characteristics are generated as a function of cold fraction and pressure ratio. As with the axial momentum equation, exit losses have not been introduced explicitly into any previous theory known to the writer, and these too are of fundamental importance. Indeed, it is found that they are likely to be the largest single source of loss in the RHT, outweighing the internal losses; and they are inevitable, because they spring from the necessity to uniformize

a flow whose nonuniformity is an essential feature of the RHT energy separation mechanism.

Consideration of exit losses also leads to the observation that any given fixed-geometry RHT has a definite design point, and off-design operation will lead to losses over and above those considered in the basic analysis, which corresponds to a performance envelope rather than a prediction for any single geometry. The theoretical implication is that the classical experimental behavior wherein the temperature drop goes to zero as cold fraction is reduced to zero (Figure 4) is strictly an effect of the mismatch between orifice size and cold flow rate. In the writer's view, this is also firmly established by experimental observations extant in the literature.

The theoretical "upper bound" performance curves predict, as do several previous theories, the qualitative and approximate quantitative performance of the RHT. The qualitative aspect is relatively inconsequential, as has been discussed in some detail. The quantitative results are more to the point, however, and here it is pointed out that the present predictions are achieved with a minimum of simplifying assumptions and without any use of empirical "calibration." Furthermore, wherever it has been possible to check various detailed implications of the theory against experiment, the two have proven to be in harmony: for example, the experimentally established presence of a core with recirculation near the inlet plane is to be expected theoretically, and the experimentally observed behavior of maximum refrigeration capacity as a function of pressure ratio is entirely consistent with theoretical expectations. Finally, the theory succeeds in bracketing the best experimental RHT data known to the writer,

which as an "upper bound" treatment it must do if it is to be of significance, and it does so by a margin which looks entirely proper: overall, the "upper bound" performance is a little less than twice that obtained experimentally. It is concluded that the present theory reflects the energy separation mechanism of the RHT with better fidelity than previous treatments, both on the basis of the success of the present analysis and in consideration of the shortcomings in previous analyses that made the present one necessary.

On this basis, it is also concluded that the limitations on RHT performance which have been recognized for at least two decades are indeed inherent. Additionally, presently achieved experimental performance is a large fraction of the ultimate potential of the device, since part of the favorable performance of the "upper bound" curves is traceable to analytical assumptions which could never be fully achieved. For example, noting the fact that exit losses are more important than internal losses, the latter are neglected altogether, whereas in fact there is an appreciable entropy rise associated with the internal flow process. Another feature of the analytical model is the assumption of uniform axial velocity at the terminal plane, whereas typical exit flow boundary conditions (axial extraction) cause the flow to depart very considerably from this state. Improved extraction techniques can, in the writer's expectation, improve the uniformity of the terminal-plane flow very considerably, but complete uniformity is not to be anticipated. Thus, the "upper bound" curves do not represent least upper bound performance, but rather are strictly generous to some extent. The writer's feeling is that the true limit on

achievable RHT performance probably lies about halfway between the best achieved to date and the "upper bound" curves.

Of course, the "upper bound" performance theory is a two-edged sword: it establishes definite limitations--and optimistic ones, at that--on the performance potential of the Ranque-Hilsch tube, but it also contains elements suggesting that considerable incremental gains over present performance are possible within these limits. For example, the uniflow configuration with improved output flow extraction techniques might well be capable of performance 25% to 50% better than that achieved heretofore with the standard counterflow configuration.

## 2. The Dynamic Pressure Exchanger "Divider"

A few brief observations concerning the DPE may be made on the basis of Appendix B. However, it must be remembered that the data base here is very narrow, consisting of experimental data only. The extent to which the fundamental capabilities and limitations of the DPE are fully reflected in the data is not known; however, it is presumed that the originators of the data would have pointed out major discrepancies between experiment and theory if such were recognized to exist. This is not done in the literature examined by the writer.

The peak cold-output adiabatic efficiency (equivalent to turbine efficiency) found experimentally is about 80%, a rather high value, and this tends to occur at a relatively high cold fraction. Therefore, at low pressure ratios at least, the performance of the DPE is very good. However, as may be seen in Figures A-5 and A-6, the reported experimental behavior of the DPE includes a strong adverse dependence of optimum cold

fraction (i.e., CF corresponding to maximum temperature drop) on pressure ratio: by a pressure ratio of 1.4, the optimum cold fraction according to Figure A-6 is already down to about 0.6. Clearly, this effect alone is potentially sufficient to degrade overall performance very substantially at somewhat elevated pressure ratios if the trend continues. The extent to which it does so must remain a matter for conjecture since the reported data are limited to low pressure ratios, but it shows little sign of abating within the range of available data.

### 3. The Foa Energy Separator

The basic equations needed for prediction of FES performance, termed "core performance" equations, have been developed for both the external-separation and internal-separation configurations. In both cases, the dependence of performance on driving pressure ratio and cold fraction (through the massflow ratio  $\mu = \frac{\dot{m}_b}{\dot{m}_a}$ ) is of course a basic ingredient, the geometric control variable for both being nozzle inclination for external separation and the ratio of nozzle areas for internal separation. The effects of nozzle efficiency, rotor torque, prerotation, and inequality of discharge pressures are also assessed for both designs; in the external separation case, the matter of unequal discharge pressures necessitated an analysis for the impingement-deflection region to enable assessment of the effect on  $\mu$ , and this introduces a strong dependence on the channel height factor,  $\frac{d_d}{\sigma_n}$ . The effect of diverting the deflected flows "a" and "b" into separate collection spaces in a cryptosteady manner is treated for the simple external-separation geometry wherein this is accomplished by offsetting the plane of flow from the plane of rotation by some small

angle. The equivalent of this in the internal-separation design is the nozzle inclination, and the effect of nozzle inclination is included. Additionally, the effects of unequal nozzle inclinations and nozzle efficiencies are considered for the internal-separation device.

The equations are developed in such a manner that the nonlinear interactions among variables are included, which renders them suitable for detailed design optimization studies. For present purposes, however, their application is illustrated by first considering "baseline" characteristics which display the basic behavior of the FES, and then assessing the performance modifications brought about by the other variables when introduced separately.

Baseline performance characteristics show that the FES is inherently a high-cold fraction device, and that maximum temperature drop is a large fraction of the limiting value set by thermodynamics. Prerotation can further substantially improve performance, though not indefinitely: for a given configuration and with other variables held constant, there is an optimum prerotation corresponding to minimum velocity (in  $F_U$ ) of the cold output flow.

Cold output performance of the FES is insensitive to small amounts of resisting torque, though larger torques have a detrimental effect. Therefore, moderate amounts of bearing friction can be incurred without significantly degrading performance. Of course, this comment does not also apply to the hot output, since whatever energy is removed from the cold flow as shaft output (frictional or otherwise) is not available to energize the hot flow. Therefore, if the hot output is of direct

use, such as in pressure boosting, rotor torque becomes a more significant matter.

The effect of nozzle efficiency, in the absence of other perturbing effects and with equal efficiencies in the case of internal-separation, could hardly be simpler: performance is linearly proportional to  $\eta$ . Furthermore, it is found that in the internal-separation case the maximum temperature drop obtainable is essentially dependent upon the "a" nozzle efficiency alone. The "b" nozzle can be less efficient (as it may indeed be, due to turning losses) without causing any decrease in obtainable performance; the only penalty paid in cold output performance is structural, in that a higher rotor speed is involved.

An application wherein "b" nozzle efficiency would be of more intrinsic concern is that of pressure boosting. Presumably, the "b" nozzle efficiency could be improved, to the extent that it may be degraded by turning losses, by reducing its inclination. It is found that a large reduction of  $\beta_b$  below  $\beta_a$  has the effect, when considered by itself, of shifting the point of maximum temperature drop to a lower cold fraction and causing substantial energy separation to be maintained well below the baseline lower operational limit of  $CF = 0.5$ . Since in an application utilizing the hot output an appreciable hot fraction is needed, the reduced cold fraction capabilities are entirely relevant.

Finally, it is interesting to observe the effect of unequal discharge pressures on performance, particularly since the effect is not the same for the two forms of the FES. A positive  $\delta p$  ( $p_b$  larger than  $p_a$ ) causes the external-separation rotor to slow down due to the increased average pressure at the nozzle exit, whereas it causes the internal-separation

rotor to speed up due to a decrease in the tangential momentum of the "b" flow. In both cases the cold fraction is increased. In the first case, this is accompanied by a slight decrease in the magnitude of the temperature drop, thanks to the rotor deceleration, but the effect on cold fraction is very much more pronounced; therefore, a given configuration operating at a cold fraction less than the optimum value has its performance improved overall by increased "b" flow back pressure. In the second case, the increased cold fraction is accompanied by an increase in the temperature drop if initial operation was at a cold fraction less than the optimum, so again the performance is improved. In either case, however, if the device is initially designed to operate at the theoretically optimum cold fraction, the effect of a positive  $\delta p$  will be detrimental, since it will cause the operating point to essentially start moving upward with increasing cold fraction toward the zero-drop condition which holds at  $CF = 1.0$ .

In addition to the core performance equations, consideration was given to two collection effects which appear particularly salient for the external-separation configuration. One such effect was the possibility of viscous reattachment of the deflected flows through mixing with the deadwater region, which could occur if the channel is long enough. It was found that this can produce a gain in performance, resulting from decreased final "a" flow velocity in the laboratory reference frame; this is brought about by increased rotor velocity and a decrease in the "a" flow velocity in the rotor-fixed reference frame. However, if the channel height is made too great, the effect is not beneficial but detrimental.

Second, an examination was made of the effects of flow non-



steadiness in the collection process, brought about by the use of turning vanes in  $F_U$  to separate flows "a" and "b". It was found that the non-steady effects so produced are very large, and that they are inherently detrimental to performance, reducing both the magnitude of the temperature drop and the cold fraction. The most basic problem is that a large fraction of the total "a" flow leaving the neighborhood of the nozzle during the time it sweeps from one turning vane to the next fails to escape out the "a" port, being trapped instead within the channel. During the next sweep by the nozzle, the nozzle flow interacts with this slug of "a" fluid in such a way that it is effectively chopped about in half, part of it progressing the rest of the way out the "a" port and the other portion being forced out the "b" port instead. This brings about a substantial reduction in cold fraction; furthermore, the half of the slug that succeeds in eventually exiting by the "a" port has been energized by wave action so that its total temperature is higher than that of the cryptosteady component of the "a" flow. An additional effect which acts to further reduce the cold fraction is a pumping effect, which transports fluid from the "a" side to the "b" side. This effect is a strong function of channel height: it may be of little importance if the channel height factor is close to unity, yet is theoretically capable of completely eliminating any net "a" flow in some cases if the channel height factor is in the neighborhood of 2.0.

Thus, it is anticipated theoretically that nonsteady collection will cause some degradation in temperature drop and, much more dramatically, in cold fraction. As a result, the output flow may be quite cold--though not as cold as with purely cryptosteady operation--even though the

hot output is not very hot. Furthermore, if the attempt is made to measure the hot output temperature with an ordinary probe placed in the exit port, substantial reading errors are to be expected due both to the fact that there is a period of inflow at the hot port and to the fact that the exit flow is highly nonuniform; and these errors are in the direction of underestimation of the true temperature. These considerations appear to explain the experimental observations made on a device of this type several years ago, wherein very cold air was indeed produced but the hot output temperature as measured with a probe in the "b" port was hardly different from ambient. This appeared to be in violation of energy conservation, since the cold fraction to be expected on a cryptosteady basis was large; but it is seen that due to nonsteady effects, the cold fraction must in reality have been small, and substantial measurement errors were doubtless also present.

## B. Some Comparative Observations

### 1. Foa Energy Separator and Ranque-Hilsch Tube

In comparing the merits of machines which are candidates for application to a given task, two considerations of great importance are those of performance and mechanical simplicity. The importance of performance is obvious, but if this is purchased at the expense of inordinate mechanical complexity in a given device, this can quite easily override performance considerations. Simplicity in a device is an important key to the achievement of important features such as low cost and reliability. In this respect, there would appear to be definite tradeoffs to be made between the RHT and FES.

First, with regard to performance, there can be no question that the FES is markedly superior to the RHT. To support this statement, a comparison will be made between the "upper bound" theoretical performance of the RHT and an internal-separation FES having nozzle inclinations of  $75^\circ$ , an "a" nozzle efficiency of 0.9, and no prerotation. Thus, in order to establish conclusively the performance superiority of the FES, the present comparison is made on the basis of a strict overestimate of RHT performance potential in conjunction with a version of the FES which lies well short of the theoretical maximum. Additionally, since the present paper has not treated FES performance perturbations which may arise at high pressure ratios, the comparison is confined to relatively low pressure ratios where RHT performance is at its best in terms of efficiency.

The comparison will be made in terms of Fulton's "turbine criterion" efficiency,<sup>14</sup> which amounts to the product of cold-output adiabatic efficiency and cold fraction. For the FES configuration considered, use of Figure 46 (interpolating easily since temperature drop is proportional to  $\eta$ ) gives a peak value for cold-output adiabatic efficiency of 0.67, occurring at CF = 0.90, so that the peak turbine-criterion efficiency is 0.60. Using the RHT "upper bound" performance curves of Figure 25, it is found that at a driving pressure ratio (DPR) of 1.5, the peak turbine-criterion efficiency is 0.39 (obtained at CF = 0.58) and that at DPR = 3.0 the peak efficiency is 0.33 (obtained at CF = 0.55). Thus, at DPR = 3.0 the theoretical peak performance of the conservatively selected FES is about twice the "upper bound" peak performance of the RHT. Noting the generosity of the "upper bound" RHT performance predictions and the expectation that proper design and development of the FES can produce performance bet-

ter than that assumed, the true disparity in obtainable performance of the two devices is probably given more nearly by a factor of anywhere from 3 to 5, depending upon the pressure ratio and perhaps other variables.

With respect to mechanical simplicity, however, the RHT has no peer: the FES has only one moving part, a rotor which itself is simple, but the RHT accomplishes energy separation with no moving parts. Better than this, one obviously cannot do. Therefore, in any application wherein power consumption and airflow rate (or more generally, gasflow rate) do not impose significant constraints as compared to the desirability of an ultimate in mechanical simplicity, the RHT largely retains the advantages it has always had. Wherever there is a premium on efficient performance, however, the slight increase in mechanical complexity that goes with the FES rapidly becomes acceptable. In this regard, it is suspected that major applications of the FES will prove to be in areas which simply cannot be served by the RHT in any case due to its inadequate efficiency.

## 2. Foa Energy Separator and Dynamic Pressure Exchanger

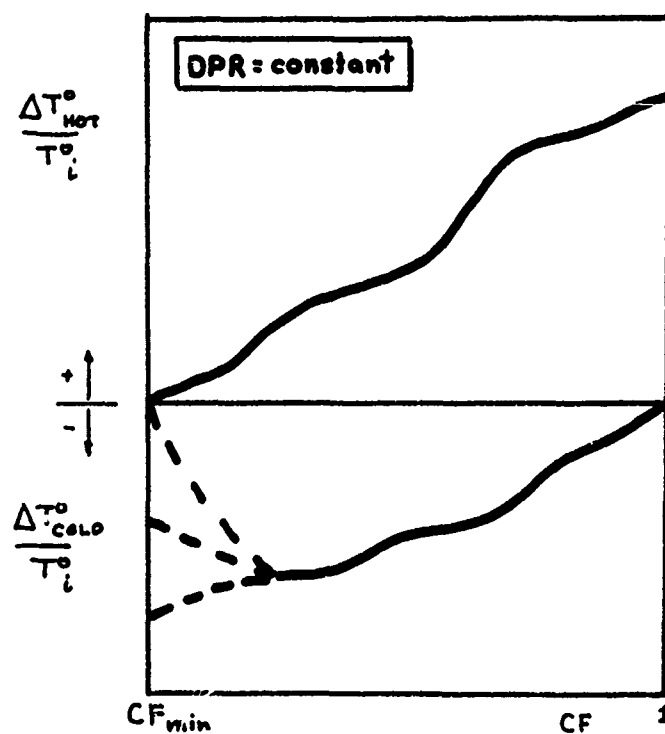
Any quantitative comparison here would be hazardous for several reasons. For one thing, the comparison would involve theory (FES) against experiment (DPE), which may inadvertently penalize either device relative to its true performance potential. Furthermore, the data base for the DPE is very narrow, both due to its restriction to very low pressure ratios and because the data does not extend to a high enough cold fraction to accurately locate the maximum "turbine criterion" efficiency point (Figure A-5). The most that can be said, therefore, is that at a pressure ratio in the neighborhood of 1.5, the DPE and the FES configuration selected above would appear to be comparable. The strong trend of optimum cold

fraction decreasing with pressure ratio in the case of the DPE (Figures A-5, A-6) suggests that with increasing pressure ratio, peak DPE performance would probably tend to drop below that of the FES, so that the DPE is most interesting at low pressure ratios such as the range for which data is presented. It is worth noting in this regard that the DPE is stated in the DPE literature<sup>13</sup> to give best performance at low pressure ratios, staging being possible if larger overall pressure ratios are needed; the basis for this statement is, however, the adverse effect of increasing pressure on the product efficiency (product of turbine and compressor efficiency) which expresses the efficiency of pressure exchange.

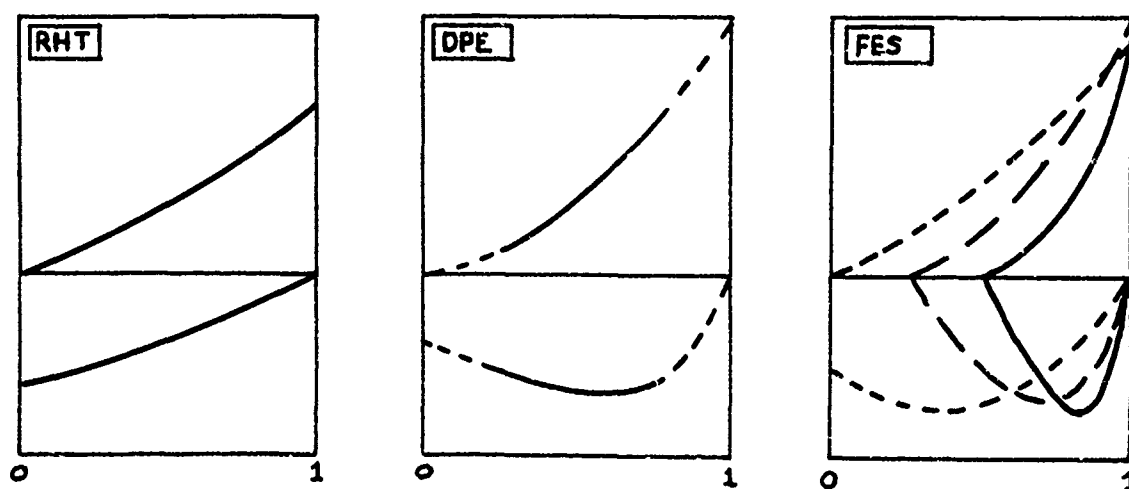
Thus, from a performance standpoint, the DPE does not possess any clear advantage over the FES, and indeed the opposite would appear to be the case. Therefore, it is particularly significant to note that the DPE is also much more complex than the FES, both mechanically and analytically. As a result, while realms of application may exist that favor use of the DPE rather than the FES, it is not at all clear what these applications would be.

### 3. The Generalized Energy Separation Performance Plot and Its Special Cases

Figure 72 summarizes the qualitative behavior of energy separation devices, part (a) presenting a generic plot while part (b) illustrates each of the three special cases. As seen in Figure 72(a), the hot-output temperature rise is zero at some minimum CF which signals the lower operational boundary of the device, and rises with increasing CF to some finite nonzero value at  $CF = 1$ . The cold-output temperature drop is zero at  $CF = 1$ , but increases as CF is reduced until a maximum occurs for some value of CF;



(a) Generalized Case



(b) Special Cases

Figure 72  
General and Special Energy Separation Plots

further reductions in CF result in a decrease in the temperature drop. At  $CF = 0$ , the temperature drop may or may not be nonzero; if the hot-output curve emanates from the  $CF = 0$  origin with a nonzero slope, then nonzero temperature drop occurs here. If  $CF_{min}$  is greater than zero, however, the temperature drop at  $CF_{min}$  is necessarily zero by virtue of the energy balance between the hot and cold outputs.

In Figure 72(b), the first sketch is for envelope performance (theoretical or experimental) of the RHT.  $CF_{min} = 0$  in this case, and here the temperature drop is not only nonzero but a maximum for a given pressure ratio. Temperature drop decreases steadily in magnitude as CF is increased. The second sketch is for the DPE; the solid curves refer to the range within which actual data has been examined, while the broken line extensions are based on presumed behavior. It is seen that in this case, the value of CF for which maximum temperature drop is obtained is large, tending toward unity as the pressure ratio tends to 1.0; a nonzero temperature drop at  $CF = 0$  appears likely. The third sketch pertains to the FES, whose basic performance characteristics are best represented by the solid "baseline" curve:  $CF_{min}$  in this case is greater than zero (equal to 0.5), and the maximum temperature drop occurs at a very large cold fraction. As a result, the hot-output temperature curves are very strongly concave upward and steep overall. A striking practical difference between the FES and the other two energy separation devices is indicated qualitatively by means of the broken lines: due to the availability of a number of control variables, the basic operating characteristics of the FES may actually be shifted around dramatically. Indeed, while there are unquestionably practical limitations on this, there is no region of the cold-

output portion of the performance plot that cannot, in principle, be reached with an appropriate FES design. The implication of this is that in terms of flexibility and applicability to widely varying tasks, the FES is unsurpassed.



## PART V

### LITERATURE CITED

1. Milton, R. M., "Maxwellian Demon at Work," Industrial and Engineering Chemistry, Industrial Edition, Vol. 38, No. 5, 1946, p. 5.
2. Ranque, G. J., "Experiences Sur la Detente Giratoire Avec Productions Simultanees d'un Echappement d'Air Chaud et d'un Echappement d'Air Froid," Journal de Physique et de Radium, 1933, p. 112.
3. Hilsch, R., "The Use of the Expansion of Gases in a Centrifugal Field as Cooling Process," Review of Scientific Instruments, Vol. 18, No. 2, February 1947, pp. 108-113.
4. Azoury, P. H., "An Introduction to the Dynamic Pressure Exchanger," Proceedings of the Institution of Mechanical Engineers, Vol. 180, Part 1, No. 18, 1965-66, pp. 451-473.
5. Spalding, D. B., British Patent No. 799 143, 1958.
6. Jendrassik, G., German Patent No. 1 030 506, 1958.
7. Foa, J. V., "Energy Separator," Rensselaer Polytechnic Institute Tech. Rept. TR AE 6401, January 1964.
8. Foa, J. V., "A New Method of Energy Exchange and Some of Its Applications," Rensselaer Polytechnic Institute Tech. Rept. TR AE 5509, December 1955.
9. Dean, R. C., Jr., "On the Necessity of Unsteady Flow in Fluid Machines," Transactions of the ASME, Vol. 81, Series D, March 1959, pp. 24-28.
10. Foa, J. V., "Method of Energy Separation and Apparatus for Carrying Out the Same," U.S. Patent No. 3,361,336, January 2, 1968.
11. Hashem, J. S., "A Comparative Study of Steady and Nonsteady-Flow Energy Separators," Rensselaer Polytechnic Institute Tech. Rept. TR AE 6504, October 1965.
12. Kentfield, J. A. C., "An Examination of the Performance of Pressure-Exchanger Equalisers and Dividers," Ph.D. thesis, University of London, 1963.
13. Kentfield, J. A. C., "The Performance of Pressure-Exchanger Dividers and Equalizers," ASME Paper No. 68-WA/FE-24, December 1968.
14. Fulton, C. D., "Ranque's Tube," Journal of the ASRE, Refrigerating Engineering, Vol. 58, May 1950, pp. 473-479.

15. Ranque, G. J., "Method and Apparatus for Obtaining From Fluid Under Pressure Two Currents of Fluids at Different Temperatures," U.S. Patent No. 1,952,281, March 1934.

16. Westley, R., "A Bibliography and Survey of the Vortex Tube," College of Aeronautics, Cranfield, England, 1954.

17. Lay, J. E., "An Experimental and Analytical Study of Vortex-Flow Temperature Separation by Superposition of Spiral and Axial Flows. Parts 1 and 2," Transactions of the ASME, Vol. 81, Series C, August 1959, pp. 202-211 (Part 1) and pp. 213-221 (Part 2).

18. Kassner, R., and Knoernschild, E., "Friction Laws and Energy Transfer in Circular Flow," Tech. Rept. No. F-TR-2198-ND, GS-USAF Wright-Patterson Air Force Base No. 78, March 1948. Part 1: "The Laws of Shear Stresses in Circular Flow," by R. Kassner. Part 2: "Energy Transfer in Circular Flow and Possible Applications (Explanation of the Hilsch or Ranque Effect)," by E. Knoernschild.

19. Scheper, G. W., Jr., "The Vortex Tube--Internal Flow Data and a Heat Transfer Theory," Journal of the ASRE, Refrigerating Engineering, Vol. 59, October 1951, pp. 985-989, 1018.

20. Fulton, C. D., "Comments on the Vortex Tube," Journal of the ASRE, Refrigerating Engineering, Vol. 59, October 1951, p. 984.

21. Deissler, R. G., and Perlmutter, M., "Analysis of the Flow and Energy Separation in a Turbulent Vortex," International Journal of Heat and Mass Transfer, Vol. 1, 1960, pp. 173-191.

22. Dornbrand, H., "Theoretical and Experimental Study of Vortex Tubes," Air Force Tech. Rept. No. 6123 (Republic Aviation Corp.), 1950.

23. Van Deemter, J. J., "On the Theory of the Ranque-Hilsch Cooling Effect," Applied Scientific Research A, Vol. 3, 1952, pp. 174-196.

24. Pengelley, C. D., "Flow in a Viscous Vortex," Journal of Applied Physics, Vol. 28, 1957, pp. 86-92.

25. Sibulkin, M., "Unsteady, Viscous, Circular Flow, Part 3. Application to the Ranque-Hilsch Vortex Tube," Journal of Fluid Mechanics, Vol. 12, 1962, pp. 269-293.

26. Vennos, S. L. N., "An Experimental Investigation of the Gaseous Vortex," D. Eng. Sci. thesis, Rensselaer Polytechnic Institute, April 1968.

27. Blatt, T. A., and Trusch, R. B., "An Experimental Investigation of an Improved Vortex Cooling Device," ASME Paper No. 62-WA-200, November 1962.

28. Linderstrom-Lang, C. U., "The Three-Dimensional Distributions of Tangential Velocity and Total-Temperature in Vortex Tubes," Journal of Fluid Mechanics, Vol. 45, Part 1, 1971, pp. 161-187.

29. Lewellen, W. S., "A Review of Confined Vortex Flows," NASA Contractor Report CR-1772 (Massachusetts Institute of Technology), July 1971.

30. Savino, J. M., and Ragsdale, R. G., "Some Temperature and Pressure Measurements in Confined Vortex Fields," Transactions of the ASME, Vol. 83, Series C, February 1961, pp. 33-36.

31. Foa, J. V., Elements of Flight Propulsion, Wiley, New York, 1960.

32. Shapiro, A. H., The Dynamics and Thermodynamics of Compressible Fluid Flow: Vol. I, Ronald Press, New York, 1953.

33. Westley, R., "Vortex Tube Performance Data Sheets," College of Aeronautics Note No. 67, Cranfield, England.

34. Brochure of Vortec Corporation, Cincinnati, Ohio, Copyright 1971. Quoted by permission.

35. Armagnac, A. P., "Hot and Cold Running Air," Popular Science, July 1969, pp. 60-61.

36. Taylor, G. I., "Oblique Impact of a Jet on a Plane Surface," Proceedings of the Royal Society A, Vol. 254, 1960, pp. 96-100.

37. Foa, J. V., unpublished notes; personal communication.

38. Rudinger, G., Nonsteady Duct Flow: Wave-Diagram Analysis, Dover, New York, 1969.

APPENDIX A  
OBSERVATIONS ON THE DPE DIVIDER

Introductory Comments

As explained in the INTRODUCTION, the principal focus of this study is the Foa energy separator (FES), but the attempt has also been made to place it in proper context within the field of energy separation as a whole, and in so doing to present a more unified view of this field than would seem to have appeared previously. There is an entire body of literature on the Ranque-Hilsch tube (RHT), and another--evidently much smaller--body which deals with the dynamic pressure exchanger "divider" (DPE), but never the twain do meet. Even the format for presentation of performance data that is standard in the DPE literature is totally different from that used for the RHT. Adding to this situation the fact that very little has been published at all on the FES, one can readily see that it is desirable to pull some loose ends together.

The purpose here is to carry out a translation of some representative DPE energy separation data into the desired format, and to make a few observations on that basis. The data used below to this end have been extracted from Azoury;<sup>4</sup> additional data were not felt to be necessary for this limited objective, but it is also worth noting that the open literature seems to contain little such data. For example, Kentfield, whom Azoury credits as the source of the experimental data he presents, himself discusses pressure-boosting performance in a paper published in 1968<sup>13</sup> but includes nothing on energy separation. It is interesting to note in passing that both of these papers discuss the divider as one possible

configuration in which the DPE can be used, other uses being discussed also (e.g., Azoury discusses its use as an "equalizer," as a gas generator, as a thrust generator, and as a thrust augmentor); thus, the context in which the divider is presented might be characterized as "the set of possible distinct uses of the DPE" rather than as "the set of possible distinct techniques for achieving energy separation," the latter more nearly describing the present context.

#### Transformation of DPE Performance Data into "Standard" Format

Energy separation characteristics are normally presented as a function of cold fraction CF at constant values of driving pressure ratio DPR (compare Figure 4) and this format has also been used for the FES. It is therefore desired to transform the DPE data into this "standard" format.

Performance characteristics of the DPE divider are normally presented in a very different fashion, utilizing the plane depicted in Figure A-1. The ordinate and abscissa are, respectively, the ratios of hot-output total pressure  $p_H^o$  and cold-output total pressure  $p_C^o$  to the input total pressure  $p_i^o$ . The slant lines are for constant values of the "overall" pressure ratio,  $p_H^o / p_C^o$ .

Figures A-2 and A-3 present experimental divider performance. Figure A-2 pertains to pressure-boosting performance, the performance criterion being the combined efficiency  $\eta_p$  (equivalent to the product of a compressor and turbine efficiency); Figure A-3 presents cooling performance, and is therefore the one relevant to the present discussion. The lines of constant overall pressure ratio shown in Figure A-1 have

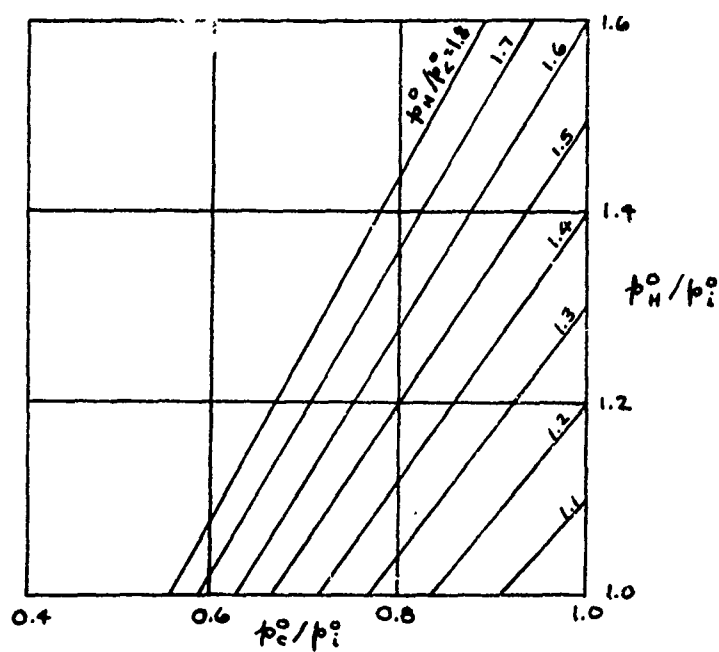


Figure A-1

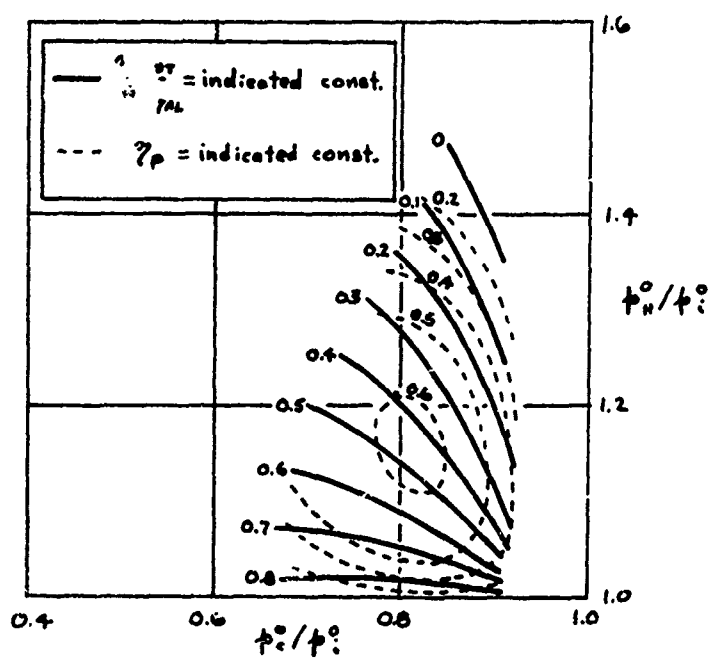


Figure A-2

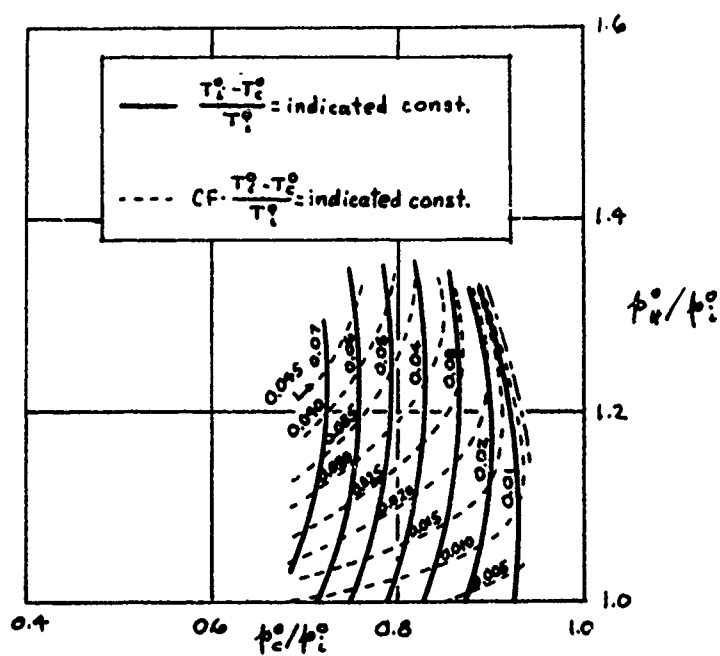


Figure A-3

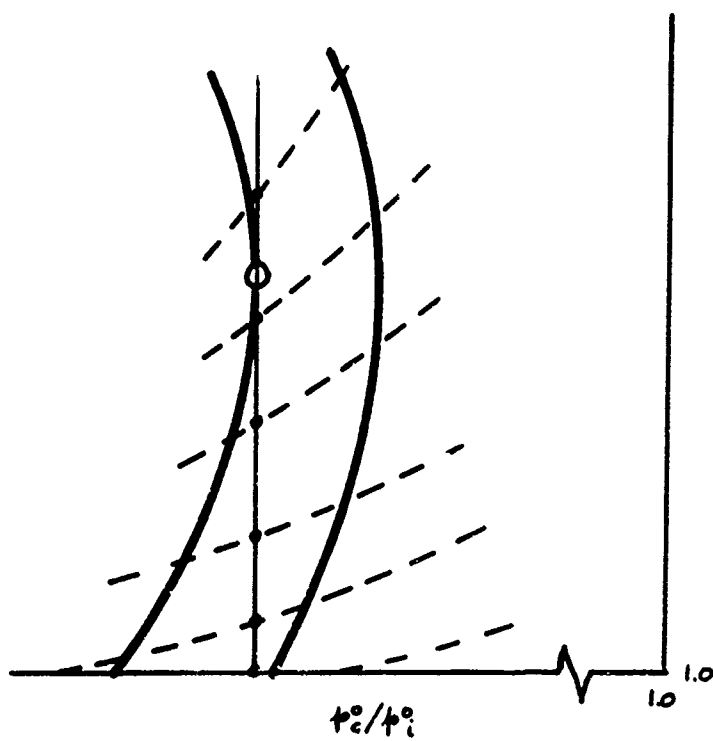


Figure A-4

been deleted, since they are not needed for purposes of the present discussion and the clarity of the plot is improved; lines of constant entering Mach number contained in the original pressure-boost map of Azoury have also been deleted for the same reason.

Figure A-4 illustrates the manner in which DPE cooling performance data has been extracted from the cooling performance map for transformation into the standard format of Figure A-5. An expanded qualitative picture is shown for a portion of the cooling performance map of Figure A-3, which has two families of curves: cold output temperature curves (solid) and refrigeration curves (broken). The point of maximum  $p_c^0/p_i^0$  on each temperature curve is located as nearly as possible, and a line of constant  $p_c^0/p_i^0$  drawn tangent to it. Readings are then taken at each point where this vertical line intersects a refrigeration curve: the value of  $CF \cdot \frac{T_i^0 - T_c^0}{T_i^0}$  is read directly from the refrigeration curve, while the value of  $\frac{T_i^0 - T_c^0}{T_i^0}$  is interpolated between the two adjacent temperature curves. Where the vertical line strikes the  $p_w^0/p_i^0 = 1.0$  axis, which will be referred to later as the "cutoff" point, both  $\frac{T_i^0 - T_c^0}{T_i^0}$  and  $CF \cdot \frac{T_i^0 - T_c^0}{T_i^0}$  are necessarily interpolated.

#### Transformed DPE Energy Separation Performance Plots

Figures A-5 and A-6 have been generated with data thus extracted from the map of experimental DPE cooling performance. Figure A-5 basically presents the lower half of a standard (a la Hilsch, Figure 4) plot of DPE performance; data for what would be the upper half is not present in the original performance map, but could of course be readily generated by assuming an adiabatic system (presumably a reasonable approximation) and



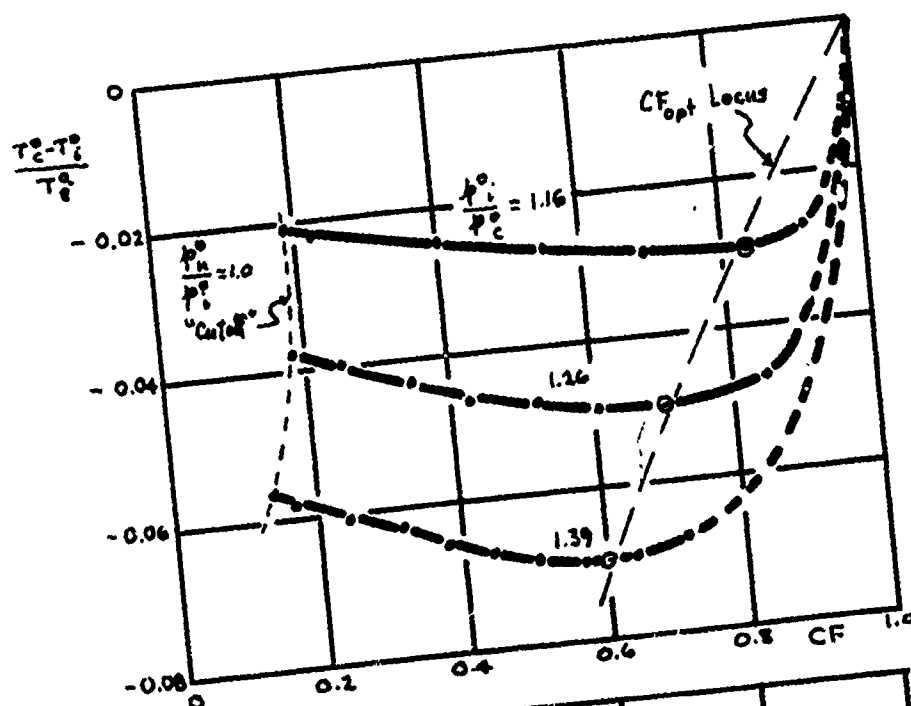


Figure A-5

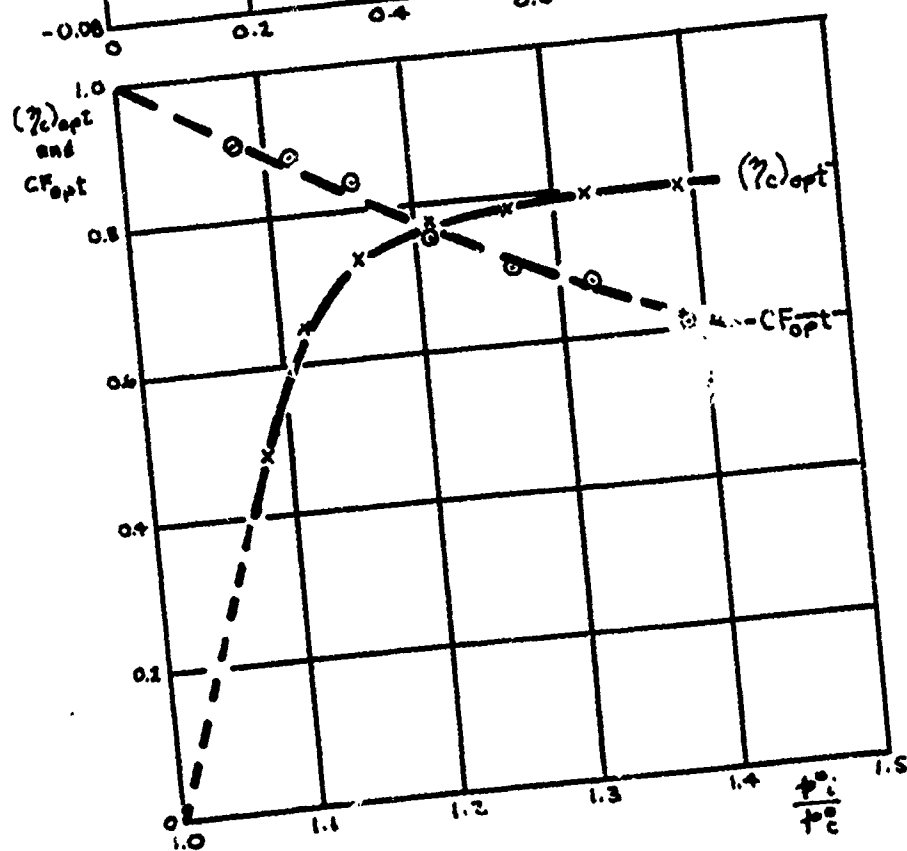


Figure A-6

using conservation of total energy from input to outputs. Figure A-6 pertains to conditions at the minimum of each constant-  $p_i^o/p_e^o$  plot; the locus of these minima is indicated in Figure A-5. In each Figure, the raw readings as extracted from the original map are indicated as well as the fairings, to help the reader gauge the reliability of the fairings.

Referring to Figure A-5, it will be noted that the complete cold fraction range  $0 \leq CF \leq 1$  is not covered for a given value of  $p_i^o/p_e^o$ . It can be seen in Figure A-3 that as  $CF \rightarrow 1$ , the range over which data was obtained is exceeded ( $p_n^o/p_i^o$  increasing), whereas as  $CF \rightarrow 0$ , the "cutoff" point ( $p_n^o/p_i^o = 1.0$ ) is reached before  $CF = 0$ . For the  $CF \rightarrow 1$  condition, it is clear that the fairing must be qualitatively as shown, with temperature drop vanishing at  $CF = 1$ , since otherwise the temperature of the fluid trapped within the DPE would tend to infinity. The fairings may be in considerable quantitative error, though, since no data is available in that region. As for the "cutoff" condition, this would appear to reflect the influence of viscous effects and the like, since it is easily shown that for equal inlet and hot-port opening times (a condition which is approximately satisfied in the configuration on which the subject data was obtained) the cold fraction should go to zero at  $p_n^o/p_i^o = 1.0$ . Indeed, it is inferred that this is the reason for selecting  $p_n^o/p_i^o = 1.0$  as the lower limit for the performance-map plane, Figure 1. It is presumed, both on physical grounds and by observing the behavior of Figure A-5, that nonzero temperature drop most probably occurs at  $CF = 0$ ; however, the "cutoff" line is simply indicated, rather than extrapolating the curves.

In Figure A-6, the cold fraction  $CF_{opt}$  at the minimum of the constant-  $p_i^o/p_c^o$  curve of Figure A-5 is presented as a function of  $p_i^o/p_c^o$ , as is the value of the maximum cold-side adiabatic efficiency  $(\eta_c)_{max}$  which occurs at the same point. For each temperature curve, Figure A-3, the rightmost point of the curve was selected by eye as in Figure A-4 and the value for CF calculated; points thus obtained are plotted in both Figures A-5 and A-6 as clear circles. The fairing of these points shown in Figure A-6 is taken as the actual estimate of  $CF_{opt}$ ; note that the " $CF_{opt}$  locus" fairing in Figure A-5 has been made to correspond to the fairing in Figure A-6. The value for  $(\eta_c)_{max}$  was calculated with the actual temperature drop noted on the temperature curve and the ideal temperature drop based on the value of  $p_i^o/p_c^o$  pertaining to the tangent vertical line depicted in Figure A-4.

### Discussion

Looking at Figure A-5, one notes that at least at low pressure ratios--the only regime where data is presented--the maximum temperature drop occurs at a large value of CF. This is in marked contrast to the RHT, which achieves its maximum temperature drop at a low cold fraction (of the order of 0.3 for a typical counterflow device). It is qualitatively similar in this respect to the FES, which produces maximum temperature drop at large cold fractions.

Figure A-6 shows furthermore that, except at very low pressure ratios, the cold-side efficiency is relatively high: above about  $p_i^o/p_c^o = 1.2$ , the efficiency at the point of maximum temperature drop (hence maximum adiabatic efficiency) is about 80%. If this persists to

Higher pressure ratios, the DPE is superior here too to the RHT; however, it is important to note in this regard the low pressure ratios at which all the CPE data were taken. The maximum driving pressure ratio  $p_1/p_2$  pertaining to any point plotted in Figure A-3 is about 1.5, which may be compared with pressure ratios of 1.5, 3, 6, and 10 in the Hilsch RHT data. Calculating cold-side efficiency for the Hilsch data at the maximum-temperature-drop points, one finds behavior which is qualitatively the inverse of that plotted for the DPE in Figure A-6: RHT efficiency initially drops off with increasing DPR, but tends to flatten out at around 40% by a pressure ratio of about 3.0. At a pressure ratio of 1.5, the peak cold-side adiabatic efficiency from the Hilsch data is also about 80%--i.e., about the same as what one would get for the DPE by projecting the curve of Figure A-6 to  $DPR = 1.5$ . This near identity is a coincidence, but points out that it is operation at higher pressure ratios that is of primary importance in distinguishing between the two devices as far as adiabatic efficiency--hence, maximum temperature drop at a given pressure ratio--is concerned.

One important question about the DPE arises from the behavior of  $CF_{opt}$  as a function of DPR. It will be noted from either Figure A-5 or A-6 that the experimental data displays a very strong, adverse effect of DPR on  $CF_{opt}$  which, if it is an inherent feature of the DPE energy separation mechanism (rather than occasioned by experimental factors capable of correction), would severely degrade the overall refrigeration performance of the DPE at higher pressure ratios. It is not known to the writer whether this effect has been explained theoretically, although it may be noted that both Azoury<sup>4</sup> and Kentfield<sup>13</sup> specifically refer to

the DPE as having acceptable performance at low pressure ratios and mention that cascading units may be employed to achieve higher pressure ratios overall.

APPENDIX B  
NONSTEADY COLLECTION WAVE DIAGRAMS

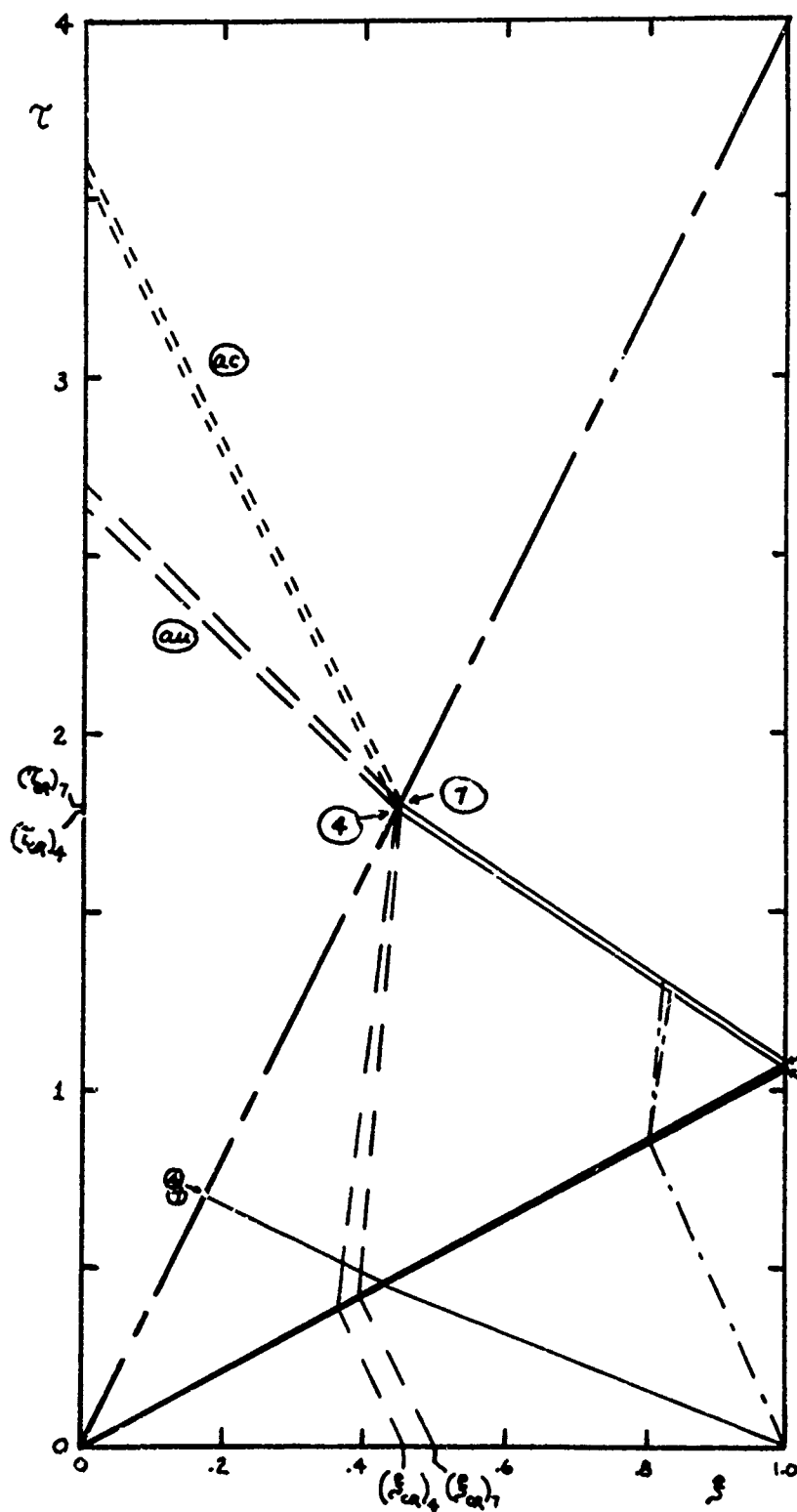


Figure B-1  
 Cases 4, 7  
 $\beta = 30^\circ$   
 $M_0 = 0.50$   
 $d_0/d_n = 1.5, 2.0$

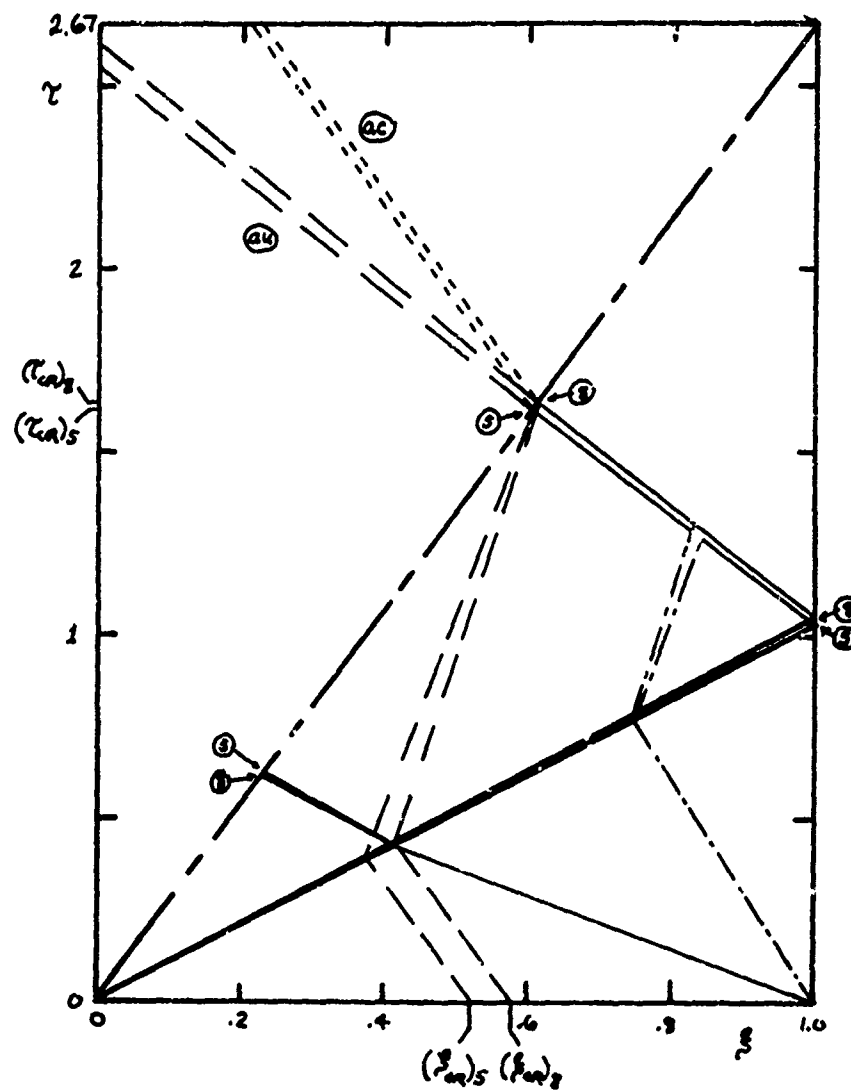


Figure B-2  
 Cases 5, 8  
 $\theta = 30^\circ$   
 $M_\infty = 0.75$   
 $\alpha_d/\alpha_n = 1.5, 2.0$



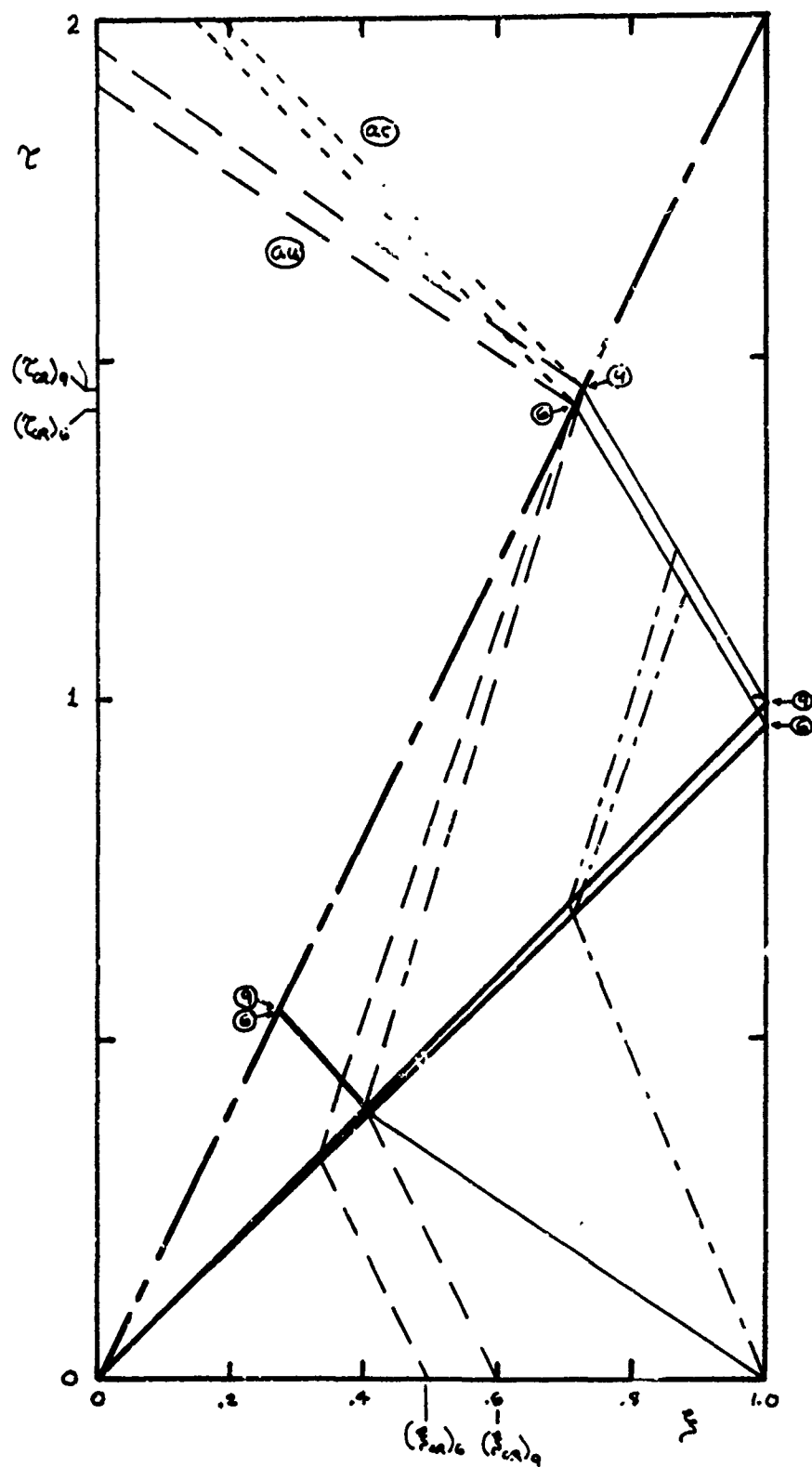


Figure B-3  
Cases 6, 9

$\theta = 30^\circ$

$M_\infty = 1.0$

$\alpha_\infty M_\infty = 1.5, 2.0$

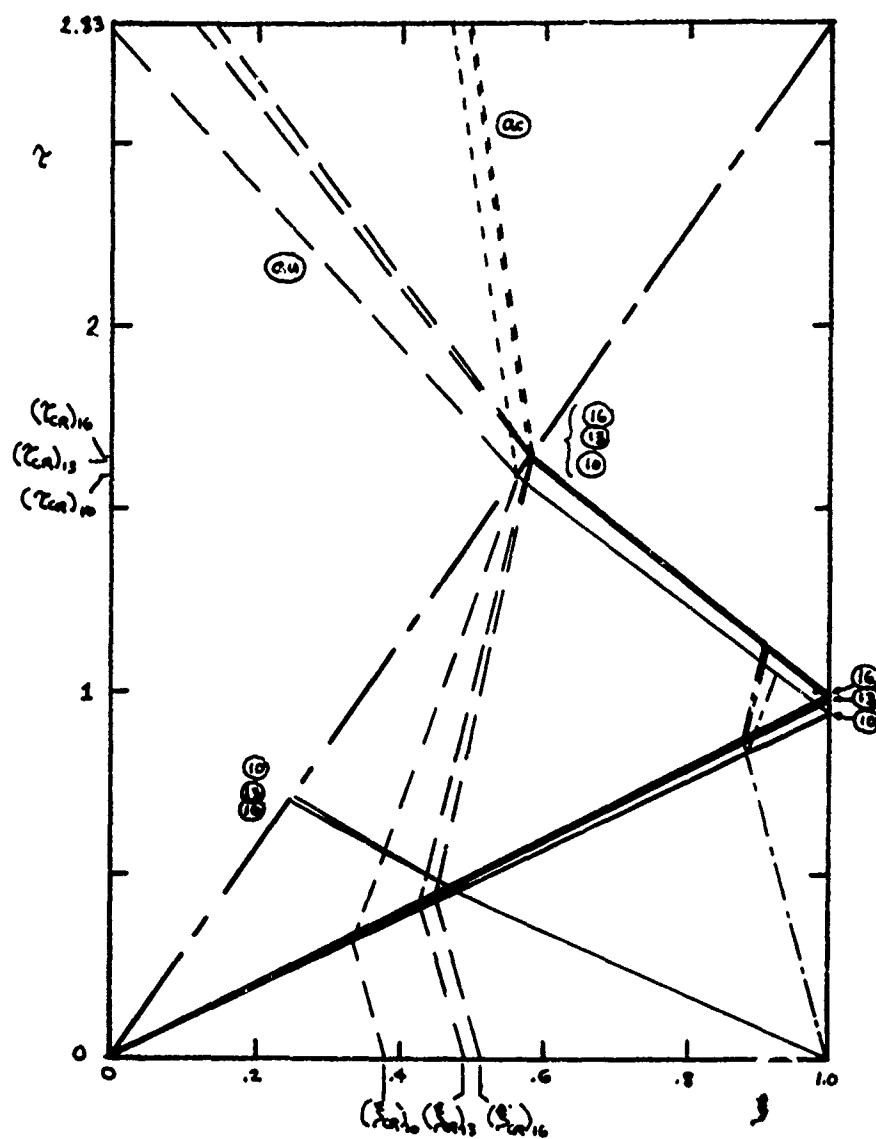


Figure B-4  
 Cases 10, 13, 16  
 $\phi = 45^\circ$   
 $M_\infty = 0.50$   
 $\alpha_d/a_n = 1.0, 1.5, 2.0$

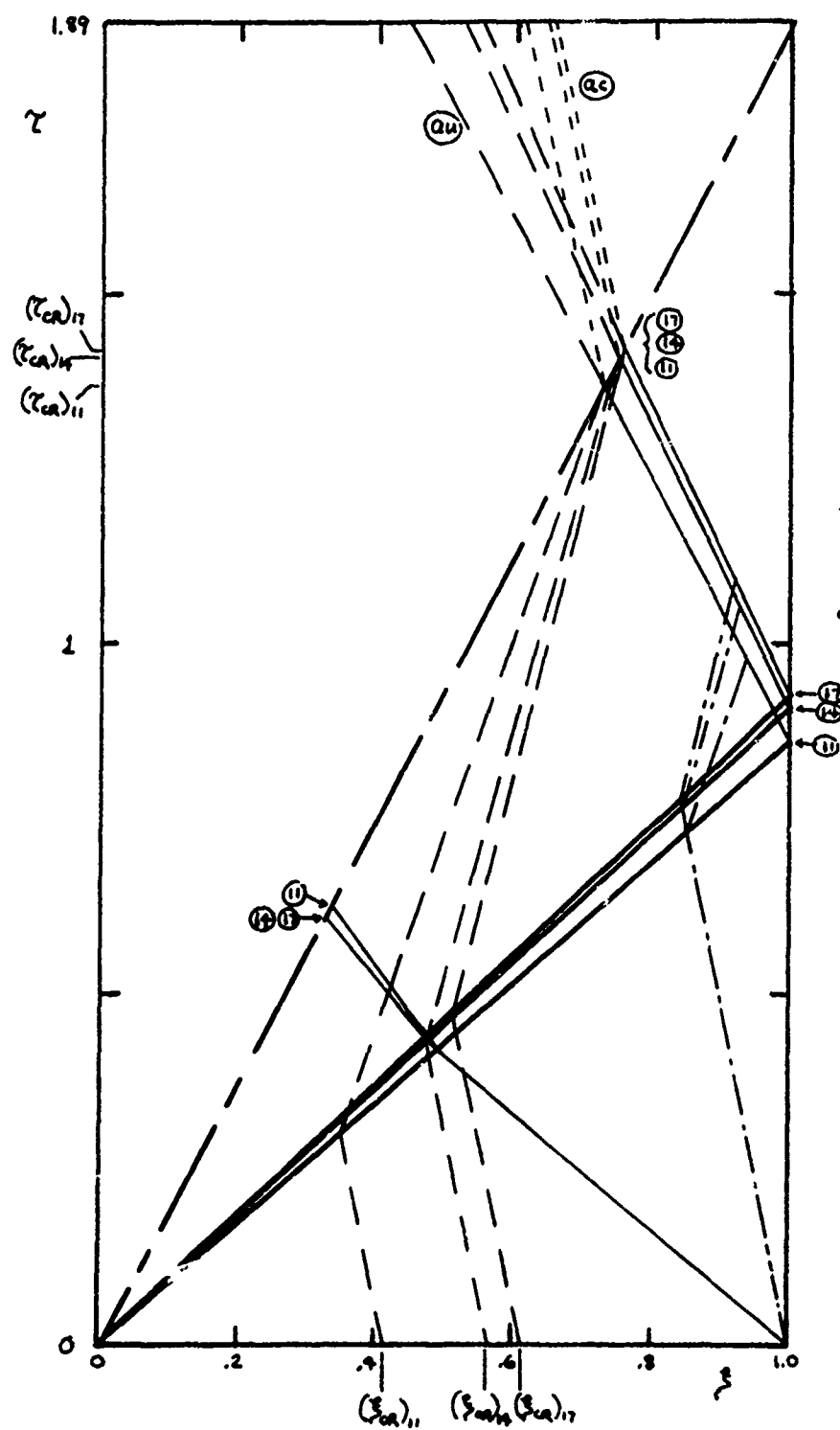


Figure B-5  
 Cases 11, 14, 17  
 $\theta = 45^\circ$   
 $M_0 = 0.75$   
 $\sigma_0 M_n = 1.0, 1.5, 2.0$

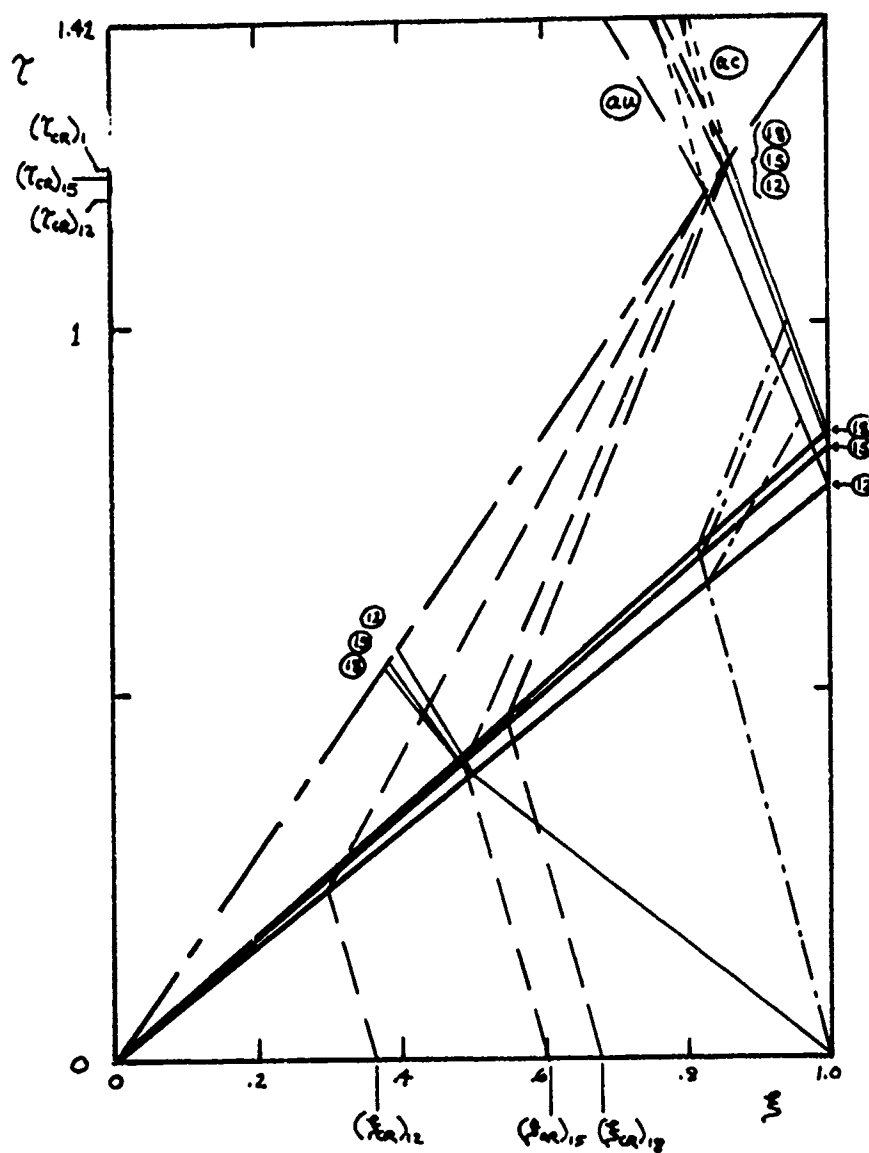


Figure B-6  
 Cases 12, 15, 18  
 $\phi = 45^\circ$   
 $M_0 = 1.00$   
 $\alpha_d/\alpha_n = 1.0, 1.5, 2.0$



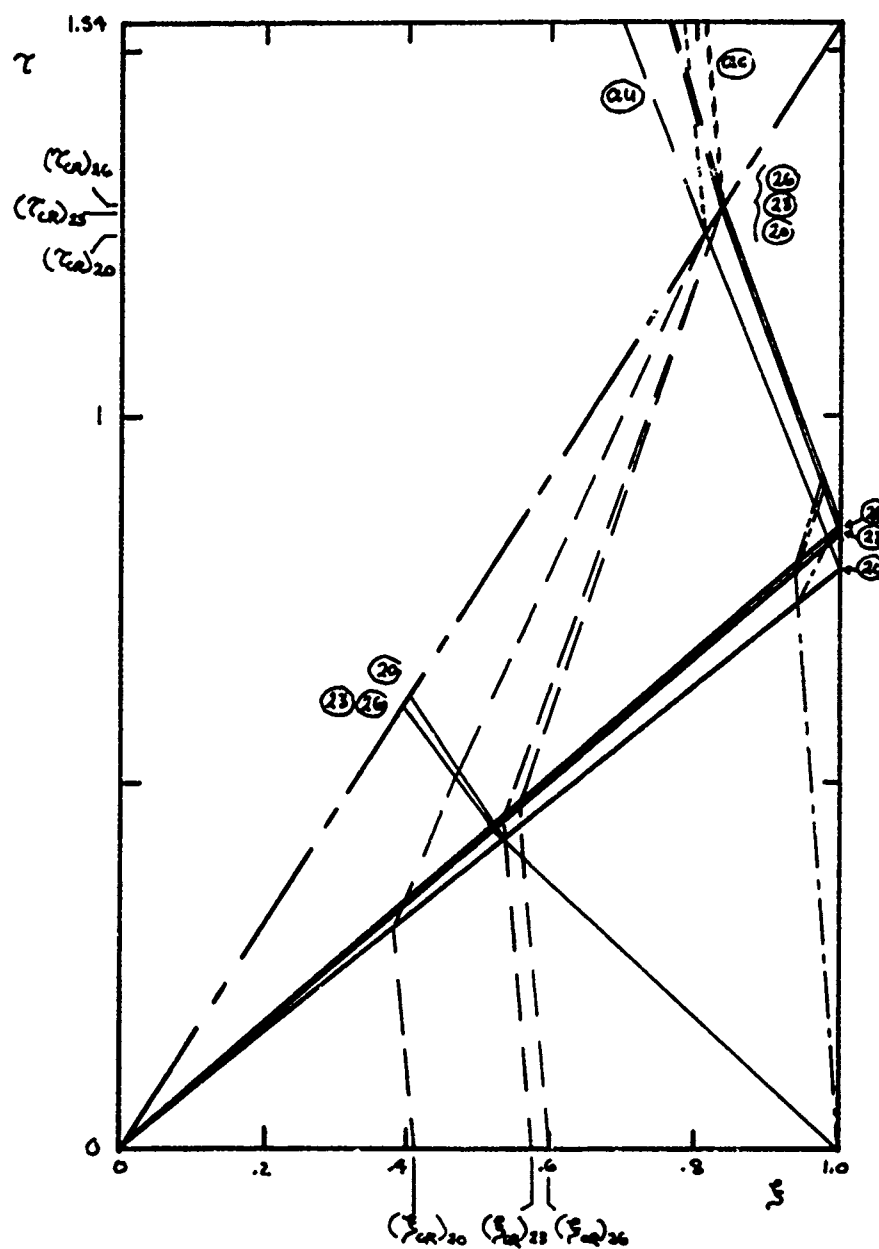


Figure B-8  
 Cases 20, 23, 26  
 $\beta = 60^\circ$   
 $M_0 = 0.75$   
 $\alpha_4/\alpha_n = 1.0, 1.5, 2.0$

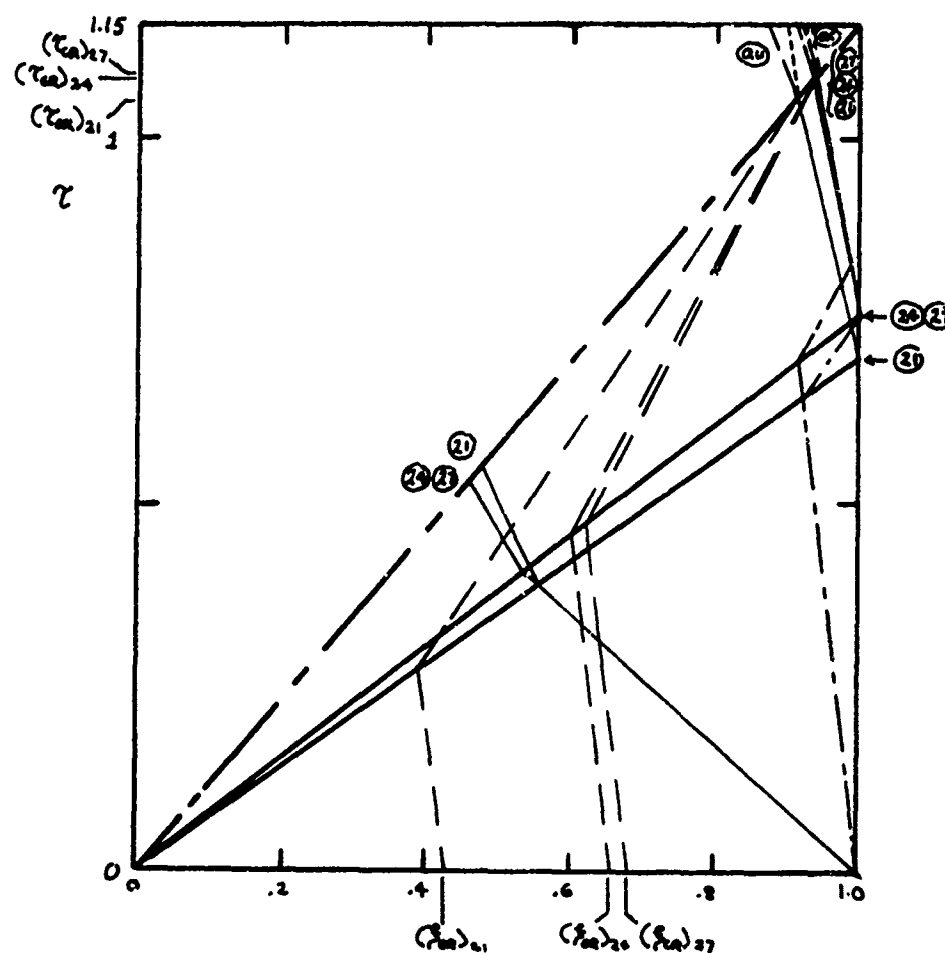


Figure B-9  
 Cases 21, 24, 27  
 $\beta = 60^\circ$   
 $M_\infty = 1.00$   
 $\alpha_{LH} = 1.0, 1.5, 2.0$

## APPENDIX C

### NOMENCLATURE

Major symbols are defined below; additional notation utilized for particular analyses are defined in the text.

#### Symbols

##### General

CF	Cold fraction (ratio of cold output to total flow rate)
DPR	Driving pressure ratio (see page 114 for RHT, page 141 for FES, page A-9 for DPE)
HF	Hot fraction (ratio of hot output to total flow rate)
$h$	Enthalpy per unit mass
M	Mach number
$p$	Pressure
$r$	Radius
R	Gas constant
T	Temperature
$\Delta T^o$	Stagnation temperature increment relative to the input value, ( $T^o - T_i^o$ )
$u, v$	Velocity
$\alpha$	Flow area
$\gamma$	Ratio of specific heats
$\mu$	Massflow ratio (ratio of hot output to cold output flow rate)



Ranque-Hilsch Tube

$\dot{X}^o$	Total stagnation-enthalpy flow through tube or specified portion thereof
$\dot{L}$	Total angular momentum flow through tube or specified portion thereof
$\dot{m}$	Total mass flow through tube or specified portion thereof
$\bar{r}$	Normalized radius, $r/r_t$
$\Phi$	Total axial stream force over tube area or portion thereof

Foa Energy Separator

$c$	Flow velocity measured in $F_S$
$F_S$	Reference frame wherein flow is seen as steady
$F_U$	Reference frame of flow usage, wherein flow is nonsteady
$K_{OPR}$	Pressure ratio scale factor (see page 146)
$K_{Sp}$	Differential pressure factor (see page 146)
$K_{\mu}$	Baseline differential-pressure sensitivity (see page 171)
$L$	Resisting torque
$NPR$	Nozzle pressure ratio (see page 142)
$\delta p$	Discharge pressure differential, $p_b - p_a$
$u$	Flow velocity measured in $F_U$
$u_i$	Prerotation velocity
$u_{oa}$	Reference discharge velocity (see page 141)
$V$	Tangential rotor speed, measured at effective nozzle discharge radius
$\frac{\alpha_d}{\alpha_n}$	Channel height factor
$\beta$	Nozzle inclination (see Figures 29, 42)

- $\epsilon$  Offset angle (see Figure 29)
- $\lambda$  Torque parameter (see pages 141, 182)
- $\eta$  Nozzle efficiency (see page 141)

### Subscripts

#### Ranque-Hilsch Tube

- C Cold output flow
- H Hot output flow
- i Input flow
- t Tube wall at station II
- I Flow injection plane
- II "Terminal vortex" plane in tube

#### Foa Energy Separator

- a De-energized output flow (moves counter to rotor velocity)
- b Energized output flow (moves in direction of rotor velocity)
- d Deflection channel
- i Input flow
- n Nozzle exit
- \* Source boundary (see Figure 74)

### Superscripts

- o Stagnation conditions as measured in  $F_U$
- Stagnation conditions as measured in  $F_S$
- (s) Measured in  $F_S$
- (u) Measured in  $F_U$

# THE GEORGE WASHINGTON UNIVERSITY

BENEATH THIS PLAQUE  
IS BURIED  
A VAULT FOR THE FUTURE  
IN THE YEAR 2036

THE STORY OF ENGINEERING IN THIS YEAR OF THE PLACING OF THE VAULT AND  
ENGINEERING HOPES FOR THE TOMORROWS AS WRITTEN IN THE RECORDS OF THE  
FOLLOWING GOVERNMENTAL AND PROFESSIONAL ENGINEERING ORGANIZATIONS AND  
THOSE OF THIS GEORGE WASHINGTON UNIVERSITY

BOARD OF COMMISSIONERS DISTRICT OF COLUMBIA  
UNITED STATES ATOMIC ENERGY COMMISSION  
DEPARTMENT OF THE ARMY UNITED STATES OF AMERICA  
DEPARTMENT OF THE NAVY UNITED STATES OF AMERICA  
DEPARTMENT OF THE AIR FORCE UNITED STATES OF AMERICA  
NATIONAL ADVISORY COMMITTEE FOR AERONAUTICS  
NATIONAL BUREAU OF STANDARDS U.S. DEPARTMENT OF COMMERCE  
AMERICAN SOCIETY OF CIVIL ENGINEERS  
AMERICAN INSTITUTE OF ELECTRICAL ENGINEERS  
THE AMERICAN SOCIETY OF MECHANICAL ENGINEERS  
THE SOCIETY OF AMERICAN MILITARY ENGINEERS  
AMERICAN INSTITUTE OF MINING & METALLURGICAL ENGINEERS  
DISTRICT OF COLUMBIA SOCIETY OF PROFESSIONAL ENGINEERS  
THE INSTITUTE OF RADIO ENGINEERS, INC.  
THE CHEMICAL ENGINEERS CLUB OF WASHINGTON  
WASHINGTON SOCIETY OF ENGINEERS  
FAULKNER KINGSBURY & STENHOUSE ARCHITECTS  
CHARLES H. TOMPKINS COMPANY BUILDERS  
SOCIETY OF WOMEN ENGINEERS  
NATIONAL ACADEMY OF SCIENCES NATIONAL RESEARCH COUNCIL

THE PURPOSE OF THIS VAULT IS INSPIRED BY AND IS DEDICATED TO  
CHARLES HOOK TOMPKINS, DOCTOR OF ENGINEERING  
BECAUSE OF HIS ENGINEERING CONTRIBUTIONS TO THIS UNIVERSITY, TO HIS  
COMMUNITY, TO HIS NATION AND TO OTHER NATIONS

BY THE GEORGE WASHINGTON UNIVERSITY

ROBERT W. FLEMING  
CHAIRMAN OF THE BOARD OF TRUSTEES

CLOYD H. MARVIN  
PRESIDENT

JUNE 11, 1955

To cope with the expanding technology, our society must  
be assured of a continuing supply of rigorously trained  
and educated engineers. The School of Engineering and  
Applied Science is completely committed to this ob-  
jective.

# END